Adsorption Studies of Hazardous Air Pollutants in Microporous Adsorbents using Statistical Mechanical and Molecular Simulation Techniques

By

Rasesh R. Kotdawala

A Dissertation Submitted to the Faculty of
WORCESTER POLYTECHNIC INSTITUTE
In partial fulfillment of the requirements for the
Degree of Doctor of Philosophy
In
Chemical Engineering
By

March 2007

Research Committee:

Prof. Nikolaos Kazantzis, Major Advisor   Prof. Jennifer L. Wilcox,
                                                         Committee member

----------------------------   ----------------------------------

Prof. R.W. Thompson, Co- Advisor   Prof. Robert E. Connors,
                                                  Committee member
-----------------------------   Department of Chemistry and
                                                  Biochemistry, WPI

Prof. David DiBiasio
Head of the Department
Department of Chemical Engineering, WPI

Abstract

The primary goal of this research is to apply statistical mechanical and computer simulation methods to describe the equilibrium behavior of hazardous dipolar/quadru polar single-gases and mixtures confined in micro porous adsorbents. Statistical mechanical models capable of handling the energetic heterogeneity by complex electrostatic interactions between adsorbate –adsorbent and adsorbate- adsorbate electrostatic interactions were developed and studied. The heterogeneous pore shape and size of different adsorbents were taken into account by two different approaches described in the following paragraphs.

The usage of Mean Field Perturbation Theories (MFPTs) is more attractive than Monte-Carlo simulations because of the enhanced physical insights that they offer as well as very low computational times. Existing literature shows that the applications of MFPTs for studying adsorption of polar molecules were limited due to the orientation dependency of the intermolecular potentials for electrostatic interactions, that in turn poses the challenging problem of seeking analytical expressions for the various thermodynamic functions involved. Furthermore, other existing approaches of accounting for complex electrostatic interactions through hydrogen bonding have limitations due to the requirement of parameter estimation related to radial distribution functions and the critical orientation values of molecules for hydrogen bonds, which are generally obtained through MC simulations and X-ray scattering techniques.

In the first stage of research efforts, an attempt has been made to express angle-dependent intermolecular potentials in the form of angle-independent intermolecular potential terms by employing statistical averaging methods. In particular, the permanent dipole-dipole and permanent dipole-induced dipole intermolecular potentials were expressed as angle-averaged intermolecular potentials. Then, angle-averaged intermolecular potentials were used to predict water isotherms in nano slit .Further, the angle-averaged intermolecular potentials were used for a binary mixture of polar molecules (water-methanol) to predict the adsorption behavior in nano slit pores. However, significant limitations of MFPTs arise when they are used for the study of adsorption in zeolites that exhibit irregular shaped cavities with surface heterogeneities. The latter represent a future meaningful research direction. The mean field approach allows us to predict equilibrium sorption properties in homogeneous adsorbents like graphitic carbon (slit), carbon nano tubes (cylinder) and highly siliceous faujasites (spherical) as they have regular shaped cavities. The applications of such kinds of theory remained limited due to unknown distribution of functional sites on adsorbents of interests (mainly activated carbons and zeolites) and their locations in the adsorbent frame work.

The second stage of research efforts are on the models which handles surface heterogeneities and consider the complex pore geometries .The models developed are on grand canonical Monte-Carlo simulations. Two types of GCMC simulations were carried out namely molecular and atomistic MC simulations .Both techniques are applied to simulate sorption isotherms on zeolites and activated carbon to remove mercury chloride

(quadru pole), Hydrogen cyanide (HCN, dipole) and Methyl ethyl ketone (MEK, dipole) from air.

The molecular based MC technique utilizes molecular properties of the molecules namely dipole, quadrupole moments, molecular polarizability and molecule size (kinetic diameter).The molecule is considered to be a spherical shaped particle. The dispersion interactions are calculated using Vaan der Waals equation and electrostatic interactions are quantified by Multi-pole expansion method. This approach was used to simulate adsorption of $HgCl_2$, HCN and MEK in zeolite- NaX and activated carbon with functional sites namely carbonyl, hydroxyl and carboxyls. Simulation results indicate that $HgCl_2$ sorption was attributed to charge- induced dipole interactions for activated carbon, suggesting that sorbents with more number surface charges can be useful except for the case of carbonyls in which quadrupole moments plays a crucial role in reducing sorbent capacities implying that relative positions of positively and negatively charged cations are important. How ever, for zeolite NaX, the performance was attributed to charge-quadrupole interactions and dispersion interactions. Zeolite-NaX performance for capturing HCN and MEK was attributed to dipole-Na interactions due to large dipole moments of the molecules. In case of activated carbon, HCN sorption is governed by mainly charge-dipole and charge-induced dipole interactions and hence carbons with carboxyls perform better than hydroxyls and carbonyls. MEK sorption was influenced by dispersion interactions (due to large polarizability of MEK)and charge-dipole interactions which makes carbon with carbonyls more efficient rather than carbons with hydroxyls having same charge densities. How ever application of molecular approach is limited to sorbents with regular shape cavities having some surface heterogeneity like activated carbons. In order account sorbents with irregular shaped cavities as silicalite and mordenite have, one needs to use atomistic MC simulations.

 The atomistic MC technique utilizes atomic size and charges on atoms of the molecules to quantify intermolecular forces among   adsorbate molecules and atoms of zeolite frame work and activated carbon. . The dispersion interactions are calculated using Van-Der Waals equation and electrostatic interactions are quantified by coulomb equation. The bond distances among atoms were kept fixed but variations in angular movement and dihedral/torsional movements were considered and appropriate harmonic potentials were used to account angle bending and torsional effects. The sorption performance was evaluated for mordenite, silicalite and zeolite beta for Si/Al ratio of 47-197 for HCN and MEK system. The results of HCN/MEK sorption suggests that silicalite has greater capacity than that of mordenites .In case of MEK Zeolite beta with sodium cations performs better than that of mordenites and silicalites. Sorption of HCN in silicalite was in straight and zigzag channel and mainly due to hydrogen bonding among HCN molecules. The increase in sodium cations however decreases capacity of silicalite, zeolite beta and mordenite slightly. The sorption of MEK in mordenite was mainly in 12 and 8 member member ring channel. Increase in sodium cations do not increase sorption capacity of mordenite significantly as most of the cations in mordenite are located in 8-member ring channel where MEK molecules can not be accommodated properly due to steric effects. How ever sorption of MEK in zeolite beta is influence by presence of sodium cations as most of the cations are at the intersection of two 12 member rings

which provide sufficient space to orient MEK molecules at the intersection to maximize electrostatic interactions. Sorption of MEK in silicalite showed same trend as in case of mordenite as all cations are at the intersection of straight and zigzag channels .In the future and concluding remarks , a comparison is made of all three approaches in terms of their significance in applications and easiness in applying them.

Acknowledgement

First, I would like to give my sincere thanks to my Advisors Prof. Nikolaos Kazantzis and Prof. Robert Thompson for their support , insights, guidance and inspirations through out this project.

Thanks to the thesis committee members Prof. Robert Connors and Prof. Jennifer Wilcox for accepting to read this work.

Thanks to Department of chemical engineering, its faculty, staff and students for their cooperation and assistance during the PhD work.

Special thanks to my labmates Dr. Ozgur Yazaydin and Dr.Joseph Gnanaraj for their support and fun I had during my stay at WPI.

Thanks to my friends and family members, here and there.

Contents

Chapter 8 Study of Adsorption of Hydrogen Cyanide and Methyl Ethyl Ketone in Silicalite, Mordenite, and Zeolite Beta Structures

Index of Figures

List of tables

Chapter-1

Introduction to Adsorption

1.1 Applications of Adsorption

Adsorption is defined as the enrichment of one or more components in a solid(adsorbent)-fluid(adsorbate) interfacial layer. If one component of a mixture is adsorbed more strongly than the others, a surface (adsorbed) phase rich in the strongly adsorbed species is created. This enrichment forms the basis of separation of mixtures by adsorption operations. In addition to separations, adsorption of fluids in solid adsorbents has technical importance in catalysis, membrane processes and oil recovery. Adsorption processes are applied in the chemical, biochemical and petroleum industries to purifications and separations of gas and liquid mixtures[1].

Adsorption has always been the main industrial method for removal of trace components from stream, e.g. the removal of organic contaminants from drinking water or toxic substances from air.In the past thirty years, large scale adsorption processes for bulk gas and liquid separations have received increased attention because of two major events: the development of new adsorbents,such as zeolite molecular sieves, carbon nanotubes and invention of new process cycles , such as Pressure swing adsorption and thermal swing adsorption [2-3]

Distillation is generally the optimum choice for separation processes. However adsorption is competitive with distillation under certain conditions[1]:

1. When the key components have separation factors of the order of 1.2 or less(e.g. distillation of isomers).
2. When the components are supercritical gases (e.g. separation of air)

3. When the components of the mixtures are sensitive to relatively high temperatures(e.g. separation of proteins)

1.2 Industrial Adsorbent Materials

The most important properties of an industrial adsorbent are capacity, selectivity and stability over a prolonged period of time. The adsorptive capacity is a function of the adsorbent's surface area and porosity. Industrial adsorbents are highly porous materials with pore size distributions ranging from micropores of width below 20Å up to mesopores of width from 20 to 500 Å.selectivity depends on the equilibrium properties of the system, diffusion rates, and steric exclusion.polarity , chemical composition of the surface and the pore size distribution determine the ability of the adsorbent to separate molecules with different characteristics (e.g. size, shape,polarity etc.)

The main classes of adsorbents used in separation processes are silica gel, activated carbon, and zeolites. A description of their structure, properties and applications is given in several reviews (1-5). Activated carbon and zeolites represent two extreme cases with respect to their structure. Activated carbon has a random porous structure with a continuous pore size distribution.Energetic heterogeneity is caused by variations in pore size and polar groups located on graphite planes.Zeolites, on the other hand , have a very well characterized crystalline structure with virtually no distribution of pore sizes. Energetic heterogeneity is mainly caused by electrostatic interactions between the adsorbates and non-framework cations of zeolite.

1.3 Activated carbons

Activated carbon is normally made by thermal decomposition of carbonaceous material followed by activation with steam or carbon dioxide at elevated temperature (700-1100 C). The activation process involves essentially the removal of tarry carbonization products formed during the pyrolisis, thereby opening the pores. The structure of

activated carbon consists of elementary micro crystallites of graphite, but these micro crystallites are stacked together in random orientation and it is the spaces between the crystals which forms the microspores. The pore size distribution is trimodal. The typical range of surface area is 10-1000 m^2/g. The surface of carbon is essentially non polar although a slight polarity may arise from surface oxidation. As a result, carbon adsorbents tend to be hydrophobic and organophilic. They are therefore widely used for the adsorption of organics in decolorizing sugar,water purification , and solvent recovery systems as well as for the adsorption of gasoline vapors in automobiles and as a general purpose adsorbent in range hoods and other air purification systems.

Adsorptive properties and pore size distributions for activated carbon were reviewed by Dubinin(6),Scholten (8),Smisek and Cerny (9), and Hassler(7).

1.4 Silica Gels

Silica gel is a partially dehydrated form of polymeric colloidal silicic acid. The chemical composition can be expressed as SiO_2. nH_2O. The water content, which is present mainly in the form of chemically, bound hydroxyl groups, amounts typically to about 5 wt %

The presence of hydroxyl groups imparts a degree of polarity to the surface so that

molecules such as water, alcohols, phenols, and amines and unsaturated hydrocarbons are adsorbed in presence to non polar molecules such as saturated hydrocarbons. Because of its selectivity for aromatics silica gel was used as the adsorbent for separation of

aromatics from paraffins and napththenes but by far the most important current application is as a desiccant. The specific surface area of the silica gel is in the range of 340-800 m^2/g and pore volume is in the range of 0.42-1.15 cm^3/g. The average pore diameter is in the range of 22-140 Å.

1.5 Zeolite molecular sieves

Zeolites are porous crystalline aluminosilicates. The zeolite framework consists of an assemblage of SiO_4 and AlO_4 tetrahedra,joined together in various regular arrangements through shared oxygen atoms, to form an open crystal lattice containing pores of molecular dimensions into which guest molecules can penetrate. Since the microstructure is determined by the crystal lattice it is precisely uniform with no distribution of pore size.About 38 different zeolite framework structures have been identified, including both natural and synthetic forms. Detail reviews have been given by Breck(10), Barrer(11)

,Meier and Smith(12-13).The " Atlas of Zeolite Structures" prepared by Meier and Olson(14) contains numerous stereoscan pictures and is especially useful for quick reference.In considering zeolite frameworks it is convenient to regard the structures as built up from assemblages of secondary building units, which are themselves polyhedra made up of several SiO_4 and AlO_4tetrahedra. Each aluminum atom introduces one negative charge on the framework which must be balanced by an exchangeable cation. The exchangeable cations are located at preferred sites within the framework and play a very important role in determining the adsorptive properties. Available information on cation locations has been summarized by Mortier(15). Changing the exchangeable cation by ion exchange provides a useful and widely exploited means of modifying the adsorptive properties.

The Si/Al ratio in zeolite is never less than 1.0 but there is no upper limit and pure silica analogs of some of the zeolite structures have been prepared. The adsorptive properties show a systematic transition from the aluminium rich sieves, which have very high affinities for water and other polar molecules, to the microporous silicas such as silicalite which are essentially hydrophobic and adsorb n-paraffins in preference to water.The transition from hydrophilic to hydrophobic normally occurs at Si/Al ratio of between 8 and 10.By appropriate choice of framework structure, Si/Al ratio and cationic form ,adsorbents with widely different adsorptive properties may be prepared.It is therefore possible ,in certain cases ,to tailor the adsorptive properties to achieve the selectivity required for a particular separation.

The intra crystalline diffusivity and hence the kinetic selectivity and, in extreme cases, the molecular sieve properties are determined mainly by the free diameters of the windows in the intra crystalline channel structure. In zeolite such as a sodalite the channels are constricted by six-membered oxygen rings with free diameter of about 2.8 Å. These pores are so small that only small polar molecules such as H_2O and NH_3 can penetrate. In the "small-port" zeolites such as type A, chabazite, and erionite ,the limiting constrictions are eight-membered oxygen rings with free diameter of 4.2 Å while in the "large-port" zeolites, X and Y and mordanite access is through twelve membered oxygen rings which have free diameters of 7-7.4 Å.

The window aperture quoted here are the free diameters calculated from structural models assuming a diameter of 1.4 Å for the oxygen. Due to the effects of vibrations of both the diffusing molecule and the crystal lattice, these windows may be penetrated by molecules with critical kinetic diameters which are somewhat greater than the nominal aperture.The effective diameters of the unobstructed 8-,10- and 12-ring sieves are therefore approximately 4.5, 6 and 8.5 Å.

The reduction in the free diameter of the windows by blocking cations causes a dramatic reduction in the diffusivity of the guest molecules. The extent to which the windows are obstructed depends on the number and the nature of the cat ions since different cat ions show differing affinities for the window sites. By appropriate choice of cationic form it is sometimes possible to develop kinetic selectivity and even, in certain cases, to obtain a molecular sieve separation between species which can both diffuse easily in an unobstructed sieve(1).

1.6 Concluding remarks

The selection of the appropriate adsorbent is the most important step in all adsorption processes. The adsorbent affects the separation factor dramatically and a separation that otherwise would require extreme conditions of temperature and pressure can be carried out at ambient conditions. In addition to activated carbon and zeolites , new adsorbents, such as carbon fiber, hydrophobic polymers, molecular-sieve carbon, carbon nano tubes are being developed during the last ten years to extend the effectiveness of adsorptive separation to a wider range of mixture s. Besides the area of separations, one recent application of these new adsorbents is the storage of methane in gas cylinder at low pressure .The challenge is to concentrate the energy density of methane to make it comparable to gasoline, so that it can be used as an alternative clean fuel(Yang 2003).

Besides the great interest in adsorption as a phenomenon with a variety of industrial applications, the understanding of the adsorption mechanism in different adsorbents is of fundamental importance. In general, the adsorbed phase is a highly homogeneous fluid with properties significantly different than those of bulk phases. During the last ten years, considerable effort has been made towards the study of the structure and phase behavior of fluids confined in pores that are a few molecular diameters wide, such as the pores of most industrial adsorbents. In addition to the technological importance in adsorption, the

theoretical interest stems from the significant deviation of adsorbed fluid properties from those of bulk fluids, the diversity of phase transitions exhibited by these systems, and from availability of new theories and computational tools for modeling. For these reasons , it becomes apparent in the following chapter, The discussion will be on the models for the prediction of adsorbed phase thermodynamic properties for single component and multi component systems.

References:

1. D.M.Ruthevan, Principles of adsorption and adsorption processes, Wiley – Interscience Pvt.Ltd(1984)

2. Yang R.T , Gas separation by adsorption processes,Butterworth,Boston(1987)

3. Yang R.T., Adsorbents: Fundamentals and applications, Wiley – Interscience(2003)

4. D.P. Valenzuela and A.L.Myers, separation and purification methods,**13**,153(1984)

5. D.P. Valenzuela, Ph.D thesis, University of Pennsylvania(1987)

6. M M Dubinin, in chemistry and physics of carbon,Vol.2 (P.L. Walker,ed.)Dekker, New York(1966)

7. J.W. Hassler, Activated carbon, Chemical Publishing Co.(1974)

8. J.J.F.Scholten, Adsorption in porous carbon solids, Academic Press,London(1967)

9. M. Smisek and S. Cerney, Active carbon, Elsevier(1970)

10. D.W. Breck, Zeolite Molecular Sieves.Wiley, New York (1974)

11. R.M. Barrer, Zeolites and clay materials, academic press,London(1978)

12. W.M.Meirer, in Molecular sieves,Proceedings of the first international conference on Zeolites. Society of chemical Industry, London,(1968)

13. J.V.Smith, Adv. Chem.,**101,**171(1971)

14. W.M. Meier and D.H.Olson, Atlas of Zeolite structure types.juris Druck and Verlag A G,Zurich,(1978)

15. W. Mortier , Compilation of extra framework sites in zeolites.Butterworths, Guildford, England(1982)

Chapter 2

Thermodynamics of Adsorption

2.1 Classical thermodynamics of adsorption of single component systems

The thermodynamic approach to the study of equilibrium is quite general and may be applied to adsorption just as to any other phase equilibrium. The only general assumption which is implicit in such an approach is that the adsorbed layer can be treated as a distinguishable phase in the thermodynamic sense. It is possible to adopt two somewhat different but entirely consistent perspectives in applying thermodynamic principles to adsorption equilibrium. The surface layer, consisting of adsorbent plus adsorbate, may be considered as a single phase having the general properties of a solution. Alternatively, if the thermodynamic and geometric properties of the adsorbent can be regarded as independent of the temperature and pressure of the surrounding gas and the concentration of adsorbed molecules, the adsorbent may be considered as thermodynamically inert. Under these conditions the adsorbed molecules themselves may be regarded as a distinct phase and the effect of the adsorbent is limited to the creation of a force field, the detailed nature of which need not be specified. This view was originally formulated and applied by Gibbs by starting the formulation of isotherm equation for the adsorbed phase by equating chemical potentials of bulk and adsorbed phase(1).

The Gibbs adsorption isotherm (equation of state) is given by(1)

$$n_a \left(\frac{\partial \phi}{\partial p} \right)_T = \frac{RT}{p} n_s \quad \text{or} \tag{2.1}$$

$$A \left(\frac{\partial \pi}{\partial p} \right)_T = \frac{RT}{p} n_s \tag{2.2}$$

ϕ is three dimensional spreading pressure
π is two dimensional spreading pressure
n_s Surface concentration (moles of sorbate)
n_a Moles of non volatile adsorbent

2.1.1 Derivation of isotherm equations from the Gibbs equation

1. **Henry's law(1)**

   If the equation of state for the adsorbed phase corresponds to ideal gas law
   $$\pi A = n_s RT \tag{2.3}$$

Substituting (2) in (1)

$$\left(\frac{\partial \pi}{\partial P}\right)_T = \frac{\pi}{P} \qquad (2.4)$$

$$\pi = K'P \qquad (2.5)$$

$$q = \frac{n_s}{A} = \frac{K'P}{RT} = Kc \qquad (2.6)$$

Thus , There is a linear relationship between pressure and adsorbed phase concentration .

2. Langmuir Isotherm and Volmer Isotherm(2)

At somewhat higher concentrations one may postulate an equation of state of the form

$$\pi(A - \beta) = n_s RT \qquad (2.7)$$

In analogy with $P(V - b) = nRT$
Where b is the excluded volume parameter
Where β is effective molecular area/volume

$$\left(\frac{\partial \pi}{\partial A}\right)_T = \frac{n_s RT}{(A-\beta)^2} \qquad (2.8)$$

Using Gibbs' equation,

$$\frac{\partial P}{P} = -\frac{AdA}{(A-\beta)^2} \qquad (2.9)$$

If we assume $\beta << 2A$,which is a reasonable assumption at low concentrations, and neglect the term in β^2 in the denominator of equation(2.9), this expression integrates to

$$bP = \frac{2\beta/A}{1 - \left(\frac{2\beta}{A}\right)} = \left(\frac{\theta}{1-\theta}\right) \qquad (2.10)$$

Which becomes identical with the Langmuir   isotherm.

If w make no approximation concerning the relative magnitude of $\dfrac{\beta}{A}$ and integrate equation (2.7) directly, and setting $\theta = \dfrac{\beta}{A}$, we can have volmer equation,

$$bP = \left(\frac{\theta}{1-\theta}\right)\exp\left(\frac{\theta}{1-\theta}\right) \tag{2.11}$$

3. Van der Waals Isotherm(2)

The assumption of a Van der Waals equation of state for the adsorbed phase

$$\left(\pi + \frac{\alpha}{A^2}\right)(A - \beta) = n_s RT \tag{2.12}$$

Leads to the following equation

$$bP = \left(\frac{\theta}{1-\theta}\right)\exp\left(\frac{\theta}{1-\theta}\right)\exp\left(-\frac{\alpha'\theta}{RT}\right) \tag{2.13}$$

Where,
α Van der Waals attraction constant
$\alpha' = 2\alpha q_m$
q_m saturation limit , mono layer coverage

4. Virial isotherm(1)

Finally we may consider the adsorbed layer to obey a general equation of state of the virial form

$$\frac{\pi}{n_s RT} = 1 + A_1 n_s + A_2 n_s^2 + ... \tag{2.14}$$

Where A_1, A_2 ,.. are virial coefficients

Applying the Gibbs equation….

$$\frac{bp}{n_s} = \exp\left(2A_1 n_s + \frac{3}{2}A_2 n_s^2 + ...\right) \tag{2.15}$$

2.1.2 Isotherm equation for heterogeneous single component systems

1 .Bragg-Williams –Beta (BWB) Equation(2)

This model is based on the Bragg-Williams approximation for adsorbate-adsorbate interactions and the beta distribution for energetic heterogeneity. Because of its flexibility , the beta distribution is the most suitable continuous distribution for a finite range of energies. If ε is defined as the negative of the energy of adsorption, then:

$$\frac{\varepsilon - \bar{\varepsilon}}{kT} = t(z - \bar{z}) \tag{2.16}$$

With the dimensionless variable z following a beta distribution

$$f(z) = \frac{1}{B(a,b)} z^{a-1}(1-z)^{b-1} \qquad\qquad 0 \le z \le 1 \tag{2.17}$$

$$B(a,b) = \frac{\Gamma(a)\Gamma(b)}{\Gamma(a+b)} \tag{2.18}$$

The beta distribution for ε has the parameters ($\bar{\varepsilon}, t, a, b$) with a,b≥1 and is symmetrical for a=b.Thus the beta deistribution is distinguished by both its flexibility and its finite range of energies. For the patch wise modelof adsorption(Ross and Olivier,1964) , the single-gas adsorption isotherm is the integral of the local adsorption isotherm with respect to the energy distribution.

$$n(P) = \frac{1}{B(a,b)} \int_0^1 n(P,z) z^{a-1}(1-z)^{b-1} dz \tag{2.19}$$

Adsorbate-adsorbate interactions are introduced to the local adsorption isotherm n(P,z) Using the Bragg-Williams approximation for a two dimensional lattice gas

$$cP = \frac{\theta}{1-\theta} \exp\left(\frac{qw\theta}{kT}\right) \tag{2.20}$$

Where, $\quad c = c_0 \exp\left(\varepsilon/kT\right)$, $\theta = n/m = $ fractional coverage, w is the nearest neighbour energy for adsorbate-adsorbate interactions, and q is the number of nearest neighbour in the two-dimensional lattice.
Equation (2.20) can be simplified as following way,

Substituting $\kappa = \dfrac{qw}{kT}$ and $\bar{c} = c^0 \exp(\bar{\varepsilon}/kT)$, equation (2.20) can be written as

$$\bar{c} P \exp\left[t(\bar{z} - z) \right] = \frac{\theta}{1-\theta} \exp(\kappa\theta)$$ (2.21)

Thus, The BWB equation for adsorption of a pure gas has six parameters $(m, \bar{c}, t, a, b, \kappa)$.

M has units of mol/kg; $\bar{c}$ has a unit of Pa^{-1}; a,b, and κ are dimensionless.

1. **Hill –Deboer model**

In Hill – Deboer model, isotherms are modeled by considering the adsorption takes place on high and low energy surface patches.This two patch heterogeneous model is given by

$$N_t = N_s + N_l$$ (2.22)

Where , N_t is the total "observed" amount adsorbed

N_s and N_l are amounts adsorbed on high energy and low energy patches respectively.

The simultaneous equilibria of each surface patch with the vapor phase is described bu Hill deboer Model as following..

$$P = \exp\left(A_i^0 - U_i^o \big/ RT \right) \frac{N_i}{\left(N_i^\infty - N_i\right)} \exp\left(\frac{N_i}{N_i^\infty - N_i} - \frac{kN_i}{TN_i^\infty} \right)$$ (2.23)

The amount adsorbed on each patch(N_i) is calculated by solving (2.22) and (2.23) implicitly for the specified pressure and temperature. N_i^∞ is the saturation capacity of component i. The total amount adsorbed is then calculated by (2.20)

The combined van der Waals constant,k, contains the interaction (α) and size (β) parameters.

$$k = 2\alpha / R\beta$$ (2.24)

Where, R is the size of zeolite cavity.

2.1.3 Classical thermodynamics of adsorption of multi component system

Generally models dealing with multi component systems were developed based on the single component data available for each component constituting multi component system. These models are used to predict multi component adsorption isotherms from single component isotherms. The ideal adsorption solution theory (IAST)(3) and Vaccuncy solution theory (5) are the well accepted by scientific community.

2.1.3.1 Ideal Adsorption Solution Theory (IAST),(3):

The IAST [33,34] is essentially an application of Raoult's law to adsorbed phases. It is used to predict binary component adsorption system using two single component adsorption systems. For a given component i, we can write:

$$Py_i = P_i^0(\pi)x_i \qquad (2.25)$$

Where y_i and x_i are the bulk and pore mole fractions of i, respectively, P is the total bulk pressure, and $P_i^0(\pi)$ is the bulk pressure corresponding to spreading pressure π in the component isotherm of component i. For a given set of single components(i) adsorption data P_i^0 and π are related according to

$$\pi(P_i^0) = \frac{RT}{A}\int_0^{P_i^0} n_i^0(p)d\ln p \qquad (2.26)$$

$n_i^0(p)$ is amount of local single component adsorption. It is possible, for example, to calculate x_i for a given P and y_i by first solving for $P_i^0(\pi)$
in the equation

$$\sum_i \frac{Py_i}{P_i^0(\pi)} - 1 = 0 \qquad (2.27)$$

This equation follows from (2.25), since the sum of the mole fractions in the pore must equal unity. One can use Unilan/Toth equation(4) to fit the single component data obtained from experiments or simulation.

2.1.3.2 Vacancy Solution Theory(VST)(5)

In this theory the adsorption equilibrium between two "vacancy " solutions having different compositions is considered .One solution represents the gas phase and the other the adsorbed phase .The vacancy solution is composed of adsorbates and vacancies .The latter is an imaginary entity defined as the vaccum space Which acts as the solvent for the system. The theory was developed by Swanayen and Danner(5) as a method of predicting multi component adsorption equilibria from single component isotherms without the assumption of an ideal adsorbed phase.

The free energy of the adsorbed phase can be written in terms of spreading pressure(π) as following(5)

$$G_s = \mu_s(T,\pi)n_s - \pi A \tag{2.28}$$

Where, $\mu_s(T,\pi)$, is chemical potential of adsorbed phase, A is the surface area of the adsorbent and n_s number of molecules or surface concentration.

Differentiating at constant temperature and spreading pressure we may define a partial molar free energy or chemical potential as following.

$$\left(\frac{\partial G_s}{\partial n_s}\right)_{T,\pi} = \mu_s(T,\pi) - \pi \bar{A} \tag{2.29}$$

Where $\bar{A} = (\partial A / \partial n_s)_{T,\pi}$ is the partial molar area. According to Suwanayuen et al (5) , the adsorbed phase is considered as a mixture of sorbate and vacancies, we may express this potential in the usual manner in terms of a standard chemical potential and an activity:

$$\mu_s = \mu_s^0(T) + RT\ln(\gamma_v X_v) + \pi \bar{A} \tag{2.30}$$

Where $\gamma_v X_v$ is the activity of the vacancies. The standards state is taken as an infinitely dilute adsorbed phase for which $\gamma_v \to 1, X_v \to 1$ and $\pi \to 0$. The equation of state of the adsorbed phase is then seen to be

$$\frac{\pi \bar{A}}{RT} = -\ln(\gamma_v X_v) = -\ln[\gamma_v(1-\theta)] \tag{2.31}$$

Where θ is the function of saturation coverage.
Suwanayuen et al used the following Wilson expression to evaluate γ_v

$$\ln\gamma_v = -\ln\left[(1-\theta) + \lambda_1\theta\right] - \theta\left(\frac{\lambda_1'}{\theta + \lambda_1'(1-\theta)} - \frac{\lambda_1}{1-\theta+\lambda_1'}\right) \tag{2.32}$$

Which leads by the same argument to the isotherm equation,

$$bp = \frac{\theta}{1-\theta}\lambda_1'\left(\frac{1-(1-\lambda_1)\theta}{\lambda_1'+(1-\lambda_1')\theta}\right)\exp\left(-\frac{\lambda_1(1-\lambda_1)\theta}{1-(1-\lambda_1)\theta} - \frac{(1-\lambda_1')\theta}{\lambda_1'+(1-\lambda_1')\theta}\right) \tag{2.33}$$

But the other expressions for the activity coefficient can be used. The above equation contains four parameters (b, λ_1, λ_1', and n_∞, which is contained in θ) and is capable of fitting virtually all single-component isotherms.

The extension to an adsorbed mixture follows naturally although the calculations are somewhat tedious. For each adsorbed species, assuming an ideal vapor phase,

$$\mu_i = \mu_{is}^0(T) + RT \ln p_i = \mu_{is}^0(T) + RT \ln(\gamma_i X_i^{'}) \tag{2.34}$$

$$p_i = \gamma_i X_i^{'} \exp\left(\frac{\Delta G_i^0}{RT} + \frac{\pi \bar{A}}{RT}\right) \tag{2.35}$$

Where $\Delta G_i^0 = \mu_{is}^0 - \mu_{ig}^0$ and $X_i^{'} = X_i \theta$ is the mole fraction of component i in the adsorbed phase, including the vacancies as a hypothetical species, X_i is the actual mole fraction in the adsorbed phase, and $\theta = \dfrac{n_m}{n_{m\infty}}$ is the total fractional coverage calculated relative to the saturation limit for a mixture of the specified composition. $\Delta G_i^0 \big/ RT$ and

$\pi \bar{A} \big/ RT$ may be derived from the single-component isotherms while the activity coefficient for the mixed phase may be derived in terms of the Wilson parameters $\lambda_1, \lambda_1^{'}$, λ_2 and $\lambda_2^{'}$ and the cross coefficients λ_{12} and $\lambda_{12}^{'}$ according to the combining formula given by Prausnitz (6)

$$\ln \gamma_k = 1 - \ln\left(\sum_{j=1}^{n} X_j \lambda_{kj}\right) - \sum_{i=1}^{n}\left(\frac{X_i \lambda_{ik}}{\sum_{j=1}^{n} X_j \lambda_{ij}}\right) \tag{2.36}$$

The parameters $\lambda_1, \lambda_1^{'}, \lambda_2$ and $\lambda_2^{'}$ are known from the fit of the single-component isotherms but additional assumptions are required in order to estimate the cross coefficients λ_{jk}.

for many systems it has been found that the cross coefficients are related by

$$\frac{\lambda_{12}}{\lambda_{21}} = \frac{\lambda_1}{\lambda_1^{'}} \frac{\lambda_2^{'}}{\lambda_2} \tag{2.37}$$

So only one parameter, in addition to those obtained from the single component isotherms, is required.

Thus, in the derived equation of state for the adsorbed phase, the non-ideality of the adsorbed solution is accounted for in terms of an activity co-efficient whose composition dependence is described by the Wilson equation.

2.2 Statistical thermodynamics of single component and multi component systems

Adsorbed fluids are highly inhomogeneous with density that varies significantly over molecular dimensions. The objective of statistical mechanical theories of adsorption is the calculation of the single-particle density profile ρ(r) , from which total amount adsorbed can be evaluated as

$$N = \int \rho(r)dr \tag{2.38}$$

Distribution function and density functional theories have been applied to problems of inhomogeneous fluids.Solutions of the Ornstein-Zernike relation for the problem of a fluid in contact with a planar wall have been obtained for a number of approximate closures, including both the hypernatted- chain (HNC) and the Percus-Yevick (PY) equations. The application of these distribution function theories has been discussed by Nicholson and Personage (7) and Hansen and McDonald(9). The distribution function theories give good results for the problem of a hard-sphere molecules adsorbed on a hard wall, but they are less satisfactory when the fluid-fluid potential has an attractive part.Rowlinson and Widom (10) discussed the solution of Yvon-Born-Green (YBG) equation to such problems and Vanderlick et al.(10) calculated with this model density profiles for a L-J fluid confined in a slit of attractive walls.

The application of density functional theories (DFT) to highly inhomogeneous L-J fluids was more successful than that of the distribution function models mentioned above.DFTs Require as input a homogeneous fluid equation of state , such as the mean-field approximation based either on a Clausius or on a Carnaham/Starling(11) hard-sphere reference fluid. The starting point of DFT is the grand potential function ,which is the appropriate function of the density profile ρ(r),when a fluid is considered in an external field U^{ex}(r)(interactions of fluid with adsorbent) , at a fixed temperature T and chemical potential μ(Hansen and McDonald(9)):

$$\Omega[\rho(r)] = F[\rho(r)] + \int \rho(r)[U^{ex}(r) - \mu]dr \tag{2.39}$$

Where $F[\rho(r)]$ is the Helmholtz free energy functional. The equilibrium density profile is the solution of the Euler-Lagrange equation for the minimization of the grand potential

as following,

$$\frac{\delta F[\rho(r)]}{\delta \rho(r)} + (U^{ex}(r) - \mu) = 0 \tag{2.40}$$

In case of perturbation theories of homogeneous fluid, $F[\rho(r)]$ id divided into two parts:

$$F[\rho(r)] = F^{hs}[\rho(r)] + \frac{1}{2}\iint \rho(r)\rho(r')\varphi^{att}(|r - r'|)drdr' \tag{2.41}$$

The first part is the hard-sphere functional and the second is the attractive contribution of the intermolecular potential $\varphi(r)$, treated in a mean-field approximation. The hard sphere functional is unknown and can be expressed as:

$$F^{hs}[\rho(r)] = \int f^{id}(\rho(r))dr + \int \rho(r)\Delta f^{hs}(\overline{\rho}(r))dr \qquad (2.42)$$

$f^{id}(\rho(r))$ is the ideal-gas part of the free energy density, $\Delta f^{hs}(\overline{\rho}(r))$ is the excess free energy of a homogeneous hard-sphere reference fluid of density ρ , and $\overline{\rho}(r)$ is a spatial average of the local density over a small domain.

Different DFTs can be derived depending on the expression for the density $\overline{\rho}(r)$. The local density approximation (Sullivan et al,(12)), that assumes $\overline{\rho}(r) = \rho(r)$ is the simpler density functional theory, but gives a poor representation of the fluid structure and fails to reproduce phase diagrams and adsorption isotherms found by simulation(Peterson et al., 1986,1988)

Vanderlick et al.(10) compared the performance of several theories involving more complex expressions for $\overline{\rho}(r)$ than that of the local density approximation. The model proposed by Tarazona et al. (15) gives the best overall results for L-J fluids confined in cylinders and slits of attractive walls(Tarazona et al.(15))

The pure fluid case was easily generalized to a special kind of mixtures for which the hard cores of the different components are equal (Heffelfinger et al.(16)). Tan et al reported an extension of Tarazona's model for hard sphere mixtures of different size near a hard wall.

In case of binary mixture, the grand potential functional is given by :

$$\Omega[\rho_1, \rho_2] = F[\rho_1, \rho_2] + \sum_{i=1}^{2}\int \rho_i(r)[U_i^{ex}(r) - \mu_i]dr + \frac{1}{2}\sum_{i,j=1}^{2}\iint drdr'\rho_i(r)\rho_j(r')\phi_{ij}^a\left(\left|r - r'\right|\right)$$

$$(2.43)$$

Here ρ_i is the number density (the subscript i indicates species i), μ_i is the chemical potential, U_i^{ex} is the external potential, and ϕ_{ij}^a is the attractive part of the pair potential ϕ_{ij} . $F[\rho_1, \rho_2]$ is the intrinsic Helmholtz free-energy functional of a hard-sphere mixture, given by

$$F[\rho_1, \rho_2] = k_b T \sum_{i=1}^{2}\int dr\rho_i(r)[\ln(\lambda_i^3\rho_i(r) - 1] + \sum_{i=1}^{2}dr\rho_i(r)\psi_i^{ex}(\overline{\rho_1}(r), \overline{\rho_2}(r)) \qquad (2.44)$$

Where T is the temperature, λ is the thermal de Broglie wave length, $\overline{\rho_i}(r)$ is the smoothed density, and ψ_i^{ex} is the excess free energy per particle, which is given by

$$\psi_i^{ex}(\bar{\rho}_1, \bar{\rho}_2) = \mu_i^{hs}(\bar{\rho}_1, \bar{\rho}_2) - \frac{p^{hs}(\bar{\rho}_1, \bar{\rho}_2)}{\bar{\rho}_1 + \bar{\rho}_2} - k_b T[\ln(\lambda_i^3 \bar{\rho}_i) - 1] \qquad (2.45)$$

In which μ_i^{hs} and p^{hs} are the chemical potential and pressure of a hard –sphere mixture

with uniform densities, $\bar{\rho}_1$ and $\bar{\rho}_2$ which can be calculated by expression mentioned by Tan et al.. The hard sphere diameters of the two components are assumed to be temperature-dependent (decreasing with increasing pressure) and are calculated by empirical equation mentioned by Tan et al.

Comparison between the theoretical results and the simulations for the density profiles of a binary mixture shows that this theory is capable of predicting the structure of hard-sphere mixtures against a hard wall up to a size ratio R=σ$_2$/σ$_1$ =3. for R greater than 3 , this theory gives some discrepancies very close to wall.

Although, for the problems studied , some theories agreed fairly well with the simulation data, serious computational problems may arise for more systems, such as zeolite cavities. To date, the application of DFTs is limited to systems in which the density profiles are a function of only one spatial coordinate and to structure less L-J molecules. The solution of the integral density functional equations becomes very difficult when the fluid-solid potential field $U^{ex}(r)$ is a function of all three spatial coordinates or when the molecules have multi pole moments.

2.3 Molecular simulations of single component and multi component systems

Computer simulations are now an established tool in many branches of science. These methods rely on the use of high- speed computers to solve complex multi body problems formulated to represent the molecular behavior of a physical system.
At the outset of a simulation stands a well-defined model describing the intermolecular interactions in the physical system, Fig.1. In particular, in adsorption problems, these intermolecular interactions can be divided into two main groups of potentials: a) solid-fluid potentials, that describe the interactions between the adsorbates and the solid surface, and b) fluid-fluid potentials., which describe the interactions between the adsorbed molecules. The potential may be based upon rigorous quantum mechanical theories (e.g. dispersion potential) and parameters determined from ab initio calculations or on empirical expressions with parameters extracted from experimental data, such as Henry constant , isosteric heat at zero coverage, etc.

A molecular simulation is performed with 100-1000 molecules that interact through the potentials describing the physical system. Simulations of many more(~10000) and fewer (~10) molecules are also encountered. Although the number of molecules in the "simulation box" is several order of magnitudes smaller than in any macroscopic system, it is surprising how well these small systems mimic macroscopic properties.

The methods of computer simulations can be divided into two basic fundamental

approaches:

1. Deterministic methods- Molecular Dynamics(MD)
2. Stochastic methods-Monte-Carlo (MC)

The idea behind MD is to use the intrinsic dynamics of the model to propagate the system. The equations of motion of the multi body system are integrated numerically and averages are recorded for the properties of interest. For a collection of particles governed by classical mechanics, that yield a trajectory of positions X^N and momenta p^N in the phase space.The main advantage of MD is that it preserves the time element of the simulation and thus allows computation of dynamical quantities, e.g. diffusion coefficients and characteristic frequencies. The MD simulation techniques will not be discussed as the goal of study is to predict adsorption thermodynamic properties.

The Monte Carlo (MC) method is essentially a numerical technique for evaluating multidimensional integrals such as the following equation efficiently (Heermann et. al.(17)).

$$\langle A \rangle = Z^{-1} \int_{\Omega} A(x) f(H(x)) dx \qquad (2.46)$$

Where: $Z = \int_{\Omega} f(H(x)) dx \qquad (2.47)$

Where A is the macroscopic property of the system with n degrees of freedom, $X=(x_1,x_2,.....,x_n)$ and a Hamiltonian H(x)

The set of all states x constitutes the available space Ω. f(H(x)) is the distribution function that specifies an ensemble with a partition function Z.
The degrees of freedom are usually molecular positions, orientations, momentum, and depending upon which ensemble the simulation is based, can include volume, number of molecules etc. The momentum part can always be integrated out, and therefore only the configurational part of the Hamiltonian is calculated. The integrals are evaluated by a probability evolution in the phase space, called Markov process. MC methods contain
 no time element, and thus can not be used to evaluate dynamical properties. However, they are generally simpler to implement than are MD simulations. An excellent description of molecular simulations methods is given by Allen and Tildesley(18) and Sadus(19).
The outputs of the simulation are thermodynamic (equilibrium) and dynamical properties
In adsorption systems, single and multi component isotherms, integral and differential heats, phase diagrams, and diffusion coefficients are the properties most frequently calculated. The motivation for calculating properties of physical systems by computer simulations is manifold. Due to their ability to provide exact solutions of complex models, computer simulation results are a standard against which approximate statistical mechanical and thermodynamic theories may be compared. In addition simulations allow the comparison of the molecular model with experiment and provide a means to assess the validity of the intermolecular potentials.Finally, with computer simulations,properties

or microscopic behaviors that may be difficult or impossible to measure in an experiment(e.g. isosteric heats of binary adsorption) can be evaluated.

2.3.1 Molecular Simulations in the evaluation of adsorption equilibria

The calculation of phase equilibrium is one of the most important applications of molecular simulation. Gubbins(8) reviewed the role and the methods of computer simulations in studying the equilibrium properties of bulk phases. In adsorption ,phase equilibrium has been studied with MD in the micro canonical ensemble , and MC in the canonical , grand canonical, Gibbs , and constant pressure ensembles.

In the grand canonical ensemble, the chemical potentials are independent variables; thus, for adsorption from pure gases and gas mixtures, isotherms are obtained directly from simulation, in contrast to other ensembles (canonical, micro canonical), in which this is not possible. The pressure and the composition of the gas phase corresponding to a particular value of the chemical potential are calculated either from the ideal-gas law or at higher pressures from equation of state. In grand canonical ensemble, any thermodynamic property for a single component system can be described as(19)

$$\langle A \rangle = \frac{\sum_{i=1}^{N} A(i) \exp[{}^{(N\mu - U(i))}\!\!\big/\!\!{}_{kT}]}{\sum_{i=1}^{N} \exp[{}^{(N\mu - U(i))}\!\!\big/\!\!{}_{kT}]} \tag{2.48}$$

Where μ is the chemical potential and $U(i)$ is the potential energy of molecule i .k is the Boltzmann's constant.

For a binary mixture system, any thermodynamic properties can be written as following (19).

$$\langle A \rangle = \frac{\sum_{i=1}^{N_j} A(i) \exp[{}^{(N_1\mu_1 + N_2\mu_2 - U(i))}\!\!\big/\!\!{}_{kT}]}{\sum_{i=1}^{N_j} \exp[{}^{(N_1\mu_1 + N_2\mu_2 - U(i))}\!\!\big/\!\!{}_{kT}]} \quad \text{where, i=1,2} \tag{2.49}$$

2.3.2 Simulation method for single component and binary component systems

Adsorption isotherms and phase diagrams are obtained as a function of chemical potentials(as a function of fugacity), that are independent variables in the grand canonical ensemble .If the bulk phase is a gas, its pressure and composition can be calculated from

an equation of state ,given the fugacity and the critical properties of the fluids; thus ,MC results can be compared directly with experimental data.

One disadvantage of the GCMC method is that it has difficulty in sampling dense regions of the configurational space(e.g. multilayer adsorption ,adsorption from liquids)
The simulations follow the methods developed for bulk fluids(Adam(20) , and Allen and Tildesley(18)) and fluids adsorbed in cylindrical pores and slits(Peterson and Gubbins,(21))The procedure is given below both for simulations of single-gas adsorption and binary mixtures(See Fig.2.2 for single gas adsorption and Fig.2.3 for adsorption from a binary mixture):

Initial configuration and equilibration:

Depending on the value of the chemical potential,2-12 molecules are placed at random Locations inside the host cavity at the start of a run. An insertion is accepted only if the total energy of the system is less than zero. Because the simulation starts from a random configuration , the first 10000-50000 cycles are discarded. Each simulation is divided into ten blocks and it is assumed that the system has reached equilibrium if the results of the first block are within the standard deviation of the results from the following blocks.

Displacement and rotation steps:

Displacements are handled using the normal Metropolis method. The maximum allowed displacement is adjusted during the simulation to give an average acceptance ratio of 50% for the attempted moves. In the case of molecules with point quadrupole moments or point dipole moments , orientations of molecules are generated using random number generator. A random number is generator between 0 to π or 0 to 2π .

For the single component and binary component system , particle displacement is accepted with probability(2):

$$p = \min\left[1, \exp\left\{\frac{-\Delta U}{kT}\right\}\right]$$ (2.50)

Creation and Destruction Steps:

A random decision is made whether to try to add a molecule to the cavity or try to remove one. In the creation step, a position in the cavity is chosen at random and a new configuration is created by inserting a molecule at this position. The molecules with point dipole/quadrupole moments , the orientation of the molecule is also chosen randomly.

The particle creation is accepted with probability(2):

$$p = \min\left[1; \exp\left\{\frac{-\Delta U}{kT} - \ln\frac{(N+1)kT}{fV}\right\}\right]$$ (2.51)

Where ΔU is the configurational energy change for creation of a particle , N is the current number of molecules in the cavity before the attempted creation,V is the volume of the cavity and f is the fugacity in the gas phase.

For adsorption from a binary mixture, the particle creation of component i is accepted with probability(2):

$$p = \min\left[1; \exp\left\{\frac{-\Delta U}{kT} - \ln\frac{(N_i + 1)kT}{Py_iV}\right\}\right] \qquad (2.52)$$

Where N_i is the current number of molecules of component i in the cavity before the attempted creation, P is the pressure and y_i is the mole fraction in the ideal gas phase.

In the destruction step, a molecule is chosen at random and a new configuration is created by removing the molecule from the cavity. The particle destruction is accepted with probability(2):

$$p = \min\left[1; \exp\left\{\frac{-\Delta U}{kT} + \ln\frac{NkT}{fV}\right\}\right] \qquad (2.53)$$

For adsorption from a binary mixture , the particle destruction of component i is accepted with probability(2):

$$p = \min\left[1; \exp\left\{\frac{-\Delta U}{kT} + \ln\frac{N_ikT}{Py_iV}\right\}\right] \qquad (2.54)$$

The particle creation and destruction steps have been performed to satisfy the condition of microscopic reversibility. For simulations of binary mixtures, first, a random decision was made to create or remove a molecule. Then, the species to be created or destroyed were selected with an equal probability. Microscopic reversibility must apply to creation and destruction of each component separately. The algorithms for the simulation of single component and binary components are given in Fig. 2.2 and 2.3.

Convergence problems may arise in a GCMC simulation, particularly for fluctuation quantities ,when the system density is near that of a dense fluid(Adams et al,(20)) These problems arise from low acceptance ratios for creation attempts. (Adams et al,(20)) argued that ensemble averages are not affected and (Mezei et al(22)) showed that liquid densities calculated by GCMC are quite accurate even when the acceptance ratio for particle creation steps is as low as 0.1%.Total number of cycles (one cycle includes the

move and creation and destruction steps) necessary to achieve an acceptable accuracy depends on the density, the molecule simulated and the number of components.

The predictive power of computer simulations has increased significantly during recent years .Because of the availability of powerful computers, complex models that describe intermolecular interactions accurately are used. Thus, computer simulations can be used as a predictive tool in "thermodynamic property evaluators", and eventually for computer aided design of new materials,(see fig.2.1) For instance, in adsorption applications, computer simulations will be used for screening alternative structure of adsorbent materials, in the same way , the properties of traditional adsorbents could be improved or new materials with the desired properties could be developed with minimum experimental effort.
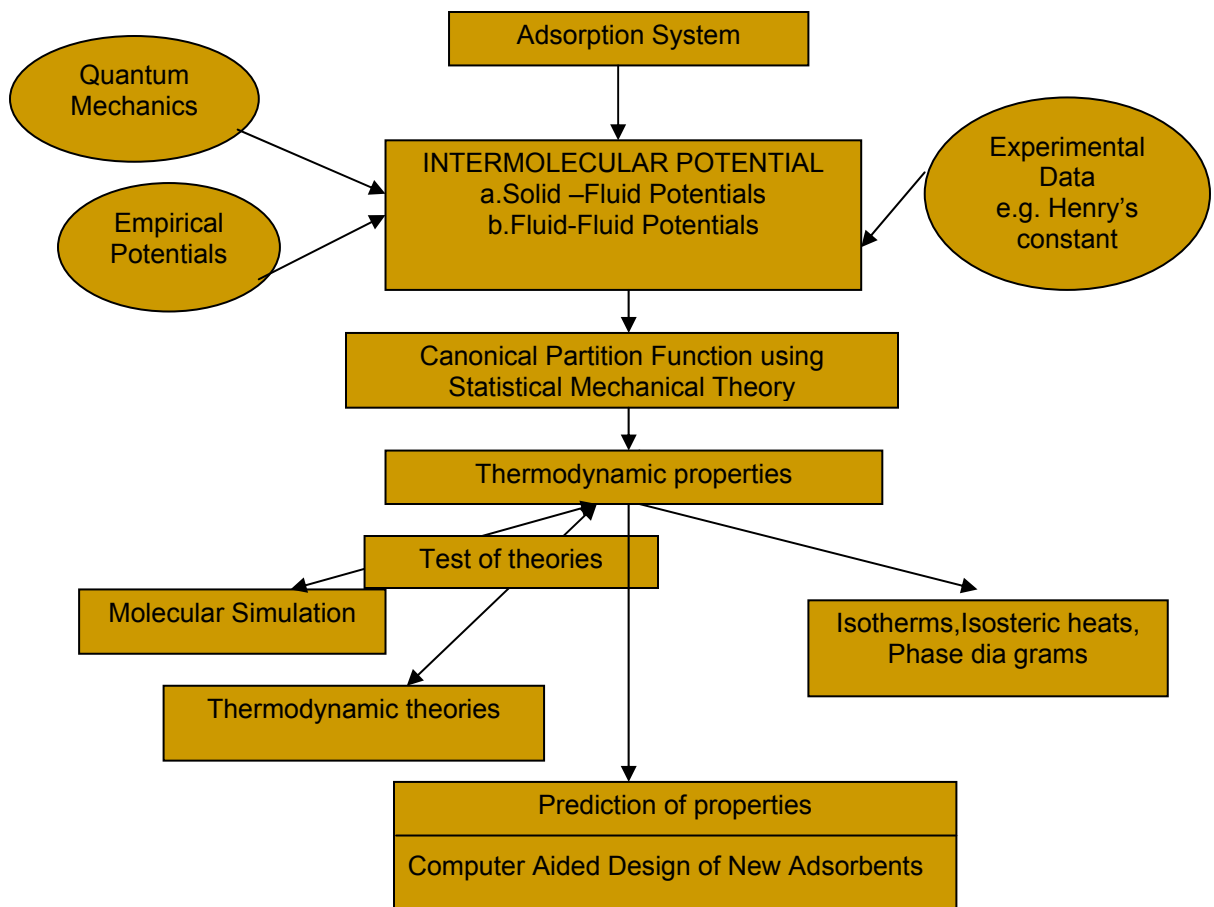
Fig. 2.1: Use and applications of molecular simulations in adsorption

```
┌─────────────────────────────────────────────────┐
│     Select initial configuration equilibration   │
└─────────────────────────────────────────────────┘
                        │
                        ▼
┌─────────────────────────────────────────────────┐
│   Random decision to move, add or remove  a molecule │
└─────────────────────────────────────────────────┘
                        │
                        ▼
┌─────────────────────────────────────────────────┐
│        Select a molecule at random and move it    │
│                                                   │
│        p = min[ 1, exp{ −ΔU / kT } ]              │
└─────────────────────────────────────────────────┘
                        │
                        ▼
┌─────────────────────────────────────────────────┐
│      Select a molecule at random and remove it    │
│                                                   │
│      p = min[ 1; exp{ −ΔU/kT + ln NkT/fV } ]     │
└─────────────────────────────────────────────────┘
                        │
                        ▼
┌─────────────────────────────────────────────────┐
│                Add a molecule with                │
│                                                   │
│     p = min[ 1; exp{ −ΔU/kT − ln (N+1)kT/fV } ]  │
└─────────────────────────────────────────────────┘
```

Select initial configuration equilibration

Random decision to move, add or remove a molecule

Select a molecule at random and move it

$$p = \min\left[1, \exp\left\{ \frac{-\Delta U}{kT} \right\} \right]$$

Select a molecule at random and remove it

$$p = \min\left[1; \exp\left\{ \frac{-\Delta U}{kT} + \ln \frac{NkT}{fV} \right\} \right]$$

Add a molecule with

$$p = \min\left[1; \exp\left\{ \frac{-\Delta U}{kT} - \ln \frac{(N+1)kT}{fV} \right\} \right]$$

Fig. 2.2 Algorithm for Monte Carlo simulation of a Grand Canonical
Ensemble for single gas adsorption
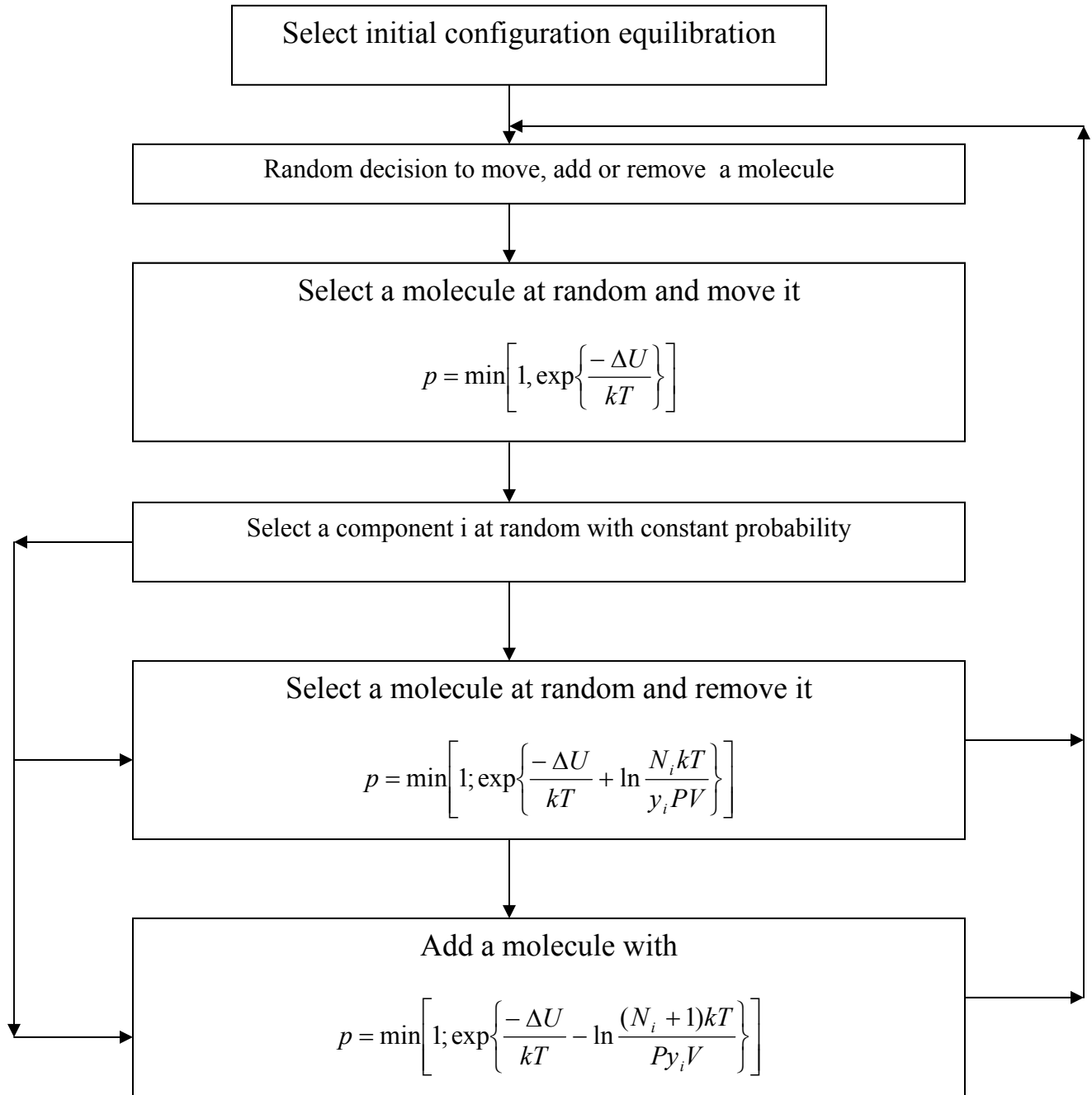
Fig. 2.3 Algorithm for Monte Carlo simulation of a Grand Canonical
Ensemble for binary mixtures

References:

1. D.M.Ruthevan, Principles of adsorption and adsorption processes, Wiley – Interscience Pvt.Ltd(1984)
2. F. Karavias, Ph.D Thesis, University of Pennsylvania (1992)
3. A.L.Myers, J.M. Prausnitz, AICHE J. ,**11**,121(1965)\
4. D.P. Valenzuela and A.L.Myers, Adsorption equilibrium data handbook, (Prentice – Hall,NJ.,1989)
5. Suwanayuen S. and Danner R.P., AICHE ,**26**,68 (1980)
6. J.M.Prausnitz, R.N.Lich Tenthaler and E.Gomes de Azevedo, Molecular Thermodynamics of Fluid-Phase Equilibria, 3rd ed.(Prentice-Hall, NJ, 1999)
7. D. Nicholson, and N.G.Parsonage, Computer simulation and the statistical mechanics of adsorption, Academic press,London(1982)
8. K.E.Gubbins, Mol.Simulation,**2,**223(1989)
9. J.P. Hansen and I.R. McDonald, Theory of simple fluids, Academic press.London(1986)
10. J.S Rowlison, B.Widom , Molecular theory of capillarity ,Clarenson Press, Oxford(1982)
10. T. K. Vanderlick, L.E.Scriven, and H.T.Davis,J. chem..Phys.,**90**,2422(1989)
11. T.M. Reed, and K.E.Gubbins, Applied Statistical Mechanics,(Mc-Graw Hill, NewYork, 1973)
12. D.E. Sullivan, Phys.Rev. B,**20,**3991(1979)
13. B.K.Peterson, J.P.R.B. Walton and K.E.Gubbins,Chem. Soc.Faraday Trans,**82,**1789(1986)
14. B.K.Peterson, K.E. Gubbins, G.D.Heffelfinger,U.M.B. Marconi, and F. van Swol, J. chem..Phys. **88**(1988)
15. P.Tarazona, U.M.B. Marconi and R.Evans, Mol.Phys.,**60,**575(1987)
16. G.S. Heffelfinger , Z.Tan ,K.E.Gubbins, U.M.B.Marconi and F. van Swol, Mol.Sim.,**2**,393(1989)
16. Z. Tan Ph.D Thesis, Cornell University (1991)
17. D.W. Heermann, Computer Simulation methods in theoretical physics,Springer-Verlang,Berlin(1986)
18. M.P. Allen, D.J.Tildesley, Computer simulation of Liquids, Clarendon Press, Oxford,(1987)
19. R.J.Sadus, Molecular simulation of fluids –Theory, Algorithms and Object-Orientation,Elsevier(1999)
20. D J Adams, Molecular Phys., **29**,307(1975)
21. B.K.Peterson, K.E.Gubbins, Mol. Phys., **62**,215(1987)
22. M.Mezei, Mol.Phys.,**61,**565(1987)

Chapter 3

Literature Review of statistical mechanical theories

3.1. Statistical Mechanical Theories for single component system

The perturbation theories and the density functional theories are the most popular statistical mechanical theories, in which thermodynamic properties of the system are expressed in terms of the densities of the molecules. The following section describes different studies on adsorption carried out by scientific community using these theories.

Peterson et al.[1] studied the behavior of LJ fluid confined within the cylindrical pore .The simulations were carried out at different pore radius, pressure, temperature and strength of fluid-wall forces to predict density profile and grand potential of the fluid within the pore for argon/carbon dioxide- graphite system. They found that the gas-liquid transition takes place below the bulk vapor pressure in all the cases and for a fixed temperature, when the pore radius is decreased the gas-liquid co-existence curve ends in a critical point.

Evans et al[2] studied the capillary condensation phenomena in cylindrical and slit-like pores using simple density functional theory (As explained in chapter 2) and Kelvin equation for L-J fluid. The reference fluid was hard sphere fluid modeled by Carnhan-Starling equation of state. For temperature T corresponding to a partial wetting situation , a first –order phase transition from dilute 'gas' to dense 'liquid' occurs at relative pressure(P/Psat) close to those predicted by macroscopic Kelvin equation, even for radius R or wall separation H as small as 10 molecular diameters. In a complete wetting situation ,where thick film develops , the Kelvin equation is , in general not accurate. At fixed T, the adsorption coverage exhibit a loop; The coverage jumps discontinuously at the first-order transition, but the accompanying metastable portions of the loop could produce hysteresis similar to that observed in adsorption measurements on meso-porous solids. Meta stable thick films persists to larger P/P_{sat} .in slits than in cylinders and this has repercussions for the shape of hysteresis loops. For a given pore size the loop in the adsorption coverage shrinks with increasing T and disappears at a capillary critical temperature T_C^{cap} ($<T_c$) .If $T > T_C^{cap}$, condensation no longer occurs.

Truskett et al.[3-4] proposed an analytical model for studying the thermodynamics and phase behavior of water like fluid(polar fluid) confined between hydrophobic surfaces based on mean field perturbation theory.. The model accounts the hydrogen bonding term as a intermolecular fluid-fluid forces and van –der waals's interaction fluid-fluid forces. The model was developed for mean field theory and non-local density functional theory. The hydrogen bonding interaction energy was modeled based on the following hypothesises.

1. One of the two participating molecules must have a cavity of radius r_i, empty of any molecular centers, surrounding it as shown in Fig. 1 .
2. The pair must be separated by a distance r that lies within the hydrogen –bonding shell of the central molecule, with $r_i \leq r \leq r_o$
3. The pair must exhibit mutually favorable orientation, $\Phi_1, \Phi_2 \leq \Phi^*$;
4. The presence of additional molecules in the hydrogen bonding shell "crowds" and thereby probably weakens the existing bond. We assign strength $-\varepsilon_{max} = -23KJ/mol$ to a hydrogen bond and a penalty $\varepsilon_{pen} = 3KJ/mol$ for each nonbonding molecule in the hydrogen-bonding shell. It follows that if more than seven nonbonding molecules are contained in the hydrogen-bonding shell, the central molecule is not available for bonding.

Based on the above considerations the proposed hydrogen bonding energy term is given by the following equation.(6)

$$U_{HS} = -N\beta \left[\ln(4\pi) + \sum_{j=1}^{8} p_j^{pore}(\rho_p, \zeta) \ln f_j \right] \tag{3.1}$$

Where β is Boltzman constant

$$f_j = \left[1 + \frac{j}{4}(1 - \cos\Phi^*)^2 (\exp\{\beta\varepsilon_j\} - 1) \right] \tag{3.2}$$
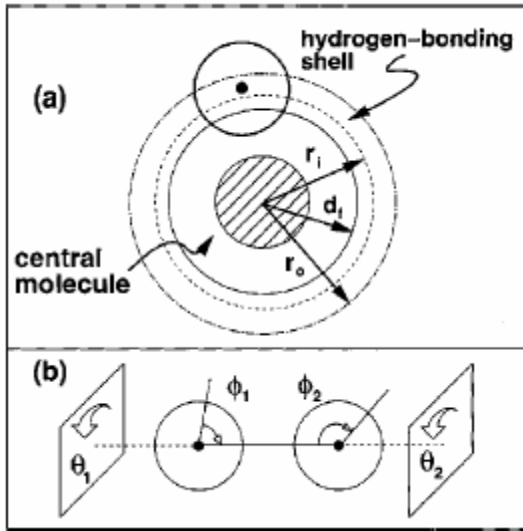
Fig.3.1(a) schematic presentation of central molecule and the molecule in the hydrogen bonding shell(the ring between $r=r_i$ and $r=r_0$). (b)Two participating molecules must be properly oriented ($\Phi_1, \Phi_2 \leq \Phi^*$) regardless of θ_1 and θ_2 (6)
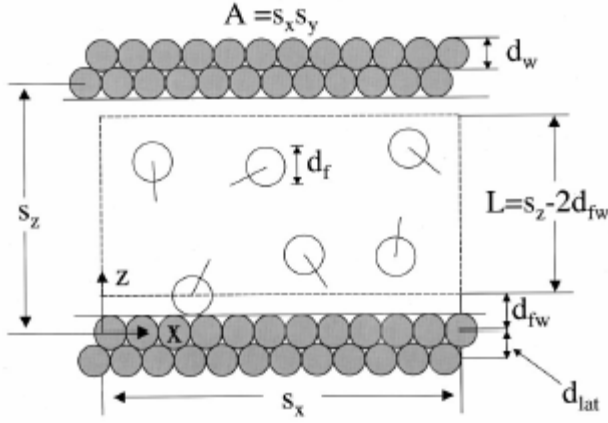
Fig.3.2 Schematic presentation of fluid confined between two parallel plates

Where, $\varepsilon_j = -\varepsilon_{max} + (j-1)\varepsilon_{pen}$, (j-1) is the number of non-bonded molecules in the hydrogen bonding shell of the central molecule.

The function $p_j^{pore}(\rho_p, \varsigma)$ represents the probability that, in a confined hard-sphere fluid at a density ρ_p, a given hard sphere fluid has a cavity of radius r_i surrounding it and that j other sphere centers lie within its hydrogen-bonding shell (see Fig.3.1), which is given by

$$p_j^{pore} = \exp\left[-\frac{24\eta}{\sigma_f^3}\int_{\sigma_f}^{r_i} r^2 G(r)dr\right] \times \frac{1}{j!}\left(\frac{24\eta}{\sigma_f^3}\int_{\sigma_f}^{r_i} r^2 G(r)dr\right)^j \times \exp\left[-\frac{24\eta}{\sigma_f^3}\int_{\sigma_f}^{r_o} r^2 G(r)dr\right] \quad (3.3)$$

Here, $\varsigma = \dfrac{s_z - 2d_{fw}}{d_{fw}}$, $\eta = \dfrac{\pi\sigma_f^3 \rho_p}{6}$

Where, s_z is the size of pore shown in Fig.3.2 and d_{fw} is the effective fluid-wall diameter. However Giaya et al.(5-6) applied the model for predicting the stable phase of fluid confined in silicalite -1 and dealluminated zeolite Y(DAY) ,when the bulk phase is liquid water. They noticed the following limitations.

1. The hydrogen bond strength predicted by the Truskett et al(3-4) model did not influence the liquid-vapor coexistence curve for the confined fluid;
2. The hydrogen bonding contribution to the Helmholtz free energy hardly changes with density.
3. The expression used by Truskett et al model to calculate the number of neighbour implies that at least one of the molecules participating in the hydrogen bonding has a cavity surrounding it. This poses a problem describing liquid water at normal density.
4. The model assumes that water molecules form only one hydrogen bond in the hydrogen bonding shell.

Based on the above limitations ,Giaya et al(5-6) modified the hydrogen bonding energy term proposed modification in the term by removing the limitation of only one molecule(one hydrogen bond) in the hydrogen bonding term by four hydrogen bonds per molecule as shown in Fig.3.3
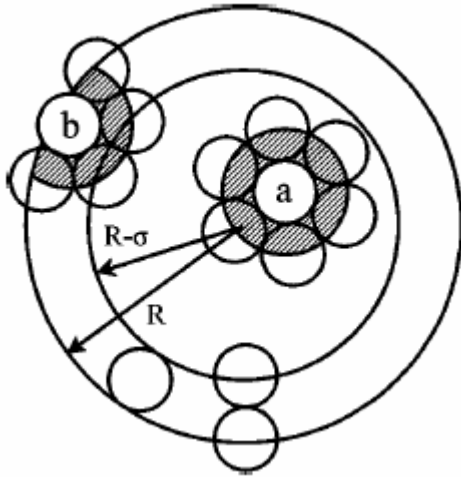
Fig.3.3 schematic presentation of a molecule having more than one molecule in the
       hydrogen bonding shell(6)

.The modified hydrogen bonding energy term can be written as following.(6)

$$U_{HB} = \frac{1}{2}C\left[\sum_{j=1}^{4} jp_j\varepsilon^{HB} + \sum_{5}^{7}(8-j)p_j\varepsilon^{HB}\right] \tag{3.4}$$

Where, p_j is the probability that j molecules are in the hydrogen bonding shell, and ε^{HB} is the energy of one hydrogen bond .Constant C accounts for uncertainties on the ε^{HB} values and on the oriental dependence of the hydrogen bond. Giaya et al.(5-6) proposed the hydrogen bonding interaction term for water confined in cylindrical as well as slit shaped pores.

Schoen et al.(7) proposed a model for a simple fluid(L-J) confined to a slit pore using mean field perturbation theory , in which the free energy is split into a zero order contribution from a hard sphere fluid reference system and a correction accounting for both fluid-fluid and fluid-wall attractions. The resulting equation of state for pore phase has same parameter and density dependence as van der waals equation of state for the bulk fluid, although it differs from later in that the parameter a_p is a function of the separation s_z of the slit pore surfaces.
The equation of state for pore phase is given by

$$P = \frac{\rho_p k_b T}{1 - b\rho_p} - a_p(s_{z)})\rho_p^2 \tag{3.5}$$

where,

$$\rho_p = \frac{N}{A(s_z - 2\sigma_{fw})} \tag{3.6}$$

$$a_p = a_b \left[1 - \frac{3 \frac{\sigma_f}{\sigma_{fw}}}{4(\varsigma - 2)} + \frac{\left(\frac{\sigma_f}{\sigma_{fw}}\right)^3}{8(\varsigma - 2)^3} \right] \tag{3.7}$$

$$\varsigma = \frac{s_z}{\sigma_{fw}} \tag{3.8}$$

And $a_b = \frac{8\pi\varepsilon_f \sigma_f^3}{3}$ (3.9)

And the equation of state for bulk phase is given by:

$$P = \frac{\rho_b k_b T}{1 - b\rho_b} - a_b \rho_b^2 \tag{3.10}$$

The inequality $a_p(s_z) \leq a_b$ holds, from which it follows that the critical temperature of the pore fluid is lower than that of the bulk fluid. The excess coverage and gas-liquid coexistence temperature were calculated by varying fluid-wall attraction parameter using the proposed model. If the fluid-wall attraction is great enough, then the excess coverage Vs T may exhibit a discontinuity reflecting pore condensation. The model predicts pore condensation over a density range comparable with experimental one.

Lastoskie et al.(8) used local and non-local (Mean Field)DFT for the determination of pore size distribution (PSD)of porous graphite carbon. The hard-sphere excess free energy was modeled by Carnahan –Starling equation of state. The adsorption isotherms predicted by non-local DFT for individual slit pores are correlated as a function of pressure and pore width. The PSD is then calculated by fitting the correlation to the experimental adsorption isotherm of the sorbent. The obtained PSD was compared with the PSD obtained using Kelvin equation.

Mitchell et al.(9) applied the Tarazona's model(2) to determine the adsorption isotherms and density distribution of Xenon atoms in zeolite NaA. The alpha cage of NaA was

considered to be fully three dimensional. The two parameters involved in calculating weighing factor for computing local densities were calculated by Newton-Raphson procedure which minimizes the grand potential. The contributions of excess, ideal and external energy to the grand potential are discussed. It is shown that the magnitudes of ideal energy and the external energy (fluid-wall interactions) are almost same. The excess energy contribution is negligible compared to the other two energies. At higher loadings, the agreement between the proposed model and GCMC simulations was quite good. At higher loadings the isotherms showed that the model under predicted the adsorption.

Concluding Remarks:

It was seen that the DFTs and perturbation theories have been applied extensively to study adsorption of L-J molecules in the pores of regular shape like slit, cylindrical and spherical. Due to the limitation of converting intermolecular potential terms in one dimensional integral , the applications of such theories are restricted to regular shaped cavities.It is also noted that applications of such theories is also rare for polar molecules (Except Giaya and Truskett et al(3-6)) because of the angle dependency of intermolecular potentials for electrostatic interactions which are difficult to convert into one dimensional integral in order to get equilibrium density profile.
The approach proposed by Truskett et al.(3-4) and Giaya et al(5-6) for considering electrostatic interactions for water molecule by introducing hydrogen bonding term has following limitations.
1. It requires explicit (analytical) expression of radial distribution function of the polar molecule which is generally obtained by MC simulations or X-ray scattering experiments.
2. The geometric criteria used for water molecule can not be applied to other polar molecules and needs to be modified for particular polar molecules.

There is a need to consider a n intermolecular potential for electrostatic interactions which can be used in general to any type of polar molecule. Generally, it can be achieved by considering orientation dependent dipole-dipole and dipole –induced dipole interactions. The main hurdle of using these orientation dependent intermolecular potentials is to convert them into angle independent potentials by statistical averaging method. We will discuss this method in detail in Chapter 5.

3.2 Statistical Mechanical Theories for multi components system

Jiang et al.(10-11)reported a systematic theoretical study of the influence of pore width, intermolecular potential parameters and state conditions on the selective adsorption of trace components(ethane, propane, butane, water etc) from simple(L-J) fluid mixtures.
The pore was of slit shape, and the carrier fluid was methane. Calculations were based on non-linear density functional theory and show the influence of the relevant variables on the selectivity for the trace component at infinite dilution in the bulk fluid phase.

Tan et al.(12) reported mean field theory results for L-J mixtures (argon-krypton)in straight cylindrical pores. The effect of temperature and pore size on density profiles, adsorption isotherms and phase diagrams were discussed. In similar kind of study Tan et al.(12)simulated hard –sphere mixtures of different sizes near a hard –wall using both Monte-Carlo method and density functional theory. The comparison between the theoretical results and the simulations for the density profiles of both species and mole fraction profiles showed that the present density functional theory was capable of describing the structure of hard-sphere mixtures against a hard wall up to size ratio, R=σ_2/σ_1(Where, σ_2 and σ_1 are the sizes of component 1 and 2 respectively) of about 3. For R values of greater than 3 , the theory gives some discrepancies for densities very closed to the wall.

They also reported the simulation results of ethane-methane mixtures (12) in slit pores using density functional theory .The following 10-4-3 model was used for solid –fluid interactions.

$$U'_{1fw}(z) = \varepsilon_{w1}\left[\frac{2}{5}\left(\frac{\sigma_{fw1}}{z}\right)^{12} - \left(\frac{\sigma_{fw1}}{z}\right)^{4} - \left(\frac{\sigma^{4}_{fw1}}{3s_z(z+0.61s_z)^3}\right)\right]$$

(3.11)

where,

$$\varepsilon_{w1} = 2\pi\rho_s\varepsilon_{fw1}\sigma^2_{fw1}s_z$$

(3.12)

where, s_z is the pore width, σ_{fw1} is effective fluid-wall collision diameter; ρ_s is the atom density of the adsorbent.

They focused on the selectivity of ethane relative to methane for a wide range of system parameters.

Challa et al(13) simulated adsorption isotherms of hydrogen isotopes and mixture of them from GCMC simulations in carbon nano-tubes of sizes from (3,5)(diameter,length) to (10,10) and interstices presented. Adsorption isotherms of H_2-T_2 mixtures in nano-tubes and interstices are determined at 20 and 77 K. Selectivities for T_2 over H_2 are calculated over a range of pressures and comparisons are made with the simulations from IAST.

Comments:
It was evident from the literature survey that the applications of DFT to multi component Adsorption was restricted to binary component system and in particular to the mixture of non polar molecules. The radial distribution functions are considered to be 1 in order to seek analytical solutions of equilibrium density profiles. However, there is a need to apply binary mixture theory proposed by Tan et al (10) or to extend the perturbation theory proposed by Schoen et al (6) to a mixture of polar –polar and polar-non polar molecules. We will address this issue in chapter 6.

3.3 Molecular (Monte- Carlo Simulation) Simulations for single component system

Jiang et al.(10-11) studied layering transitions, freezing transitions, capillary condensation and adsorption hysteresis for methane molecule confined in slit carbon micro pores from temperature 60 K to 135 K and for pore width from 19 Å to 76 Å using GCMC and MD simulation method. The methane molecule was modeled by L-J(12,6) potential and 10-4-3 solid-fluid potential(Eqn.3.10) was used to consider solid-fluid interactions. The adsorption isotherms were obtained using GCMC method. The critical temperature for 0-1 layering transition is slightly lower than $T^*=0.5(T^*=T/T_c)$, while that for capillary condensation is a little above $T^*=0.7$.The diffusion of methane was calculated using MD method .Diffusion near the wall is much slower than in the bulk, with very low probability for a molecule to move out of the contact layer, especially at the lower temperatures. Packing in that layer limits the mobility of adsorbed molecules parallel to the wall. The mobility of molecules perpendicular to the wall can be described by the fraction of molecules which remain in a layer over time. The fraction was found to depend exponentially on time, and the rate constant can be converted into an effective diffusion coefficient perpendicular to the walls($D\perp$).This effective $D\perp$ depends on the density of the adjacent layers as well as on the phase of the layers.

Striolo et al.(14-15) simulated water isotherms and isosteric heat of adsorption in graphite slit pores and single-walled carbon nano tubes using SPC/E water model in the range of 6 -30 Å pore size. The resulting adsorption isotherms indicated negligible adsorption at low pressures, pore –filling by a capillary-condensation- like mechanism, and adsorption/desorption hysteresis loops. It was observed that the size of the hysteresis loop decrease with decreasing pore width and pore radius. Adsorption isotherms simulated for water in carbon nano tubes show pore filling at low relative pressures and narrower adsorption-desorption hysteresis. The zero coverage isosteric heat of adsorption was in the range of 6-15 KJ/mol and at high coverage , it was approximately the heat of condensation of bulk water. Ulberg et al.(16) also simulated the water isotherm in graphite pores using GCMC simulation at 298 K for 500-1000 water molecules and 2016 carbon atom over 30-50 million configurations .The simulated water isotherms were of V type as per IUPAC classification. The simulated results show that the water molecules prefer an orientation with their plane parallel to the wall. However, Jorge et al (17-18) simulated water isotherms with graphite slit pores having carbonyl, carboxyl and hydroxyl sites up to 2.67 sites/nm^2 at 298 K. Henry's constant and gas-liquid equilibrium data were predicted. Results show that the local distribution of sites has strong effect on low –pressure adsorption. For pores having size less than 1 nm , both capillary condensation depend on relative distance between active sites located on opposite walls.It was also concluded that the amount of water adsorbed is mainly affected by number of oxygen atoms on the surface ,rather than by functionality.
Ohba et al(19) also simulated water molecules in carbon-slit pores of width 1.1 nm with no functional group on the carbon surface and compared the results with experimental water isotherms on an activated carbon fiber (ACF), having uniform slit pores.

Soto et al.(20) developed the theory to take into account both dispersion and electrostatic energies(ion-Dipole, ion-induced dipole etc.) for the sorption of gases in zeolite Na-X and Zeolite Na –A .The inter molecular potential for dispersion energy was developed for the spherical cavity based on the Lennard-Jones and Devonshire (LJD) theory of liquids

.Henry's constant, dispersion energy and electrostatic energy were calculated with the spherical cavity model for Ar, Kr and Xe gases and agreed well with experimental data.

Mellot et al.(21) carried out Monte-carlo simulations in NVT ensemble for adsorption of trichloroethylene (TCE) in siliceous faujacite, NaY(Si:Al-2.6) and NaX(Si:Al=1.2) .The calculated isosteric heats of adsorption were compared with measured heat of adsorption from calorimetric techniques. At fixed loading, TCE heats of adsorption increases in the sequence of host basicity and cation contents: siliceous faujacite~ 40 kJ/mol,<NaY-55kJ/mol<NaX-80 kJ/mol. The reason for high isosteric heat of adsorption was due to stronger Cl_{TCE}-Na_{zeo} interactions in NaX and NaY than H_{TCE}-O_{zeo} interactions.The pair distribution functions(PDFs) of host/guest atoms, nicely illustrate the specific interactions involved in TCE adsorption in NaX. The key features are the appearance of a distinctive peaks in the H_{TCE}-O_{zeo} PDF at 2.4 Å, showing promotion of hydrogen bonding in this zeolite, and the enhancement of the Cl_{TCE}-Na(II,III') zeolite interactions with a more pronounced peak around 2.8 Å in the PDF. The latter provides clear evidence for the crucial role of the additional Na cations in sites III' of the NaX structure(located in 12 ring windows) when compared with the corresponding Cl_{TCE}-Na(II)$_{zeo}$ in NaY. In the light of above PDFs, the enhancement of the electrostatic interactions is the direct consequences of the greater ionicity of the NaX structure, and especially the greater number of Na cations accessible to the sorbate molecules in the super cages.

3.4 Molecular(Monte- Carlo Simulation) Simulations for multi components system

3.4.1 Binary component System

Jorge et al. (22) simulated adsorption isotherms for ethane-water mixture on activated carbon in the temperature range of 273 ^{0}K to 323 ^{0}K. The presence of carbonyl sites in the pore is considered. The acid site concentration was in the range of 1to 2.214 μmol/m^{2}Using simulated isotherms for the individual pore size and PSD of BPL activated carbon; the adsorption isotherms were predicted and compared with experimental data. The results indicate that the presence of carbonyl sites enhances the water adsorption in the pore.

Shevade et al (23-24) studied adsorption behavior of water-methanol mixture in slit carbon(graphite) and in uncharged alumino-silicate micro pores at 298 K. The pore width of slit carbon was 2 nm. The elementary cell of graphite surface was 0.425 nm X 0.246nm.The graphite surface was constructed from 7X12 arrays of elementary cells, leading to sum dimension of 2.982nm X 2.951 nm. The simulation was carried out with 500-600 water molecules. The results show that the graphite and uncharged silicate surfaces are covered by dense layer of flatly adsorbed water and methanol molecules having weaker hydrogen bonding. In the interior of the pore, the fluid exhibits bulk-like behavior with a stronger hydrogen bonded structure.

Crachnell et al.(25-26) simulated ethane-methane mixture in slit shaped pore .The selectivity of ethane over methane was predicted at different temperature(250K -500 K), pressure(up to 30 atm) and pore width(up to 30 Å). The spherical model (24) for LJ

methane and ethane was used for the simulation. Adsorption selectivity was found to depend on packing considerations as well as the relative potential well depths of the adsorbate- wall interactions. The results were in good agreement with the results obtained from Ideal adsorption theory (27).

Karavias et al.(28) performed simulations for binary adsorption of L-J molecules namely C_2H_4-CO_2, CO_2-CH_4 and i-C_4H_{10}-C_2H_4 with point multi-pole moments in Zeolite cavities of type X. Fluid-solid electrostatic interactions were taken into account. The phase diagram and coverage for above mentioned binary system were simulated and compared with the results obtained from Ideal adsorption theory(16).Density distribution of molecules shows that the components compete for the high energy sites inside the cavity, depending on its relative strength of adsorption, one component may be excluded from such positions(CH_4 in CO_2-CH_4), or two species may share sites inside the cavity(C_2H_4-CO_2).

Chempath et al. (29-30) has carried out configurational biased GCMC simulations combined with identity-swap moves (See Eqn. (3.12)) to study binary mixture of n-alkanes (C_5- C_{10}) in silicalite in the temperature range of 277-300 K. The adsorption isotherms were simulated for C_5/C_6, C_5/C_7, C_6/C_7, C_6/C_8, C_6/C_{10}, C_7/C_8, $C_8/C_9$and, C_8/C_{12} The simulated results were compared with the results obtained from batch adsorption experiments.It was concluded that if the force-field parameters are optimized for single component adsorption in micro porous materials, they work very well for multi component adsorption as well. A site based analysis of the adsorption data reveals that, in general, shorter alkanes are pushed into the less favorable zigzag channels while the longer alkanes occupy the straight channels. Both the intra molecular energies and zeolite-sorbate energies are lower for alkanes adsorbed in straight channels compared to those in zigzag channels. In another study by Chempath et al.(30) on adsorption of binary liquid mixtures of P-xylene, m-xylene and toluene in silicate, the excess adsorption isotherms are obtained for the straight channel, zig-zag channel and intersection of the two. The computed total excess adsorption isotherms were compared with experimental results. The agreement was good between simulations and experimental results when the PARA form of the silicate is used in the simulations. It was argued that after adsorption of aromatics from a liquid phase, the silicalite changes structure from the ORTHO to another form close to the structure of PARA silicalite. The main difference between the ORTHO and PARA structures is the availability of more space for adsorption in the zigzag channels of PARA. Predictions from IAS theory were found to give reasonable estimates of binary adsorption for these liquid phase system.

Nicholson et al(31) studied the adsorption of methane-CO_2 mixtures in micro pores having either slit or cylindrical geometries, and different adsorption energy using GCMC method. Four types of trial moves were implemented .Apart from moving, creating and destroying a molecule (As explained chapter 2) , a new type of move of interchanging the identity of two particles was introduced. In order to change the identity of particles, a particle of type I was chosen at random and the identity change accepted with probability

$$P_{i-j}^{acc} = \min[1, \frac{z_j N_i}{z_i (N_i + 1)} \exp(-\beta \Delta U)] \qquad (3.13)$$

Identity changes from j to i are given by above equation but with the subscripts interchanged. Microscopic reversibility requires that the number of swaps attempted from i to j is the same as the number from j to i. ΔU is the change in intermolecular energy after interchanging the identity. The absolute activity ,z_i, is given by

$$z_i = \frac{\exp(\beta \mu_i)}{\lambda_{t,i}^3 \lambda_{r,i}} \qquad (3.14)$$

Where, μ_i is the chemical potential of component i, $\lambda_{t,i}$ is the reciprocal of the translational molecular partition function in one dimension, and $\lambda_{r,i}$ is the reciprocal of the rotational partition function of i. The selectivity of CO_2 over CH_4 was calculated as a function of pore size at different fluid wall interactions. The selectivity was found to be maximum between pore size of 6 and 8 Å. The slit and cylindrical pore models studied show several intensity differences that can be attributed mainly to geometrical effects arising from the greater constraint on freedom of rotation for the CO_2 molecule in the cylindrical geometry. However, it was demonstrated that energetic effects play a major role in determining selectivity.

3.5 Concluding remarks on molecular simulation:

For studying adsorption systems, Monte Carlo simulations are generally carried out in Grand canonical ensemble. The simulations can be carried out by considering interactions at molecular level and at atomic level. The former approach is more suitable for small molecules (σ =0.6 nm) but the molecular polarizability, dipole moment and other multi pole moments must be known for the molecule. However, the latter approach is suitable from small molecules like water to large molecules like proteins, starch etc. The atom size and charges on individual atoms must be known .The atomic level simulations take large computing times. The atomic level simulations are useful when the geometry of the adsorbent is complicated but the atomic positions of the adsorbent atoms are known(for example adsorption in silicalite).One of the major disadvantage of the MC method is that it requires complete knowledge of different types of atoms and their positions constituting adsorbent in order to get reliable results. The approach is not suitable especially when the porous material is amorphous or little knowledge of its structure is available.
Monte Carlo simulations for multi component systems is also limited to binary systems especially due to very large computational time.One of the advantage of MC method in the context of studying selectivity of a compound over the other is that, one can change the surface characteristics of the adsorbent by placing different functional groups (Like – OH, -COOH) or cations on the surface. The effect of functional group/cations locations in adsorbent on selectivity can be studied.

Referacies:

1. B.K.Peterson, J.P.R.B.Walton, and K.E. Gubbins, Chem. Soc.Faraday Trans.2,**82,**1789(1986)

2. R.Evan ,U.M.B.Marconi, and P.Tarazona , Chem. Soc. Fara. Trans. 2, **82**,1763 (1986)

3. T.M.Truskett., P.G.Debenedetti,S.Shastry,and S.Torquato, J. Chem. Phys., **111**, 2647(1999)

4. T.M.Truskett, P.G.Debenedetti.,and S.Torquato, J. Chem. Phys.**114,** 2401(2001)

5. A.Giaya and R.W.Thompson, J. Chem. Phys., **116**, 2565 (2002)

6. A.Giaya and R.W.Thompson , J. Chem. Phys.**117,**3464(2002)

7. M.Schoen, D.J.Diestler, J. Chem. Phys. 109 (1998) 5596

8. C.Lastoskie ,K.E.Gubbins ,and N.Quirke, J.Phys. chem..,**97,**4786,(1993)

9. M.C. Mitchell, A.V. McCormick, H.T.Davis, Z.Phys. B,**97,**353(1995)

10. S. Jiang , C.L.Rhykerd and K.E.Gubbins, Molecular Physics **79**, 373(1993)

11. S.Jiang, K.E. Gubbins and P.B.Baluena, J.Phys.chem.,**98**,2403(1994)

12. Z.Tan, Ph.D Thesis, 1992

13. S.R.Challa, D.S.Sholl and J.K.Johnson, J.chem.Phys., **116,** 814(2002)

14.A. Striolo, A.A.Chialvo, P A Cummings, and K E Gubbins, Langmuir **19**, 8583 (2003)

15.A. Striolo, A.A. Chialvo, P A Cummings, and K E Gubbins, Mol. Phys. ,**102**, 243 (2004)

16. D.E Ulberg and K.E. Gubbins, Molecular Phys.,**84,**1139(1995)

17. M.Jorge and N.A.Seaton, Mol.Phys.,**100,**2017(2002)

18. M.Jorge, C.Schumacher and N..A. Seaton,Langmuir,**18**,9296(2002)

19. T.Ohba, H.Kanoh, and K.Kaneko, J.Phys. Chem.B,**108,**14964(2004)

20. J.L.soto, P.W.Fisher, A.J.Glessner and A.L.Myers, J.chem.Soc.faraday Trans. I, **77,**157(1981)

21. C.F.Mellot, A.K.Cheetham, S.harms, S.Savitz, R.J.Gorte and A.L.Myers, Langmuir,**14,**6728(1998)

22. M.Jorge and N.A.Seaton, AICHE J.,**49,**2059(2003)

23. A.V. Shevade, S.Jiang and K.E. Gubbins, Mol.Phys., **97**,1139(1999)

24. A.V. Shevade, S.Jiang and K.E. Gubbins, J. chem..Phys,**113**, 6933(2000)

25. .F.Cracknell, D.Nicholson and N.Quirke, Mol. Physc., **80,**885(1993)

26. R.F.Cracknell, D.Nicholson and N.Quirke in Molecular simulation and industrial applications Methods, Examples and prospects edited by K.E.Gubbins and N.Quirke, G& B science publishers(1996)

27.A.L.Myers and J.M.Prausnitz, AICHE Journal.,**11,**121(1965)

28. F. Karavias, Ph.D Thesis, Uni. of Pennsylvania (1992)

29. S.Chempath, J.F.M.Denayar,K.M.A.D.Meyer, G.V.Baron and R.Q.Snurr,Langmuir, **20,**150(2004)

30. S. Chempath and R.Q.Snurr, AICHE J.,**50,**463(2004)

31. D. Nicholson, K.E.Gubbins, J.chem.Phys.,**104**,8126(1996)

Chapter 4

Preliminary Research: Mean field theory for polar molecules

4.1. Introduction

One of the most successful approaches to the study of liquids in recent years has been through the development of perturbation theories. Their essential physical basis is the separation of the roles of attractive and repulsive intermolecular forces. It is proposed that the structure of simple liquids, as revealed by their radial distribution functions (RDFs), is chiefly determined by the packing requirements of the molecules, which in turn reflects the repulsive intermolecular forces (1-4). The attractive forces are thought to serve essentially as the "glue" that holds molecules together, maintaining the high density, but otherwise playing no major structural role (1-4). When the structures of hard sphere liquids are compared with those of real monatomic liquids, close similarities are seen (1-4). This suggests that the effects of the soft repulsive forces of real molecules may be modeled with reasonable accuracy using a hard-sphere system. The properties of hard-sphere systems are well known from computer simulations and from statistical mechanical theories (1-4). In the formal development of perturbation theories, the effects of changes in the form of the intermolecular potential on the properties of a system of molecules are studied (1-4). For pair wise–additive systems the pair potential energy function is the sum of the reference potential, $U_o(r)$, and the perturbation potential, $U_1(r)$ (1):

$$U(r) = U_o(r) + U_1(r) \tag{4.1}$$

The properties of the system of molecules interacting through $U_o(r)$ are assumed to be known, and those of the perturbed system are expressed in terms of $U_1(r)$ and the properties of the reference system. For example, the configuration energy, U_N, for a system of N molecules interacting through $U(r)$ may be written, to first order in classical perturbation theory as below (1):

$$U_N = U_N^0 + \frac{N^2}{2V} \int_0^\infty 4\pi r^2 g^0(r) U_1(r) dr \tag{4.2}$$

where, U_N^0 is the configuration energy of the reference system, whose RDF is $g^0(r)$. Similar expressions for other properties may also be written, and these are also quite easily calculated if $g^0(r)$ is known (1). Higher-order perturbation terms may also be added, but their calculation is much more demanding, and the successful application of this theory depends on the rapid convergence of the expansion (1). This, in turn, will depend on the choice of a reference system whose structure faithfully mimics that of the system under study (1-4). The success of this approach has thus rested on the correct choice of the division of $U(r)$ into reference and perturbation potentials (1). The results of the first-order perturbation theory are found to be sensitive to the choice of the hard-

sphere diameter, d. Barker and Henderson (described in 1-4) considered the effect of temperature but not of density in their perturbation theory. They were able to calculate the first- and second-order perturbation terms, using computer simulation results. Calculations of the properties of Lennard-Jones liquids were found to be in very good agreement with those obtained from direct computer simulation (1-4). The second–order term, though small, was found to be necessary to achieve the excellent level of agreement. Week, Chandler, and Anderson have proposed a perturbation theory based on a novel choice of reference and perturbation potentials. They assigned the whole repulsive region of U(r) to the role of the reference potential and determinant of the structure, rather than just the positive portion of U(r), as in the Baker-Henderson theory. A consequence of this division is that the perturbation energy $U_1(r)$, is now a very smoothly varying function of r, and this has the useful effect of reducing the higher–order fluctuation terms, giving a very accurate equation of state even when restricted to a first-order treatment (1,2,4). Due to their ability to predict liquid properties, perturbation theories seem to be attractive to study gas-liquid phase transitions in micro porous materials, especially to study the behavior of fluid molecules in nano materials and sorption in micro porous materials.

Several efforts have been made to simulate adsorption isotherms and isosteric heats of adsorption using density functional and mean field theories for non-polar compounds like Leonard-Jones fluids (5-9) for slit and cylindrical shaped pores. For the adsorption of polar compounds the general approach is to use Monte–Carlo technique, because of the presence of angle-dependent electrostatic interactions (10-11). However, Truskett et al. (12,13) and Giaya et al. (14,15) proposed an analytical treatment of partition functions for the water–slit pore system by including a hydrogen bonding term by extending the model proposed by Schoen et al. (5) However, their approach requires the exact analytical expressions of RDFs at different densities and temperatures, which are not available in the literature for some polar molecules. In order to overcome the difficulty of integrating the intermolecular potential over all possible orientations of molecules, we use in the present study, the method of averaging the orientation-dependent electrostatic intermolecular potential over all possible molecular orientations developed by Reed et al. (3).In particular, the approximate intermolecular potential function that is derived by statistical averaging is used in the context of the proposed mean-field perturbation model presented here, and the electrostatic interactions are explicitly computed. The model developed here is then used to predict the sorption of water confined in nanoslit-pores.

The chapter is organized as follows. Section 4.2 introduces the proposed mean-field perturbation approach and statistical averaging method associated with the electrostatic molecular potential. In Section 4.3, the resulting statistical-mechanical model's prediction of the adsorption isotherms as well as isosteric heat of adsorption of water molecules adsorbed in a nanoslit-pore domain are compared with available results in the literature and the proposed method's advantages/limitations discussed.

4.2. Model development
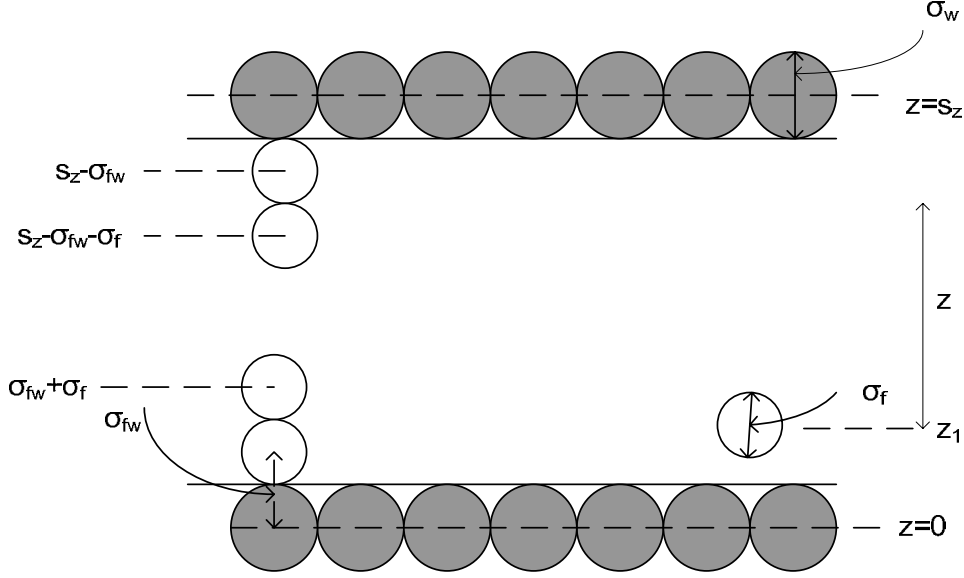
Figure 4.1. Side view of the slit pore model showing wall atoms and fluid molecules

Consider the fluid confined in the slit shaped pore of s_z width shown in Figure 4.1.
From previous work (5,12-15) the Helmholtz free energy for the fluid confined between two parallel plates is given by

$$F = -\beta^{-1} \ln\left(\frac{Z^{(0)}_N}{N! \lambda^{3N}}\right) + \langle U^{(1)} \rangle_0 \qquad (4.3)$$

where, $\langle U^{(1)} \rangle_0 = \langle u_{ff}(r) \rangle + \langle u_{fw}(z_i) \rangle$., $\beta = 1/kT$ is a Boltzmann factor, and λ is the thermal wave length.

Where, $Z^{(0)}$ is the configuration partition function for a confined hard sphere fluid, it is referred as configuration integral of the reference system and $\langle u_{ff}(r) \rangle$ and $\langle u_{fw}(z_i) \rangle$ are average potential energies of, fluid-wall and fluid-fluid (electrostatic + dispersion) interactions respectively. Collectively they are also called as the energy of the perturbation from the reference system ($\langle U^{(1)} \rangle_0$).

4.2.1 Energy of the reference system

A hard sphere fluid confined in a hard sphere slit shaped pore is considered as a reference system, in analogy with previous work (5,12-15). Moreover, the wall is

considered to be smooth, that is, ignoring local variations on the wall surface. First, we define the potential energy of the reference system $U^{(o)}$ as follows.

$$U^{(0)} = \frac{1}{2}\sum_{i=1}^{N}\sum_{j\neq 1}^{N} u_{hs,ff}(r_{ij}) + \sum_{i=1}^{N} u_{hs,fw}(z_i),$$ (4.4)

Where,

$$u_{hs,ff}(r_{ij}) = \begin{cases} 0, & r_{ij} > \sigma_f \\ \infty & r_{ij} \leq \sigma_f \end{cases}$$ (4.5)

And

$$u_{hs,fw}(z_i) = \begin{cases} 0, & \sigma_{fw} < z_i < s_z - \sigma_{fw} \\ \infty & z_i \leq \sigma_{fw} \quad or \quad z_i \geq s_z - \sigma_{fw} \end{cases}$$ (4.6)

In equation (4.4) $r_{ij} \equiv \|r_i - r_j\|$ is the distance between a pair of hard spheres with centers located at r_i and r_j, $\sigma_{fw} = (\sigma_f + \sigma_w)/2$ is the distance between a fluid molecule and a substrate atom in contact, and s_z is the distance between the walls of the pore (See Figure 1). The configuration integral of the reference system ($Z^{(0)}{}_N$) can be approximated by $(Z^{(0)}{}_1)^N$, where, $Z_1^{(0)}$ is the effective single-molecule configuration integral (2,5). We take $Z_1^{(0)}$ to be equal to the volume accessible to any given molecule, $A(s_z - 2\sigma_{fw}) - Nb$, where A is the area of the wall and $b = 2\pi\sigma_{fw}^3/3$ is the volume excluded to one molecule by another (2,5). Hence, the reference system is thermodynamically characterized by:

$$Z_N^{(0)} = (A(s_z - 2\sigma_{fw}) - Nb)^N$$ (4.7)

4.2.2 Energy of the perturbation

The perturbation term is similarly given by:

$$U^{(1)} = \frac{1}{2}\sum_{i=1}^{N}\sum_{j\neq i}^{N} u_{ff}(r_{ij}) + \sum_{i=1}^{N} u_{fw}(z_i)$$ (4.8)

Where, $u_{ff}(r_{ij})$ is total pair potential for fluid-fluid interactions which includes terms for the dispersion force interaction as well as the direct electrostatic energies The following equation for the fluid-fluid interactions for polar molecules can be given (16-18),

$$u_{ff}(r_{ij}) = \left[-\frac{1}{(4\pi\varepsilon_0)^2 r_{ij}^6} \left(\frac{3\alpha_i \alpha_j \ (I_i + I_j)}{I_i I_j 4} \right) \right] + \gamma \tag{4.9}$$

where I_i and I_j are the first ionization potential for molecule i and j respectively, and ε_0 is the electric permittivity of vacuum, and where, α_i, α_j are the average polarizability of molecule i and j. r_{ij} is the distance between two molecules. γ accounts for the interactions due to permanent dipole moments between two molecules and induced dipole and permanent dipole moments between two molecules (3). $u_{fw}(z_i)$ is the fluid-wall intermolecular potential , which is given as (5,12-15):

$$u_{fw}(z_i) = \frac{-2\pi\rho_w \varepsilon_{fw} \sigma_{fw}^6}{3d} \left[z_i^{-3} + (s_z - z_i)^{-3} \right] \quad , \ \sigma_{fw} < z_i < s_z - \sigma_{fw} \tag{4.10}$$

Here, $\varepsilon_{fw} = (\varepsilon_f \varepsilon_w)^{1/2}$, ρ_w is the aerial density of the solid substrate, and d is the distance between two wall atoms.

The term γ is given by the following expression:

$$\gamma = u_{\mu\mu} + u_{\mu\alpha} \tag{4.11}$$

where,

$$u^{\mu\mu} = \frac{\mu_i \mu_j}{r_{ij}^3} g \tag{4.12}$$

where, μ_i, μ_j are permanent dipole moments between molecule i and molecular j, with, $g = \sin\theta_i \sin\theta_j \cos\phi_{ij} - 2\cos\theta_i \cos\theta_j$, and

$$u_{\mu\alpha} = \frac{-1}{r_{ij}^6} \left(\alpha_i \mu_j^2 (3\cos^2\theta_j + 1) + \alpha_j \mu_i^2 (3\cos^2\theta_i + 1) \right) \tag{4.13}$$

$$\gamma = -\frac{\mu_i \mu_j}{r_{ij}^3} g - \frac{1}{r_{ij}^6} \left(\alpha_i \mu_j^2 (3\cos^2\theta_j + 1) + \alpha_j \mu_i^2 (3\cos^2\theta_i + 1) \right) \tag{4.14}$$

4.2.3 Statistical averaging for the dipole-dipole intermolecular potential

The coordinate systems for two charge distributions representing molecules i and j are shown in Figure 2 in one particular relative orientation determined by the polar

angles θ_i and θ_j, **a**nd the azimuthal angle φ_{ij} at a separation r. We have chosen each z axis as the direction of the dipole-moment vector μ.
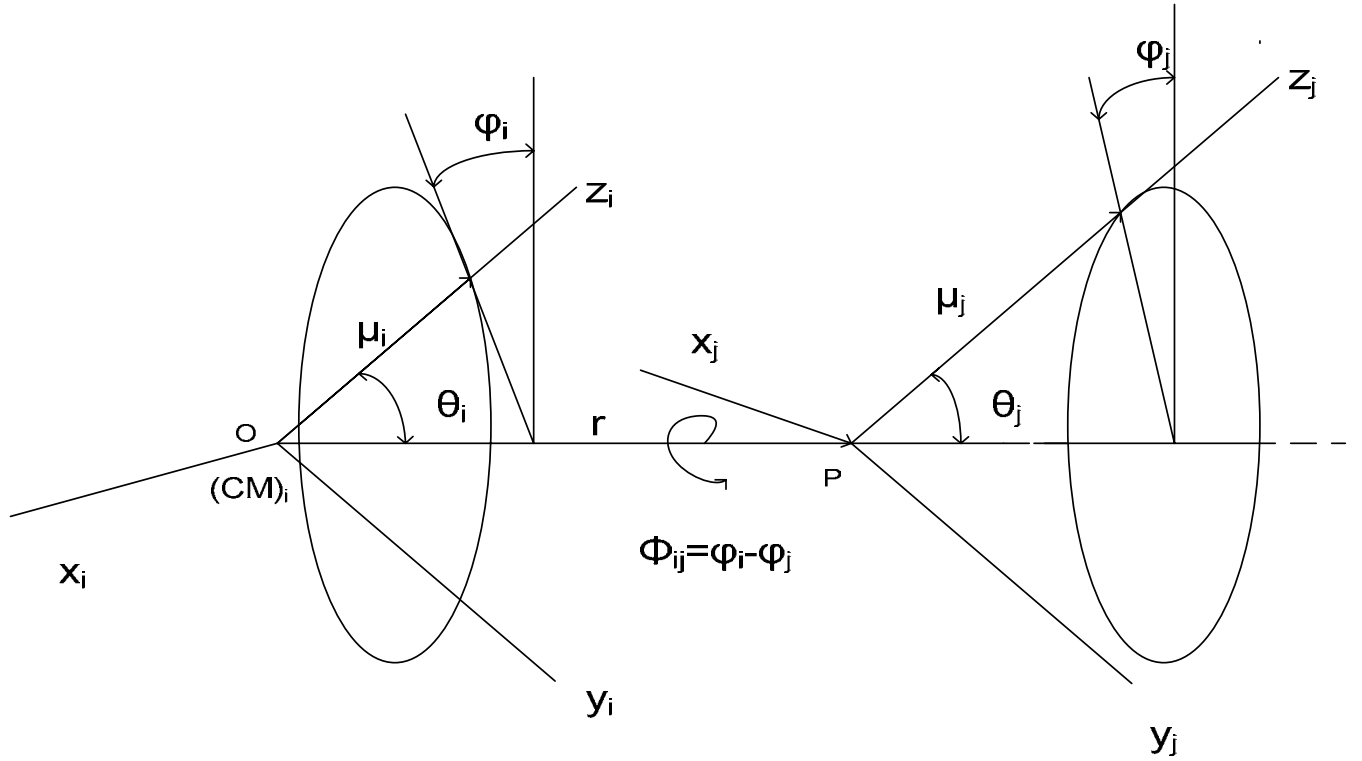
Figure 4.2. Two static charge systems with z axes in the direction of the dipole moments and separated by distance r between centers of mass (3).

The configuration integral $Z_{\mu\mu}$ for the pair of molecule is given by (3):

$$Z_{\mu\mu} = \frac{1}{16\pi^2} \int ....\int e^{-\beta u_{\mu\mu}} dr_i dr_j d\omega_i d\omega_j \qquad (4.15)$$

where $d\omega_i d\omega_j = \sin\theta_i \sin\theta_j d\theta_i d\theta_j d\phi_i d\phi_j$. Using the relative coordinates

$r = r_i - r_j$ and $\phi_{ij} = \phi_i - \phi_j$, the configuration-space volume element can be written as:

The integrals in $Z_{\mu\mu}$ over dr_i and $d\phi_i$ give V and 2π, respectively and there fore,

$$Z_{\mu\mu} = \frac{V}{8\pi} \iint e^{-\beta u_{\mu\mu}} dr d\omega \qquad (4.16)$$

where, $d\omega = \sin\theta_i \sin\theta_j d\theta_i d\theta_j d\phi_{ij}$.

Let $\varsigma_{\mu\mu}$ be the phase integral for the angular coordinates of a pair of molecules

$$\varsigma_{\mu\mu} = \frac{1}{8\pi} \int e^{-\beta u_{\mu\mu}} d\omega \qquad (4.17)$$

If we now define a function by $\varsigma_e \equiv e^{-\beta\gamma}$, where γ_1 is an angle-averaged energy function, we can replace an angle-dependent pair-potential energy function $u_{\mu\mu}(r,\theta_i,\theta_j,\theta_{ij})$ by the angle-independent function $u_{\mu\mu}(r,T)$. Eqn. (4.16) can be written as:

$$Z_{\mu\mu} = V \int e^{-\beta\gamma_1} dr \qquad (4.18)$$

Note that $\varsigma_{\mu\mu}$ and γ_1 are functions of r and T. The term $e^{-\beta\gamma_1}$ plays the role of an apparent Boltzman factor. Furthermore, γ_1 is actually a Helmholtz free energy of orientation for the molecular pair. From its definition γ_1 is calculated by:

$$\gamma_1 = -\frac{1}{\beta} \ln \varsigma_{\mu\mu} = -kT \ln\left(\frac{1}{8\pi} \int e^{-\beta u_{\mu\mu}} d\omega\right) \qquad (4.19)$$

where,

$$u^{\mu\mu} = \frac{\mu_i \mu_j}{r_{ij}^3} g \qquad (4.20)$$

and $g = \sin\theta_i \sin\theta_j \cos\phi_{ij} - 2\cos\theta_i \cos\theta_j$.

It can be shown that when the temperature is not too low, for example, T>100 K for $\mu \le 2D$ or T>200 ^{0}K for $\mu \le 3D$, the infinite series expansion of the exponential function converges rapidly, and hence (3):

$$\varsigma_{\mu\mu} = \frac{1}{8\pi} \int \left(1 - \frac{\mu_i \mu_j}{r_{ij}^3} \beta g + \frac{\mu_i^2 \mu_j^2}{2r_{ij}^6} \beta^2 g^2 - ....\right) d\omega \qquad (4.21)$$

The integration is over the three variables in g, $\theta_a \in [0,\pi]$, $\theta_b \in [0,\pi]$, and $\phi_{ij} \in [0,2\pi]$, and the following integration results hold here:

$$\int d\omega = 8\pi \qquad \int g d\omega = 0 \qquad \int g^2 d\omega = \frac{16}{3}\pi \qquad \int g^3 d\omega = 0$$

In the light of the above integration results, a term by term integration of the uniformly convergent series in equation (4.21) yields,

$$\varsigma_{\mu\mu} = 1 + \frac{\mu_i^2 \mu_j^2 \beta^2}{3r_{ij}^6} + \ldots \ldots$$

(4.22)

Note that γ, the free energy averaged potential for dipole-dipole energy, can be obtained by substituting equation (4.22) into equation (4.19):

$$\gamma_1 = -kT \ln \left(1 + \frac{\mu_i^2 \mu_j^2 \beta^2}{3r_{ij}^6} + \ldots \ldots \right)$$

(4.23)

which can be further approximated as follows:

$$\gamma_1 = u_{\mu\mu} \approx -\frac{\mu_i^2 \mu_j^2}{3kTr_{ij}^6}$$

(4.24)

whenever the argument $\left| \dfrac{\mu_i \mu_j}{kTr_{ij}^3} \right| \ll 1$, namely in a regime where T>300 K and μ_i , μ_j < 3 D.

4.2.4   Dipole–induced dipole moment interactions

Let us now consider the potential term associated with the dipole- induced dipole moment interactions:

$$u_{\mu\alpha} = \frac{-1}{r_{ij}^6} \left(\alpha_i \mu_j^2 (3\cos^2 \theta_j + 1) + \alpha_j \mu_i^2 (3\cos^2 \theta_i + 1) \right)$$

(4.25)

After carrying out the aforementioned statistical averaging method, in a similar way as before, one obtains an expression for the corresponding energy terms:

$$u_{\mu\alpha} \approx -\left(\frac{\mu_i^2 \alpha_j - \mu_j^2 \alpha_i}{r_{ij}^6} \right)$$

(4.26)

Combining equations (4.11),(4.24),and (4.26) one obtains,

$$\gamma = -\frac{\mu_i^2 \mu_j^2}{3kTr_{ij}^6} - \frac{\mu_i^2 \alpha_j}{r_{ij}^6} - \frac{\mu_j^2 \alpha_i}{r_{ij}^6}$$

(4.27)

where, μ_i, μ_j are permanent dipole moments between molecule i and molecule j and α_i, α_j are the average polarizability of molecule i and j. For the same kind of molecule i=j, (dropping subscripts and combining equation (4.9) and equation (4.27)), we have :

$$u_{ff}(r) = \left[-\frac{1}{(4\pi\varepsilon_0)^2 r^6}\left(\frac{3\alpha^2 I}{4}\right)\right] - \frac{1}{r^6}\left(\frac{\mu^4}{3kT} + 2\mu^2\alpha\right) \tag{4.28}$$

Note that:

$$\langle u_{ff}(r)\rangle = (1/2)\int_V dr_1 \int_V dr_2\, g(r_1, r_2)\rho_0^{(1)}(r_1)\rho_0^{(1)}(r_2)u_{a,ff}(r_{ij}) \tag{4.29}$$

We now seek an equation of state under the mean-field assumption, ignoring intermolecular correlations and setting (5,12-15),

$$g(r_1, r_2) = \begin{cases} 0, & r_{12} < \sigma_f \\ 1, & r_{12} \geq \sigma_f \end{cases} \tag{4.30}$$

Also considering the fluid to be homogeneous throughout the pore volume, that is we approximate the local density by (5,12-15)

$$\rho_0^{(1)}(r_1) = \rho_0^{(1)}(r_2) = \rho_p = \frac{N}{A(s_z - 2\sigma_{fw})} \tag{4.31}$$

Using approximations in equation(4.30) and equation(4.31), volume integral in equation (4.29) can readily be simplified in one dimensional integral by substituting equation (4.28) into (4.29) and transforming variables in the double integral in equation (4.29) from $\{r_1, r_2\}$ to $\{r_1, r_{12}\}$, we use the definition of a_p and obtain:

$$a_p = \frac{a_{p1}}{A(s_z - 2\sigma_{fw})}\int_V dr_1 \int_V dr_{12}\, g(r_{12})r_{12}^{-6} \tag{4.32}$$

$$= \frac{a_{p1}}{(s_z - 2\sigma_{fw})}\int_{\sigma_{fw}}^{s_z - \sigma_{fw}} dz_1 \int_{V(z_1)} dr_{12} r_{12}^{-6} \tag{4.33}$$

$$= \frac{2\pi a_{p1}}{(s_z - 2\sigma_{fw})}\int_{\sigma_{fw}}^{s_z - \sigma_{fw}} dz_1 \left\{\int dz \int d\rho\, \rho(z^2 + \rho^2)^{-3}\right\}_{V(z_1)} \tag{4.34}$$

48

$$a_{p1} = \frac{1}{(4\pi\varepsilon_0)^2}\left[\left(\frac{2\mu^4}{3kT}\right) + 2\mu^2\alpha + \left(\frac{3\alpha^2 I}{4}\right)\right] \qquad (4.35)$$

where, $\overline{V(z_1)}$ denotes the z_1-dependent volume restricted by hard cores of fluid molecules and by the hard walls. Note that, for $s_z > 2(\sigma_{fw}+\sigma_f)$, the integration on z_1 breaks down into three ranges: (1) $\sigma_{fw} < z_1 < \sigma_f$, (2) $\sigma_{fw} + \sigma_f < z_1 < s_z - (\sigma_{fw}+\sigma_f)$, and (3) $s_z - (\sigma_{fw}+\sigma_f) < z_1 < s_z - \sigma_{fw}$. (5).

In turn the integrations on z and ρ can be broken into either two or three regions within each range of z_1. Thus a_p splits into three contributions $a_p = a_1 + a_2 + a_3$. First note that, by symmetry $a_1 = a_3$

For a_1, one obtains:

$$a_1 = a_3 = \frac{2\pi a_{p1}}{(s_z - 2\sigma_{fw})}\int_{\sigma_{fw}}^{\sigma_{fw}+\sigma_f} dz_1\left\{\int_{-z_1+\sigma_{fw}}^{\sigma_f} dz \int_{\sqrt{\sigma_f^2 - z^2}}^{\infty} \frac{d\rho\rho}{(z^2+\rho^2)^3} + \int_{\sigma_f}^{s_z - \sigma_{fw} - z_1} dz\int_0^{\infty} \frac{d\rho\rho}{(z^2+\rho^2)^3}\right\} \qquad (4.36)$$

$$= \frac{2\pi a_{p1}}{(s_z - 2\sigma_{fw})}\left\{\frac{11}{24\sigma_f^2} - \frac{1}{24}\left[\frac{1}{(s_z - 2\sigma_{fw} - \sigma_f)^2} - \frac{1}{(s_z - 2\sigma_{fw})^2}\right]\right\} \qquad (4.37)$$

In a similar fashion we obtain,

$$a_2 = \frac{2\pi a_{p1}}{(s_z - 2\sigma_{fw})}\int_{\sigma_{fw}+\sigma_f}^{s_z - \sigma_{fw} - \sigma_f} dz_1\left\{\int_{-z_1+\sigma_{fw}}^{-\sigma_f}dz\int_0^{\infty}\frac{d\rho\rho}{(z^2+\rho^2)^3} + \int_{-\sigma_f}^{\sigma_f}dz\int_{\sqrt{\sigma_f^2-z^2}}^{\infty}\frac{d\rho\rho}{(z^2+\rho^2)^2} + \int_{\sigma_f}^{s_z - z_1 - \sigma_{fw}}dz\int_0^{\infty}\frac{d\rho\rho}{(z^2+\rho^2)^3}\right\} \qquad (4.38)$$

$$= \frac{4\pi a_{p1}}{(s_z - 2\sigma_{fw})}\left\{\frac{1}{3\sigma_f^3}[s_z - 2\sigma_{fw} - 2\sigma_f] + \frac{1}{24}\left[\frac{1}{(s_z - 2\sigma_{fw} - \sigma_f)^2} - \frac{1}{\sigma_f^2}\right]\right\} \qquad (4.39)$$

Combining equations (4.36), (4.39), and (4.29) yields:

$$\langle u_{ff}(r)\rangle = -2a_p\rho_p N \qquad (4.40)$$

where,

$$a_p = \frac{4\pi a_{p1}}{3\sigma^3_f (s_z - 2\sigma_{fw})} \left[-\frac{3}{2}\sigma_f + 2(s_z - 2\sigma_{fw}) + \frac{\sigma^3_f}{4(s_z - 2\sigma_{fw})^2} \right] \tag{4.41}$$

4.2.5 Fluid-wall interactions

Consider equation (4.10) for the potential term associated with the fluid-wall interactions, the average fluid-wall interactions can be given by (5,12-15)

$$\langle u_{fw}(z_i) \rangle = \int_V dr_1 \rho_0^{(1)}(r_1) u_{a,fw}(z_1) \tag{4.42}$$

One can approximate integral in (4.42) using (4.31):

$$\langle u_{fw}(z_i) \rangle = \frac{2\pi \rho_w \varepsilon_{fw} \sigma^6_{fw} \rho_p A}{3d} \int_{\sigma_{fw}}^{sz-\sigma_{fw}} \left[z_i^{-3} + (sz - z_i)^{-3} \right] dz \tag{4.43}$$

$$= \frac{2\pi \rho_w \varepsilon_{fw} \sigma^6_{fw} \rho_p A}{3d} \left(\frac{s_z(s_z - 2\sigma_{fw})}{(s_z - \sigma_{fw})^2 \sigma^2_{fw}} \right) \tag{4.44}$$

$$\langle u_{fw}(z_i) \rangle = \psi(\xi) = \frac{2N\pi \rho_w \varepsilon_{fw} \sigma^3_{fw}}{3d(\xi - 2)} \left[\frac{1}{(\xi - 1)^2} - 1 \right], \xi > 2 \tag{4.45}$$

where, $\xi = \dfrac{s_z}{\sigma_{fw}}$

Note that equations (4.8)-(4.13) now yield

$$\langle U^{(1)} \rangle_0 = \langle u_{ff}(r) \rangle + \langle u_{fw}(z_i) \rangle \tag{4.46}$$

$$\langle U^{(1)} \rangle_0 = \psi(\xi)N - 2Na_p\rho_p \tag{4.47}$$

Finally, substituting equations (4.7) and (4.47) into equation (4.3), one obtains the following expression for the Helmholtz free energy:

$$F = -\beta^{-1}\left\{ N \ln\left[\frac{1 - b\rho_p}{\rho_p \lambda^3} \right] + N \right\} + N\psi(\xi) - 2a_p N\rho_p \tag{4.48}$$

4.2.6 Determination of equilibrium pore density

At equilibrium the following equation must be satisfied.

$$\mu_b(T,\rho_b) - \mu_P(T,\rho_P) = 0 \tag{4.49}$$

where $\mu_b(T,\rho_b)$ and $\mu_P(T,\rho_P)$ are the chemical potential for the bulk phase and the pore phase respectively. They can be calculated using equation (4.48) for the Helmholtz free energy as follows:

$$\mu_P(T,\rho_P) = \left(\frac{\partial F}{\partial N}\right)_{T,A,s_z} = \beta^{-1}\ln\left(\frac{\lambda^3\rho_P}{1-b\rho_p}\right) + \frac{\beta^{-1}b\rho_p}{1-b\rho_P} + \psi(\xi) - 2a_P(\xi)\rho_P \tag{4.50}$$

$$\mu_b(T,\rho_b) = \lim_{\xi \to 0} \mu_P(T,\rho_P) = \beta^{-1}\ln\left(\frac{\lambda^3\rho_b}{1-b\rho_b}\right) + \frac{\beta^{-1}b\rho_b}{1-b\rho_b} - 2a_b\rho_b \tag{4.51}$$

where, $a_b = \dfrac{4\pi a_{p1}}{3\sigma_f^3}$ \qquad\qquad (4.52)

$$a_p = \frac{4\pi a_{p1}}{3\sigma_f^3(s_z - 2\sigma_{fw})}\left[-\frac{3}{2}\sigma_f + 2(s_z - 2\sigma_{fw}) + \frac{\sigma_f^3}{4(s_z - 2\sigma_{fw})^2}\right] \tag{4.53}$$

Equation (4.49) is a (nonlinear) algebraic equation with unknown equilibrium pore density, keeping all other thermodynamic variables fixed. In the case of multiple real positive roots, the density value that minimizes the excess grand potential per unit wall area is typically selected, since it corresponds to the thermodynamically stable phase in the pores. It should be also emphasized that the proposed framework allows also an insightful sensitivity analysis to be performed on the effect of parameters such as pore – size and fluid–wall interaction parameter on the density of the confined phase and its thermodynamic stability. Furthermore, issues pertaining to the structural characteristics of the corresponding liquid-vapor phase diagram as above parameters vary can also be addressed since they are critically linked to any adsorbent design method.

4.3. Results and discussion
4.3.1 Pore filling

Figure 3(a) shows the adsorption isotherms at 298 K and a fixed value of the fluid-wall interaction parameter for different pore sizes. The vertical lines are drawn for

guiding eyes. The pressure at which gas to liquid transition (pore filling) takes place decreases as the pore size decreases. Figure 3(b) shows the isotherms before the pore–filling takes place which are not seen clearly in Figure 3(a). The pore density increases with decrease in pore sizes due to increased fluid-wall interactions. For 20, 25, and 30 Å pore sizes, the pore density after pore filling is close the density of liquid water, suggesting the capillary condensation takes place in the pores while in case of 15 and 18 Å pores the pore densities are between water vapor and liquid water. This can be explained by studying the magnitudes electrostatic interactions at different pore sizes.

The pore filling phenomena can be interpreted by studying the relative contributions of the fluid-fluid and fluid-wall interactions over the entire operating pressure range. The contributions as a function of operating bulk pressure are shown in Figure 4 for 20 Å pores. The fluid-fluid interactions are split into two parts namely electrostatic and dispersion interactions. The results in Figure 4 suggest that the fluid–wall interactions dominate over fluid-fluid interactions before pore filling takes place, but after pore filling by the liquid phase, the fluid-fluid interactions dominate due to strong electrostatic interactions attributed to the polar nature of water molecules.

The relative contributions of fluid-fluid and fluid–wall interactions at different pore sizes are shown in Figures 5(a,b) at two different external pressures. Figure 5(a) shows these values for conditions that result in capillary condensation of a liquid-like fluid. The results show that after pore filling the dispersion energy and the electrostatic energy increases with increase in the pore size. Figure 5(b) shows values for a vapor-like confined fluid. The results in Figure 5(a) show that the electrostatic interaction energy increases as pore size increases, which is attributed to the orientation-dependent electrostatic interactions. The small pore size restricts the mobility of molecules in the pore, and hence the hydrogen bonds between water molecules get disrupted. Results in Figure 5(b) show that as the monolayer forms the electrostatic and dispersion interactions increase with decrease in pore size due to neighboring molecules in the monolayer. This is attributed to an increase in the fluid-wall interactions which result in completion of monolayer formation at relatively low pressure.

4.3.2 Gas phase heat of adsorption

The isoteric heat of adsorption, q_{st}, is the heat released (per mole) on transferring an infinitesimally small amount of the adsorbate from the coexisting bulk gas phase to the adsorbed phase at constant temperature, pressure (constant adsorption loading), surface area A, and pore width H. As defined, q_{st}, can be related to entropies (S), Internal energies (U), and volumes (V) of the two phases by (8):

$$q_{st} = T(S^{(g)}-S^{(a)}) = U^{(g)}-U^{(a)} + P(V^{(g)}-V^{(a)}) \qquad (4.54)$$

where the subscripts (a) and (g) refer to the values for the adsorbed and bulk gas phases, respectively. The isoteric heat obeys the Clapeyron equation:

$$\left(\frac{dP}{dT}\right)_{A,S_z,\Gamma} = \frac{S^{(g)} - S^{(a)}}{V^{(g)} - V^{(a)}} \tag{4.55}$$

where P is the pressure of the bulk gas phase in equilibrium with the adsorbed phase, and the derivative on the left hand side of the equation is taken at constant adsorption levels, Γ. If we further assume that $V^{(a)} \ll V^{(g)}$ and the ideal gas law holds for the coexisting gas phase so that $V^{(g)} - V^{(a)} \approx \frac{RT}{P}$ then, with this approximation, and combining equations (4.54) and (4.55), we have (8):

$$\left(\frac{d \ln P}{dT}\right)_{\Gamma,A,H} = \frac{q_{st}}{RT^2} \tag{4.56}$$

Over small temperature intervals it is usually possible to neglect the temperature dependence of q_{st} so that equation (4.56) can be integrated to give:

$$(\ln P)_{\Gamma} = \left(\frac{-q_{st}}{RT}\right) + cons\tan t \tag{4.57}$$

We used equation (4.57) to calculate the isosteric heat of adsorption. Figure 6(a) shows the isosteric heat of adsorption at different pore sizes at low surface coverage, i.e., the number of adsorbed molecules per square nanometer of pore surface. The results in Figure 6(a) show that the heat of adsorption increases linearly, but modestly, with surface coverage, which is attributed to increased fluid-wall interactions. The results in Figure 6(b) show the heat of adsorption at somewhat higher loadings where fluid-fluid interactions are more important than fluid-wall interactions. At high loadings, the heat of adsorption increases as pore size increases from 11 Å to 35 Å, because of increased hydrogen bonding between water molecules, although on the vertical scale the differences are modest.

4.3.3 Comparison with the results of Monte-Carlo simulations (Striolo et al.(10))

The simulated isotherms for 10, 16, and 20 Å slit-pores are compared with results of Striolo et al. (10) in Figure 7. The simulation results are noted to be quite close in agreement with the Monte-Carlo simulations, both in the transition pressures and the loadings at higher pressures. The small deviations in pore densities after the transition pressure might be due to the approximation of the Radial Distribution Functions (RDFs).

The simulated pore densities before pore filling are in excellent agreement with Striolo's simulations, because the RDF values used were more accurate for water vapor.

Figure 8 shows the comparisons of the simulated isosteric heats of adsorption at low coverages, which are in excellent agreement with Striolo's Monte-Carlo results. Deviations were observed in the predicted isosteric heats of adsorption at high coverages, shown in Figure 9, and might be attributed to the approximation of RDFs at higher densities.

4.4 Conclusions

The perturbation theory proposed by Schoen et al. (5) was extended by including the electrostatic interactions in the configuration integral. The angular orientation-dependent electrostatic intermolecular potential was approximated by averaging it over all molecular orientations. This change enabled the model to simulate the thermodynamic properties of polar molecules confined in the nanoporous materials. The simulated isotherms and isosteric heats of adsorption of water in nanoslit-pores are in good agreement with the results obtained by Striolo et al. (10) using Monte-Carlo simulations.
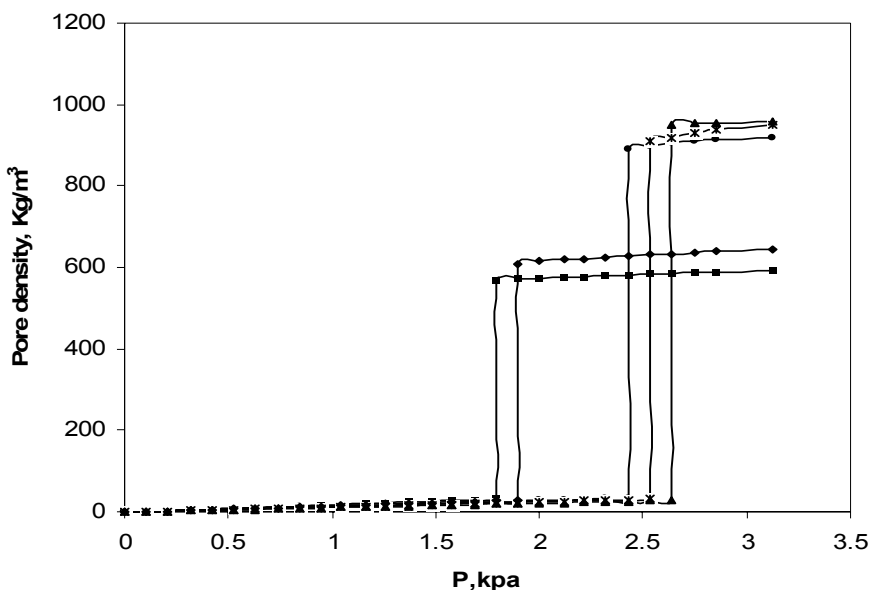
Figure 4.3(a). Pore density of water molecules as a function of bulk pressure for water adsorbed in slit pores at 298 K and $\varepsilon_{fw} = 0.66$ kJ/mol. Results shown for pores of width 16 (■), 18 (♦), 20 (●), 25 (✗) and 30 (▲) Å.
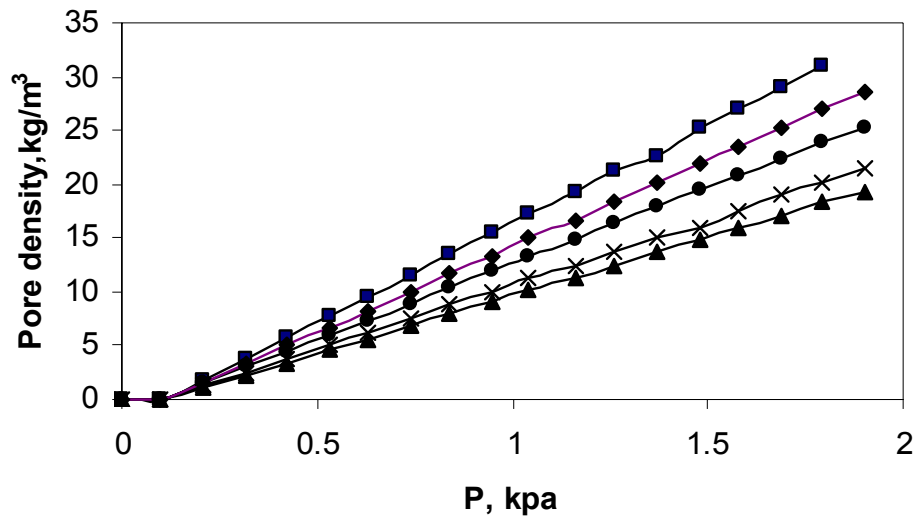
Figure 4.3(b). Pore densities of water molecules before pore filling by capillary condensation takes place at 298 K and ε_{fw} = 0.66 kJ/mol. Results shown for pores of width 16 (■), 18 (♦), 20 (●), 25 (✗) and 30 (▲) Å.
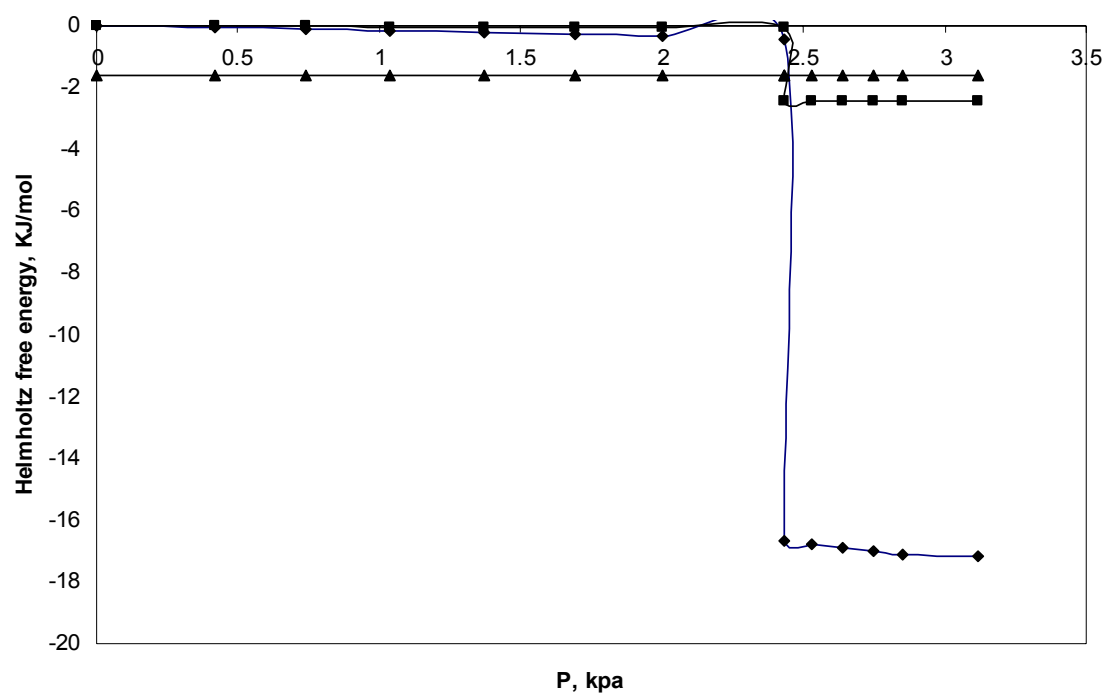
Figure 4.4 Relative magnitudes of the fluid-fluid electrostatic (♦), fluid-fluid dispersion (■), and fluid-wall interactions (▲). Helmholtz free energy as a function of bulk pressure for 20 Å pore width at 298 K and ε_{fw} = 0.66 kJ/mol.
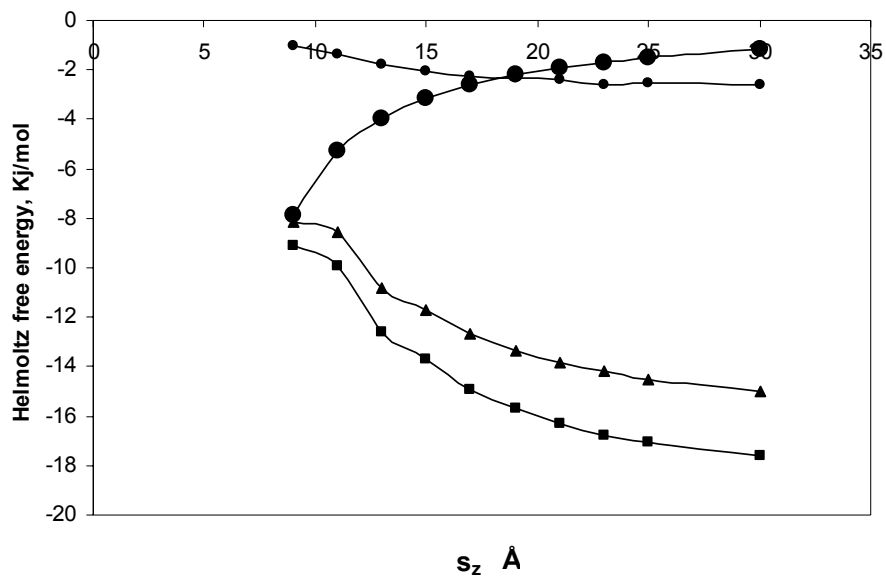
Figure 4.5(a). Fluid-wall (●), fluid-fluid electrostatic (▲), fluid-fluid dispersion (•) and total fluid-fluid, dispersion + electrostatic (■) interaction energy as a function of pore sizes at 3.1 kPa, 298 K and ε_{fw} = 0.66 kJ/mol. The fluid is liquid-like at these conditions.
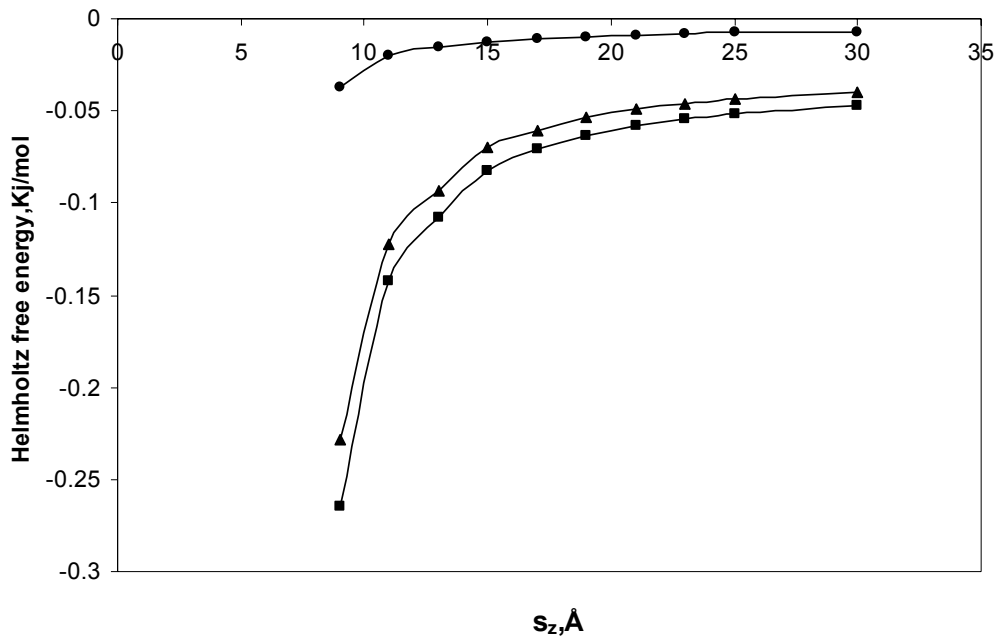
Figure 4.5(b).   Fluid-fluid electrostatic (▲), fluid-fluid dispersion (●) and total fluid-fluid, dispersion + electrostatic (■) interaction energy as a function of pore sizes at 0.7 kPa, 298 K and $\varepsilon_{fw} = 0.66$ kJ/mol. The fluid is vapor-like at these conditions.
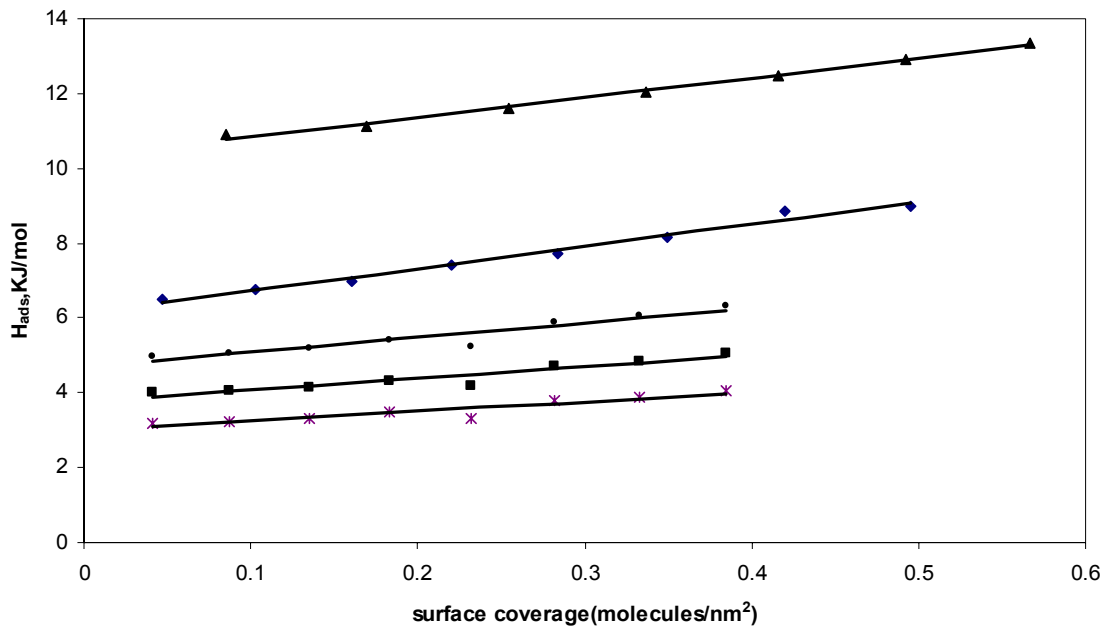
Figure 4.6(a). Isosteric heat of adsorption at low surface coverage (number of water molecules adsorbed per nm^2 of pore surface) for pore width of 11 (▲), 15 (♦), 20 (●), 25 (■) and 30 (×) Å.
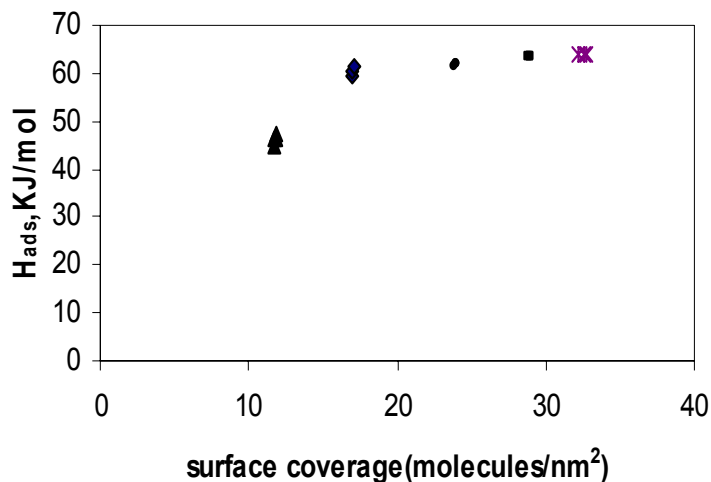
Figure 4.6(b). Isosteric heat of adsorption at high surface coverage (number of water molecules adsorbed per nm^2 of pore surface) for pore width of 11 (▲), 15 (♦), 20 (●), 25 (■), and 30 (×) Å.
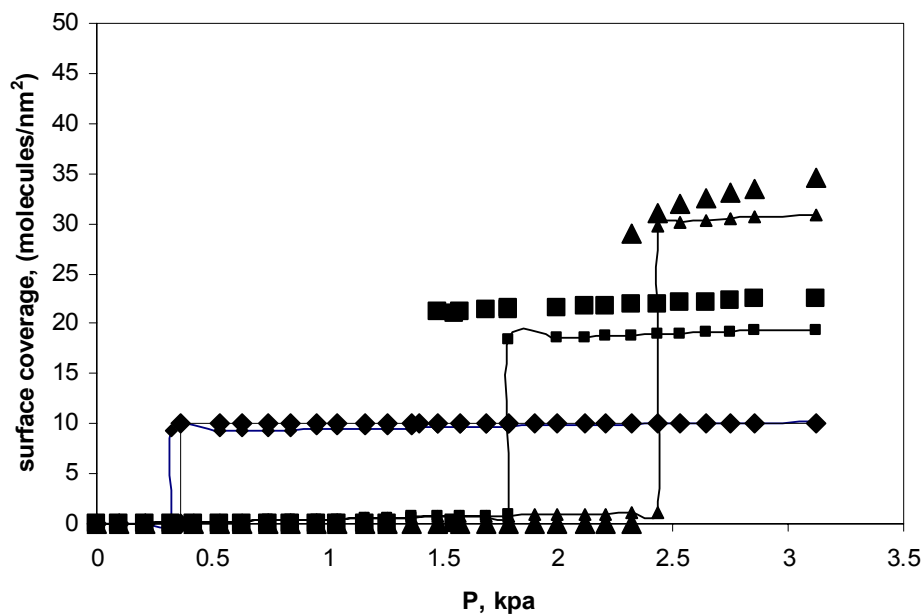
Figure 4.7. Comparison of simulated surface coverage as a function of bulk pressure (small symbols) with the results of Striolo et al. [10] (large symbols) for pore sizes of 10 (♦), 16 (■), and 20 (▲) Å at 298 K and ε_{fw} = 0.336 kJ/mol.
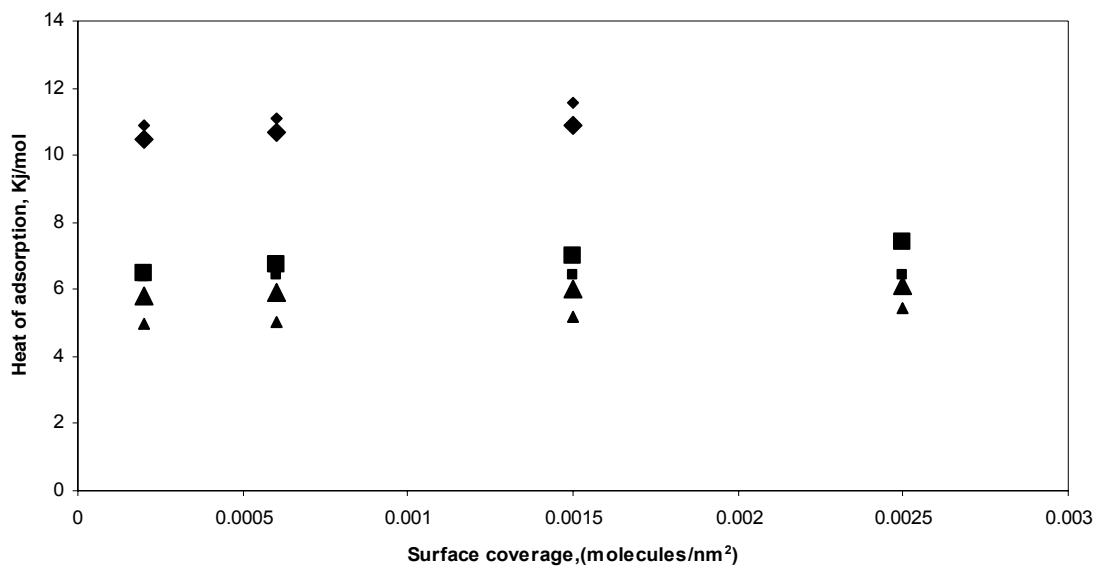
Figure 4.8. Comparison of simulated heat of adsorption as a function of low surface coverage (small symbols) with the results of Striolo et al. [10] (large symbols) for pore sizes of 10 (♦), 16 (■), and 20 (▲) Å at 298 K and ε_{fw} = 0.336 kJ/mol.
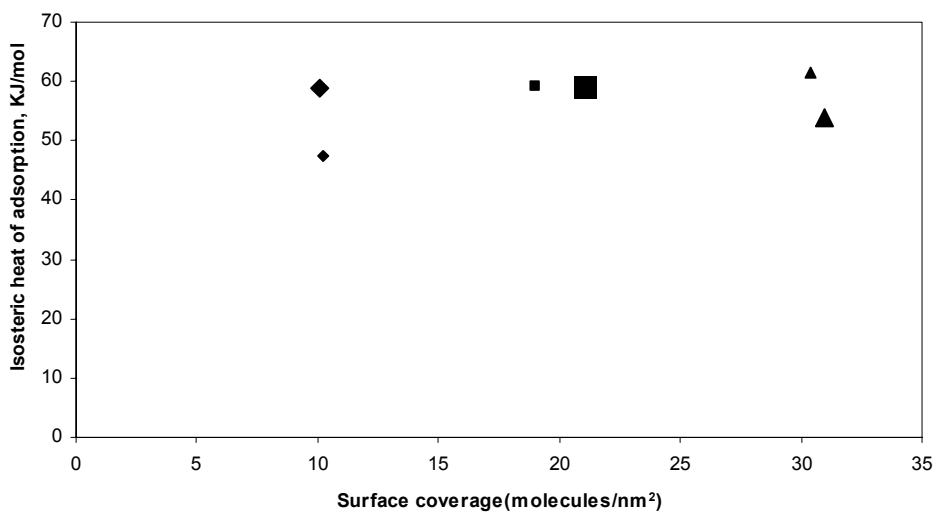
Figure 4.9. Comparision of simulated heat of adsorption as a function of high surface coverage (small symbols) with the results of Striolo et al. [10] (large symbols) for pore sizes of 10 (♦), 16 (■), and 20 (▲) Å at 298 K and ε_{fw} = 0.336 kJ/mol.

61

References

1. M.Rigby, E.B.Smith, W.A.Wakeham, and G.C.Maitland, The forces between molecules, (Clarendon Press, oxford,1986)
2. D.A.McQuairrie, Statistical Mechanics,(Harper & Row, New York, 1976).
3. T.M. Reed, and K.E.Gubbins, Applied statistical Mechanics,(Mc-Graw Hill, NewYork, 1973)
4. C.G.Gray and K.E.Gubbins, Theory of molecular fluids,Vol.1: Fundamentals,(Clarendon Press, Oxford 1984)
5 . M.Schoen, D.J.Diestler, J of Chem. Phys. **109,**5596(1998)
6 . S. Jiang , C.L.Rhykerd and K.E.Gubbins, Molecular Physics **79,** 373(1993)
7. R.Evan ,U.M.B.Marconi, and P.Tarazona , Chem. Soc. Fara. Trans. 2, **82,**1763 (1986)
8. P.B.Balbuena, and K.E.Gubbins, Langmuir**, 9,**1801 (1993)
9. Z.Tan, K.E.Gubbins, J. of Phys. Chem., **94,** 6061 (1990)
10. A. Striolo, A.A.Chialvo, P.T.Cummings, and K.E.Gubbins, Langmuir **19,**8583 (2003)
11. G.M.Davis and N.A.Seaton, langmuir **15,**6263 (1999)
12. T.M.Truskett, P.G.Debenedetti.,and S.Torquato, J. Chem. Phys.**114,**2401 (2001)
13. T.M.Truskett., P.G.Debenedetti,S.Shastry,and S.Torquato, J. Chem. Phys., **111,**2647(1999)
14. A.Giaya and R.W.Thompson , J. Chem. Phys.**117,**3464(2002)
15. A.Giaya and R.W.Thompson, J. Chem. Phys., **116,**2565 (2002)
16. J.M.Smith, H.C.Van Ness, and M.M.Abbott, Intro. Chem. Eng. Thermodynamics, Ch.3, 5th ed.(McGraw Hill, 1996)
17. J.M.Prausnitz, R.N.Lich tenthaler and E.Gomes de Azevedo, Molecular Thermodynamics of Fluid-Phase Equilibria, 3rd ed.(Prentice-Hall, NJ, 1999)
18. J.W.Tester, M.Modell, Thermodynamics and its Applications, 3rd ed.(Prentice Hall, 1997)

Chapter 5

Mean field theory for binary mixture of polar and non polar molecules

5.1. Introduction

The adsorption of fluid mixtures in micro porous materials is a frequently encountered process in natural gas purification, and in the design of porous polymeric membranes in fuel cells. In the case of natural gas purification, methane is separated from the hydrocarbon mixture containing ethane, propane, and butane as well. Even though some experimental data are available for sorption of the binary mixtures of methane with ethane, propane, and butane[1-4], very few studies based on molecular theory have been carried out[5-8]. Tan and Cracknell[5,6,9,10] addressed the effect of pore size, operating pressure, temperature on the selectivity of ethane over methane in methane-ethane mixtures using non-linear mean field theory (NLMFT) and Grand Canonical Monte-Carlo (GCMC) simulations, respectively. Jiang et al.[7] studied the influence of pore width, intermolecular potential parameters and state conditions on the selective adsorption of trace components like propane in methane, butane in methane, and nitrogen in methane using NLDFT. Davies et al.[11] also predicted adsorption equilibrium data for methane-ethane mixtures in activated carbon by combining pore size distribution and GCMC simulations, and compared their results with existing experimental data.

Moreover, in light of the above considerations, further systematic studies on sorption of methanol, water, and methanol-water mixtures are required to characterize proton exchange membranes (PEMs) for designing efficient PEM fuel cells,[12-17] and in the dehydration process of methanol manufacturing[18,19].However, while numerous experimental studies have been carried out on this system[12,13,18-20] , to the best of our knowledge, only a few simulation results [21,22] based on molecular theory have been reported in the literature. Shevade et al.[21,22] simulated water-methanol mixture sorption in slit shaped graphite and silicalite pores, with and without acidic sites, using GCMC simulations to explain complex water-methanol mixture behavior.

Only a few attempts have been made to apply density functional/perturbation theory for studying binary mixtures of non-polar molecules[5-8,25] and to our knowledge, no attempt has been made to apply these theories to a mixture of polar molecules. In the present work, we extend the single component mean-field perturbation theory reported by Schoen and Diestler[23] and Kotdawala et al.[24] for studying the sorption of binary mixtures of methane-ethane (non-polar molecules) and methanol-water mixtures (polar molecules) in slit shaped pores. For modeling the non polar system, we consider standard L-J intermolecular potentials to account for dispersion forces, while in the case of the polar system, we consider orientation dependent dipole-dipole and dipole–induced dipole intermolecular potentials to account for electrostatic interactions in addition to dispersion

interactions. In order to explicitly derive an analytical equation/expression for the Helmholtz free energy of the thermodynamic system under consideration, we need to use intermolecular potentials for orientationally dependent interactions which are in the form of orientation independent intermolecular potentials. This can be achieved by using the statistical averaging method recently adopted by Kotdawala et al(24) .

5.2. Model Development

Consider two different fluids confined in the slit-pore, of width s_z and area A, shown in Figure 1.

The partition function for the two component system is given by(25),

$$Q = \frac{Z_N}{N_1! N_2! \lambda_1^{3N_1} \lambda_2^{3N_2}} \tag{5.1}$$

where, Z_N is the associated configuration integral, N_1 and N_2 are the number of molecules of components 1 and 2 respectively, λ_1 and λ_2 are the thermal wave lengths of components 1 and 2,(23,24) and:

$$Z_N = \int d\omega_1^{N_1} \int dr_1^{N_1} \int dr_2^{N_2} \int d\omega_2^{N_2} \exp(-\beta U_c) \tag{5.2}$$

where , $\beta = 1/kT$ and U_c is the configuration internal energy of the system, which is defined as follows:

$$U_c = U_c^0 + U_c' \tag{5.3}$$

In the above expression U_c^0 is the configuration energy of the reference (nominal) system, and U_c' is the configuration energy of the system perturbed from the above nominal one.

The configuration integral can be conveniently calculated by identifying the following two parts:

$$Z^0 = \int d\omega_1^{N_1} \int dr_1^{N_1} \int dr_2^{N_2} \int d\omega_2^{N_2} \exp(-\beta U^0{}_c) \tag{5.4}$$

which is the configuration integral associated with the reference system, and

$$Z^P = \int d\omega_1{}^{N_1} \int dr_1{}^{N_1} \int dr_2{}^{N_2} \int d\omega_2{}^{N_2} \exp(-\beta U'_c)$$

(5.5)

which is the configuration integral associated with the perturbation from the above reference system.

Note that the mean-field configuration integral can be approximated by (23)

$$Z_N = \exp(-\beta <U'_c>)$$

(5.6)

where, $\langle U'_c \rangle = \langle U'_{11f} \rangle + \langle U'_{22f} \rangle + \langle U'_{12f} \rangle + \langle U'_{1fw} \rangle + \langle U'_{2fw} \rangle$

(5.7)

In the above expression $\langle U'_{11f} \rangle$ is associated with the fluid-fluid interactions pertaining to component 1 , $\langle U'_{22f} \rangle$ is associated with the fluid-fluid interactions pertaining to component 2, $\langle U'_{12f} \rangle$ is associated with the fluid-fluid interactions pertaining to component 1 and component 2, $\langle U'_{1fw} \rangle$ is associated with the fluid-wall interactions between component 1 and the pore wall, and $\langle U'_{2fw} \rangle$ is associated with the fluid-wall interactions between component 2 and the pore wall.

5.2.1 Model equations for binary mixture of non-polar gases

The overall configuration energy accounts for the following intermolecular energy terms:

1. The fluid –fluid interactions associated with components i and j (23)

$$U'_{iif}(r) = -4\varepsilon_{ffij}(\frac{\sigma_{ffij}{}^6}{r^6}) \qquad \text{where ,i,j=1,2}$$

(5.8)

where, σ_{ffij} is the collision diameter of component i and j and r is the distance between two molecules i and j . Note that ε_{ffij} is the fluid-fluid interaction parameter for component i and component j.
The average value of $U'_{11f}(r)$ for a slit pore geometry is obtained by a method of integration introduced by Schoen and Diestler (23), and later used by Kotdawala et al (24)

$$\langle U'_{11f} \rangle = a_{p1}N_1\rho_{p1}$$

(5.9)

where the pore density of component 1 is given by

$$\rho_{p1} = \frac{N_1}{As_z} \qquad (5.10)$$

$$a_{p1} = a_{b1}\left[1 - \left(\frac{3\sigma_{ff11}/\sigma_{fw1}}{4(\xi_1 - 2)}\right) + \left(\frac{\sigma^3_{ff11}/\sigma^3_{fw1}}{8(\xi_1 - 2)^3}\right)\right] \qquad (5.11)$$

with,

$$\xi_1 = s_z/\sigma_{fw1} \qquad (5.12)$$

$$\sigma_{fw1} = \left(\sigma_{ff11}\sigma_w\right)^{1/2} \qquad (5.13)$$

where, σ_w is the effective diameter of the atom of pore wall, and:

$$a_{b1} = \frac{8\pi\varepsilon_{ff11}\sigma^3_{ff11}}{3} \qquad (5.14)$$

Similarly, the average fluid –fluid interactions associated with component 2 (23) can be given by:

$$\langle U^{'}_{22f}\rangle = a_{p2}N_2\rho_{p2} \qquad (5.15)$$

An explicit characterization of the various terms in Eqn.(5.15) is given in the Appendix A(Eqns. A.1-A.5)

The average value of fluid–fluid interactions associated with component 1 and component 2 ($U^{'}_{12f}(r)$) for a slit pore geometry is given by:

$$\langle U^{'}_{12f}\rangle = a_{p12}N_1\rho_{p1} \qquad (5.16)$$

Similarly, an explicit characterization of the various terms in Eqn.(5.16) is given in the Appendix A(Eqns. A.6-A.10)

2. The fluid–wall interactions between component i and the pore wall can be expressed mathematically as follows: (23)

$$U'_{ifw} = \frac{-2\pi\rho_w \varepsilon_{fwi}\sigma_{fwi}^6}{3d}\left[z_i^{-3} + (s_z - z_i)^{-3}\right], \quad \sigma_{fwi} \leq z_i \leq s_z - \sigma_{fwi}, \; i=1,2 \qquad (5.17)$$

Here, $\varepsilon_{ifw} = (\varepsilon_{fij}\varepsilon_w)^{1/2}$, i,j=1,2 ρ_w is the aerial density of the solid substrate, and d is the distance between two wall atoms.

The average value of U'_{1fw} is given by (23,24)

$$\langle U'_{1fw}\rangle = \psi_1(\xi_1) = \frac{2N\pi\rho_w \varepsilon_{fw1}\sigma_{fw1}^3}{3d(\xi_1 - 1)}\left[\frac{1}{(\xi_1 - 1)^2} - 1\right], \xi_1 > 2 \qquad (5.18)$$

Similarly, the average value of U'_{2fw} is given by (23,24)

$$\langle U'_{2fw}\rangle = \psi_2(\xi_2) = \frac{2N\pi\rho_w \varepsilon_{fw2}\sigma_{fw2}^3}{3d(\xi_2 - 1)}\left[\frac{1}{(\xi_2 - 1)^2} - 1\right], \xi_2 > 2 \qquad (5.19)$$

5.2.2 Model equations for binary mixtures of polar molecules

In the case under consideration, the configuration energy accounts for the following intermolecular energy terms:
1. The fluid –fluid interactions associated with component i and j are represented by(24,26-29):

$$U'_{ijf}(r) = \left[-\frac{1}{(4\pi\varepsilon_0)^2 r^6}\left(\frac{3\alpha_i \alpha_j (I_i + I_j)}{I_i I_j 4}\right)\right] - \frac{1}{(4\pi\varepsilon_0)^2 r^6}\left[\frac{\mu_i^2 \mu_j^2}{3kT} + \mu_i^2\alpha_i + \mu_j^2\alpha_j\right] \quad (5.20)$$

where, i=1,2

In the above expression, μ_i and μ_j are the permanent dipole moment of component i and j respectively, α_i and α_j are the average polarizibility of component i and component j respectively, I_i and I_j are the first ionization potential of component i and j, respectively, and r is the distance between molecules i and j. Notice that the first term in Eqn. (5.20) accounts for the dispersion interactions and the second term accounts for the angle independent electrostatic interactions obtained through a statistical averaging method(24-26). The first term in the second bracket in Eqn. (5.20) accounts for dipole-dipole interactions and the other terms account for dipole-induced dipole interactions.

The average value of the interaction energy can be obtained by integrating Eqn. (5.20) over the pore dimensions, as shown by Kotdawala et al.(24) , leading to the following expression:

$$\langle U'_{11f} \rangle = a_{p11} N_1 \rho_{p1} \tag{5.21}$$

where,

$$a_{p11} = \frac{4\pi a_{p1}}{3\sigma^3_{ff11}(s_z - 2\sigma_{fw1})} \left[-\frac{3}{2}\sigma_{ff11} + 2(s_z - 2\sigma_{fw1}) + \frac{\sigma^3_{ff11}}{4(s_z - 2\sigma_{fw1})^2} \right] \tag{5.22}$$

$$a_{p1} = \frac{1}{(4\pi\varepsilon_0)^2} \left[\left(\frac{2\mu_1^4}{3kT} \right) + 2\mu_1^2\alpha_1 + \left(\frac{3\alpha_1^2 I_1}{4} \right) \right] \tag{5.23}$$

Similarly, the average value of the fluid-fluid interaction energy for component 2 can be given by:

$$\langle U'_{22f} \rangle = a_{p22} N_2 \rho_{p2} \tag{5.24}$$

Notice that an explicit characterization of the various terms in Eqn.(5.24) is given in the Appendix A(Eqns. A.11-A.12)

The average fluid–fluid interactions between components 1 and 2 are given by the expression below :

$$\langle U'_{12f} \rangle = a_{p121} N_1 \rho_{p1} \tag{5.25}$$

An explicit characterization of the various terms in Eqn.(5.25) is given in the Appendix A (Eqns. A.13-A.14)

2. Finally, the fluid–wall interactions for component i and the wall can be calculated from Eqn. (5.17). Therefore, $\langle U'_{1fw} \rangle$ can be calculated through Eqn(5.18) and $\langle U'_{2fw} \rangle$ through Eqn.(5.19).

5.2.3 Helmholtz free energy and chemical potential for pore and bulk phases

The Helmholtz free energy can be calculated as follows:(23)

$$F = -\beta^{-1} \ln(Q) \tag{5.26}$$

$$= -\beta^{-1} \ln\left(\frac{Z^0 \langle \exp(-\beta U'_c) \rangle}{N_1! N_2! \lambda_1^{3N_1} \lambda_2^{3N_2}}\right) \tag{5.27}$$

$$= -\beta^{-1} \ln\left(\frac{Z^0}{N_1! N_2! \lambda_1^{3N_1} \lambda_2^{3N_2}}\right) - \beta^{-1} \ln(\langle \exp(-\beta U'_c) \rangle) \tag{5.28}$$

$$= -\beta^{-1} \ln\left(\frac{Z^0}{N_1! N_2! \lambda_1^{3N_1} \lambda_2^{3N_2}}\right) + \langle U'_c \rangle \tag{5.29}$$

Note that(23): $Z^0 = (As_z - N_1 bp_1 - N_2 bp_2)^{N_1 + N_2}$ (5.30)

where, $b_{p1} = \dfrac{8\pi\sigma^3_{ff11}}{3}$ (5.31)

and $\quad b_{p2} = \dfrac{8\pi\sigma^3_{ff22}}{3}$ (5.32)

Combining Eqns. (5.9,5.15,5.16,5.18, and 5.19) or Eqns. (5.21, 5.24, 5.25, 5.18, and 5.19) with (5.7 and 5.29), one obtains the following expression for the Helmholtz free energy associated with the pore phase:

$$F_p = \frac{-(N_1 + N_2)}{\beta}\left[\ln(As_z - N_1 bp_1 - N_2 bp_2)\right] + \ln N_1! + \ln N_2! + N_1 \ln \lambda_1 \tag{5.33}$$
$$+ N_2 \ln \lambda_2 - N_1 \psi_1 - N_2 \psi_2 - N_1 a_{p1} \rho_{p1} - N_2 a_{p2} \rho_{p2} - N_1 a_{p121} \rho_{p1}$$

Similarly, the Helmholtz free energy, F_b for the bulk phase is given by:

For $\rho_{b2} < \rho_{b1}$

$$F_b = \frac{-(N_1 + N_2)}{\beta}\left[\ln(As_z - N_1 b_{b1} - N_2 b_{b2})\right] + \ln N_1! + \ln N_2! + N_1 \ln \lambda_1 \tag{5.34}$$
$$+ N_2 \ln \lambda_2 - N_1 a_{b1} \rho_{b1} - N_2 a_{b2} \rho_{b_2} - N_2 a_{b12} \rho_{b2}$$

For $\rho_{b1} < \rho_{b2}$

$$F_b = \frac{-(N_1 + N_2)}{\beta}\left[\ln(As_z - N_1 b_{b1} - N_2 b_{b2})\right] + \ln N_1! + \ln N_2! + N_1 \ln \lambda_1$$
$$+ N_2 \ln \lambda_2 - N_1 a_{b1} \rho_{b1} - N_2 a_{b2} \rho_{b2} - N_1 a_{b121} \rho_{b1} \qquad (5.35)$$

where, for polar molecules, a_{b1}, a_{b2}, and a_{b121} are:

$$a_{b1} = \frac{4\pi a_{p1}}{3\sigma_{ff11}^3} \qquad (5.36)$$

$$a_{b2} = \frac{4\pi a_{p2}}{3\sigma_{ff22}^3} \qquad (5.37)$$

$$a_{b121} = \frac{4\pi a_{b12}}{3\sigma_{ff12}^3} \qquad (5.38)$$

Note that for non-polar molecules, a_{b1}, a_{b2}, and a_{b121} are given by Eqns. (5.14), (A.3), and (A.7).

Furthermore, at equilibrium, the chemical potentials of bulk and adsorbed phases are equal, thus:

$$\mu_{P1} = \mu_{b1} \qquad (5.39)$$

$$\mu_{P2} = \mu_{b2} \qquad (5.40)$$

5.2.4 Equilibrium pore densities in the low pressure regime:

Note that at low pressures, fluid-fluid interactions can be ignored, and therefore, the equilibrium density for component 1 in the pores is given by (5,6)

$$\rho_{p1} = \rho_{b1} \exp(-\psi_1/kT) \qquad (5.41)$$

while the equilibrium density for component 2 in the pores is given by (5,6)

$$\rho_{p2} = \rho_{b2} \exp(^{-\psi_2}/_{kT})$$

(5.42)

5.2.5 Equilibrium pore densities in the moderate to high pressure regime:

Fileti et al.(30) showed through Ab Initio calculations that the dipole moments of methanol and water monomers are 1.71 and 1.88 D and 2.49 and 2.91 D for dimmers. Water and methanol generally exist as monomers in vapor phase, while in the liquid phase they are typically found in the form of dimmers/clusters. Water and methanol might exist as a vapor or liquid in the pore depending on the external pressure, temperature, and fluid-wall interactions. In that case it would be convenient to consider the dipole moment variations with respect to pore densities. In the absence of information about the exact relationship between the dipole moment and pore densities, a linear relationship between the two variables was assumed. We assigned 1.71 D to the vapor phase density of methanol and 2.49 to liquid phase density of methanol at normal temperature and pressure and a linear fit was performed in the following fashion:

$$D_{methanol} = C_2 * \rho_{p2} + X_2$$

(5.43)

The dipole moment variations for water were fitted in a similar manner, yielding:

$$D_{water} = C_1 * \rho_{p1} + X_1$$

(5.44)

The values of C_1, C_2 , X_1 and X_2 are the respective slopes and intercepts of the above linear fits. Therefore, the equilibrium density profile can be obtained by solving the systems of algebraic Eqns. (5.39), (5.40), (5.43) and (5.44) simultaneously.

5.3. Results and Discussion

5.3.1 Selectivity of component 2 over component 1

Selectivity, S, of component 2 over 1 can be defined as follows (5,6)

$$S = \frac{^{x_{p2}}/_{x_{p1}}}{^{y_{b2}}/_{y_{b1}}}$$

(5.45)

where, x_{p2}, and x_{p1} represent the mole fraction of component 1 and 2 respectively in the pore phase, while y_{b2} and y_{b1} are the mole fractions of components 1 and 2 in the bulk phase. Alternatively, we may define the selectivity as follows:

$$S = \dfrac{\dfrac{\rho_{p2}}{\rho_{b2}}}{\dfrac{\rho_{p1}}{\rho_{b1}}} \tag{5.46}$$

The following parameter values were used in all simulation runs for the methanol-water system under consideration.

Table 5.1: Parameters for fluid-fluid interactions for methanol-water system

component	Component name	I(eV)	$\alpha*10^{24}(cm^3)$	μ(Debye)
1	Water[27]	12.6	1.5	1.9
2	Methanol	10.7[31]	3.4[28]	1.7[28]

Table 5.2 : Parameters for fluid-wall interactions for methanol-water system

Component	ϵ(Kj/mol)	σ(Å)
Water[32]	0.6485	3.11
Methanol	0.7887	3.4225
Carbon[5]	0.2328	3.4

Methanol molecule parameters were obtained from Shevade et al(21,22) by averaging the values of the atoms that form the methanol molecule.

The following parameter values were used in the simulation runs for the methane-ethane system of interest (5,6)

Table 5.3 : Parameters for fluid-fluid and fluid-wall interactions for ethane-
        Methane system

Component	Component name	ϵ(Kj/mol)	σ(Å)
1	Methane	1.22	3.81
2	Ethane	2.01	3.95
-	Carbon[21]	0.2328	3.4

5.3.2 Comparison with Ideal Adsorption Solution Theory (IAST)(33-34):

IAST (33-34) represents essentially an application of Raoult's law to adsorbed phases. It can be used to predict the behavior of binary component adsorption systems by a methodological reduction technique that uses two single component adsorption systems(33,34) . For a given component i, one can write:

$$Py_i = P_i^0(\pi)x_i \tag{5.47}$$

where y_i and x_i are the bulk and pore mole fractions of component i respectively, P is the total bulk pressure, and $P_i^0(\pi)$ is the bulk pressure corresponding to the spreading pressure π in the component isotherm of component i. For a pore width of 9.7 and 15.4 Å, we used the mean field theory (23) for methane and ethane for which P_i^0 and π are related according to the following formula:

$$\pi(P_i^0) = \frac{RT}{A}\int_0^{P_i^0} n_i^0(p)d\ln p \tag{5.48}$$

It is possible, for example, to calculate x_i for a given P and y_i by first solving for $P_i^0(\pi)$ in the equation

$$\sum_i \frac{Py_i}{P_i^0(\pi)} - 1 = 0 \tag{5.49}$$

This equation follows from (5.47), since the sum of the mole fractions in the pore must equal unity. We used Unilan equation (30) to fit the single component data obtained from the simulation studies.

5.3.3 Comparisons with the results of Tan Z.(5,6) and Shevade A. et al.(21,22)

In order to compare our simulation results with Tan Z.(5,6) and Shevade et al(21,22), we replaced the fluid-wall intermolecular potential in Eqn. (5.17) with the following intermolecular potential expressions .

- The fluid –wall interactions between component i and the pore wall are represented as follows:(5,6)

$$U_{ifw}'(z) = \varepsilon_{wi}\left[\frac{2}{5}\left(\frac{\sigma_{fwi}}{z}\right)^{12} - \left(\frac{\sigma_{fwi}}{z}\right)^4 - \left(\frac{\sigma_{fwi}^4}{3s_z(z+0.61s_z)^3}\right)\right] \tag{5.50}$$

$$\varepsilon_{wi} = 2\pi\rho_s\varepsilon_{fwi}\sigma_{fwi}^2 s_z, \text{ i=1,2} \tag{5.51}$$

where, ρ_s is the aerial density of the solid substrate, ε_{fwi} is fluid-wall interaction

parameter for component i and σ_{fwi} is the effective fluid –wall collision diameter for component i. Then, the average value of $U'_{ifw}(z_i)$ is given by

$$\psi_i = \int_0^{s_z} U'_{ifw}(z) + U'_{ifw}(s_z - z)dz = \langle U'_{ifw} \rangle \tag{5.52}$$

5.3.4 Methane-ethane mixtures

Figure 2 shows how the relative contributions of the fluid-wall (methane-wall and ethane-wall) interactions and fluid-fluid (methane-methane, methane-ethane, and ethane-ethane) interactions change as a function of pore size. The figure indicates that the fluid-wall interactions dominate over fluid-fluid interactions, due to weaker fluid-fluid dispersion interactions attributed to the non-polar nature of methane and ethane. In the pore size range of 10 Å or greater, the magnitudes of fluid-fluid interactions are less than one hundredth of the fluid-wall interactions, which suggests that adsorption is mainly governed by fluid-wall interactions. From Figure 2, it is difficult to compare fluid-fluid interactions between ethane-ethane, ethane-methane and methane-methane. Figure 3 shows that the magnitudes of interactions between, methane-ethane, and methane–methane are almost the same because of the small differences in molecular sizes and the L-J interaction parameter. However, the ethane-ethane interactions are almost 100 times greater than those of methane-methane and methane–ethane due to the higher density of ethane molecules within the pore.

Figure 4 shows the selectivity calculated using Eqn. (46). As the pore size decreases, the selectivity for ethane increases due to increased fluid–wall interactions, which favor ethane (Figure 2). The selectivity at pressures of 0.0146 and 0.146 atm show different behavior. The selectivity decreases due to molecular sieving effects and contact layer formation from pore size of 7.8 Å to 12.5 Å and again increases with pore sizes up to 14.5 Å due to space available for ethane molecules to enter into the pore. Above 14.5 Å selectivity decreases due to molecular sieving effects and weak fluid-wall interactions in large pores.

In order to test the sensitivity of the proposed model to the temperature, the selectivity was simulated as a function of temperature. Results in Figure 5 show that the selectivity decreases as temperature increases due to the high kinetic energy of the molecules, in the range of 3-5 kJ/mol.

Figure 6 shows that the ethane selectivity increases as the pressure increases from zero, due to increased fluid-wall interactions in the monolayer, in the range of 6-12 kJ/mol. However, S then decreases, because of the completion of monolayer formation, which results in weak fluid-fluid interactions in the range of 0.2-0.5 kJ/mol.

Figure 7 shows the ethane selectivity as a function of bulk mole fraction of methane at three different pressure values: 0.0146, 0.146, and 1.46 atm at 280 K for a 13 Å pore size. The selectivity decreases as the methane concentration increases in the bulk phase.

The selectivity was found to be more sensitive to methane bulk mole fraction at higher pressures due to enhanced ethane-wall interactions as compared to lower pressures.

In order to compare the simulated results from the proposed model with the predictions from IAST and results from Tan et al., we simulated single component isotherms of methane and ethane for the pore size of 9.7 Å at 286 K which were obtained by using mean–field theory(23). The single component isotherms were fitted using the UNILAN equation and applying IAST(33,34) for binary component systems and are shown in Figure 8.

Figure 9 shows the comparison of the selectivity as a function of bulk pressure. The results from IAST and work by Tan Z.(5,6) are in good agreement with the simulated results obtained on the basis of the proposed model.

5.3.5 Methanol-water mixtures

The variation of dipole moment in the pore as the operating pressure increases are shown in Figure 10. The values are observed to increase linearly, as discussed in the text. The values of the dipole moments actually used to generate isotherms, shown in Figure 11, are shown as points in Figure 10, and depend on the density of the fluid (water or methanol) in the pores.

Figure 11 shows the single component isotherms of methanol and water at 298 K in a 30 Å pore. Results show that the pore filling in the case of methanol takes place at relatively lower pressure than that of water, due to greater methanol-wall interactions which cause the completion of monolayer formation at low pressure. According to the simulation results of Fileti et al.(30) these results imply that the methanol and water are both in vapor- like states before the pore filling, and in a liquid-like state (clusters of dimmers) after the pore filling takes place because of hydrogen bonds.

Figure 12 shows the relative magnitudes of fluid-wall (methanol-wall, water-wall) and fluid-fluid (methanol–methanol, water-methanol, and water-water) interactions at 298 K for 15 Å pore width. Before pore filling takes place, the fluid-wall interactions (2-3 kJ/mol) dominate over the fluid-fluid interactions (<0.5 kJ/mol). However, after pore filling, water-water interactions are more significant than other interactions, indicating the preferential adsorption of water due to dipole-dipole (electrostatic) interactions (~10 kJ/mol).Thus, the results imply that the adsorption phenomena is governed by fluid-wall interactions before the pore filling takes place, and by fluid-fluid interactions, mainly water-water interactions, after the pore filling.

Figures 13, 14, and 15 show the isotherms of a 50-50 mole % of water-methanol mixture for 15, 18, and 25 Å pore sizes. In all cases, before pore filling takes place, methanol adsorbs preferentially over water, because of greater methanol-wall interactions due to the greater polarizability of methanol compared to water. However, once the monolayer forms on the wall, water starts dissolving in methanol and forming clusters through hydrogen bonding with other water molecules. This, in turn, increases the water density

in the pores as pressure increases by displacing methanol molecules out of the pore, and implying that the hydrogen bonding between water-methanol and methanol-methanol are less stable than the water-water hydrogen bonds in the pore. The size of the slit pore relative to the size of adsorbing molecules might be responsible for unstable hydrogen bonds between water-methanol and methanol-methanol. Thus, water adsorbs selectively in the pore after pore filling. The figures also indicate that, as the pore size increases from 15 to 25 Å, the transition pressure for condensation increases due to the larger separation between the interacting walls. Simultaneously, the pore densities of methanol and water decrease before capillary condensation takes place in the pore due to a decrease in fluid-wall interactions. Also, as the pore spacing increases the water and methanol densities at the point of capillary condensation increase due to the increased space available for molecules to participate in hydrogen bonding. However, after capillary condensation, the water density continues to increase with increasing pressure, while the confined methanol density decreases. The stronger hydrogen bonding between water molecules increasingly displaces the methanol out of the pore.

Figure 16 shows the selectivity of methanol over water as a function of operating pressure for pore sizes of 15, 18, and 30 Å. The selectivity of methanol is greater than one before the pore filling takes place, due to greater methanol-wall interactions than water-wall interactions, which are attributed to the greater polarizability of methanol molecules. The selectivity is less than one after pore filling because water-water interactions are more significant than fluid-wall, methanol-methanol, and methanol-water interactions, as shown in Figure 12. The figure also indicates that selectivity increases as pore size decreases before the pore filling takes place due to increased methanol-wall interactions before it begins to be displaced.

Figure 17 shows a comparison with the results of Shevade et al(21,22). In order to perform a meaningful comparison, we calculated the saturation pressure of 50% mole fraction of bulk water-methanol mixture using the method described by Schoen et al(23). The following expressions for bulk pressure were used to determine bulk gas-liquid coexistence properties:

$$P = \frac{(\rho_{b1} + \rho_{b2})kT}{(1 - \rho_{b1}b_{b1} - \rho_{b2}b_{b2})} - a_{b1}\rho_{b1}^2 - a_{b2}\rho_{b2}^2 - a_{b12}\rho_{b2}^2 \qquad (\rho_{b2} < \rho_{b1}) \qquad (5.53)$$

$$P = \frac{(\rho_{b1} + \rho_{b2})kT}{(1 - \rho_{b1}b_{b1} - \rho_{b2}b_{b2})} - a_{b1}\rho_{b1}^2 - a_{b2}\rho_{b2}^2 - a_{b12}\rho_{b1}^2 \qquad (\rho_{b2} > \rho_{b1}) \qquad (5.54)$$

The bulk saturation pressure was found to be 15.6 kpa .The simulated pore densities of methanol and water and the pore filling pressure deviate somewhat from the values in Shevade et al(21-22). However, the simulated isotherms were qualitatively in agreement with the aforementioned study. It should be pointed out, that additional simulation results based on more advanced, detailed and computationally demanding techniques like GCMC are required in order to further elucidate these deviations.

5.4. Conclusions

The mean-field perturbation theory proposed by Schoen et al.(23) and Kotdawala et al.(24) was extended to account for binary component mixtures of non-polar and polar molecules. The theory enabled us to predict the thermodynamic properties of binary mixtures of polar and non-polar molecules in confined narrow slit-pores. The following conclusions were made.

1. The adsorption of non polar molecules (methane-ethane) is governed by fluid-wall interactions. The selectivity of ethane was found to be more sensitive to pore size than other variables like ethane mole fractions and operating pressure.
2. The predictions of the selectivity using the proposed model were found in good agreement with the results of Tan et al(5,6) and predictions using IAST.
3. In case of methanol-water mixture adsorption, the fluid-wall interactions dominate over fluid-fluid interactions before pore filling takes place. However. the trend reverses after pore filling, resulting in the preferential adsorption of methanol before the pore filling, and preferential adsorption of water after pore filling. The preferential adsorption of methanol before pore filling was attributed to the greater polarizability of the methanol molecule, while the post pore filling phenomena was attributed to the formation of much stronger water-water hydrogen bonds than hydrogen bonds between water-methanol and methanol-methanol molecules.
4. The usage of angle-averaged dipole-dipole and dipole-induced dipole intermolecular potentials enabled us to predict adsorption isotherms of methanol-water mixture qualitatively. The simulated isotherm of methanol-water mixtures deviated somewhat from the results of Shevade et al.(21,22) However, the results were qualitatively similar. In this particular case, sophisticated Monte–Carlo simulations are required to further elucidate and comment on the simulated results obtained by using the proposed statistical mechanical model and the mean-field perturbation approach.
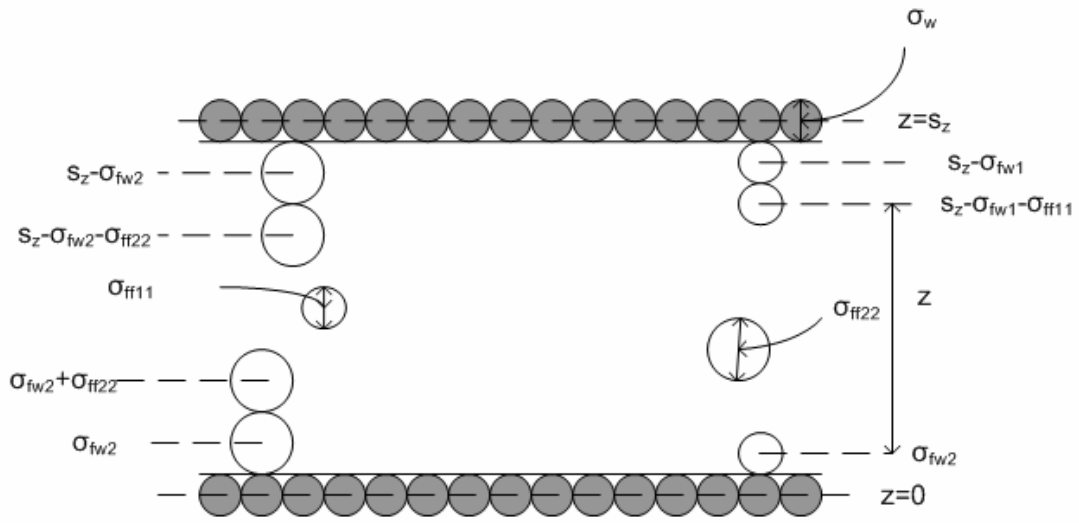
Fig. 5.1. Side view of the slit-pore model showing wall atoms and fluid molecules
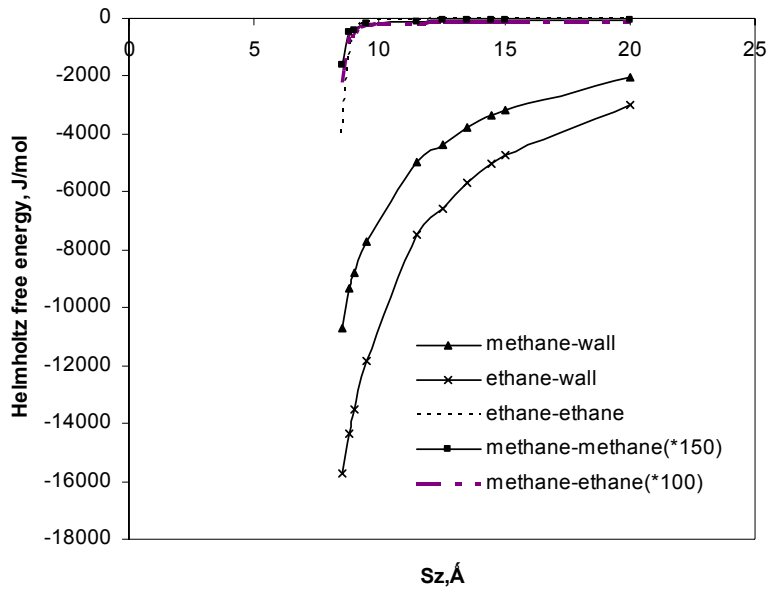
Fig. 5.2 Relative magnitudes of methane-wall, ethane-wall, ethane-ethane, methane-methane(*150), and methane-ethane(*100) interactions as a function of pore width for y_{b1}=0.9 (methane) at 280 K.
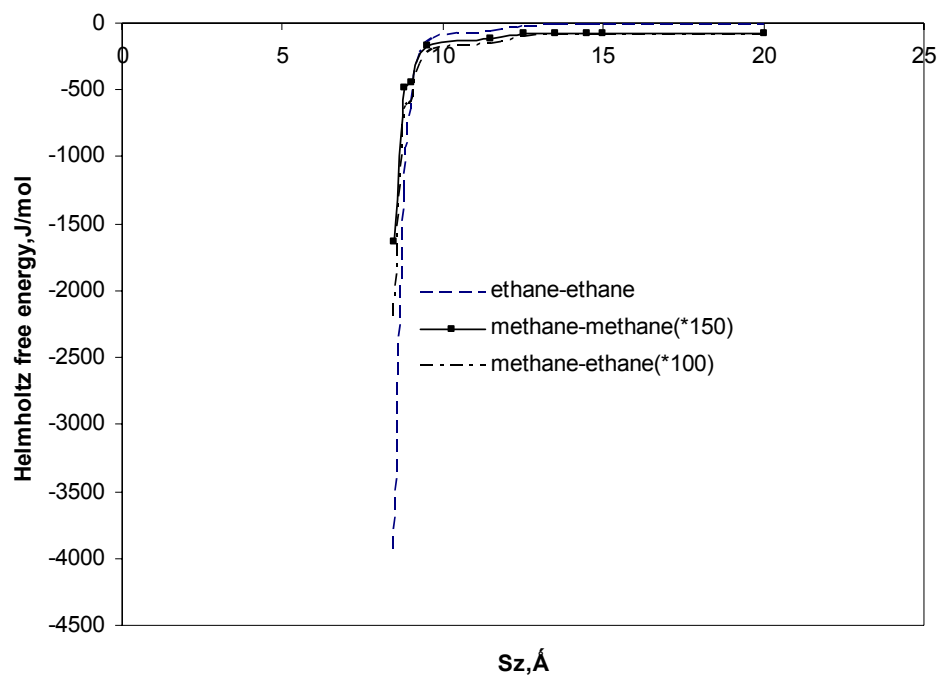
Fig. 5.3 Relative magnitudes of ethane-ethane, methane-methane (*150), and methane-ethane (*100) interactions as a function of pore width for y_{b1}=0.9 (methane) at 280 K.
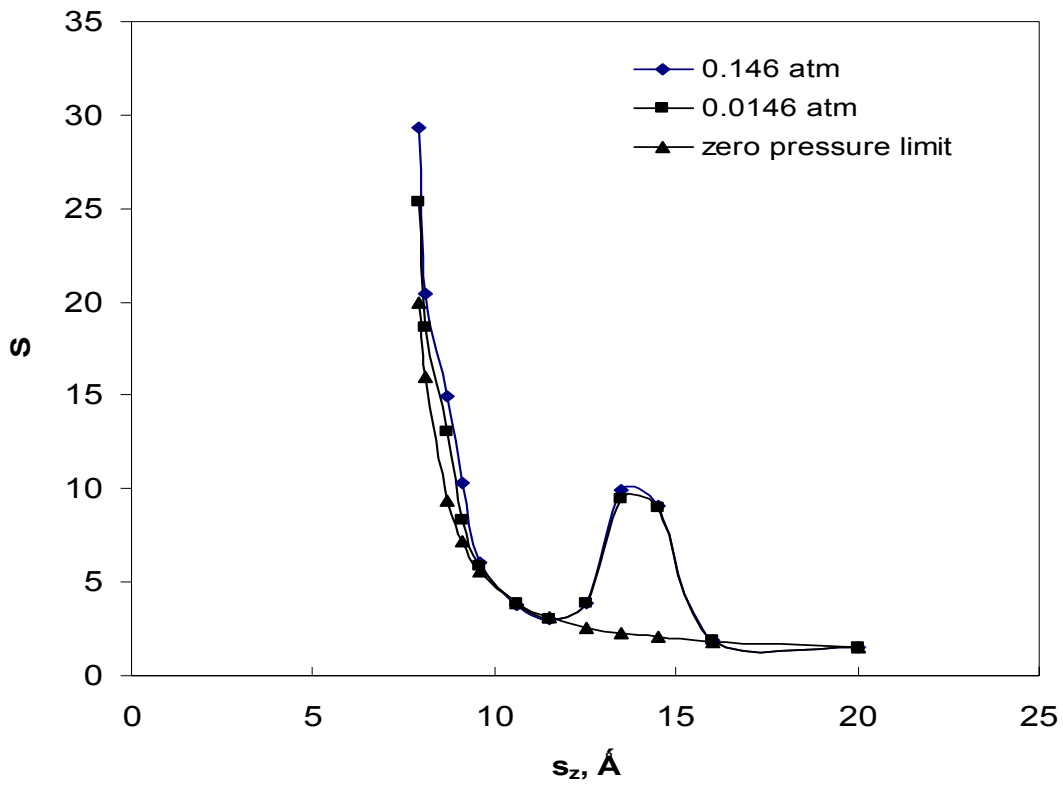
Fig.5.4 Selectivity of ethane over methane as a function of pore size at 280 K and y_{b1}=0.1 (methane). Results shown for operating pressures in the limit of zero pressure to 0.146 atm.
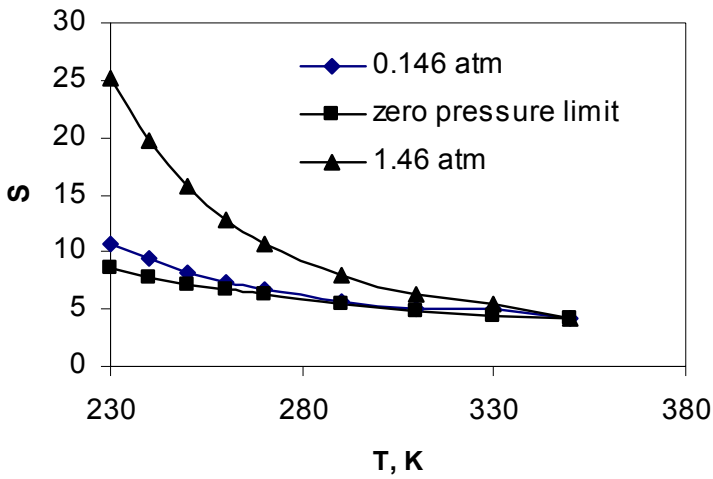
Fig. 5.5 Selectivity of ethane over methane as a function of temperature for 9.5 Å pore size at y_{b1}=0.5 (methane). Results shown for operating pressures in the limit of zero pressure to 1.46 atm
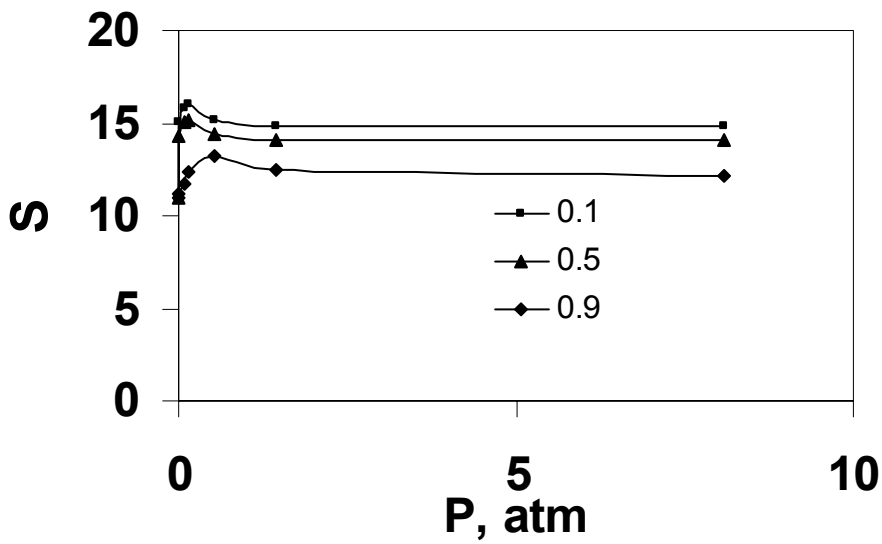
FIG. 5.6 Selectivity of ethane over methane as a function of operating pressure for 10 Å pore size at 280 K. Results shown for y_{b1}=0.9, 0.5, and 0.1 (methane).
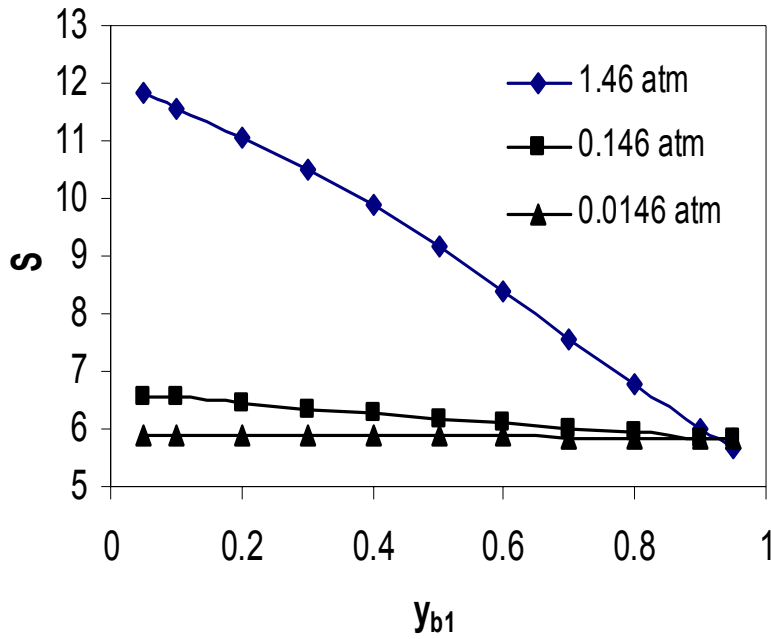
FIG.5.7 Selectivity of ethane over methane as a function of bulk methane mole fraction (y_{b1}) for 13 Å pore size at 280 K. Results shown for operating pressures of 0.0146, 0.146 and 1.46 atm.
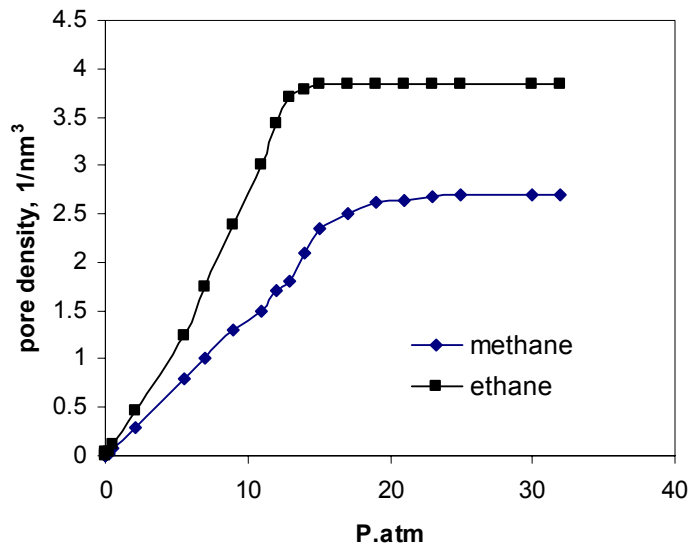
FIG. 5.8 Pore densities of methane and ethane as a function of operating pressure for 9.7 Å pore width at 286 K.
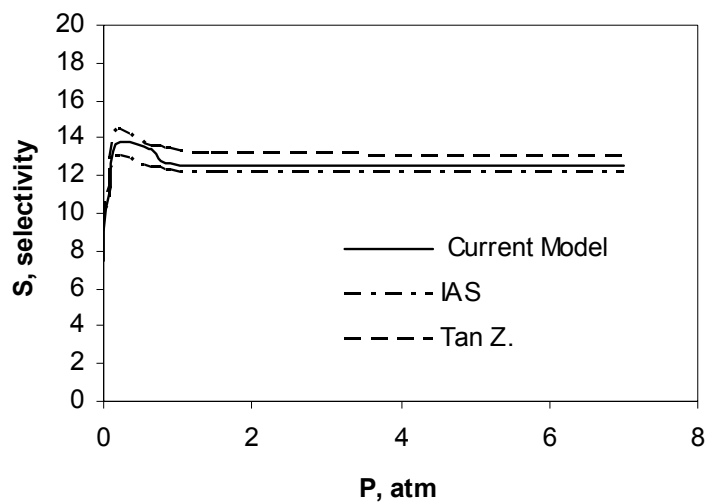
Fig. 5.9 Comparison of simulated ethane selectivity as a function of operating pressure with the results of Tan Z. et al.[5,6] and results from IAST for pore width of 9.7 Å at y_{b1}=0.9 (methane) and T=286 K.
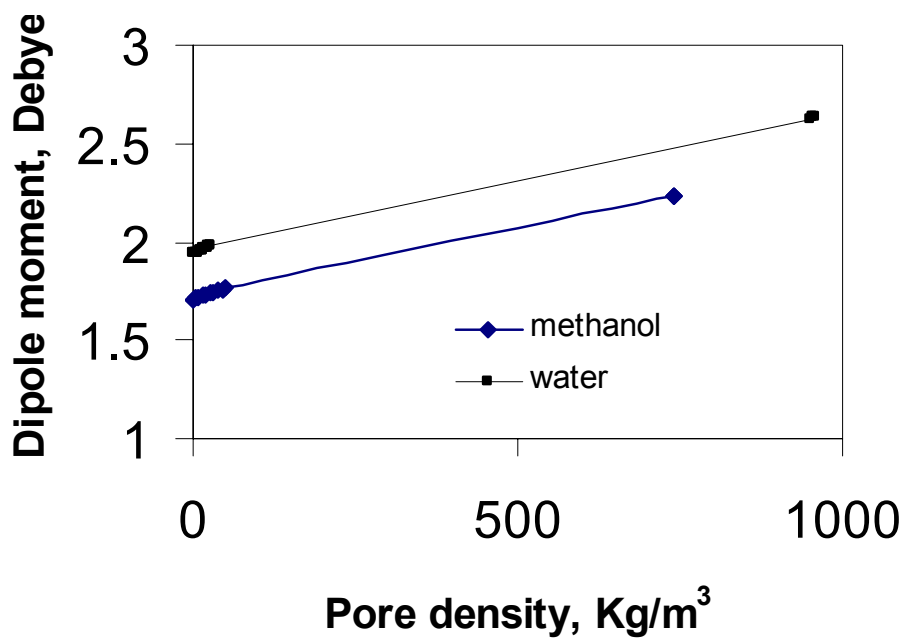
Fig. 5.10 Variations in dipole moments of methanol and water as a function of their pore densities for a pore width of 30 Å at 298 K with reference to their single component isotherms in Figure (11).
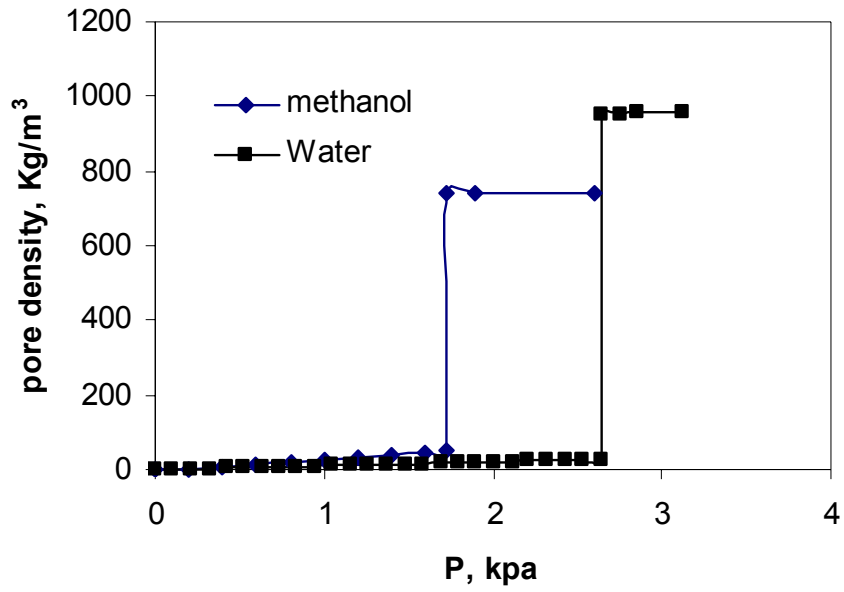
Fig. 5.11 Single-component pore densities of confined methanol and water as a function of operating pressure for pore width of 30 Å at 298 K.
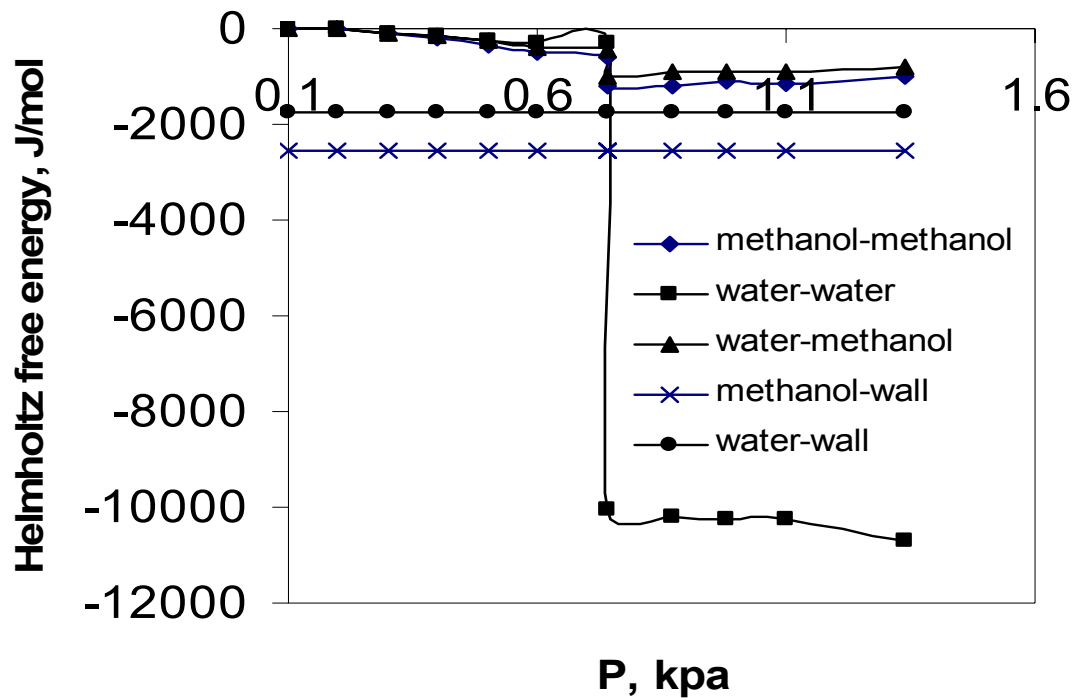
Fig. 5.12 Relative contributions of methanol-methanol, water-water, water-methanol, methanol-wall, and water-wall interactions in Helmholtz free energy as a function of bulk pressure for 15 Å pore size at y_{b1}=0.5 (methanol) and 298 K.
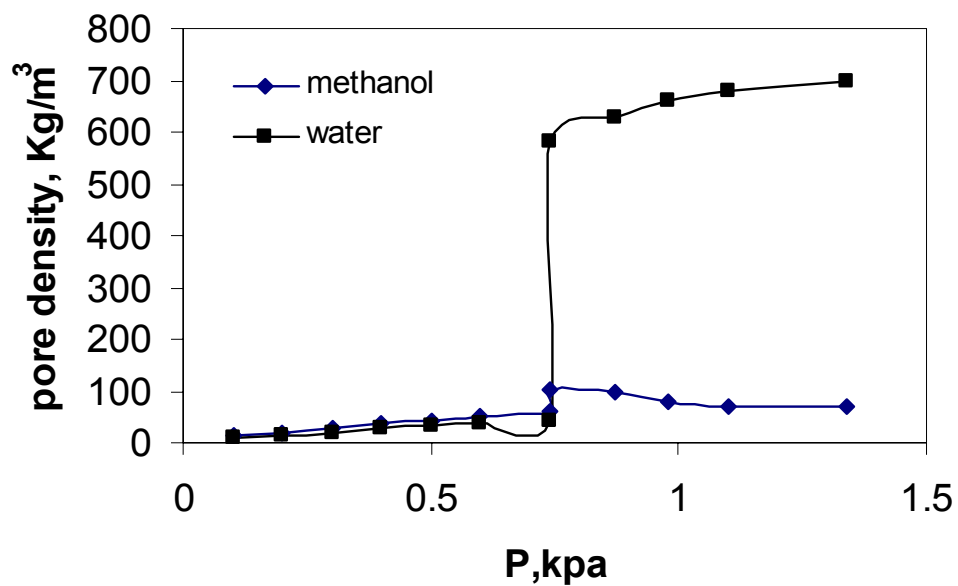
Fig.5.13 Pore densities of methanol and water as a function of bulk pressure for 50-50 mole % mixture of methanol–water in 15 Å pore width at 298 K.
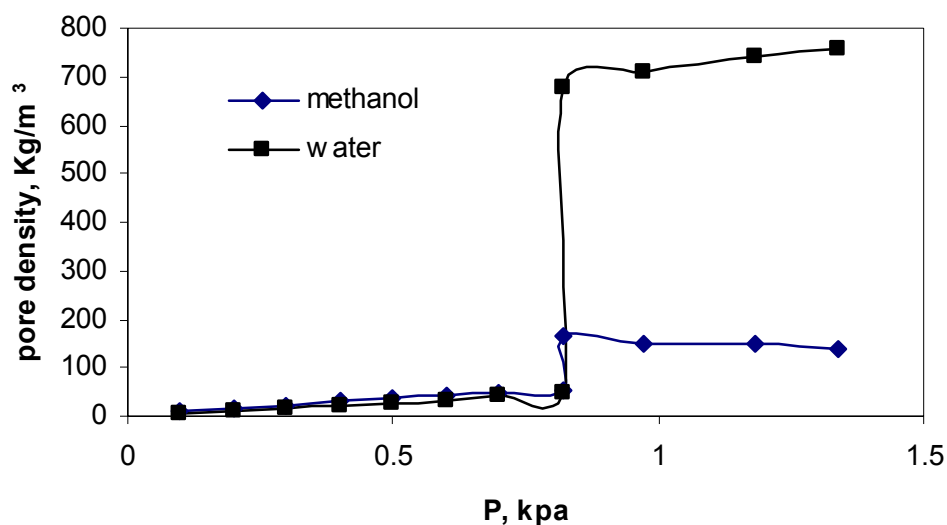
Fig.5.14   Pore densities of methanol and water as a function of bulk pressure for 50-50 mole % mixture of methanol–water in 18 Å pore width at 298 K.
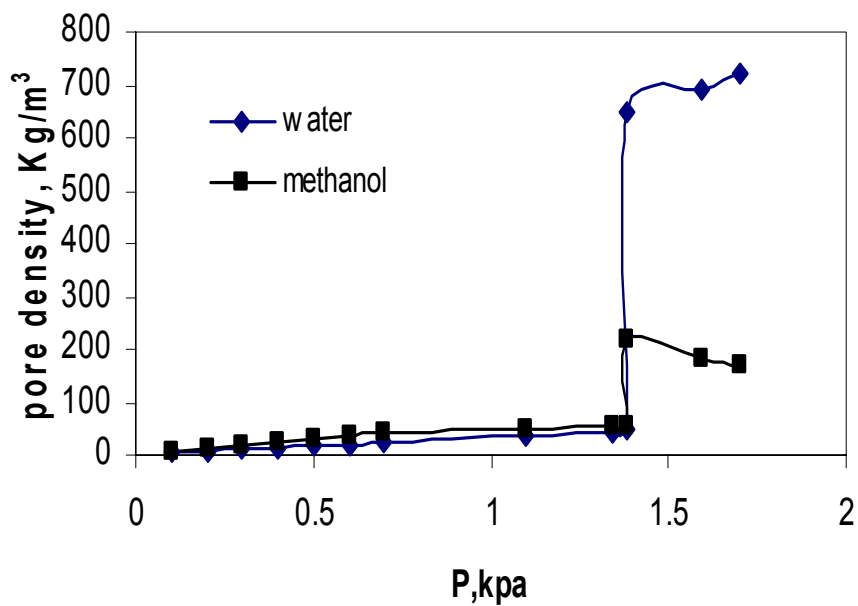
Fig. 5.15   Pore densities of methanol and water as a function of bulk pressure for 50-50 mole % mixture of methanol–water in 25 Å pore width at 298 K.
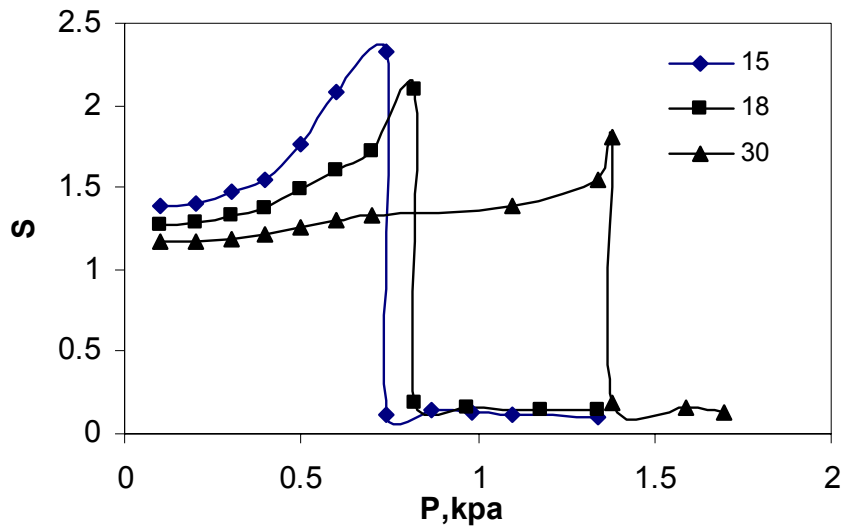
Fig. 5.16 Selectivities of methanol over water as a function of bulk pressure for y_{b1}=0.5 (methanol) at 298 K. Results shown for 15, 18, and 30 Å pore size.
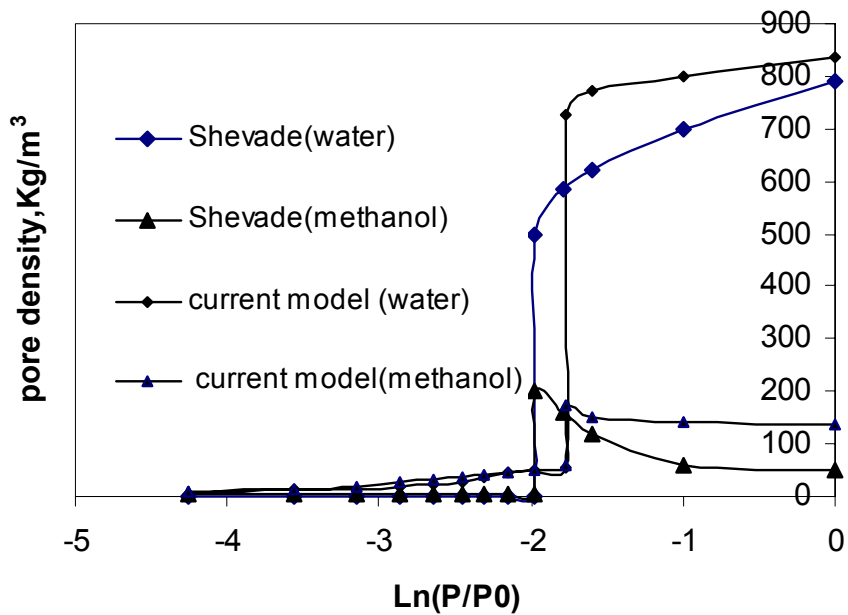
FIG. 5.17. Comparison of simulated pore densities of methanol and water with the results of Shevade et al. (big symbols) as a function of relative pressure for 20 Å pore size at y_{b1}=0.5 (methanol) and 298 K.

References:

1. T.Nakahara, M.Hirata, S. Komatsu, J.Chem.Eng.Data,**26**,161(1981)

2. R.J.Grant and M.Manes, Ind.Eng.Chem.Fundam.,**5**,490(1966)

3. L.Szepesy,V.Illes,Acta. Chim.Hung. ,**35**,245(1963)

4. R.Reich.,W.T.Ziegler and K.A.Rogers,Ind.Eng.Chem.Process.Des.Dev.,**19**,336(1980)

5. Tan Z. Ph.D Thesis, 1991

6. Tan Z. and K.E. Gubbins, J.Phys. Chem,**96,**845(1992)

7. S.Jiang, K.E. Gubbins and P.B.Balbuena, J.Phys. Chem,**98,**2403(1994)

8. H.Pan, J.A.Ritter and P.B.Balbuena, Langmuir, **15**, 4570(1999)

9. R.F.Cracknell, D.Nicholson and N.Quirke in Molecular simulation and industrial applications Methods, Examples and prospects edited by K.E.Gubbins and N.Quirke, (G& B science publishers,1996)

10. R .F.Cracknell, D.Nicholson and N.Quirke, Mol. Phys., **80,**885(1993)

11. G.M. Davies, N.A.Seaton,AICHE J., **46,**1753(2000)

12. V.Gun'ko and T.J.Bandosz, Phys. Chem.Chem.Phys.,**5**,2096(2003)

13. D. V. Baelen, B.V.D.Bruggen,K.V.D.Dungen, J.D.C.Vandecasteele,Chem.Eng. Sci.,**60,**1583(2005)

14. N.H.Jalani, P.Choi and R.Datta, J.Mem. Sci.,2005, in press.

15. N.H.Jalani, P.Choi and R.Datta, Sol. Sta. Ion.,**175,**815(2004)

16. C.Gates, J.Newman, AICHE J.,**46,**2076(2004)

17. B. Smitha, S.Sridher, A.A.Khan, J. Mem. Sci.,**225**,63(2003)

18. S.M. Taqvi, W.S. Appel and M.D.Levan, Ind.Eng.Chem.Res.38,240(1999)

19. M.J.D.Linders, L.J.P.van den Broeke, F.Kapteijn , J.A. Moulijn and J.J.G.M. van Bokhoven, AICHE J.,**47,**1885(2001)

20. S.Hietala, S.L.Maunu and F.Sundholm, J.Pol. Sci.:part B:polymer phys.,**38,**3277(2000)

21. A.V. Shevade, S.Jiang and K.E. Gubbins, Mol.Phys., **97**,1139(1999)

22 .A.V. Shevade, S.Jiang and K.E. Gubbins,J. Chem. Phys. ,**113**,6933(2000)

23. M.Schoen, D.J.Diestler, J. Chem. Phys. 109 (1998) 5596

24. R.R.Kotdawala, N. Kazantzis and R.W.Thompson, J.

Math. Chem, 2005, in press.

25. D.Nicholson and K.E.Gubbins, J.Chem.Phys., **104(20),**8126(1996)

26.T.M. Reed, and K.E.Gubbins, Applied Statistical Mechanics,(Mc-Graw
    Hill, NewYork, 1973)

27.J.M.Smith, H.C.Van Ness, and M.M.Abbott, Intro. Chem. Eng. Therm.,
    Ch.3, 5th ed.(McGraw Hill, 1996)

28. J.M.Prausnitz, R.N.Lichtenthaler and E.Gomes de Azevedo, Molecular
    Thermodynamics of Fluid-Phase Equilibria, 3rd ed.(Prentice-Hall, NJ, 1999)

29. J.W.Tester, M.Modell, Thermodynamics and its Applications, 3rd ed.(Prentice Hall,
    1997)

30. E.E. Fileti, P.Chaudhuri and S.Canuto, Chem. Phys. Lett., **400,** 494(2004)

31. D.M.Lubman and M.N.Kronlck, Anal.Chem.,**55,**867(1983)

32. A. Striolo, A.A.Chialvo, P.T.Cummings, and K.E.Gubbins, Langmuir **19**, 8583(2003)

33. A.L.Myers, J.M. Prausnitz, AICHE J. ,**11**,121(1965)

34. D.P. Valenzuela and A.L.Myers, Adsorption equilibrium data handbook, (Prentice –
    Hall,NJ.,1989)

Chapter 6
Monte Carlo Simulation of Adsorption of Mercury Chloride

6.1. INTRODUCTION

Mercury emissions from coal combustion and waste incineration have been a great environmental concern. Mercury is highly volatile and exists almost exclusively in the vapor phase of combustion flue gases either in the form of elemental mercury or in the form of oxidized mercury like $HgCl_2$, HgO, HgS and $HgSO_4$. Amongst the most promising methods of capturing elemental mercury are chemisorption on adsorbents, the conversion of mercury into oxidized form and finally the capturing of oxidized mercury through physisorption or absorption in aqueous solutions (scrubbing).

Several experimental studies have been carried out by capturing Hg^0 on activated carbon impregnated with halogens especially Cl, I, Br, and F,(1-4) as well as impregnated with $Ca(OH)_2$ and CaO, with acid functional sites and other sulfur compounds(4-7). Studies by Ghorishi (1) and Lee et al.(2) showed that mercury capture can be achieved up to 4800 µg/g in the operating range of 100-200 °C with carbons impregnated with halogens in particular iodine and chlorides. Relying on temperature programmed desorption techniques, Li et al (3) suggested that carbonyl and lactone functional sites seem to be more effective in capturing elemental mercury. Huggins et al (4) showed that the presence of HCl and H_2SO_4 in the flue gas, which eventually gets adsorbed on activated carbon sites, enhances mercury capture capacity by convincingly demonstrating how mercury species react with acidic species. Furthermore, Lancia et al.(6) carried out mercury chloride adsorption experiments on activated carbon with calcium hydroxide and showed that in the temperature range of 70-150 C physical sorption takes place. However above the 150 °C temperature level, mercury chloride is adsorbed irreversibly suggesting that calcium hydroxide has better capacity of capturing mercury chloride than 'raw' activated carbon.

Padak et al (7) simulated the binding energy of Hg^0 in activated carbon with different acid functional sites namely carbonyl, carboxyls, lactones, and halogens using *ab initio* quantum mechanical calculations. Their density functional calculations also suggested that carbonyl and lactone functional groups have high binding energy with elemental mercury, and that embedding fluorine into activated carbon enhances mercury sorption. One should mention that there are several notable approaches to the problem of capturing elemental mercury through absorption in aqueous solutions containing oxidizing agents and Hg^{+2}.(8-12) Rio et al.(8) showed that mercury (II) from water can be removed effectively using silico-alumino and sulfo-calcic fly ash. The mercury removal was found to be effective with increasing pH, and suggested that sulfo-calcic fly ash is more effective in capturing mercury than silico-alumino fly ash.

Zhao et al.(9) studied the absorption of Hg vapor in aqueous solution of mercury (II) with different acids HNO_3/H_2SO_4 and HCN. The experimental data suggest that the presence of HNO_3 and H_2SO_4 enhances mercury absorption, whereas the presence of HCN hinders the absorption rate. In another study conducted by Zhao et al.(10), it was shown

that mercury vapor absorption can be achieved by contacting it with sodium hypochlorite solution in the temperature range of 25-60 °C. It was suggested that low pH, high Cl⁻ and high temperature favor mercury absorption.

Roy et al.(11) reported absorption data of mercury and chlorine into aqueous sulphite/bisulphite in the pH range of 4.7-5.7. It was suggested that mercury doesn't absorb in water and S(iV) solution unless an oxidant like chlorine is present in the solution. The addition of sulfite, which generally appears in the solution through the SO_2 absorption from flue gases containing mercury, considerably reduces mercury absorption rates.

Several other significant approaches have been made to remove oxidized mercury, namely in the form of mercuric chloride, through adsorption on activated carbons(5,6,13-17). Indeed, it is recognized that oxidized mercury is more easily removed than elemental Hg by adsorption due to its higher polarizability and by absorption due to its high solubility in water. Therefore, the emissions of mercuric chloride from municipal solid waste (MSW) incinerators and coal burning power plants can be considerably reduced by adsorption on dry sorbents, which can be carried out either by injecting the sorbents into the exhaust gases, or by using multistage fixed beds for selective adsorption of acid gases, mercuric chloride and dioxins(13,14). It should be pointed out, that flue gases from MSW incinerators typically contain 1-4 mg/m³ of mercury chloride(15-17), and power plants based on coal combustion generate mercury concentrations profiles in parts per billion by volume (ppbv). Finally, it should be also mentioned that processes based on adsorption on dry sorbents do not pose the problem of the treatment and stabilization of waste liquid streams, and therefore, they appear to be very attractive for both small and large combustors such as those used for incineration of hospital wastes for example (13-16).

In another interesting domain of research activity, Hsi et al.(5) showed that impregnation of activated carbon with elemental and organic sulfur increases mercury chloride sorption up to 4500 µg/g. $HgCl_2$ adsorption on "raw" activated carbon was also studied by Karatza et al(16) , who suggested that activated carbon can adsorb $HgCl_2$, and impregnation of activated carbon with sulfur improves the mercury capture capacity. Furthermore, Lancia et al.(6,15) carried out $HgCl_2$ vapor adsorption experiments on solid particles of calcium hydroxide in a fixed bed in the temperature range of 100-2000 °C, and suggested that 95% mercury chloride could be captured by optimizing feed velocity, as well as gas inlet concentration and temperature profiles. Finally, Wu et al.(17) studied the sorption of elemental mercury and $HgCl_2$ on bituminous chars and suggested that $HgCl_2$ sorption is two times higher than that of elemental mercury, being also proportional to the available surface area of the adsorbent employed (implying that $HgCl_2$ sorption develops in a rather natural manner).

In light of the above considerations, one recognizes that the need to develop technologies capable of achieving high removal efficiencies for mercuric chloride emission control leads many researchers to focus their attention on the evaluation of the adsorption capacity and selectivity displayed by different solids. Furthermore, increasingly stringent

performance requirements imposed on the selection of the appropriate adsorbents compel researchers to better understand and characterize the adsorption behavior of mercuric chloride at the molecular level. The latter, would then enable the development of systematic, insightful and comprehensive adsorbent design methods, tailored to recent acute needs for the introduction of efficient air pollution reduction measures and pertinent environmental technologies. To achieve these goals, activated carbon has been identified as an economically and performance-wise suitable adsorbent for capturing mercury chloride, due to its surface characteristics, and in particular, the presence of acid functional sites, calcium and sulfur-based compounds and halogens. To the best of our knowledge, no detailed and systematic molecular simulation studies have been carried out in order to enhance our understanding on the role of individual sites in the sorption of oxidized mercury. In the present research study, an attempt is made to better understand the effect of acid functional groups and calcium-based compounds, in particular calcium hydroxide, on the sorption of oxidized mercury, by conducting detailed molecular simulation studies. Furthermore, the performance of zeolite NaX is compared with activated carbon in order to evaluate the respective advantages and limitations, as well as simultaneously assess the possibility of using zeolites for mercury capture.

The next Section provides the requisite information on the structure and details of the particular simulation models proposed for both the zeolite NaX and activated carbon cases, followed by a description in Section 3 of the Grand Canonical Monte Carlo (GCMC) simulation scheme that has been employed in the present research study. Section 4 discusses the simulation results derived and insights that could be drawn in the study of the problem under consideration. Finally, a few concluding remarks are provided in Section 5.

6.2. MODEL DESCRIPTION

6.2.1 The Zeolite NaX Model

Zeolite NaX was modeled by considering the zeolite cavity as spherically shaped with sodium cations located uniformly in the cavity(18) (Figure 6.1). In particular, the specific locations of sodium cations were taken from Karavias et al.(18) Furthermore, interactions with the spherical cavity were calculated using a spherically–averaged potential for dispersion and repulsion given by (19-20):

$$\psi^{disp} = 4C\varepsilon_{1s}\left[\left(\frac{\sigma_{1s}}{R}\right)^{12} L\left\{\frac{r^2}{R^2}\right\} - \left(\frac{\sigma_{1s}}{R}\right)^6 M\left\{\frac{r^2}{R^2}\right\}\right] \tag{6.1}$$

where,

$$L\{x\} = (1 + 12x + 25.2x^2 + 12x^3 + x^4)/(1-x)^{10} \tag{6.2}$$

$$M\{x\} = (1+x)/(1-x)^4 \tag{6.3}$$

with, $x = \dfrac{r}{R}$

and the potential ψ^{disp} being a function of r, the radial distance of the adsorbed molecule from the center of the cavity. The cavity radius R was chosen as the distance from the center to the nearest oxygen atom. For zeolite NaX, the cavity radius (R) is 7.057 Å (18-19). In the above expression, $C\varepsilon_{1s}$ and σ_{1s} are the Lennard-Jones energy and collision diameters of molecule i with the solid wall respectively. The electrostatic interactions of mercuric chloride with sodium cations are mainly cation-induced dipole and cation-quadrupole moment interactions which can be calculated using Equations (6.4) and (6.5) respectively, as shown below (18):

$$\psi^{ind} = -\dfrac{\alpha q^2}{2r^4(4\pi\varepsilon_o)^2} \qquad\qquad r \geq \sigma_{sf} \tag{6.4}$$

$$= \infty \qquad\qquad r < \sigma_{sf}$$

where α is the polarizability of the molecule, q is the electronic charge of the ion on the surface, ε_o is the permittivity of vacuum, and r is the distance between the centers of the interacting pair(20). σ_{sf} is the collision diameter of molecule i with the solid wall. The interactions between the ion field and the point dipole is given by (20):

$$\psi^{quadrupole} = -\dfrac{Qq(3\cos^2\theta - 1)}{4r^3(4\pi\varepsilon_o)} \qquad\qquad r \geq \sigma_{sf} \tag{6.5}$$

$$= \infty \qquad\qquad r < \sigma_{sf}$$

where, Q is the linear quadrupole moment of the molecule, and θ is the angle between the direction of the field and the axis of the quadrupole.

Moreover, total interaction terms between HgCl$_2$ molecules and the zeolite cavity can be calculated as follows:

$$\psi_{fw} = \psi^{disp} + \psi^{ind} + \psi^{quadrupole} \tag{6.6}$$

It should be pointed out, that two types of interactions are considered in the present study, namely dispersion interactions and quadrupole-quadrupole interactions given by Equations (6.4) and (6.5). The following adsorbate (i)-adsorbate (j) interactions also were considered (21-22):

$$U_{ij}^{QQ} = \dfrac{3Q_iQ_j}{4r^5}\left(\begin{array}{l} 1 - 5\cos^2\theta_i - 5\cos^2\theta_j + 17\cos^2\theta_i\cos^2\theta_j + 2\sin^2\theta_i\sin^2\theta_j\cos^2\phi_{ij} \\ -16\cos\theta_i\cos\theta_j\sin\theta_i\sin\theta_j\cos\phi_{ij} \end{array}\right)$$

$$r \geq \sigma_{ff}$$

$$= \infty \hspace{6cm} r < \sigma_{ff}$$

$$(6.7)$$

$$U_{ij}^{disp}(r) = \left[-\frac{1}{(4\pi\varepsilon_0)^2 r_{ij}^6} \left(\frac{3\alpha_i\alpha_j \ (I_i + I_j)}{I_i I_j 4} \right) \right] \hspace{2cm} r \geq \sigma_{ff} \hspace{2cm} (6.8)$$

$$= \infty \hspace{2cm} r < \sigma_{ff}$$

where I_i and I_j are the first ionization potentials for molecules i and j, respectively. σ_{ff} is the collision diameter of molecule i with molecule j.

6.2.2   The Activated Carbon Model

The pores of activated carbon were modeled by considering two parallel walls, each of which comprises an infinite-sized layer of graphite. The graphite layers are composed of Lennard-Jones sites, but these are smeared out uniformly over each layer (See Figure 6.2). The interaction between an adsorbate molecule and this smooth carbon surface is represented by the 10-4-3 potential of Steele (23). Three types of polar surface sites were considered in the simulations, namely hydroxyl (H), carboxyl (C), and carbonyl (Ca) groups, and are represented schematically in Figure 6.3. The calcium hydroxide layers were modeled by replicating in all x, y, and z directions. The carboxyl, hydroxyl, carbonyl sites, and calcium hydroxide can be considered as a collection of five, two, three, and five point charges, respectively. The parameters (size of charge atom and partial charge) of point charges and their positions were taken from Jorge et al and Cruz et al. (24-25). Figure 6.4 describes the type of site, number of sites, and their distributions. In particular, each site was placed 5 Å apart from its neighbor site (see Figure 6.4). Furthermore, a symbol is assigned to each type of configuration and the number in the symbol represents the total number of sites in the pore. The single digit indicates that half of the sites are on each plate, while the double digit indicates that all sites are located on a single plate. The cross–species parameters were calculated using the Lorentz-Berthelot combining rule (26-27). As mentioned earlier, the electrostatic interactions namely charge-induced dipole moment and charge-quadrupole moment were calculated using Equations (6.4) and (6.5), respectively.

6.3. SIMULATION METHODS

Adsorption isotherms were calculated using Grand Canonical Monte Carlo (GCMC) simulations, in which the temperature (T), volume (V), and chemical potentials (μ) were kept constant. The algorithm for GCMC simulations is well documented (24-25), and we used the general methodology. The pressure (P) was calculated from the chemical

potential and the equation of state for an ideal gas, and all simulations were performed at equilibrium bulk gas temperatures in the range of 400-500 K. Each type of Monte Carlo trial (creation, destruction, and displacement/rotation) was chosen randomly with the same probability. The number of equilibrium steps in the simulations varied according to the operating conditions, in the range of 30 to 80 millions. To calculate statistical uncertainties, simulations were divided in five blocks of trials (each varied from 5 to 12 million) and the observed standard deviation of block average was within 5%. During the sampling period, typical configurations for each run were stored in files and then converted into images. In the case of zeolite NaX, the interactions with molecules in four neighboring cavities also were considered. The molecules in the neighboring cavities were the images of molecules in the central cavity. In the case of activated carbon slit pores, the size of the simulation box was 3 x 1.5 x 3 nm.

We used rectangular simulation cells, bound in the Y direction by pore walls and replicated in X and Z directions using periodic boundary conditions. In order to account for the long range interactions, especially charge–quadrupole, charge-induced dipole and quadrupole–quadrupole interactions, the interactions of molecules in the central cavity with neighboring cavities were considered.

6.4. RESULTS AND DISCUSSION

6.4.1 Adsorption in zeolite NaX.

GCMC simulation results of mercuric chloride adsorption in zeolite NaX in the temperature range of 400-500 K are shown in Figure 6.5, up to an operating pressure of 0.6 kPa. The sorption capacity was predicted to decrease with temperature, as expected. In order to understand the phenomena, the interaction energies of the molecules with the zeolite cavity and sodium cations, were studied (and their respective contribution explicitly assessed), and are shown in Figure 6.6. The figure indicates that the Na–quadrupole moment and fluid-wall dispersion interactions with the spherical cavity dominate over the Na-induced dipole and other interactions amongst mercuric chloride molecules. However, the Na-induced dipole plays a significant role when one considers the total fluid-wall interactions. The higher quadrupole interaction is attributed to the high quadrupole moment (28) (-1.48×10^{-39} $C.m^2$) of the molecule and sodium cations, and dispersion interactions are attributed to the high polarizability (9.3 Å^3) of the molecule(29). Please notice, that the values of the quadrupole moment and polarizability are taken from references where the experimentally derived values are reported. How ever these values were verified by carrying out Ab-Initio calculations in Gaussian with HF, QCISD/SDD and B3LYP methods. The basis set that for HF was CEP-121G , for B3LYP it was 6-31 G and for QCISD it was SDD. The B3LYP (density functional theory) accounts exchange energy and the electron correlation which is omitted from Hartree-Fock(HF) theory where QCISD accounts electron correlations of order two or three(30-32).

In Hartree-Fock theory, the energy has the form:

$$E_{HF} = V + <hP> + 1/2<PJ(P)> - 1/2<PK(P)> \qquad (6.9)$$

where the terms have the following meanings: V is the nuclear repulsion energy. P is the density matrix, $<hP>$ is the one-electron (kinetic plus potential) energy,

$1/2<PJ(P)$ is the classical coulomb repulsion of the electrons., $-1/2<PK(P)>$ is the exchange energy resulting from the quantum (fermion) nature of electrons. In density functional theory (B3LYP)and QCISD methods , the exact exchange (HF) for a single determinant is replaced by a more general expression, the exchange-correlation functional, which can include terms accounting for both exchange energy and the electron correlation which is omitted from Hartree-Fock theory:

$$E_{KS} = V + <hP> + 1/2<PJ(P)> + E_X[P] + E_C[P] \qquad (6.10)$$

where $E_X[P]$ is the exchange functional, and $E_C[P]$ is the correlation functional.How ever ,mercury chloride is relatively small molecule and hence QCISD should give reasonable good results. The predicted values for polarizability from HF, QCISD and B3LYP were 11.1, 10.3 and 9.67 $Å^3$ respectively which are very close to experimental one (9.3 $Å^3$) reported by Pandey et al (28). The quadrupole moments from HF, QCISD and B3LYP were (-1.62 x 10^{-39}, -1.49 x 10^{-39} ^{and} 1.52 x 10^{-39} C.m^2) which were very close to experimental one (-1.48 x 10^{-39} C.m^2) reported by Watanabe et al. (29).The results show that predicted results from B3LYP and QCISD match more closely to experimental value of Quadrupole and polarizability than HF theory. This differences might be attributed to Elctron correlation effects and exchange correlations.

Figure 6.7 shows the effect of mercuric chloride sorption with different carbonyl site concentrations from zero to four sites per pore. The results indicate that the sorption capacity increases with an increase in the number of carbonyl sites, due to increased (more pronounced) ion-induced dipole interactions.

The effect of hydroxyl and carboxyl site on sorption is shown in Figure 6.8. The capacity of adsorbing $HgCl_2$ in carbon with carboxyl sites is found to be greater than that of hydroxyl sites. The sorption capacity of carbon with two carboxyl and hydroxyl sites appear to be the same at low pressures (<60 Pa), but the carboxyl site performs a little better in adsorbing mercury chloride at a regime of high pressures. However, loading in the carbon with 3 carboxyl sites is far greater than loading in carbon with 3 and 4 hydroxyl sites. This is attributed to greater ion-induced interactions in the case of 3 carboxyl sites due to high charge density, and hence, greater ion-induced interactions.

In order to understand these phenomena, we analyzed the magnitudes of different electrostatic interactions among mercuric chloride and acid sites in Figure 6.9 at 150 Pa (for the same case and conditions associated with Figure 6.8). Figure 6.9 indicates that

the ion-induced interactions contribute the most to total mercury chloride and activated carbon (fluid-wall) interactions, followed by dispersion interactions with carbon surface, thus implying that the presence of a functional group has a significant impact on the sorption of mercuric chloride in activated carbon. However, the magnitude of the ion-quadrupole interactions seems to be very low, which might be attributed to a cancellation of the quadruple interactions that can be repulsive/attractive in nature depending on the orientation of molecules, as well as the presence of positive and negative charges as suggested by Equation (6.5). The hydroxyl and the carboxyl sites consist of a large number of charged atoms which lead to greater ion-induced dipole interactions than that of carbonyl sites, entailing an increased sorption of mercuric chloride. The low sorption of carbon with carbonyl sites is due to a low density of charges, the presence of an equal number of positive and negative charges which might cancel the ion-quadrupole interactions, or might be generating net repulsive forces between charges and molecules. Figure 6.10 suggests that interactions among mercury chloride can be up to 20 % of total mercury chloride-'activated carbon' especially in the case of C33 and H33 where clustering of HgCl$_2$ molecules takes place. Figures 6.11, 6.12 and 6.13 show the isotherms at different temperatures for Ca4, H4 and C33 respectively, indicating that an increase in temperature reduces the sorption capacity. Figure 6.14 shows the sorption capacity in plain carbon deposited with calcium hydroxide with different wt% in the carbon pore. It suggests that sorption capacity improves drastically after introducing calcium hydroxide as compared to sorption in H4 and C33. The flattening isotherms in the case of calcium hydroxide doped carbons indicate that all low energy sites are occupied at relatively low operating pressures. Figure 6.15 explains that the performance of the calcium hydroxide doped carbons is attributed to large ion-induced interactions. However, the contributions from dispersion and interactions amongst HgCl$_2$ molecules can not be ignored. Figures 6.16 and 6.17 show the snapshots of the sorption in slit pores with hydroxyl and carboxyl sites respectively. The majority of molecules (golden) are clustered around the functional sites indicating that the presence of these sites increase sorption in activated carbon.

6.4.2 Evaluations of Henry's Constant and Heat of Adsorption in the Zero Pressure Limit

The available experimental data on the sorption of HgCl$_2$ on activated carbon, suggest that the concentration of HgCl$_2$ in the carrier gas is in μg/m^3 (very low), and hence it is reasonable to compare the experimental heat of adsorption with the heat of adsorption in the zero pressure limit and mercury loadings with Henry's constant (loading in the zero pressure limit). Notice, that Henry's constant is given by the following expression (24)

$$H = \frac{\left\langle \exp(-\beta \psi_{fw}) \right\rangle}{kT} \tag{6.11}$$

and the heat of adsorption at low pressures can be given by (18)

$$Q = RT + \frac{\left\langle \exp(-\beta\psi_{fw}).\psi_{fw} \right\rangle}{\left\langle \exp(-\beta\psi_{fw}) \right\rangle} \qquad\qquad (6.12)$$

Activated carbons contain pores ranging from 8 to 20 Å. We simulated Henry's constant as well as the heat of adsorption in the zero pressure limit for 8 and 20 Å pore sizes and for different types of sites and corresponding distributions. In order to mimic the activated carbon pore with low sites concentration, up to 4 sites per pore (i.e., up to 0.22 sites/nm^2) are considered in the simulations.

Figures (6.18)-(6.20) show Henry's constant for carbonyls (with plain carbon), hydroxyls (including zeolite-NaX), and carboxyls, respectively. The loading for plain carbon was in the range of 0.25-1 µg/g. Loadings for carbonyls, hydroxyls and carboxyls were 1-12 µg/g, 1-80 µg/g and 110-9000 µg/g respectively. However, zeolite Na-X is able to adsorb around 24 µg/g at 400 K. Hsi et al (5) reported the details of mercury chloride sorption on activated carbon derived from bituminous and lignite in the range of 100-300 µg/g, suggesting the presence of more than four hydroxyls or carboxyls in the activated carbon sample. However, the loadings (400-2310 µg/g) cited by Lee et al.(2) at 120 °C suggest that the sample under consideration might have contained more than two carboxyls. In order to compare experimental values of the heat of adsorption with simulated heat of adsorption values, the heat of adsorption in the zero pressure limit was obtained using Equation (6.10). Figure 6.21 compares Henry's constant of activated carbon with Ca(OH)$_2$ impregnation. The figure suggests that the capacity of activated carbon with calcium hydroxide is approximately 30 times greater than carbons with H4 and around 1.5 times in the C33 case.

The heat of adsorption for carbonyls, hydroxyls, and carboxyls as shown in Figures 6.22, 6.23, and 6.24 is in the range of 18-45, 20-70, and 41-110 kJ/mol respectively, depending on their concentrations and distributions. The value for plain carbon was in the range of 19-25 kJ/mol, implying weak HgCl$_2$-carbon interactions. High values in the case of carbonyls, especially >80kJ/mol, suggest that high concentrations of carbonyls with small pore size (around 8 Å) can lead to the chemisorption of mercuric chloride. However, the values for hydroxyls and carboxyls are "far away" from the experimental value (30 kJ/mol) reported by Lancia et al (15) , suggesting that the activated carbon sample used by the authors may have had only carbonyls or a few hydroxyls located very far from each other. In order to test this hypothesis, we simulated the heat of adsorption for 8 and 20 Å for two sites in the pore separated by a distance ranging from 5 to 20 Å, as shown in Figures 6.25 and 6.26. The results imply that the interactions become less energetic if the distance between two sites increases from 5 to 20 Å. The figures indicate that if two hydroxyl sites are separated by 15 Å or more, this arrangement results in a heat of sorption within the range of 20-30 kJ/mol. However for all types of sites, the heat of adsorption reaches the value of a single site adsorption as the separation between the two sites increases. Figure 6.27 compares the isosteric heat of sorption in the zero pressure limit for carbons impregnated with Ca(OH)$_2$ with different concentrations with H4 and C33. The high values of Q (>100 kJ/mol) imply that there is a possibility of chemisorption of mercury chloride in activated carbons.

6.5. CONCLUDING REMARKS

The sorption of $HgCl_2$ on zeolite NaX and activated carbons with three different acid sites and calcium hydroxide was studied using GCMC simulations. The following conclusions could be drawn:

1. The presence of sodium cations in zeolite NaX increases the sorption of mercuric chloride molecules due to appreciable in magnitude Na-induced dipole and Na-quadrupole interactions.

2. The presence of carbonyl, hydroxyl, and carboxyl sites result in increased $HgCl_2$ sorption capacity, mainly due to charge-induced dipole interactions which are attributed to the high polarizability of the $HgCl_2$ molecule. However, the interactions among $HgCl_2$ molecules become also significant at higher pressures, especially in the case of H33 and C33.

3. The performance of activated carbon doped with calcium hydroxide was found to be superior to carbon with acid functional sites due to relatively large electrostatic interactions. Furthermore, the sorption capacity increases with an increase in the amount of calcium hydroxide present in the slit pores.

4. Carboxyls promote the highest $HgCl_2$ sorption followed by hydroxyls and carbonyls, respectively, which is due to the high charge densities and energetic charge-induced dipole interactions.

5. Comparison of experimental data for $HgCl_2$ sorption and the heat of adsorption in activated carbon (through the computation of Henry's constant and the zero pressure heat of adsorption) was performed by emulating experimental operating conditions at the infinite dilution limit of $HgCl_2$ for two extreme pore sizes in activated carbon with low acid site concentrations. The reported experimental values of $HgCl_2$ loading and heat of adsorption fell within the ranges of the simulated Henry's constant and heat of adsorption in the zero pressure limit, suggesting that the proposed computational modeling framework while structurally simple, is capable of capturing the main features and aspects of the underlying phenomenon. However, as computational capabilities advance over time, more precise, yet complex, pore size distributions and acid site concentrations for real carbons could be considered that would intuitively lead to a more favorable comparison between simulation and experimental results.

REFERENCES

1. S B Ghorishi, R M Keeney, D S Serre, B K Gullett and J S Wojciech, *Env. Sci & Tech.*, **36**, 4454 (2002)

2. S J Lee, Y C Seo, J Jurng and T G Lee, *Atm. Env.*, **38**, 4887(2004)

3. Y H Li, C W Lee, and B K Gullett, *Fuel*, **82**, 451(2003)

4. F E Huggins, G P Huffman, G E Dunham and C L Senior, *Energy & Fuels*, **13**, 114(1999)

5. H C Hsi, M J Rood, M Rostam-Abdai, S Chen and R Chang, *J. Env. Eng.*, **128**, 1080 (2002)

6. A Lancia, D Karatza, D Musmarra and F Pepe, *J. Chem. Eng. Japan*, **29**, 939(1996)

7. B Padak., M Brunetti , A Lewis and J. Wilcox , *Env. Prog.*,**25**, 319 (2006)

8. S Rio and A Delebarre , *Fuel*, **82**,153 (2003)

9. L L Zhao and G T Rochelle, *I&EC Res*, **37**,380(1998)

10. L L Zhao and G T Rochelle, *Chem. Eng. Sci.*, **54,** 655(1999)

11. S Roy and G T Rochelle, *Chem. Eng. Sci.*, **59**, 1309(2004)

12. C J Lin, and S O Pehkonen, *Chemosph.*, **38**, 1253(1999)

13. B Hall, O. Lindquvist, and E. Ljungstrom, *Env. Sci. Tech.*, **24**, 108(1990)

14. S V Krishnan, B K Gullett, and W Jozevicz, *Env. Sci. & Tech.*, **28**, 1506(1994)

15. A Lancia, D Musmarra, F Pepe and G Volpicelli, *Comb. Sci. & Tech.*, **93**, 277(1993)

16. D Karatza, A Lancia, D Musmarra, F Pepe, and GVolpicelli, *Comb. Sci. & Tech.*, **112**, 163 (1996)

17. B Wu, T W Peterson, F Shadman, C L Senio, J R Morency , F E Huggins, and G P Huffman, *Fuel Proc. Tech.*, **60**, 93(2000)

18. F. Karavias, *Ph.D Thesis*, 1992, Univ. of Pennsylvania

19. J.L. Soto and A L Myers, *Mol. Phys.*, **42**, 971(1981)

20. R T Yang , *Adsorbents: Fundamentals and Applications*, 2003**,** Wiley Interscience, New York.

21. T M Reed, and K E Gubbins, *Applied Statistical Mechanics*, 1973**,** McGraw-Hill, New York

22. J M Prausnitz, R N Lichtenthaler, and E Gomes de Azevedo, *Molecular Thermodynamics of Fluid-Phase Equilibria*, 3rd edn, 1999, Prentice-Hall, New Jersey

23. W A Steele, *The Interaction of Gases with Solid Surfaces*, 1974**,** Pergamon Press, Oxford

24. M Jorge, C Schumacher, and N A Seaton, *Langmuir*, **18**, 9296 (2002)

25. F J A L Cruz, J N C Lopes, J C G Calado, and M E M D Piedade, *J. Phys. Chem. B*, **109**, 24473(2005)

26. D. Frenkel and B. Smit, *Understanding Molecular Simulation*, 1996**,** Academic Press, London

27. M P Allen and D J Tildesley, *Computer Simulation of Liquids*, **1989**, Clarendon Press, Oxford

28. A N Pandey, A Bigotto, and .K Gulati, *Acta Phys. Polon. A*, **80**, 503(1991**)**

29. K Watanabe, *J. Chem. Phys.*, **26**, 542(1957)

30. Gaussian 03, Revision C.02, M. J. Frisch, G. W. Trucks, H. B. Schlegel, G. E. Scuseria, M. A. Robb, J. R. Cheeseman, J. A. Montgomery, Jr., T. Vreven, K. N. Kudin, J. C. Burant, J. M. Millam, S. S. Iyengar, J. Tomasi, V. Barone, B. Mennucci, M. Cossi, G. Scalmani, N. Rega, G. A. Petersson, H. Nakatsuji, M. Hada, M. Ehara, K. Toyota, R. Fukuda, J. Hasegawa, M. Ishida, T. Nakajima, Y. Honda, O. Kitao, H. Nakai, M. Klene,

X. Li, J. E. Knox, H. P. Hratchian, J. B. Cross, V. Bakken, C. Adamo, J. Jaramillo, R. Gomperts, R. E. Stratmann, O. Yazyev, A. J. Austin, R. Cammi, C. Pomelli, J. W. Ochterski, P. Y. Ayala, K. Morokuma, G. A. Voth, P. Salvador, J. J. Dannenberg, V. G. Zakrzewski, S. Dapprich, A. D. Daniels, M. C. Strain, O. Farkas, D. K. Malick, A. D. Rabuck, K. Raghavachari, J. B. Foresman, J. V. Ortiz, Q. Cui, A. G. Baboul, S. Clifford, J. Cioslowski, B. B. Stefanov, G. Liu, A. Liashenko, P. Piskorz, I. Komaromi, R. L. Martin, D. J. Fox, T. Keith, M. A. Al-Laham, C. Y. Peng, A. Nanayakkara, M. Challacombe, P. M. W. Gill, B. Johnson, W. Chen, M. W. Wong, C. Gonzalez, and J. A. Pople, Gaussian, Inc., Wallingford CT, 2004.

30. I. N. Levine, Quantam Chemistry, 5th Ed. Prentice hall, New Jersey (2000)
31. F. Jensen, Introduction to computational chemistry, Wiley Interscience, England(2003)

APPENDIX

In order to discuss the sorption results for the different types of sites located at different points in the carbon pore, we assign symbols to each type of configuration of sites in the pore.

The Notation of acidic sites is realized as follows: "Ca" refers to a carbonyl site, "H" refers to a hydroxyl site and "C" refers to a carboxyl site. The number in the symbols indicates the total number of sites in the pore. Two digits of the same number indicate that all the sites are on a single plate. A single digit implies that half of the sites are on the opposite plate.

Ca4   4 carbonyl sites, two on each plate
H1   1 hydroxyl on a single plate
H2   1 hydroxyl on each plate
H22   2 hydroxyl on a single plate
H33   3 hydroxyl, 2 on opposite plate, one on the other
H4   4 hydroxyl, two on each plate
C1   1 carboxyl
C2   1 carboxyl on each plate
C22   2 carboxyl on single plate
C33   3 carboxyl on single plate
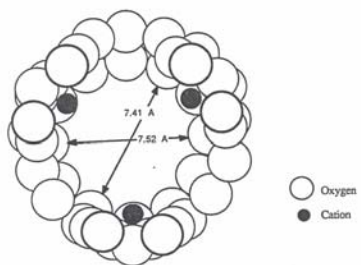
Fig. 6.1 Cross-section of a zeolite NaX adsorption cavity (18)
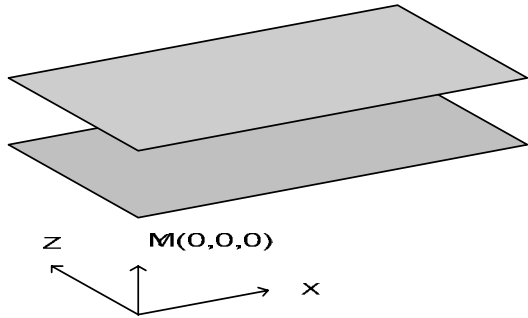
Fig. 6.2 A schematic diagram of a slit pore with origin at M(0,0,0)
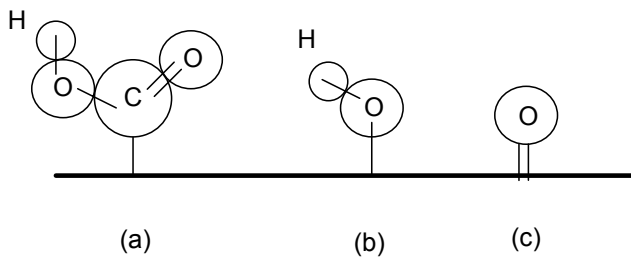
Fig. 6.3 Schematic representation of the surface sites on carbon: (a) a carboxyl group, (b) a hydroxyl group, and (c) a carbonyl group

Site distribution for H4, C2,Ca4 and H22

Site distribution for C3, H33 and Ca33

Site distribution for H2, C2 and Ca2 (on each plate)
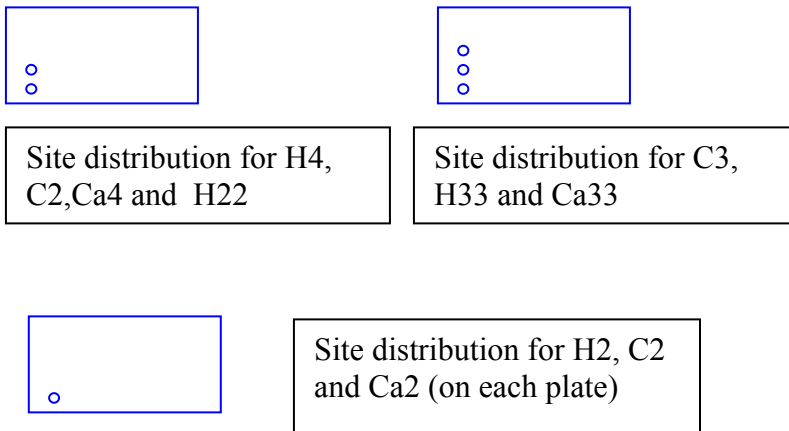
Fig. 6.4 Schematic diagram of different site distributions in activated carbon
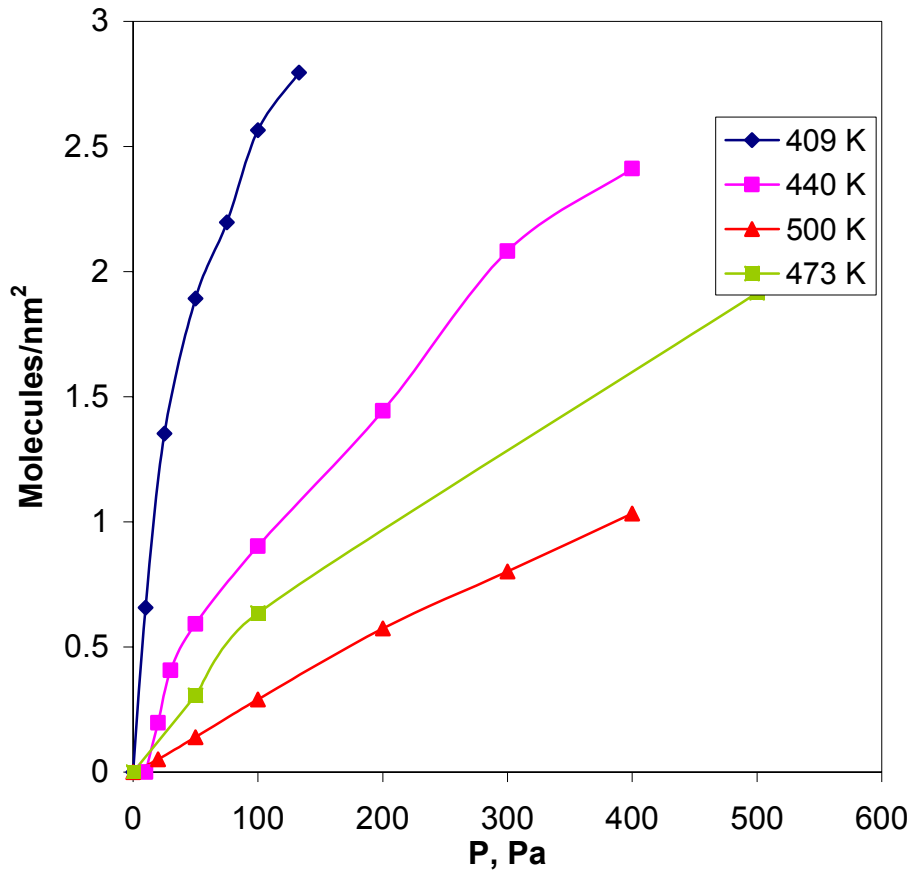
Fig. 6.5 Adsorption isotherm from GCMC simulation for $HgCl_2$ in zeolite NaX
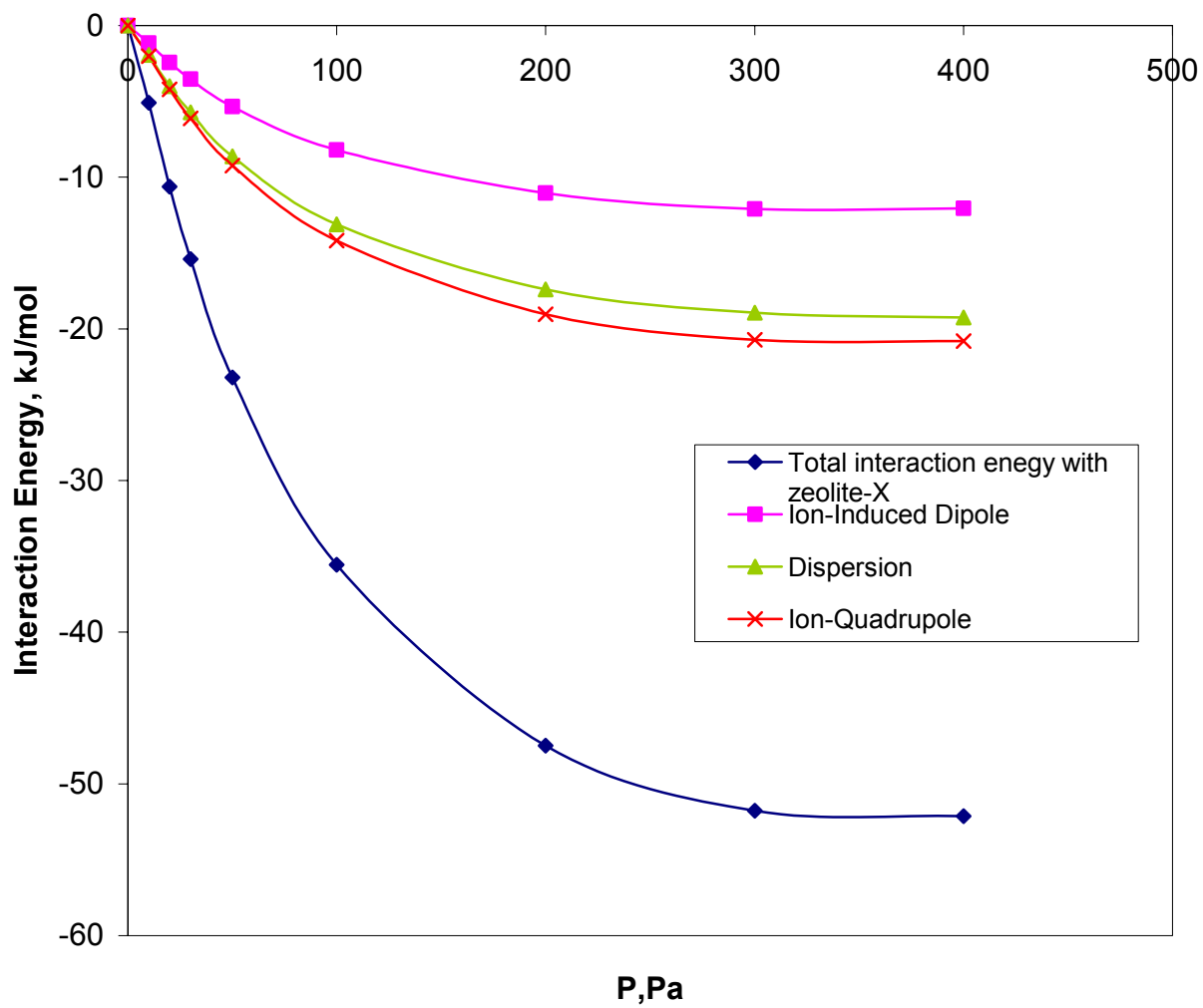
Fig. 6.6 Relative energy contributions to adsorption for zeolite NaX at 500 K
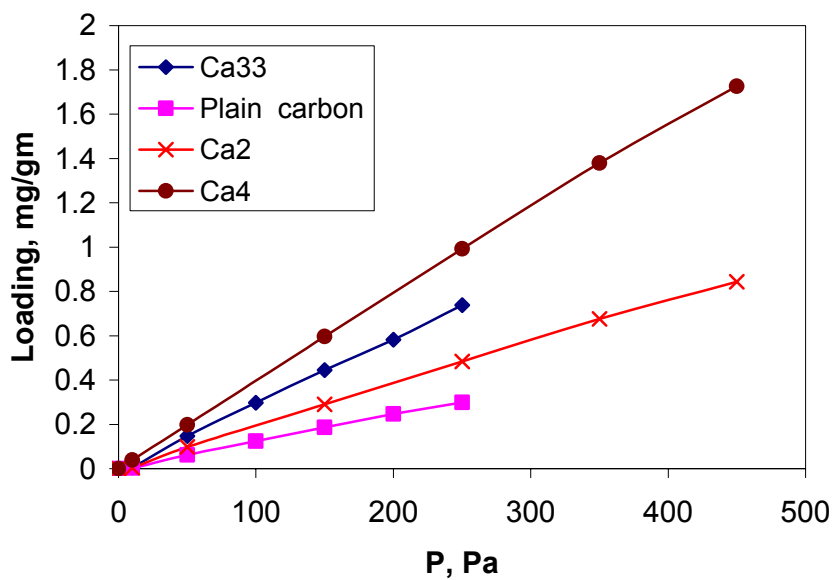
Fig. 6.7 Isotherms for HgCl$_2$ in activated carbon (15 Å pore) with and without carbonyl sites at 450 K
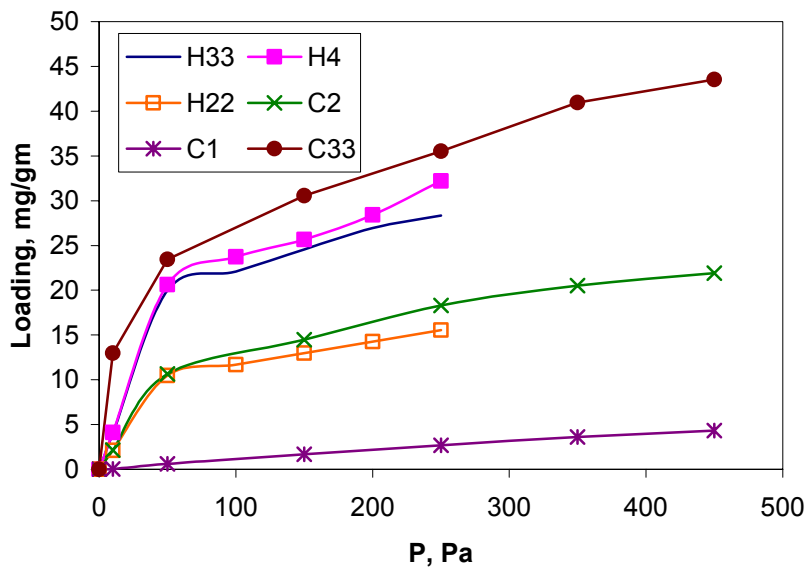
Fig. 6.8 Isotherms for HgCl$_2$ in activated carbon (15 Å pore) with carboxyl and hydroxyl sites at 450 K
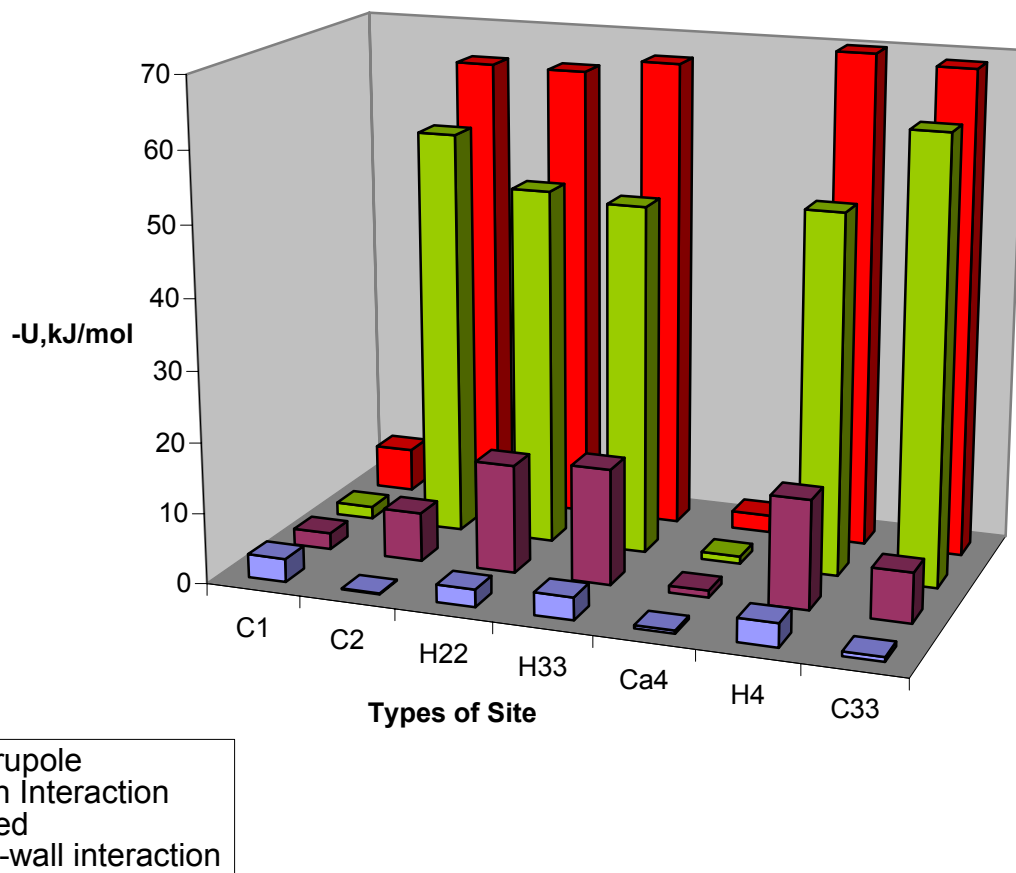
Fig. 6.9 Contribution of different energies in HgCl$_2$ adsorption in activated carbon (15 Å pore) with different sites at 150 Pa and 450 K
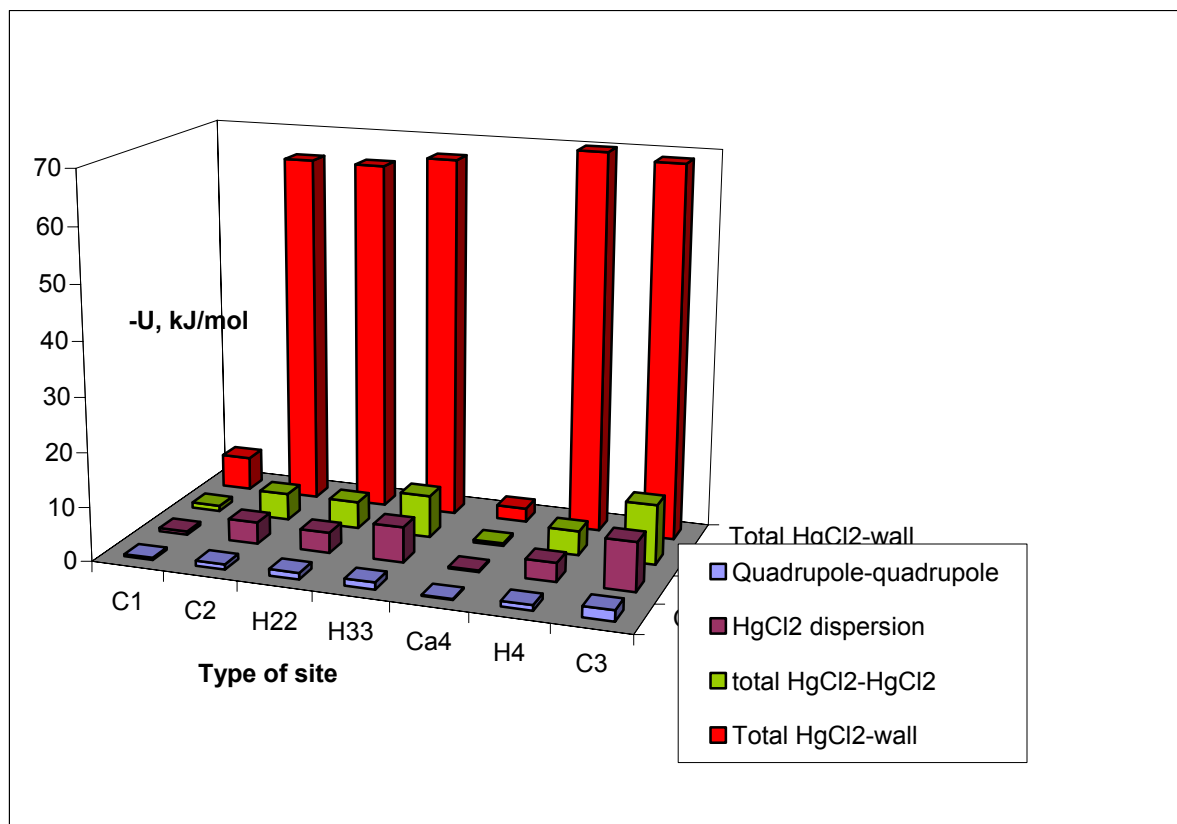
Fig.6.10 Comparison of HgCl$_2$–HgCl$_2$ interactions with HgCl$_2$–'activated carbon' interactions at 250 Pa at 450 K.
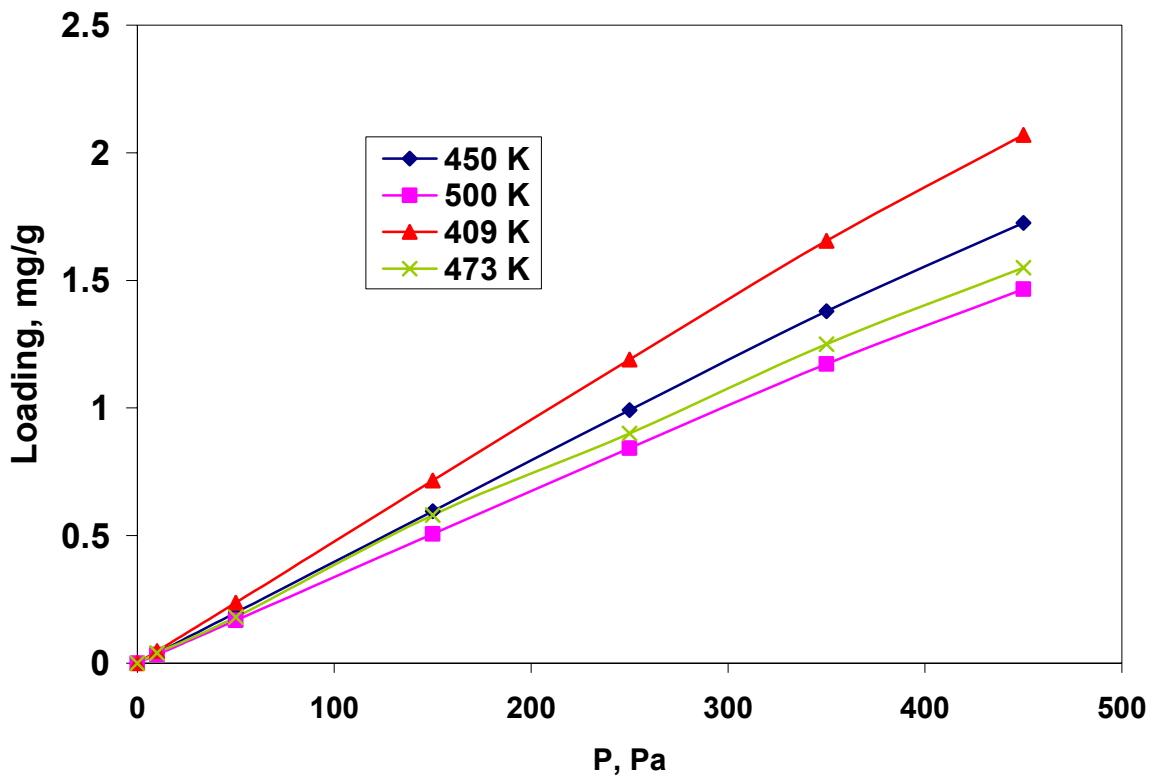
Fig. 6.11 Sorption in Ca4 at four different temperatures in 15 Å pore
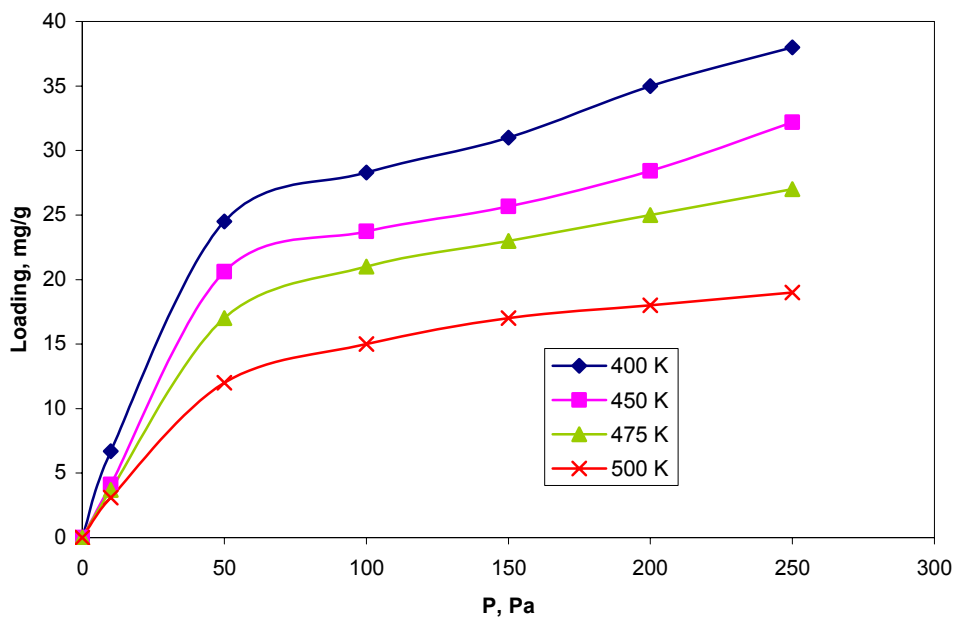
Fig. 6.12 Sorption in H4 at four different temperatures in 15 Å pore
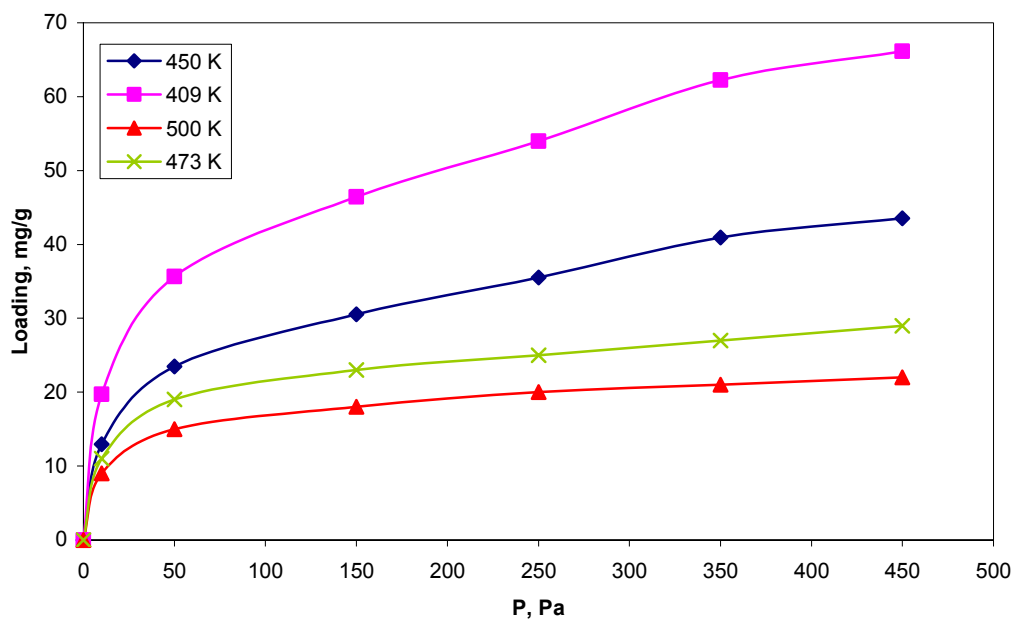
Fig. 6.13 Sorption in C33 at four different temperatures in 15 Å pore
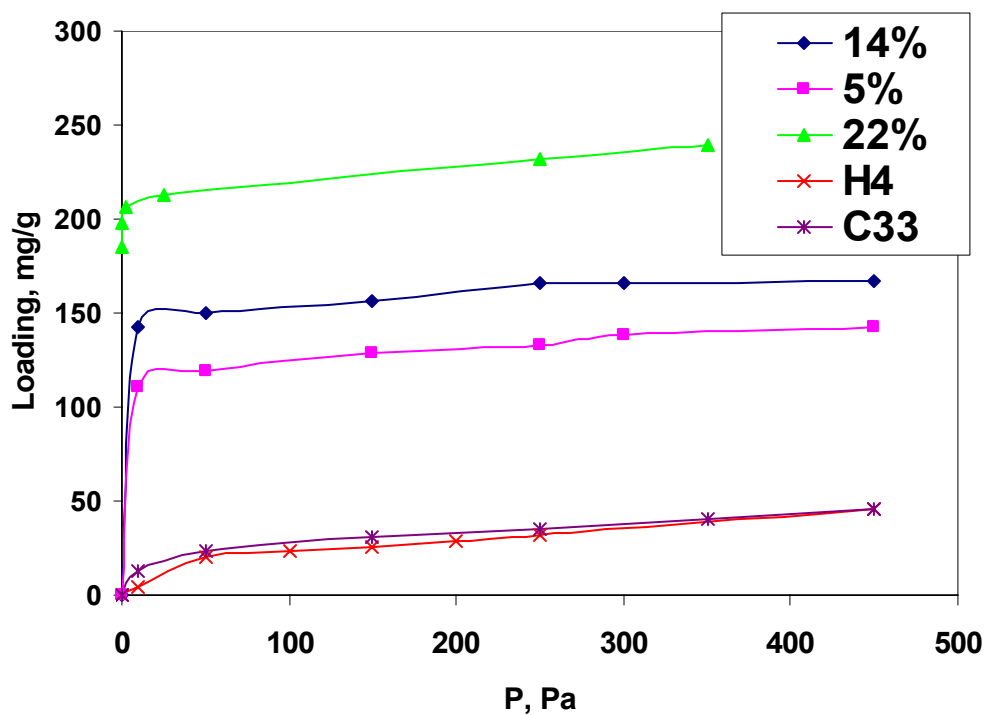
Fig.6.14 Comparison of sorption capacity of carbon coated with calcium hydroxide with different weight % and with H4 and C33
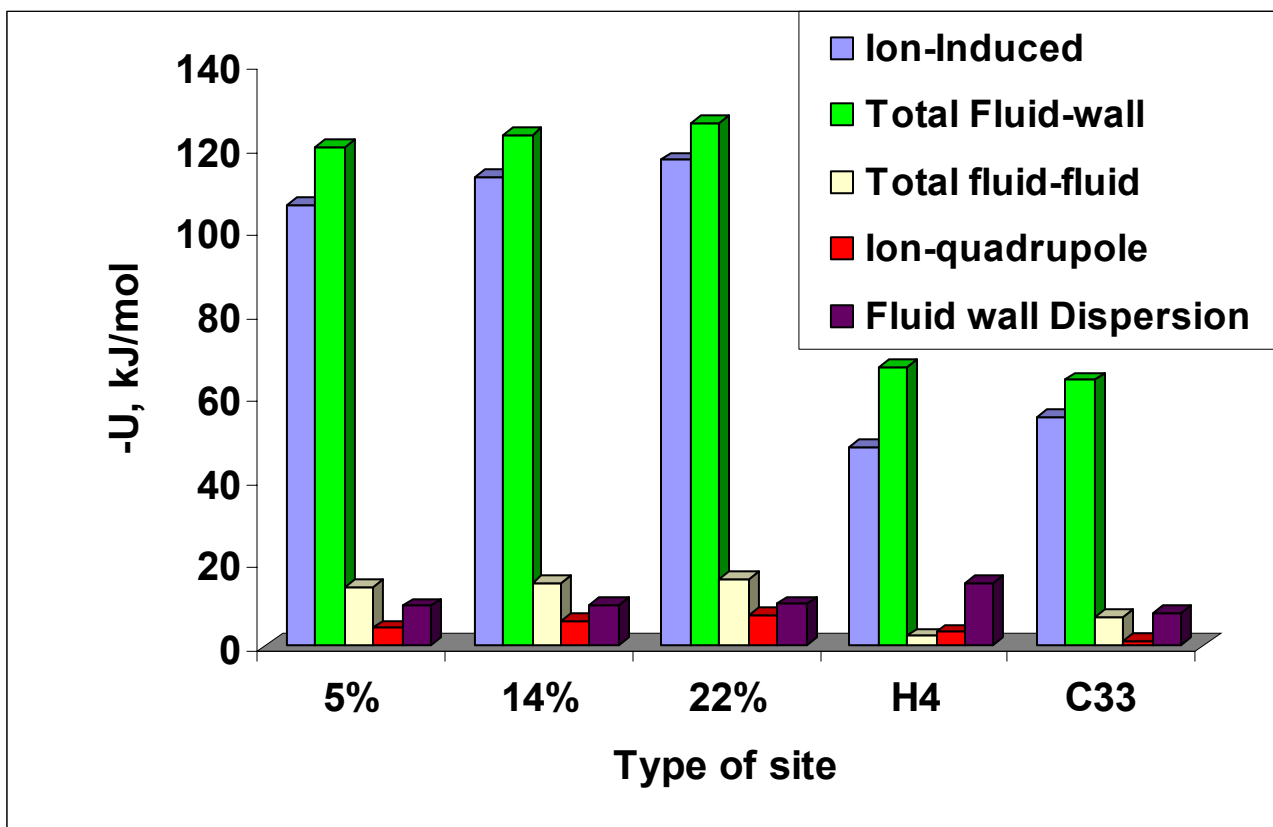
Fig. 6.15 Contribution of different energies in $HgCl_2$ adsorption in activated carbon (15 Å pore) with different sites at 150 Pa and 450 K
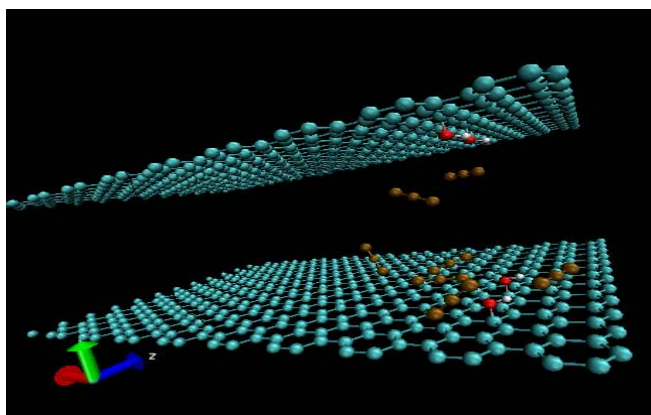
Fig. 6.16 Snapshots of the sorption of $HgCl_2$ in H4 at 50 Pa and 450K
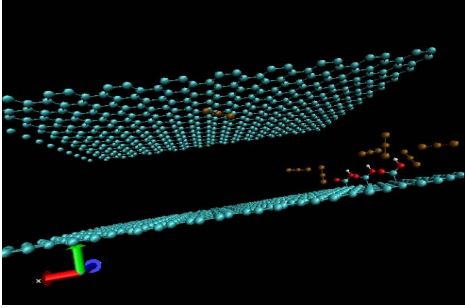
Fig. 6.17 Snapshots of sorption of $HgCl_2$ in C33 at 20 Pa and 450K
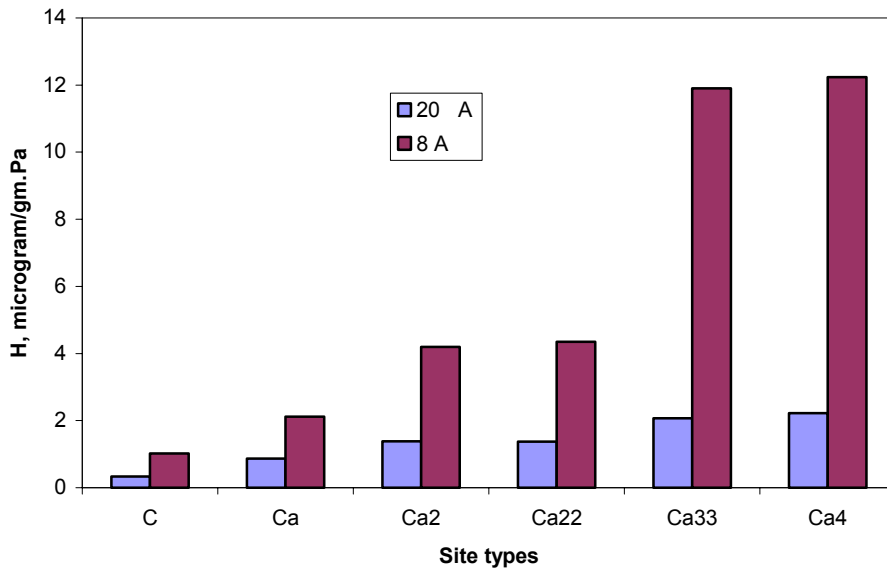
Fig. 6.18 Henry's Constant for different carbonyl sites at 400 K and different pore sizes
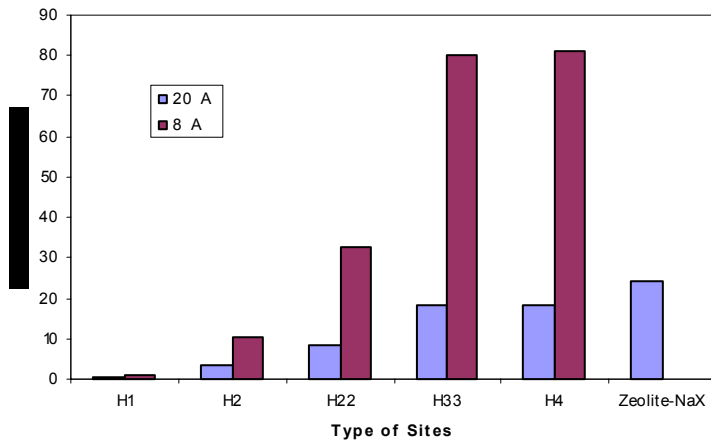
Fig. 6.19   Henry's Constant for different hydroxyl sites and zeolite NaX at 400 K and different pore sizes

113
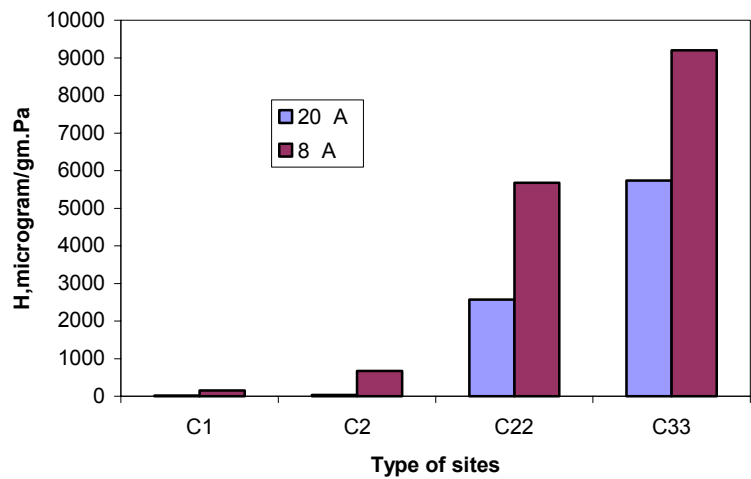
Fig. 6.20   Henry's Constant for different carboxyl sites at 400 K and different pore sizes
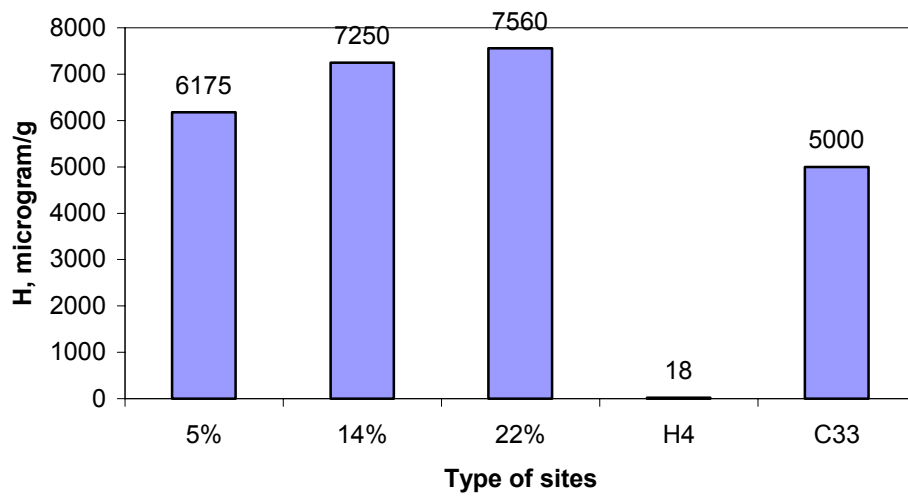
Fig. 6.21 Comparison of Henry's Constant for carbon impregnated with 5% , 14% and 22% (by wt) Ca(OH)$_2$ with H4 and C33 at 400 for K 20 Å pore size
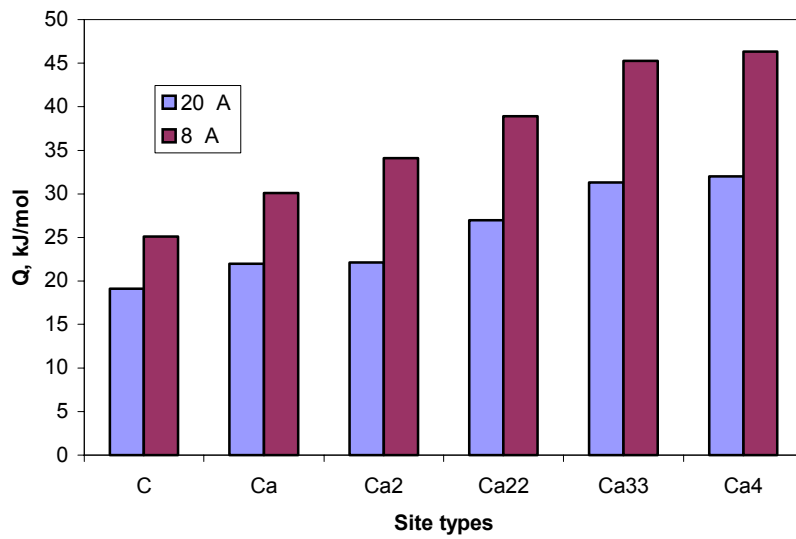
Fig. 6.22 Zero pressure heat of adsorption at 400 K for carbonyl sites and different pore sizes
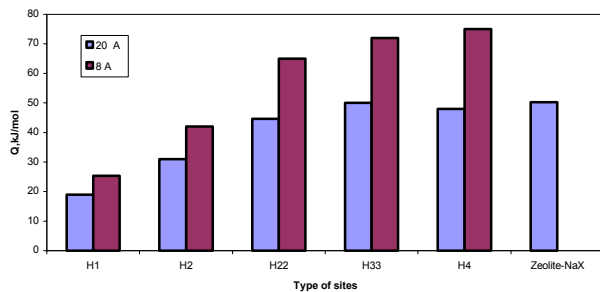
 Fig. 6.23 Zero pressure heat of adsorption at 400 K for hydroxyl sites and zeolite NaX for different pore sizes
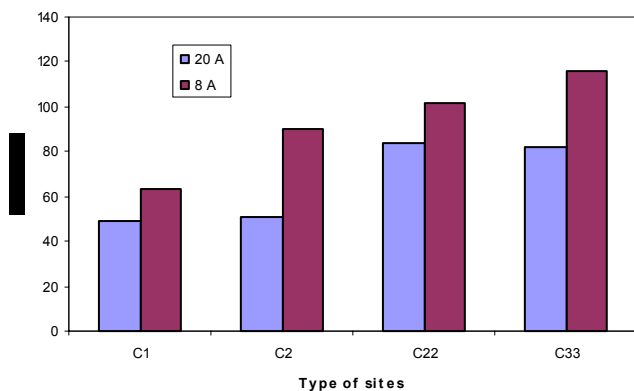
Fig. 6.24 Zero pressure heat of adsorption at 400 K for carboxyl site and different pore sizes
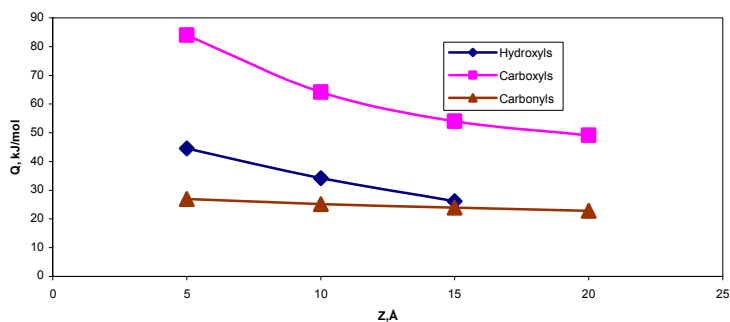
Fig. 6.25 Heat of adsorption for 20 Å pore size as a function of distance between two sites
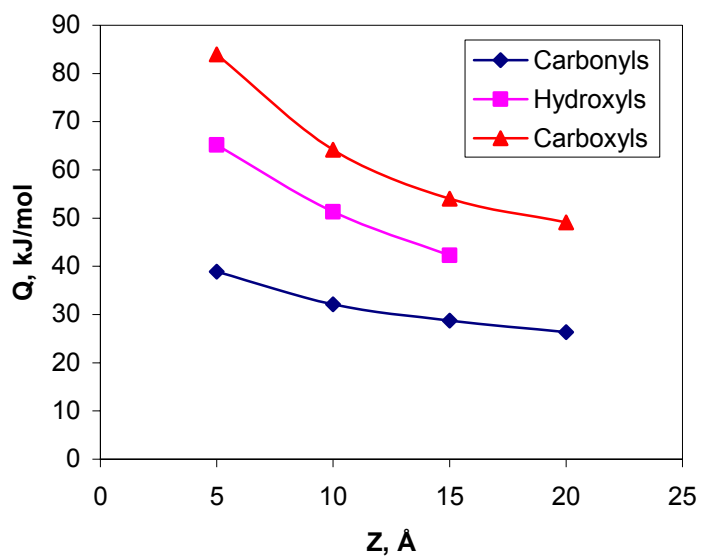
Fig. 6.26 Heat of adsorption for 8 Å pore size as a function of distance between two sites
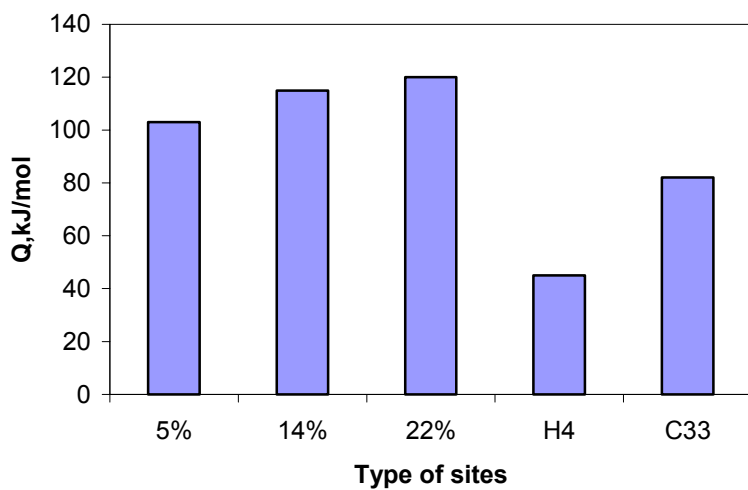
Fig. 6.27 Comparison of isosteric heat of adsorption for carbon impregnated with 5%, 14% and 22% (by wt) Ca(OH)$_2$ with H4 and C33 at 400 K and 20 Å pore size

Chapter 7

Adsorption of hazardous Air Pollutants-Hydrogen Cyanide and Methyl Ethyl Ketone

7.1. INTRODUCTION

Methyl ethyl ketone (MEK) is used as a solvent for gums, resins, and cellulose nitrate, as well as in consumer products such as lacquers, varnishes, paint remover, and glues (1-2). Typically, it is exposed to air by gases emitted from the pertinent manufacturing industries producing the abovementioned products, or it is directly discharged in wastewater. It should be pointed out, that an exposure of 200 ppm of MEK causes irritation to the eyes, nose (mucous membranes) and throat. In addition to this, high MEK levels are associated with smog formation due to photochemical reactions with olefinic hydrocarbons (2-3). In light of the above considerations and the hazardous nature of MEK under certain conditions, adsorption is considered to be one of the most preferable and operationally advantageous methods to effectively remove MEK from industrial gases especially using activated carbon and zeolites as adsorbents (2).

Following the above line of research, Yen et al. (2) carried out vapor phase adsorption experiments on zeolite Y and ZSM-5 of different Si/Al ratios varying from 5 to 31, where the concentration of MEK in the vapor phase was in the range of 100-1500 ppm. In this particular study, Zeolite Y was found to be more effective than ZSM-5 in removing MEK from air stream. Monneyron et al. (4) conducted vapor phase single component and binary component (with toluene and 1,4-dioxane) adsorption experiments on zeolite Y and ZSM-5. It was found that the component having the higher molecular weight adsorbed preferentially over the other, except in the case of MEK-toluene mixture adsorption on ZSM-5, where toluene was believed to be excluded due to steric effects. Pires et al (5) studied the effect of dealumination of zeolite Na-Y on the sorption of MEK at 298 K, and showed that an increase in the percentage of de-alumination reduced MEK adsorption, suggesting that sodium cations favor MEK. Uguina et al. (6) studied MEK desorption from silicalite and activated carbon beds, and suggested that the regeneration temperature for silicalite was in the range of 90-170 °C, whereas in the case of activated carbon it was found to be within the range of 150-240 °C. These findings suggest that dispersion interactions might be dominant in the case of silicalite, and electrostatic interactions might be the dominant ones in the case of activated carbon due to the presence of acid sites. Despite the aforementioned research efforts, the experimental data available in the pertinent body of literature are not currently adequate to understand the mechanism of MEK adsorption in activated carbons and zeolites, especially at the molecular level. Motivated by the above realization, one of the objectives of the present research study is to enhance our understanding and characterize the adsorption properties of MEK by focusing specifically on the effect of sodium cations in zeolite Y, as well as hydroxyl, carbonyl and carboxylic sites in activated carbon on the adsorption capacity of MEK using molecular simulation methods.

Furthermore, and in a conceptually similar methodological framework, the adsorption of hydrogen cyanide (HCN) will be studied as well, recognizing the fact that it represents an acutely poisonous compound, which might enter the human body by breathing contaminated air. The HCN vapors are commonly released to the air from various sources, including vehicle exhaust emissions, chemical processing, extraction of gold and silver from low grade ores, metal plating, steel, iron, and finishing industries, petroleum refineries, and waste disposed of in landfills. Currently, the best-known adsorbents for the removal of HCN from air are metal salt-impregnated activated carbons (7). Freeman (7) and Reucroft (8) studied the adsorption of HCN and the mixture of HCN-water on BPL activated carbon, a granular activated carbon supplied by Calgon Carbon Inc. The experimental results suggested that, adsorption of HCN strongly dominates over water, and HCN discourages additional adsorption of water vapor, which might be attributed to the greater polarizability and dipole moment of HCN.

In another study of the removal of HCN from air by Oliver et al. (9), copper containing and copper free synthetic activated carbons produced from porous sulfonated styrene/divinylbenzene resin were studied for assessing the removal efficiency of HCN. The prepared adsorbent performance was comparable to ASC Whetlerite carbons that contain salts of chromium, copper, and silver. Incorporation of copper into the starting material significantly increased HCN breakthrough times, but decreased the surface area and pore volume of the adsorbent. The results of X-ray photoelectron spectroscopy (XPS) analysis revealed partial or complete reduction of the starting divalent copper on the surface of the adsorbents, amply confirmed by the lack of formation of $(CN)_2$ during the adsorption of HCN, while the use of conventional Whetlerite carbon produced poisonous $(CN)_2$ gas. However, detailed and good-quality experimental data on the sorption of HCN from flue gases are limited, and do not suggest any suitable adsorbents to remove HCN. To elucidate the above phenomenon and identify proper adsorbents, in the present research study we also examine the sorption characteristics of zeolite NaX and activated carbon for HCN using molecular simulation methods.

The present paper is organized as follows: Section 2 provides a brief description of the particular molecular modeling approaches used, followed by a succinct description of the molecular simulation methods employed in the present study. Section 4 encompasses the study's main results along with a detailed discussion on the primary research findings. Finally, a few concluding remarks are provided in Section 5.

7.2. MOLECULAR MODEL DESCRIPTION

7.2.1 Zeolite NaX Model
Zeolite NaX was modeled by considering the zeolite cavity as spherically shaped with sodium cations located uniformly in the cavity (10-11) as shown in fig. 7.1. The specific locations of the sodium cations were taken from Karavias et al. (11). Moreover, the interactions with the spherical cavity were calculated using a spherically–averaged potential for the dispersion and repulsion given by (11):

$$\psi^{disp} = 4C\varepsilon_{1s}\left[\left(\frac{\sigma_{1s}}{R}\right)^{12}L\left\{\frac{r^2}{R^2}\right\} - \left(\frac{\sigma_{1s}}{R}\right)^{6}M\left\{\frac{r^2}{R^2}\right\}\right] \tag{7.1}$$

where,

$$L\{x\} = (1 + 12x + 25.2x^2 + 12x^3 + x^4)/(1-x)^{10} \tag{7.2}$$

$$M\{x\} = (1+x)/(1-x)^4 \tag{7.3}$$

with, $x = \dfrac{r}{R}$ and ψ^{disp} being a function of r, the radial distance of the adsorbed molecule from the center of the cavity. The cavity radius, R, was chosen as the distance from the center to the nearest oxygen atom. For zeolite NaX, R is 7.057 Å (11). In the above expression, $C\varepsilon_{1s}$ and σ_{1s} are the Lennard-Jones energy and collision diameter of molecule i with the solid wall, respectively. The interactions of the hazardous molecules of interest with sodium cations are mainly cation-induced dipole and cation-quadrupole moment interactions which can be calculated using equations (7.4) and (7.5), respectively, as shown below (12):
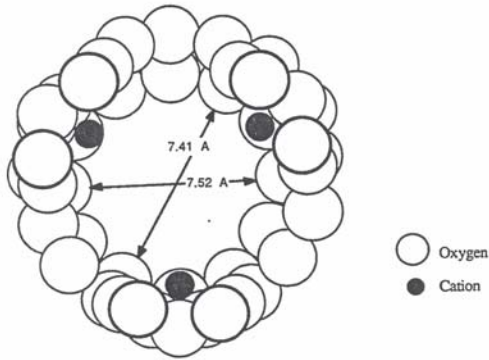
Figure 7.1: Cross-section of a zeolite NaX adsorption cavity (11).

$$\psi^{ind} = -\frac{\alpha q^2}{2r^4(4\pi\varepsilon_o)^2} \tag{7.4}$$

where α is the polarizability of the molecule, q is the electronic charge of the ion on the surface, ε_o is the permittivity of vacuum, and r is the distance between the centers of the interacting pair (12). Notice, that interactions between the ion field and the point dipole are given by (12):

$$\psi^{dipole} = -\frac{q\mu\cos\theta}{r^2(4\pi\varepsilon_o)} \tag{7.5}$$

where μ is the dipole moment of the molecule, and θ is the angle between the direction of the field and the axis of the dipole.

The total interactions between HCN/MEK molecules and the zeolite cavity can be calculated as follows:

$$\psi_{fw} = \psi^{disp} + \psi^{ind} + \psi^{dipole} \tag{7.6}$$

It should be pointed out, that two types of interactions are considered in the present study, namely dispersion interactions and dipole-dipole interactions given by Eqns. (7.4) and (7.5). The following adsorbate (i)-adsorbate (j) interactions also were considered (13-14):

$$U_{ij}^{\mu\mu} = \frac{\mu_i\mu_j}{r^3}\left(\sin\theta_i\sin\theta_j\cos\phi_{ij} - 2\cos\theta_i\cos\theta_j\right) \tag{7.7}$$

$$U_{ij}^{disp}(r) = \left[-\frac{1}{(4\pi\varepsilon_0)^2 r_{ij}^6}\left(\frac{3\alpha_i\alpha_j\ (I_i + I_j)}{I_iI_j\,4}\right)\right] \tag{7.8}$$

where I_i and I_j are the first ionization potentials for molecules i and j, respectively.

7.2.2   Activated Carbon Model

The pores of activated carbon were modeled by considering two parallel walls, each of which comprises an infinite number of layers of graphite (Fig.7.3). The graphite layers are composed of Lennard-Jones sites, but these are smeared out uniformly over each layer. The interaction between an adsorbate molecule and this smooth carbon surface is represented by the 10-4-3 potential of Steele (14). Three types of polar surface sites: hydroxyl (H), carboxyl (C), and carbonyl (Ca) groups, were considered in the simulations, and are represented schematically in Fig. 7.2. The carboxyl, hydroxyl, and carbonyl sites can be considered as a collection of five, two and three point charges. The parameters (size of charge atom and partial charge) of point charges and their positions were taken from Jorge et al. (15-16). Figure 4 describes the type of site, number of sites, and their distributions. Each site was placed at 5 Å apart from its neighbour site (Fig. 7.4), and a symbol is assigned to each type of configuration. Moreover, Ca, H, and C refer to carbonyl, hydroxyl, and carboxyl sites, respectively. The number in the symbol represents the total number of sites in the pore. The single digit indicates that half of the sites are on each plate, while the double digit indicates that sites are located on a single plate. The cross–species parameters were calculated using the Lorentz-Berthelot combining rule (14-17). As mentioned earlier, the electrostatic interactions namely charge-induced dipole moment and charge-quadrupole moment were calculated using equations (7.4) and (7.5), respectively.
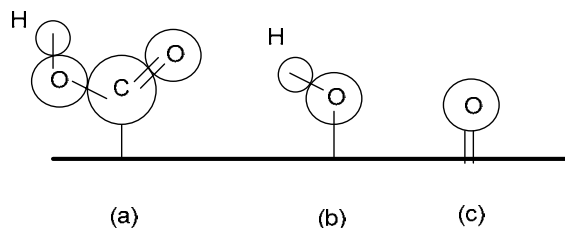
Figure 7.2: Schematic representation of the surface sites on carbon: (a) a carboxyl group, (b) a hydroxyl group, and (c) a carbonyl group (15-16).
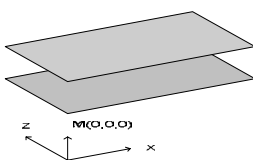
Figure 7.3: Schematic diagram of a slit pore with origin at M(0,0,0) (14).

Site distribution for H4, C2, Ca4, and H22

Site distribution for C3, H33, and Ca33

Site distribution for H88

Site distribution for Ca88

Site distribution for H8 and Ca8
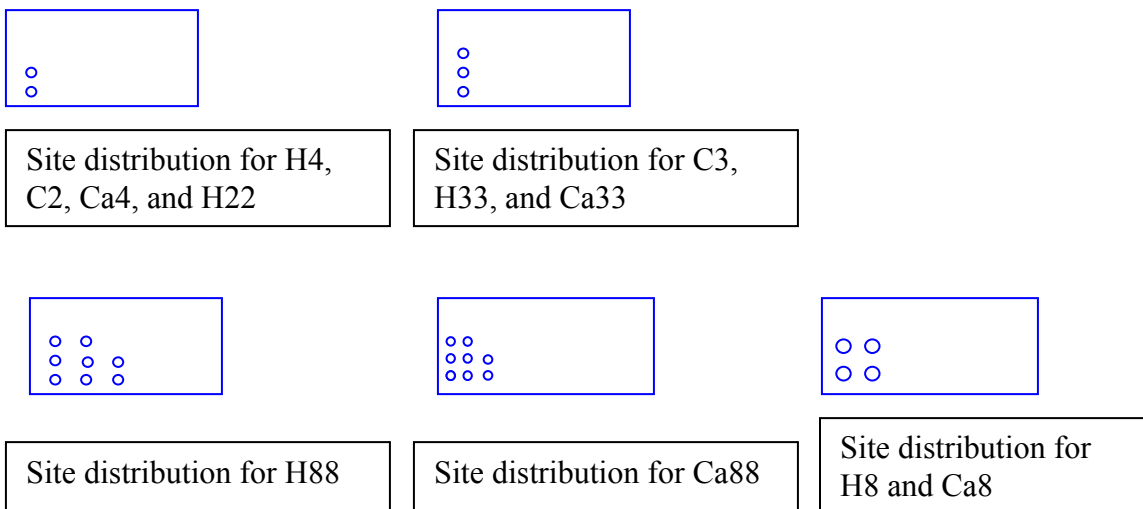
Figure 7.4: Schematic diagram of different site distributions in activated carbon.

7.3. SIMULATION METHODS

We calculated adsorption isotherms using grand canonical Monte Carlo (GCMC) simulations, in which the temperature (T), volume (V), and chemical potentials (μ) were kept constant. The algorithm for GCMC simulations is well documented (11), and we used the general methodology. The pressure (P) was calculated from the chemical potential and the equation of state for an ideal gas, and all simulations were performed in equilibrium bulk gas temperature of 298 K. Each type of Monte Carlo trial (creation, destruction, and displacement/rotation) was chosen randomly with the same probability. The number of equilibrium steps in the simulations varied according to the operating conditions, in the range of 30 to 70 million. To calculate statistical uncertainties, simulations were divided into five blocks of trials (each varied from 5 to 12 million) and

the observed standard deviation of block average was within 5%. During the sampling period, typical configurations for each run were stored in files and then converted into images. In the case of zeolite NaX, the interactions with molecules in four neighboring cavities also were considered. The molecules in the neighboring cavities were the images of molecules in the central cavity. In the case of activated carbon slit pores, the size of the simulation box was 3x1.5x3 nm.

We used rectangular simulation cells, bound in the y-direction by pore walls and replicated in x- and z-directions using periodic boundary conditions. In order to account for the long-range interactions, especially charge–dipole, charge-induced dipole, and dipole–dipole interactions, the interactions of molecules in the central cavity with neighboring cavities were considered.

7.4. RESULTS AND DISCUSSION

7.4.1 Sorption of hydrogen cyanide

Fig.5 shows Henry's constant (H) for different carbonyl sites at 298 K. The Henry's Law constant (H) values were in the range of 3-40 µg/g Pa. The heat of adsorption (Q) in the zero pressure limit for carbonyls sites were in the range of 10-35 kJ/mol (Fig.6). Values of H and Q were greater in the case of Ca22 than that of Ca2. This difference is attributed to the relative distance between two sites of 5 Å in case of Ca22 as compared to 15 Å in Ca2. Fig.7 shows the H values for different hydroxyl sites and zeolite NaX. H values for hydroxyls were in the range of 2-100 µg/g Pa and for zeolite NaX was 600 µg/g Pa, implying that zeolite NaX has a very high affinity for the HCN molecule. However, Q values were in the range of 15-40 kJ/mol (Fig.8). Figs. 7.9 and 7.
10 represent the H and Q values for activated carbon with different carboxyl sites. H values for carboxyls were in the range of 5-180 µg/g Pa, which is greater than that of hydroxyls and carbonyls. Q values were in the range of 15-45 kJ/mol for carboxyls.

Fig. 7.11 indicates that the sorption capacity of the carbons with H4 and H33 were greater than with Ca33 and Ca4. Performance of H2 and H22 were found to be almost same. The higher sorption capacity of H4 and H3 can be explained from Fig.7.12. The sorption in carbons with carbonyls and hydroxyls are attributed to charge-dipole and charge-induced dipole interactions. The magnitude of fluid-wall dispersion and charge-induced dipole were comparable in magnitudes. The performance of H4 and H33 was attributed to higher charge-dipole interactions.

The sorption isotherms for carboxyls and zeolite NaX indicate that zeolite NaX has the highest sorption capacity followed by C33 and C22 of activated carbons with carboxyls (Fig.7.13). Fig. 7.14 explains that the higher sorption with pore filling in NaX is due to greater charge-dipole interactions, which is attributed to the presence of cations and the

higher dipole moment of the HCN molecule (2.98 Debye). The performance of C33 and C22 was attributed to charge-dipole and charge-induced dipole interactions that were comparable in magnitudes (in the range of 15-30 kJ/mol). However, the interactions among HCN molecules were not found to be significant in carboxyls and the NaX.
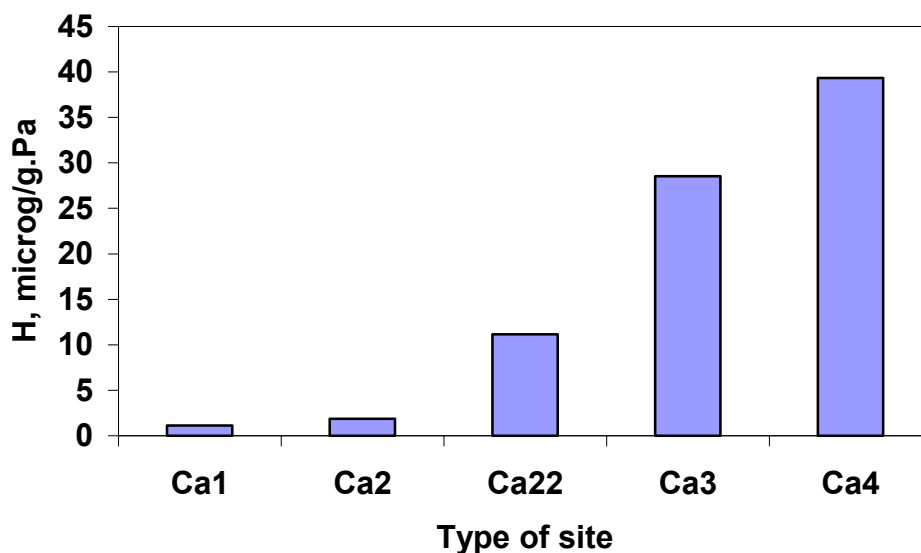
Figure 7.5: Henry's Law constant, H, for different carbonyl sites at 298 K.
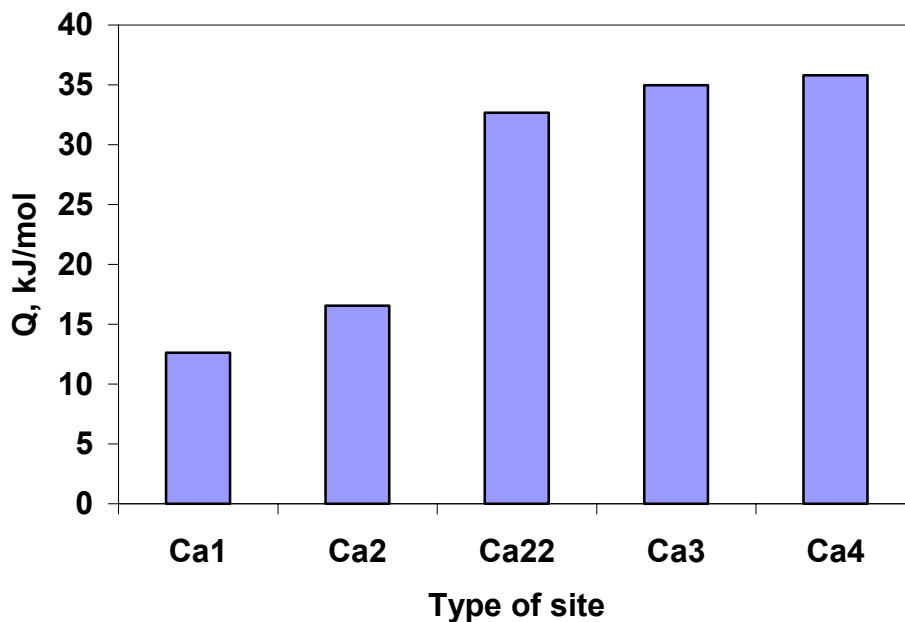
Figure 7.6: Heat of adsorption, Q, for different carbonyl sites at 298 K.
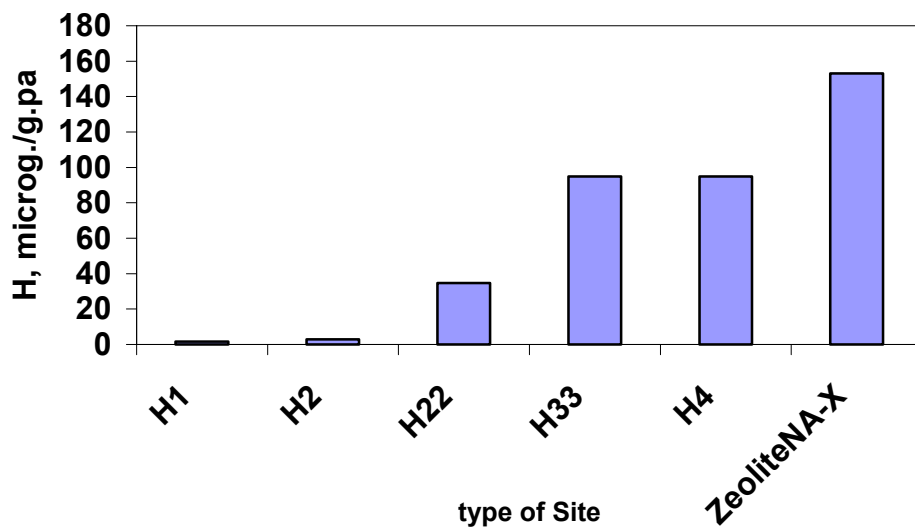
Figure 7.7: Henry's Law constant, H, for different hydroxyl sites at 298 K.
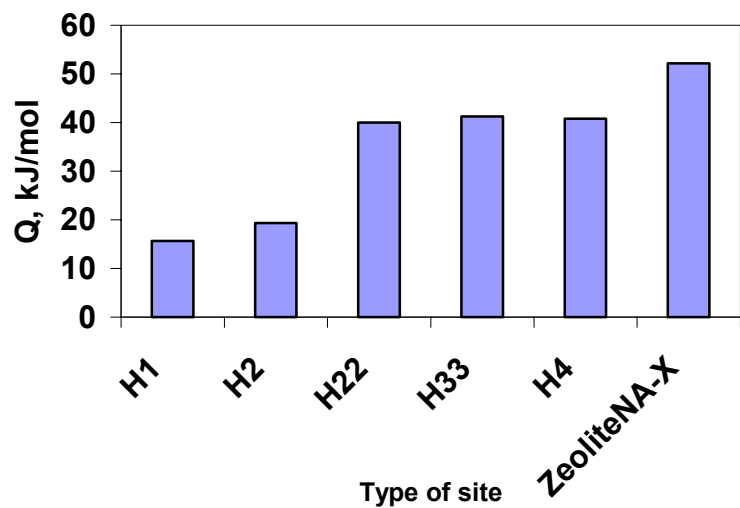
Figure 7.8: Heat of adsorption, Q, for different hydroxyl sites at 298 K.
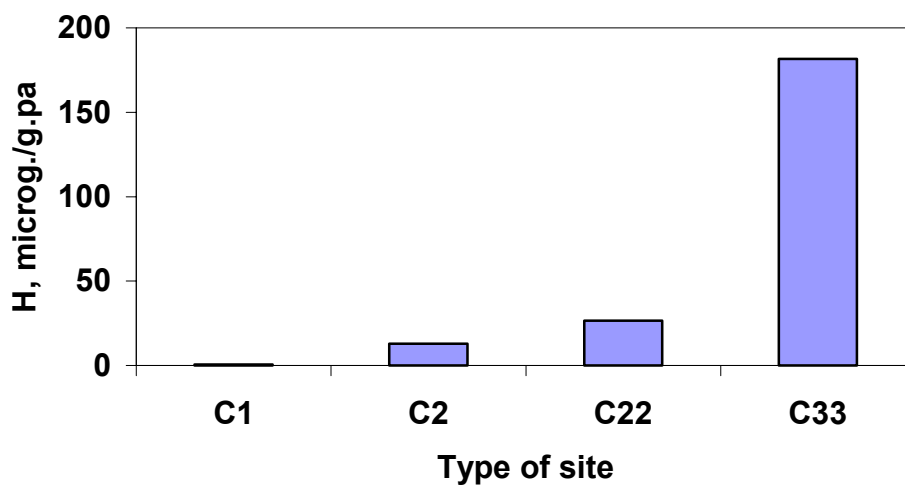
Figure 7.9: Henry's Law constant, H, for different carboxyl sites at 298 K.
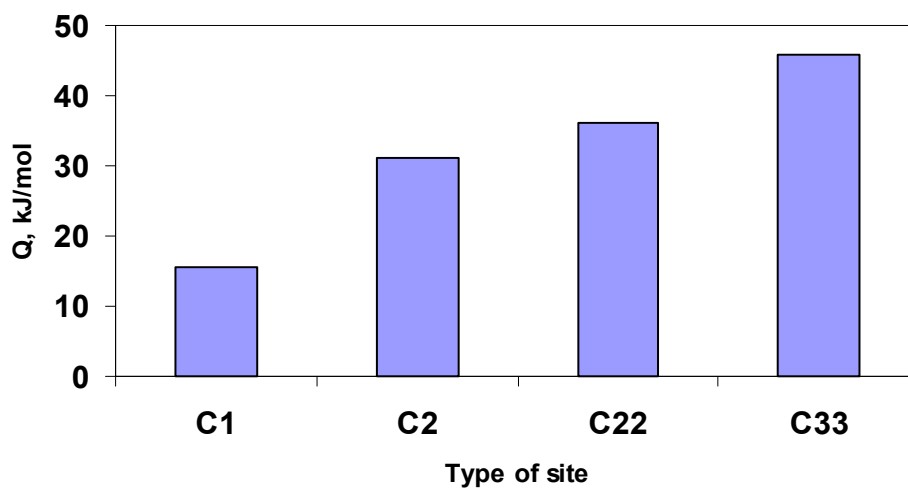
Figure 7.10: Heat of adsorption, Q, for different carboxyl sites at 298 K.
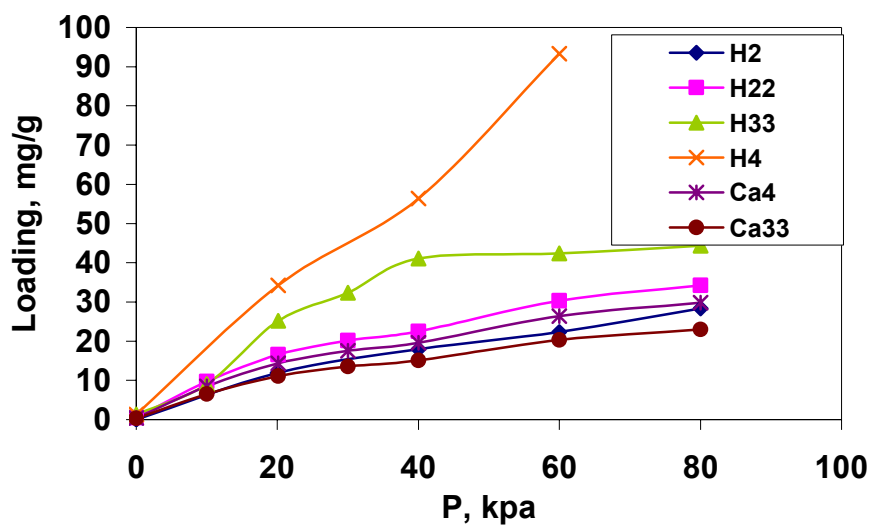
Figure 7.11: Adsorption isotherms for HCN in activated carbon with hydroxyl and carbonyl sites at 298 K.
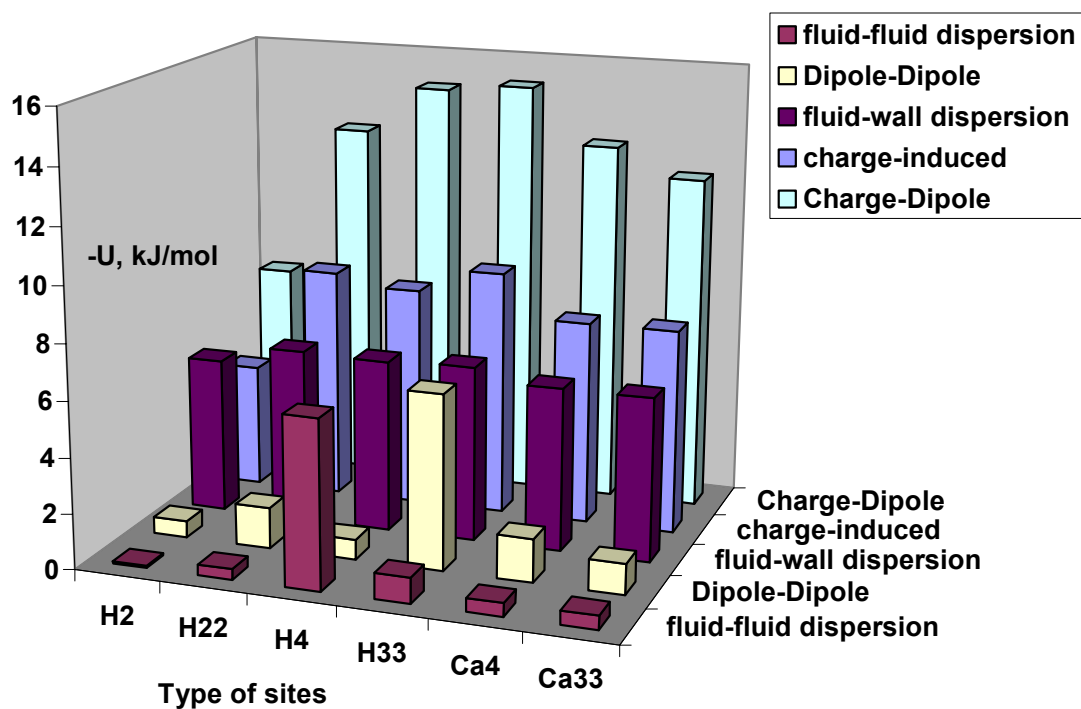
Figure 7.12: Energy contributions for hydroxyl and carbonyl sites at 40 kPa and 298 K (with reference to Fig. 7.11).
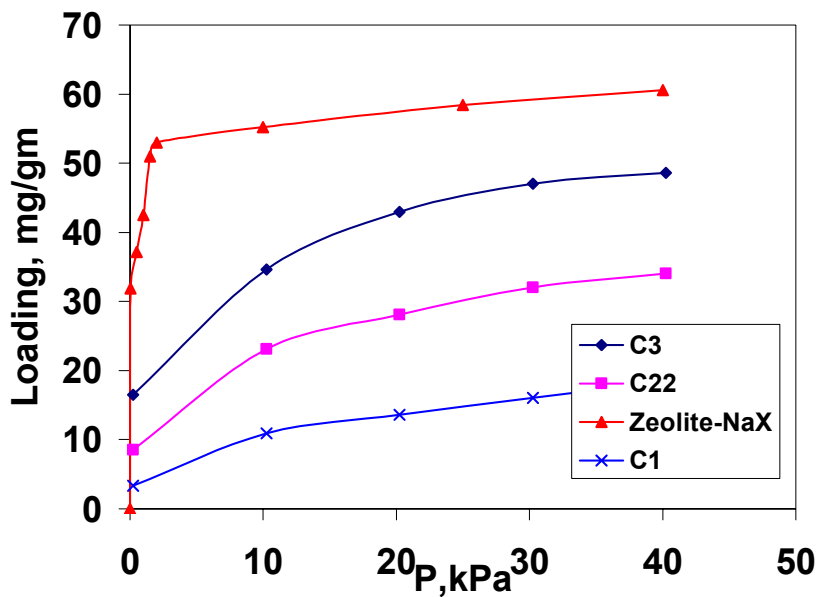
Figure 7.13: Adsorption isotherms for HCN in activated carbon with carboxyl sites and zeolite NaX at 298 K.
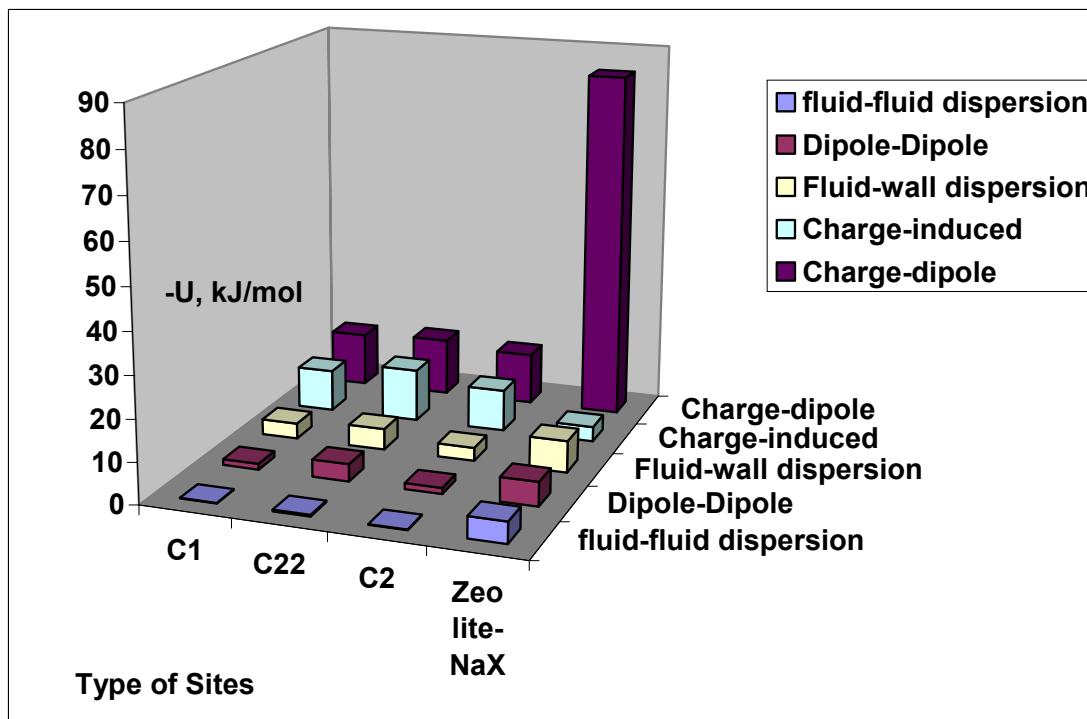
Figure 7.14: Energy contributions for carboxyl sites at 40 kPa and 298K (with reference to Fig.7.13).

7.4.2 Sorption of methyl ethyl ketone

Figure7.15 shows the H values for carbon with different carbonyls at 298K, which is in the range of 1-10 µg/g Pa, whereas Q values in the range of 12-30 kJ/mol are shown in Fig.7.16. H values for hydroxyls were in the range of 1-15 µg/g Pa, and Q values were in the range of 15-35 kJ/mol, however in the case of zeolite NaX. H value was 4 µg/g Pa and Q value was 12 kJ/mol (Figs. 7.17 and 7.18). The H values for carboxyls were found in the range of 3-50 µg/g Pa and Q values were in the range of 17-40 kJ/mol (Figs.7.19 and 7.20).
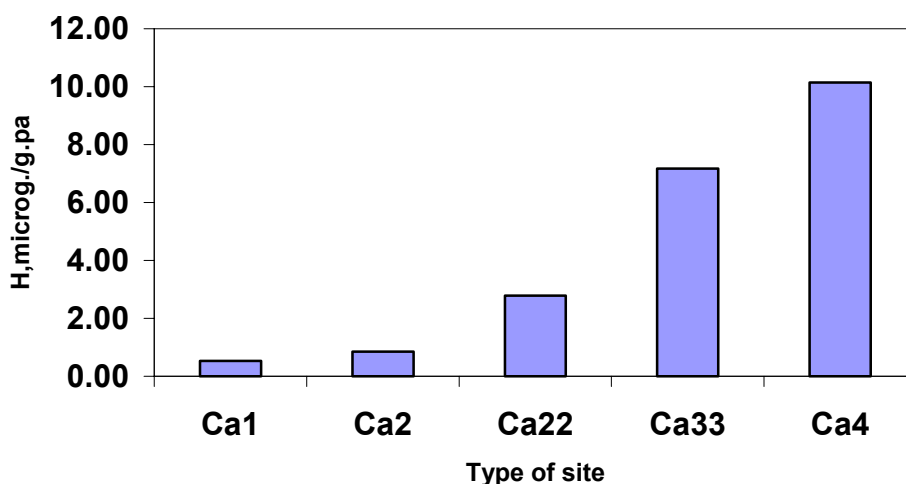
Figure 7.15: Henry's Law constant H for different carbonyl sites at 298 K.
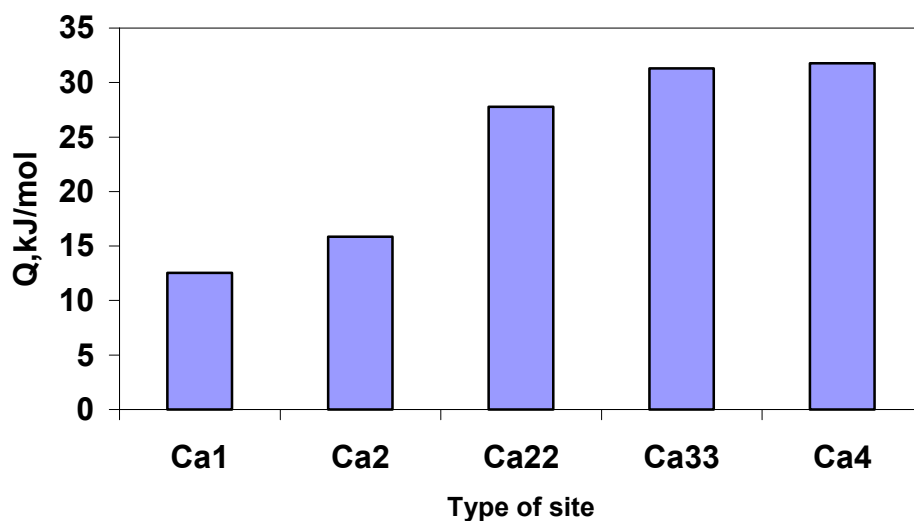
Figure 7.16: Heat of adsorption Q for different carbonyl sites at 298 K.
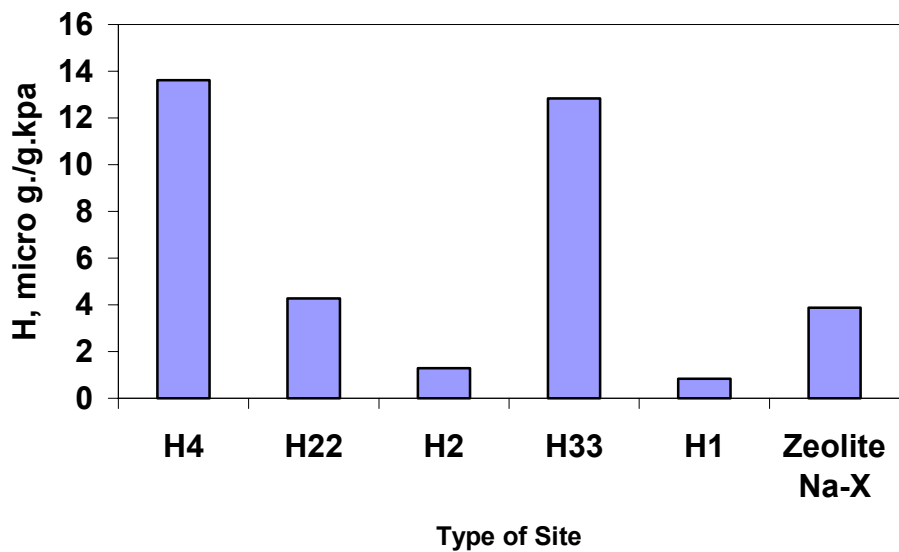
Figure 7.17: Henry's Law constant, H, for different hydroxyl sites at 298 K.
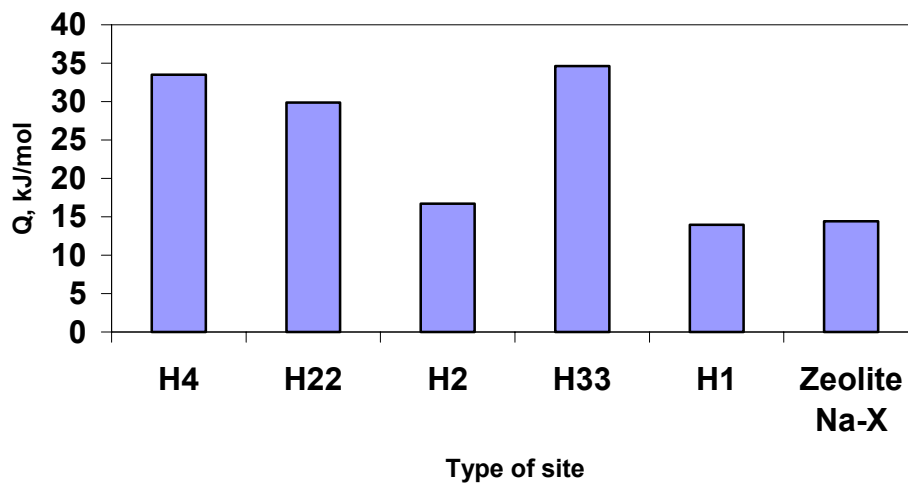
Figure 7.18: Heat of adsorption, Q, for different hydroxyl sites at 298 K.
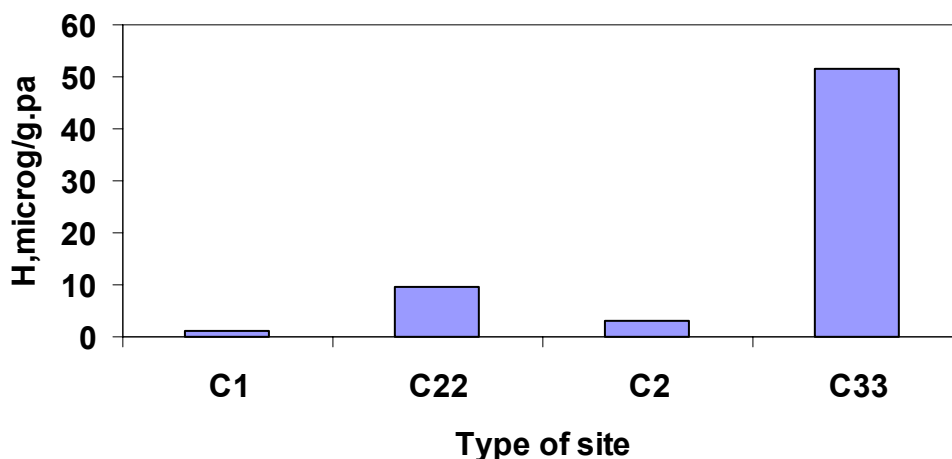
Figure 7.19: Henry's Law constant, H, for different carboxyl sites at 298 K.
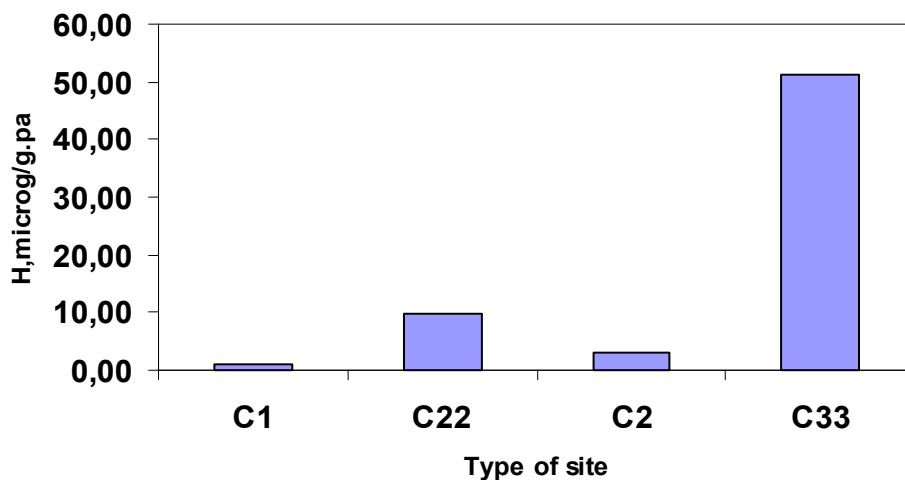
Figure 7.20: Heat of adsorption, Q, for different carboxyl sites at 298 K.

Figure 7.21 shows the isotherms of carbon with hydroxyls, carbonyls, plain carbon (without any functional sites) and zeolite NaX. The NaX shows pore filling at low pressures, however, H33 shows more adsorption than the Ca4 carbon at pressures greater than 1 kPa. Figure 7.22 illustrates the magnitudes of interactions among MEK molecules, MEK-functional site (charge-induced and charge-dipole). The sudden pore filling in zeolite NaX is attributed to charge-dipole interactions (~ 78 kJ/mol). The greater adsorption in the case of H33, as compared to H22 and H2, was due to higher charge-induced and fluid-wall dispersion forces.
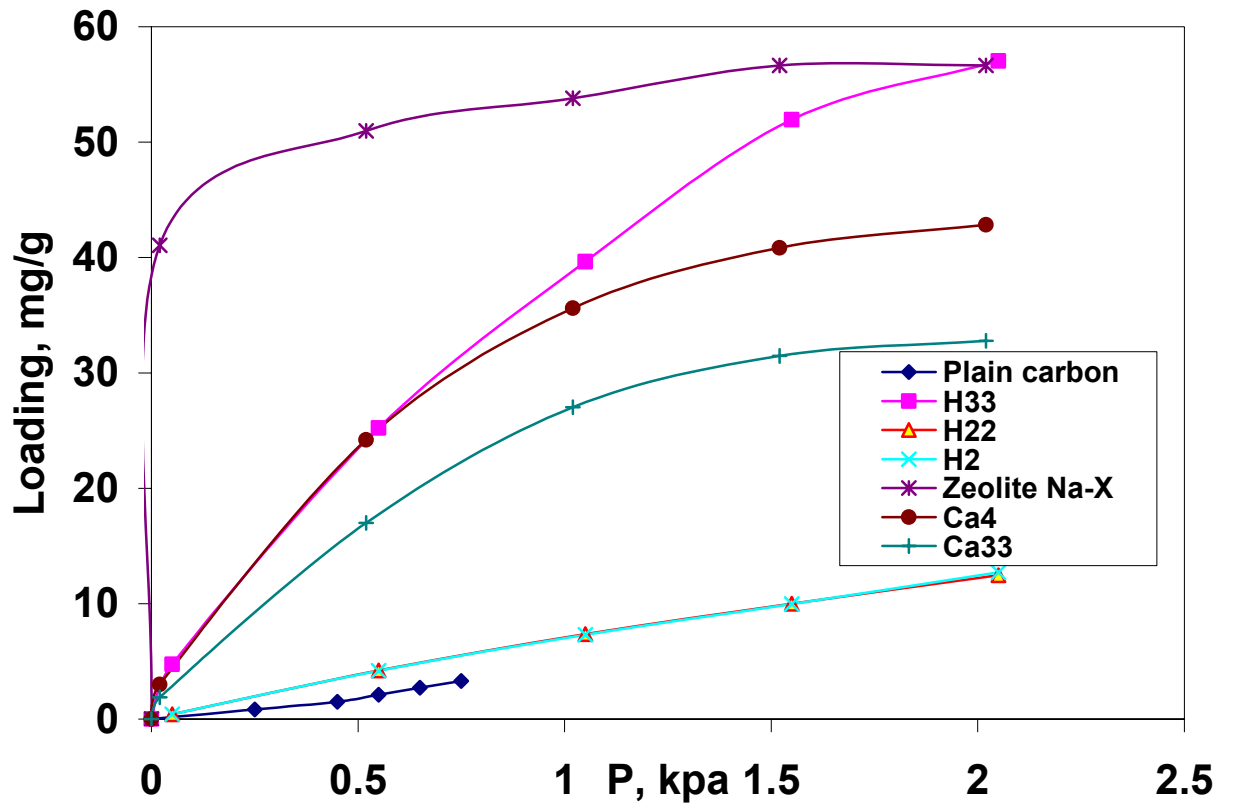
Figure 7.21: Adsorption isotherms for carbonyl, hydroxyl, plain carbon, and zeolite NaX at 298 K.
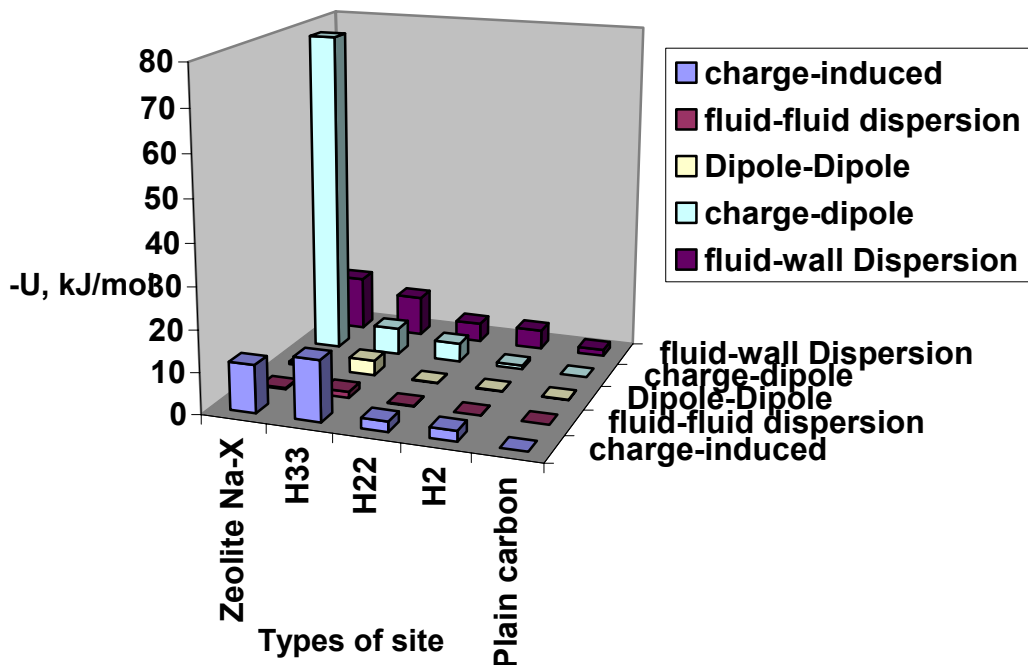
Figure 7.22: Energy contributions for carbonyl, hydroxyl, plain carbon, and zeolite NaX at 2 kPa and 298 K.

Figure 7.23 shows the adsorption isotherms for carbon with carboxyls at 298 K. Sorption in the case of C33 and C22 was above 50 mg/g for operating pressures greater than 1 kPa. This capacity is greater than that of zeolite NaX. This might be due to limited space available for MEK molecules in the spherical cavity. Figure 7.24 suggests that the adsorption in the carbon with carboxyls is dominated by charge-induced and charge-dipole interactions. The greater magnitude of charge-induced dipole interactions is attributed to the high polarizabilty (8.12 A^3) per MEK molecule.
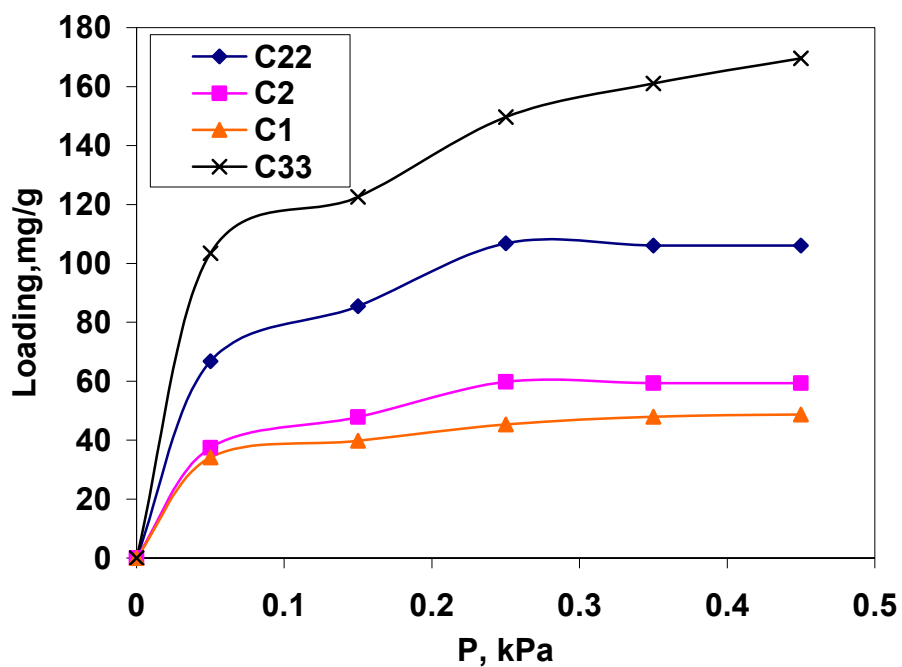
Figure 7.23: Adsorption isotherms for carboxyl sites at 298 K.
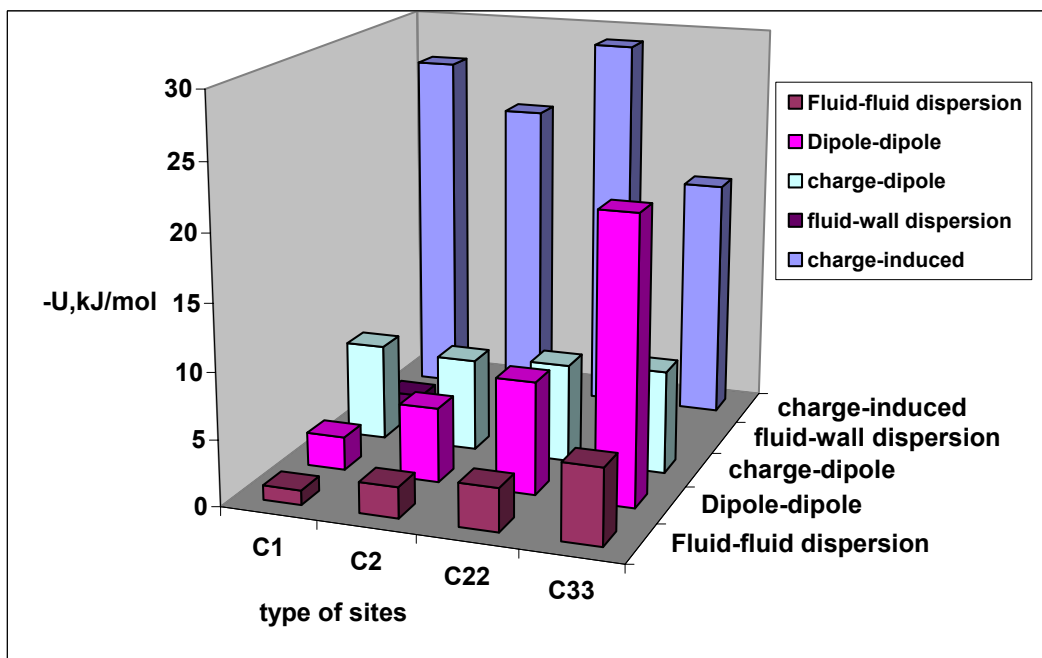
Figure 7.24: Energy contributions for carboxyl sites at 0.45 kPa and 298 K.

7.5. CONCLUDING REMARKS

In the present research study the adsorption of HCN and MEK on zeolite NaX and activated carbons with three types of acid sites was studied using GCMC simulations. On the basis of the research findings presented earlier, the following conclusions could be drawn:

1. Henry's Law constants (H) and heat of adsorption (Q) values for zeolite NaX and carbons with carboxyls were greater than that of carbons with carbonyls and hydroxyls. The low affinity of the carbons with carbonyls and hydroxyls was attributed to low charge densities, and hence low electrostatic interactions with the functional groups.

2. The presence of sodium cations increases the sorption of HCN, as well as MEK, due to large Na-dipole interactions.

3. The presence of carbonyl, hydroxyl, and carboxyl sites help in increasing HCN sorption, mainly due to charge-dipole interactions that are attributed to the high dipole moment of the molecule (2.98 Debye). However, in the case of carboxyls, charge-induced and fluid-wall interactions were also significant.

4. The presence of carbonyl, hydroxyl, and carboxyl sites help in increasing MEK sorption, mainly due to charge-dipole interactions, which are attributed to the high dipole moment of the molecule, and charge-induced dipole interactions due to the high polarizabilty of the MEK molecule

5. Zeolite NaX shows the highest HCN adsorption with pore filling, followed by carbons with carboxyls, hydroxyls, and carbonyls, respectively, which is due to high charge densities and energetic charge-induced dipole and charge-dipole interactions for operating pressures less than 40 kPa.

6. Carbons with C33 and C22 show the highest MEK sorption, followed by carbons with C1, zeolite NaX, and carbons with hydroxyls and carbonyls, respectively, which is due to high charge densities and energetic charge-induced dipole and charge-dipole interactions for operating pressures less than 0.5 kPa. The low adsorption capacity of zeolite NaX, and sudden pore filling is attributed to limited energetic places available for MEK molecules to occupy in the spherical cavity.

REFERENCES

1. http://www.spacelab.com/compound/c78933.htm

2. S.H. Yen, F.T. Jeng, *J. Environ. Sci. Health, A* **32** (8), (1997) 2087

3. S.W. Blocki, *Environ. Prog.* **12,** (1993) 226

4. P. Monneyron, M. Manero and J. Foussard, *Environ. Sci. Technol*, **37**, (2003) 2410

5. J. Pires, A.Carvalho, P.Veloso and M.B.D. Carvalho, *J. Mat. Chem.*, **10**, (2002) 3100

6. M.A. Uguina, J.L. Sotelo, J.A. Delgado, J.M.Gomez and L.I. Celemin, *Sep. Purif. Techn.*, **42,** (2005) 91

7. G.B. Freeman, P.J. Reucroft, *Carbon*, **17**, (1979) 313

8. P.J. Reucroft, P.B. Rao and G.B. Freeman, *Carbon*, **21**, (1983) 171

9. T.M. Oliver, K. Jugoslav, P. Aleksandar and D. Nikola, *Chem. Eng. Proc.*, **44,** (2005) 1187

10. J.L. Soto, and A.L. Myers, *Mol. Phys.*, **42,** (1981) 971

11. F. Karavias, *Ph.D. Thesis*, Univ. of Pennsylvania (1992)

12. R.T.Yang, *Adsorbents: Fundamentals and Applications*, Wiley – Interscience, New York (2003)

13. T.M. Reed and K.E. Gubbins, *Applied Statistical Mechanics*, McGraw-Hill, New York (1973)

14. Z.Tan, *Ph.D Thesis*, Cornell University (1992)

15. M. Jorge and N.A. Seaton, *Mol. Phys.*, **100,** (2002) 2017

16. M. Jorge, C. Schumacher, and N. A. Seaton, *Langmuir*, **18**, (2002) 9296

17. J.M. Prausnitz, R.N. Lichtenthaler and E. Gomes de Azevedo, *Molecular Thermodynamics of Fluid-Phase Equilibria*, 3rd ed., Prentice-Hall, NJ (1999)

Chapter 8

Studies of Adsorption of Hydrogen Cyanide and methyl Ethyl Ketone in Silicalite, Mordenite, and Zeolite Beta Structures

8.1. Introduction

Methyl ethyl ketone (MEK) is frequently used as a solvent for gums, resins, cellulose nitrate, as well as in consumer products such as lacquers, varnishes, paint removers, and glues (1-2). Typically, it is released to air in gases emitted from the pertinent manufacturing industries producing the aforementioned products, or it is directly discharged in wastewater streams associated with a multitude of industrial processes. It is interesting to note that an exposure of 200 ppm of MEK causes irritation to the eyes, nose (mucous membranes), and throat. In addition to this, high MEK levels are associated with smog formation due to photochemical reactions with olefinic hydrocarbons (2-3). In light of the above considerations and the hazardous nature of MEK under certain conditions, adsorption is considered to be one of the preferable and operationally advantageous methods to effectively remove MEK from industrial gases especially using activated carbon and zeolites as adsorbents (2).

Pursuing the above line of research, Yen et al. (2) carried out vapor phase adsorption experiments on zeolite Y and ZSM-5 for different Si/Al ratios varying from 5 to 31, where the concentration of MEK in the vapor phase was in the range of 100-1500 ppm. In this particular study, Zeolite Y was found to be more effective than ZSM-5 in removing MEK from the air stream under consideration. Furthermore, Monneyron et al. (4) conducted vapor phase single component and binary component (with toluene and 1,4-dioxane) adsorption experiments on zeolite Y and ZSM-5. They found that the component having the higher molecular weight adsorbed preferentially over the other, except in the case of MEK-toluene

mixture adsorption on ZSM-5, where toluene sorption was less than MEK due to steric effects. Pires et al (5) studied the effect of dealumination of zeolite Na-Y on the sorption of MEK at 298 K, and showed that an increase in the percentage of de-alumination reduced MEK adsorption, suggesting that sodium cations favor MEK. Uguina et al. (6) studied MEK desorption from silicalite and activated carbon beds, and suggested that the regeneration temperature for silicalite was in the range of 90-170 °C, whereas in the case of activated carbon it was found to be within the range of 150-240 °C. These findings suggest that dispersion interactions might be dominant in the case of silicalite, whereas electrostatic interactions might be dominant in the case of activated carbon due to the presence of acid sites.

Despite the aforementioned research efforts, the experimental data available in the pertinent body of literature are not currently adequate to understand the mechanism of MEK adsorption in activated carbons and zeolites, especially at the molecular level. Meininghaus et al. (7) obtained single component experimental data at relative pressure (P/P$_{sat}$) of 0.007 and showed that dealuminated zeolite Y has greater capacity than H-Mordenite and H-ZSM5 and Na-ZSM-5. Recently, Kotdawala et al (8) studied the effect of sodium cations in zeolite Na-X, as well as hydroxyl, carbonyl and carboxylic sites in activated carbon on the adsorption capacity of MEK using molecular simulation methods, and suggested that the relative magnitudes of charge-dipole, dispersion, and charge-induced dipole interactions determine the sorption capacity of MEK in activated carbon and zeolite Na-X. In particular, it was suggested that MEK sorption capacity is less than 70 mg/g in zeolite-X as compared to activated carbon which displays a capacity ranging from 20-180 mg/g, depending on which functional sites exist in the carbon pore. However, to the best of our knowledge, the capacity and affinity of MEK sorption in silicalite, zeolite beta, and mordenite structures have not been yet adequately and systematically

evaluated, either through experimental studies or simulation techniques. Indeed, these zeolites are

likely

to be good sorption candidates as their nominal pore sizes are slightly greater than the size of MEK molecules. Lack of experimental data and information of favorable sites in the aforementioned zeolites provide ample motivation and research incentive to study the adsorption of MEK using molecular simulation techniques.

In a conceptually similar methodological framework, the adsorption of hydrogen cyanide (HCN) was studied as well, recognizing that it is an acutely poisonous compound, which might enter the human body by breathing contaminated air. HCN vapors are commonly released into air from various sources, including vehicle exhaust emissions, chemical processing, extraction of gold and silver from low grade ores, metal plating, steel, iron, and finishing industries, petroleum refineries, and waste disposed in landfills. Currently, the best-known adsorbents for the removal of HCN from air are metal salt-impregnated activated carbons (9). Freeman (9) and Reucroft (10) studied the adsorption of HCN and the mixture of HCN-water on BPL activated carbon, a granular activated carbon supplied by Calgon Carbon Inc. The experimental results suggested that, adsorption of HCN strongly dominates over water, and HCN discourages additional adsorption of water vapor, which might be attributed to the greater polarizability and dipole moment of HCN.

In another study of the removal of HCN from air conducted by Oliver et al. (11), copper containing and copper-free activated carbons produced from porous sulfonated styrene/divinylbenzene resin were considered to assess the removal efficiency of HCN. The adsorbent performance was comparable to ASC Whetlerite carbons that contain salts of chromium, copper, and silver. Incorporation of copper into the starting material significantly increased HCN breakthrough times, but decreased the surface area and pore volume of the adsorbent. The results of X-ray photoelectron spectroscopy (XPS) analysis revealed partial or complete reduction of the starting divalent copper on the surface of the adsorbents, amply

confirmed by the lack of formation of $(CN)_2$ during the adsorption of HCN, while the use of conventional Whetlerite carbon produced poisonous $(CN)_2$ gas. However, detailed and good-quality experimental data on the sorption of HCN from flue gases are limited, and do not suggest any suitable adsorbents for the removal of HCN. Recently, Kotdawala et al (8) simulated the sorption characteristics of zeolite Na-X and activated carbon for HCN using molecular simulation methods, and suggested that Zeolite Na-X displays superior capacity than that of activated carbon due to the presence of cations which are responsible for large cation-dipole interactions. However, the pore size in the above simulations was of the order of 14-15 Å. Notice, that mordenite's 10-membered rings have openings of around 7 Å and its 12-membered rings have about 10 Å pores which might improve dispersion interactions with HCN molecules due to its high polarizability. Silicalite could in principle be a good candidate too, as it possesses 10-membered rings of approximately 5.6 Å diameter. Therefore, the smaller pore sizes of mordenite and silicalite, as well as the polarizability of HCN, suggested the study of the sorption of HCN, especially in the absence of enough and reliable experimental data (7).

The present paper is organized as follows: Section 2 provides a brief description of the particular atomistic modeling approach pursued, followed by a description of the molecular simulation methods employed in the context of the present study. Section 3 encompasses the paper's main results with a discussion about the primary findings. Finally, concluding remarks are provided in Section 4.

8.2. Molecular Modeling and Simulation Framework

A pairwise-additive potential function is considered, which is comprised of a (12-6)-type of Lennard-Jones (LJ) potential term plus a purely Coulombic one, in order to quantitatively characterize the site-site non-bonded interactions (12):

$$V_{ij} = 4\varepsilon_{ij}\left[\left(\frac{\sigma_{ij}}{r_{ij}}\right)^{12} - \left(\frac{\sigma_{ij}}{r_{ij}}\right)^{6}\right] + \frac{q_i q_j}{4\varepsilon_0 r_{ij}} \qquad (8.1)$$

where i and j are atoms of HCN/MEK or on the zeolite lattice, and r_{ij} is the distance between atoms i and j. ε_{ij} and σ_{ij} represent the LJ parameters, namely well-depth and diameter respectively. Finally, q_i and q_j are the partial charges of the interacting sites.

The proposed modeling framework for the interacting sites is realized through the following three groups: HCN/MEK-HCN/MEK, Zeolite-Zeolite and Zeolite-HCN/MEK. The first two types of interacting sites (and the associated model parameters) were adequately characterized in the relevant literature from where we borrow the corresponding values (13-19), whereas the last one is assumed to obey the Lorentz-Berthelot mixing rules (20-21):

$$\varepsilon_{ij} = \sqrt{\varepsilon_{ii}\varepsilon_{jj}} \qquad \sigma_{ij} = \frac{\sigma_{ii} + \sigma_{jj}}{2} \qquad (8.2)$$

MEK-MEK interactions were modeled using the Trappe-UA force field (13-16) in which the methyl sites were represented by a united atom, bonds were kept rigid, and angle bending and torsion terms were treated as flexible. The harmonic potential was used for angle bending and a cosine series form was used to account torsional interactions for sites separated by three bonds. The values of the parameters for angle bending and torsion interactions for MEK were taken from Stubbs et al. (16). HCN-HCN interactions were modeled using the OPLS force field (17-18) in which bonds and angles are assumed rigid. The interaction parameters between the zeolite framework atoms and Na^+ cations in the framework were taken from Beerdsen et al. (19,20)

Table 1 contains all the pertinent zeolite, HCN and MEK interaction parameters. Furthermore, unit cell structures of silicalite, mordenite, and zeolite beta used in the present study are derived from studies conducted by Artioli et al. (22), Gramlich (23), and Newsam et al. (24), respectively. Finally, the justification for the particular procedure and basis for choosing Al sites in the mordenite and silicalite cases is thoroughly discussed in (20) and (25), respectively.

Table 8.1 Parameters for zeolite, HCN and MEK interaction [13-19]

Lennard-Jones			Coulombic	
Interacting Sites	σ (A°)	ε (K)	Sites	q(e)
O(MEK)	3.05	79.0	Si	2.050
C(MEK)	3.82	40.0	Al	1.75
CH_2 (MEK)	3.95	46.0	Na	1.0
CH_3(MEK)	3.75	98.0	[a]$OZ_{Si-OZ-Si}$ / $OZ_{Si-OZ-Al}$	-1.025 / -1.200
H(HCN)	0	0	O(MEK)	-0.424
N(HCN)	3.2	88	C(MEK)	0.424
C(HCN)	3.63	77	CH_3(MEK)	0
Si/Al	0	0	CH_2(MEK)	0
Na	2.33	46.8	H(HCN)	0.15
			C(HCN)	0.28
			N(HCN)	-0.43

[a]$OZ_{Si-OZ-Si}$: Oxygen of zeolite bridging two Si atoms, $OZ_{Si-OZ-Al}$: Oxygen of zeolite bridging Si and Al atoms

For Grand Canonical (μVT) Monte Carlo simulations conducted in the context of the present research study, the Towhee (26) simulation package was used. Periodic boundary conditions were applied in all directions and an Ewald sum was explicitly used to calculate the electrostatic interactions (21). For simulation purposes, two unit cells were considered in the silicalite case, four unit cells in mordenite, and four unit cells in the zeolite beta case. Final simulation box dimensions for silicalite were chosen as follows: a=20.0511 Å, b=19.87570 Å, c=26.73640 Å, for mordenite a=18.011 Å, b=20.53 Å, c=30.112 Å, and for zeolite beta a=25.32278 Å, b=25.32278 Å, c=26.40612 Å. Cutoff distances for each simulation run were set less than half the shortest box side, in order to conform with the minimum image convention (21), namely 9.5 Å, 9.0 Å, and 12.0 Å for silicalite, mordenite, and zeolite beta respectively. Simulation runs were initialized by considering Na^+ cations at their equilibrium

positions. For this reason, NVT Monte Carlo simulations were conducted, where the number of molecules, volume, and temperature were kept constant, and the Na$^+$ cations were placed near the aluminum sites. For each zeolite simulation box we placed 1 to 4 Na$^+$ cations per system (not per unit cell). These loadings correspond to Si/Al ratios of 197, 95, 63, and 47 for silicalite and mordenite, and 255, 127, 84, and 63 for zeolite beta. Then, for 10 million steps, Na$^+$ cations were displaced randomly and zeolite structures were kept fixed. Final positions of the Na$^+$ cations were fixed and used for future Monte Carlo simulations in the (μVT) ensemble case.

Prior to these simulations, chemical potentials at each pressure point were computed by using the Widom Insertion Method (27) in a series of NPT Gibbs Ensemble Monte Carlo (GEMC) simulation runs. (28,29) In this particular ensemble, pressure, temperature, and the number of fluid molecules were considered fixed. A simulation box containing 100 MEK (or HCN) molecules was set up. Translation and rotation moves of the MEK (or HCN) molecules and the volume change of the simulation box were sampled with probabilities of 50%, 45%, and 5%, respectively. At each pressure point the system was

equilibrated for 20,000 cycles and a 20,000-cycle production run, followed by an equilibration run in which the chemical potential was calculated through the Widom Insertion Method every five cycles. Please notice, that a cycle corresponds to *N* Monte Carlo moves, where *N* is the number of molecules in the system (20).

The chemical potentials calculated at each pressure point were used to set up the simulation runs in the grand canonical ensemble, and obtain the adsorption isotherms of MEK (or HCN) in silicalite, mordenite, and beta zeolite structures. In these GCMC simulation runs insertion/deletion, regrowth, intramolecular atom translation, translation, and rotation of MEK (or HCN) molecules were sampled with probabilities of 30%, 5%, 5%, 30%, and 30%, respectively. No biasing was applied for insertions. Each simulation started with a 10 million step equilibration run, which was followed by a 10 million step production run. Statistical uncertainties were calculated by dividing the production run into ten

blocks. Finally, the reader should be reminded that during the GCMC simulation runs both zeolite structures and cation positions were kept fixed (20,25).

8.3. Results and Discussion

8.3.1 MEK sorption in silicalite, mordenite, and zeolite beta

Figures 8.1 and 8.2 show the sorption capacity of zeolite beta with Si/Al ratios ranging from 63 to infinity. They suggest that the presence of Na^+ cations increases the sorption capacity (200 mg/g at Si/Al = 63 as compared to 50 mg/g for Si/Al $\rightarrow$ infinity) of zeolite beta by a factor of four, due to more pronounced electrostatic interactions. Also notice, that, an increase in the number of Na^+ ions in this framework does not seem to affect the capacity of zeolite beta at a higher operating pressure (4-5 kPa). However, Figure 8.2 implies that the effect of Si/Al ratio remains significant in the low pressure regime. Figure 8.3 shows that MEK molecules are located in the short channels made of a 12 membered ring (7 Å). The polar part (white color) of MEK is pointed towards the sodium cations (blue), implying that electrostatic interactions may be influencing the sorption capacity of zeolite beta.

Sorption in silicalite and mordenite reveals that MEK has a high affinity for the silicalite pore surface and higher capacity than that of mordenite, as shown in Figures 8.4 and 8.5. In particular, Figure 8.4 shows that the sorption capacity of silicalite should be about 60% greater than that of mordenite. The presence of Na^+ ions improves the sorption capacity of mordenite slightly at low pressures, as seen in Figure 8.5, but has less impact on its capacity at higher pressures (>1 kPa) as shown in Figure 8.5. An increase in the number of cations in silicalite from 0 to 4 (from Si/Al = infinity to 47), increases sorption of MEK at low pressure significantly, as seen in Figure 8.5, but the saturation capacity of silicalite decreases by 30% (see Fig. 8.4). This can be explained by the presence of sodium cations which occupy some of the pore volume and lead to reduced capacity. The snapshots in Figures 8.6 and 8.7 imply that

sorption in silicalite might be reaching its saturation capacity as all molecules are in the straight/zig-zag channels located one by one in row without overlapping and utilizing all available pore volume (see Fig. 8.6), but in the case of mordenite sorption reaches a plateau-like regime as some of the eight membered ring channels remain empty (see the white circle regime in Fig. 8.7).

Figure 8.8 shows sorption of MEK in mordenite with sodium cation. The 'red' is an oxygen of carbonyl of the MEK and cyan color represents the nonpolar part of MEK consisting methyl and ethyl groups. Due to steric constraints the carbonyl of MEK is not pointed towards sodium cation (blue one) and hence the increase in sodium cations in mordenite does not improve the sorption capacity significantly (see Fig. 8.5). However, in the case of silicalite, increasing the number of cations increases the sorption capacity at low pressure is illustrated in Figure 8.9, where the carbonyl part of MEK (white) is pointed towards the sodium cation (blue) which increases the electrostatic interaction and hence the sorption.

8.3.2 HCN sorption in Silicalite and mordenite

Sorption patterns in silicalite and mordenite reveal that HCN displays high affinity towards silicalite pore surfaces, and a higher capacity (~150 mg/g) than that of mordenite (60-80 mg/g), as seen in Figures 8.10 and 8.11. These differences may be attributed to the small channel size of the 10-membered rings of silicalite (approximately 5.6 Å) compared to mordenite's 12-membered channel which increases dispersion and electrostatic interactions. Figure 8.10 shows that the sorption capacity of silicalite was almost double than that of mordenites. The presence of Na^+ ions however, improves the sorption capacity of mordenites to some extent, as shown in Figure 8.11, but has less influence on their saturation capacity. An increase in the number of cations in silicalite from 0 to 4 (i.e., Si/Al $\rightarrow$ infinity to 47) increases sorption of HCN at low pressure significantly, as seen in Figure 8.11, but the saturation capacity of silicalite decreases slightly. Fig. 8.12 shows the snap shot of HCN molecules in silicalite with sodium cations. The figure shows that negatively charged 'N' of HCN (blue) is pointed toward the sodium cation (silver) suggesting that sodium cation improves sorption in silicalite and hence it increases the sorption capacity at lower pressure (see Fig. 8.11). Figure 8.13 shows the hydrogen

bonding among HCN molecules in silicalite in the straight and in the zig-zag channels (a train of molecules). However, the presence of sodium cations in the intersection of straight and zig-zag channels disrupts the hydrogen bonding and reduces the sorption capacity of silicalite as seen in Figures 8.12. Fig. 8.14 shows a snapshot of HCN molecule adsorbed in 8-membered ring channel of mordenite with sodium cation. The figure implies that, due to the smaller size of the ring channel, HCN molecules cannot orient themselves to participate in hydrogen bonding with other HCN molecules. It also shows that the 'N' of HCN (blue) is pointed to wards sodium cation (pink).

The snapshot in Figure 8.15 implies that HCN adsorption in silicalite without cations reaches a saturation capacity as most of the places in the silicalite appear to be occupied with HCN molecules at 80 kPa. However, the mordenite structure shows some unoccupied space at 80 kPa as seen in Figure 8.16. This gives circumstantial evidence that in mordenite either the orientation of the molecules or the mordenite structure does not allow the utilization of the entire mordenite pore volume, or interactions with mordenite and other HCN molecules are not enough to fill mordenite structure with HCN.

8.4. Conclusions

Monte Carlo simulations for HCN and MEK adsorption studies in silicalite, mordenite, and zeolite beta structures with different Na^+ cation loadings were carried out. The results reveal the importance of the pore structure and cation concentration on the adsorption of MEK and HCN. Although these three zeolites have similar pore volumes, zeolite beta, with its pore structure being mostly accessible to MEK molecules, is predicted to adsorb significantly more MEK than silicalite and mordenite. The greater affinity of silicalite towards HCN and MEK as compared to mordenite was attributed to its pore size of 5.6 Å that directly contributes to the underlying Van der Waals and electrostatic interactions. Furthermore, the presence of sodium cations increases the sorption capacity of zeolite beta, mordenite, and silicalite at relatively low pressures, but does not influence the capacity at higher pressures of the zeolite under consideration. It was also found, that the sorption of MEK/HCN in silicalite occurs

only in the 10-membered ring channels (both zig-zag and straight), due to its size which is comparable to the channel size. In addition, the sorption of MEK in mordenite was mainly observed in the 8 and 12-membered ring channels. The intersection of 8 and 12 membered ring channels was identified as the most active sites for sorption due to the presence of cations. Finally, in the case of zeolite beta, 12-membered ring long and short channel intersections were shown to be quite important for MEK sorption as all sodium cations are placed at the intersection.

Acknowledgements

References

1. http://www.spacelab.com/compound/c78933.htm

2. S.H. Yen, F.T. Jeng, and J.H. Tsai, Adsorption of methyl ethyl ketone vapors on to zeolites, *Journal of Environmental Science and Health, A* **32** (8), 2087 (1997).

3. S.W. Blocki, Hydrophobic zeolite adsorbent: a proven advancement in solvent separation technology, *Environmental Progress*, **12,** 226 (1993).

4. P. Monneyron, M. Manero and J. Foussard, Measurement and modeling of single- and multicomponent adsorption equilibria of VOC on high-silica zeolites, *Environmental Science and Technology*, **37**, 2410 (2003).

5. J. Pires, A. Carvalho, P. Veloso and M.B.D. Carvalho, Preparation of dealuminated faujasites for adsorption of volatile organic compounds, *Journal of Materials Chemistry*, **10**, 3100 (2002).

6. M.A. Uguina, J.L. Sotelo, J.A. Delgado, J.M. Gomez and L.I. Celemin, Adsorption of methyl ethyl ketone and trichloroethylene from aqueous solutions on the silicalite fixed bed adsorbers *Separation and Purification Technology*, **42,** 91 (2005).

7. C.K.W. Meininghaus and R. Prins, Sorption of volatile organic compounds on hydrophobic zeolites, *Microporous and Mesoporous Materials*, **35-36**, 349 (2000).

8. R.R. Kotdawala, N. Kazantzis, and R.W. Thompson, Molecular Simulation Studies of Adsorption of Hazardous Molecules in zeolite-X and activated carbons: The Hydrogen Cyanide and Methyl Ethyl Ketone Cases, *Journal of Hazardous Materials* (under review).

9. G.B. Freeman and P.J. Reucroft, Adsorption of HCN and H_2O vapor mixtures by activated and impregnated carbons, *Carbon*, **17**, 313 (1979).

10. P.J. Reucroft, P.B. Rao and G.B. Freeman, Binary vapor adsorption by activated carbon, *Carbon*, **21**, 171 (1983).

11. T.M. Oliver, K. Jugoslav, P. Aleksandar and D. Nikola, Synthetic activated carbons for the removal of hydrogen cyanide from air, *Chemical Engineering and Processing*, **44,** 1187 (2005).

12. C.E. Ramachandran, S. Chempath, L.J. Broadbelt and R.Q. Snurr, Water adsorption in hydrophobic nanopores: Monte Carlo simulations of water in silicalite, *Microporous and Mesoporous Materials*, **90**, 293 (2006).

13. M.G. Martin, J.I. Siepmann, Transferable Potentials for Phase Equilibria. 1. United-Atom Description of *n*-Alkanes, *Journal of Physical Chemistry B*, **102**, 2569 (1998).

14. M.G. Martin, J.I. Siepmann, Novel configurational-bias Monte Carlo method for branched

molecules. Transferable potentials for phase equilibria. 2. United-atom description of branched alkanes, *Journal of Physical Chemistry B*, **103**, 4508 (1999).

15. B. Chen, J.J. Potoff, J.I. Siepmann. Monte Carlo calculations for alcohols and their mixtures with alkanes. Transferable potentials for phase equilibria. 5. United-atom description of primary, secondary and tertiary alcohols, *Journal of Physical Chemistry B*, **105**, 3093 (2001).

16. J.M. Stubbs, J.J. Potoff, J.I. Siepmann, Transferable Potentials for Phase Equilibria. 6. United-Atom Description for Ethers, Glycols, Ketones and Aldehydes, *Journal of Physical Chemistry B*, **108**, 17596 (2004).

17. W.L. Jorgenson and J.M. Briggs, Monte Carlo simulations of liquid acetonitrile with a three-site model, *Molecular Physics*., **63**, 547 (1988).

18. W.L. Jorgenson, D.S. Maxwell and J. Tirado-Rives, Development and testing of the OPLS all-atom force field on conformational energetics and properties of organic liquids, *Journal of American Chemical Society,* **118**, 11225 (1996).

19. E. Beerdsen, D. Dubbledum, B. Smit, T.J.H. Vlugt and S. Calero, Simulating the effect of Non-framework cations on the adsorption of alkanes in MFI-type zeolites, *Journal of Physical Chemistry B*, **107**, 12088 (2003).

20. A.O. Yazaydin and R.W. Thompson, Molecular Simulation of Adsorption of MTBE in Silicalite, Mordenite, and Zeolite Beta, *Journal of Physical Chemistry B*, **110**, 14458 (2006)

21. M.P. Allen and D.J. Tildesley, *Computer Simulation of Liquids*; Clarendon Press: Oxford, 1989.

22. G. Artioli, C. Lamberti and G.L. Marra, Neutron powder diffraction study of orthorhombic and monoclinic defective silicalite, *Acta Crystallographica, Section B: Structural Science*, 56, 2 (2000)

23. V. Gramlich, Ph.D. Thesis, ETH, Zürich, Switzerland (1971).

24. J.M. Newsam, M.M. J. Treacy, W.T. Koetsier, and C.B. de Gruyter, Structural characterization of zeolite beta*. Proceedings of the Royal Society of London, Series A: Mathematical, Physical and Engineering Sciences*, **420**, 375 (1998).

25. A.O. Yazaydin and R.W. Thompson, Simulating the Vapour-Liquid Equilibria of 1,4-Dioxane *Molecular Simulation*, **32**, 657 (2006).

26. hhtp://towhee.sourceforge.net

27. B. Widom, Some topics in the theory of fluids**, *Journal of Chemical Physics,* **39**, 2802 (1963).

28. A.Z. Panagiotopoulos. Direct Determination of Phase Coexistence Properties of Fluids by Monte Carlo Simulation in a New Ensemble, *Molecular Physics*, **61**, 813 (1987).

29. A.Z Panagiotopoulos, N. Quirke, M Stapleton, and D.J. Tildesley, *Molecular Physics* **63**, 527 (1988).
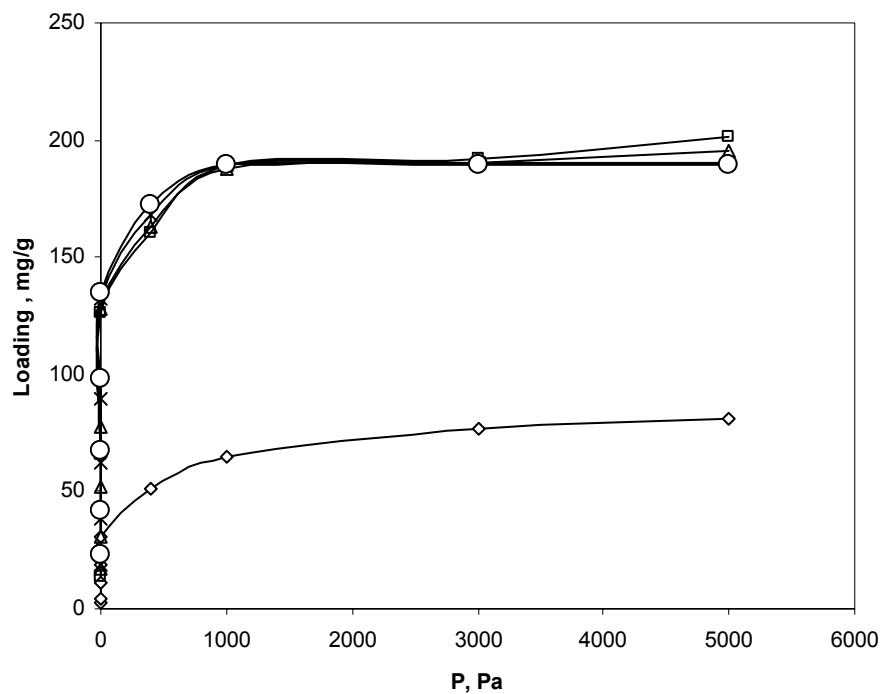
Fig. 8.1. Sorption of MEK in Zeolite beta with different Si/Al ratios, Si/Al = 64 (○), 255 (□), 127 (Δ), Infinity (◊), 84 (∗).
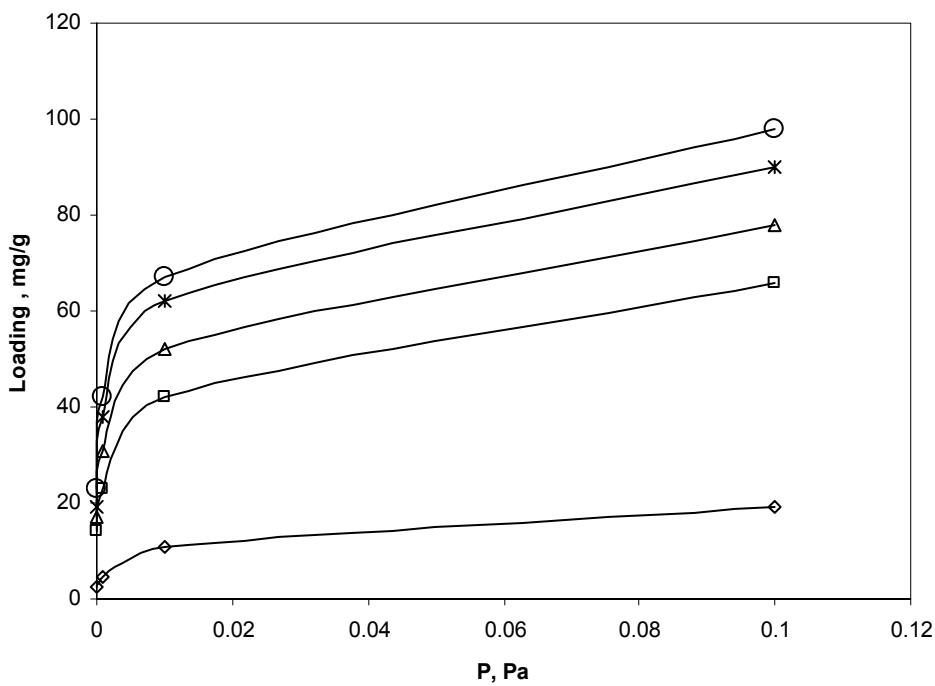
Fig. 8.2 Sorption of MEK in Zeolite beta with different Si/Al ratios in the low pressure regime ratios Si/Al= 64 (○), 255 (□), 127 (Δ), Infinity (◊), 84 (∗).
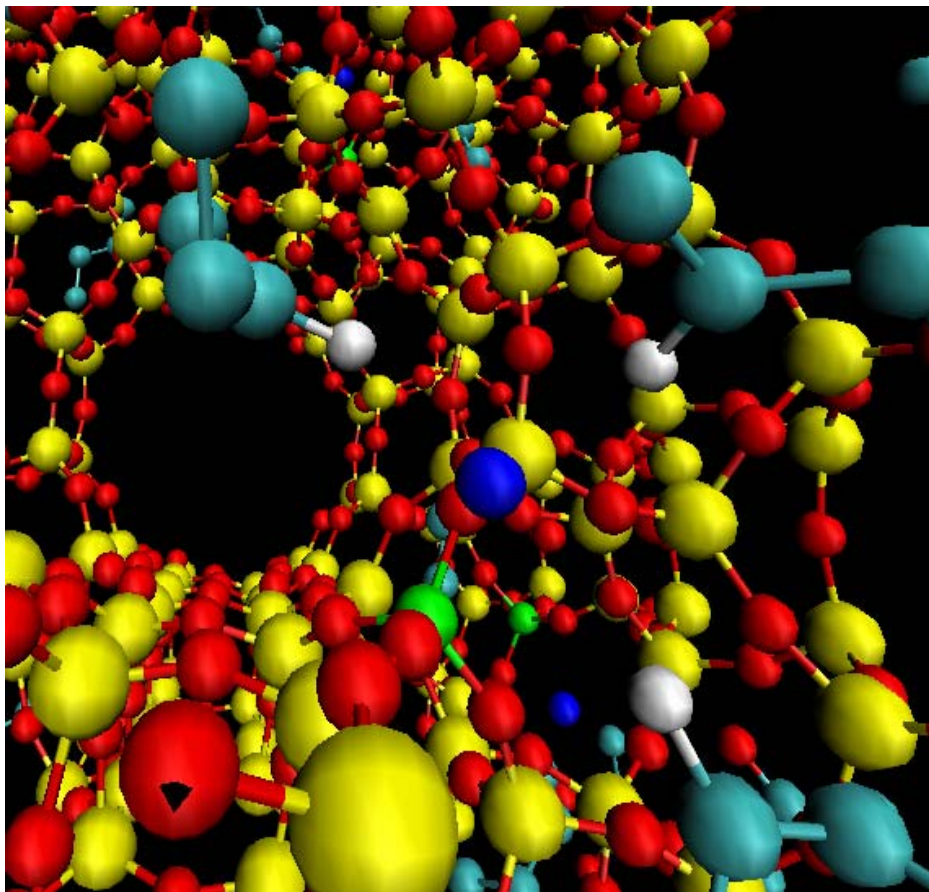
Fig. 8.3 Prominent sites of MEK sorption in Zeolite beta with sodium cations (blue) associated with Al sites (green).
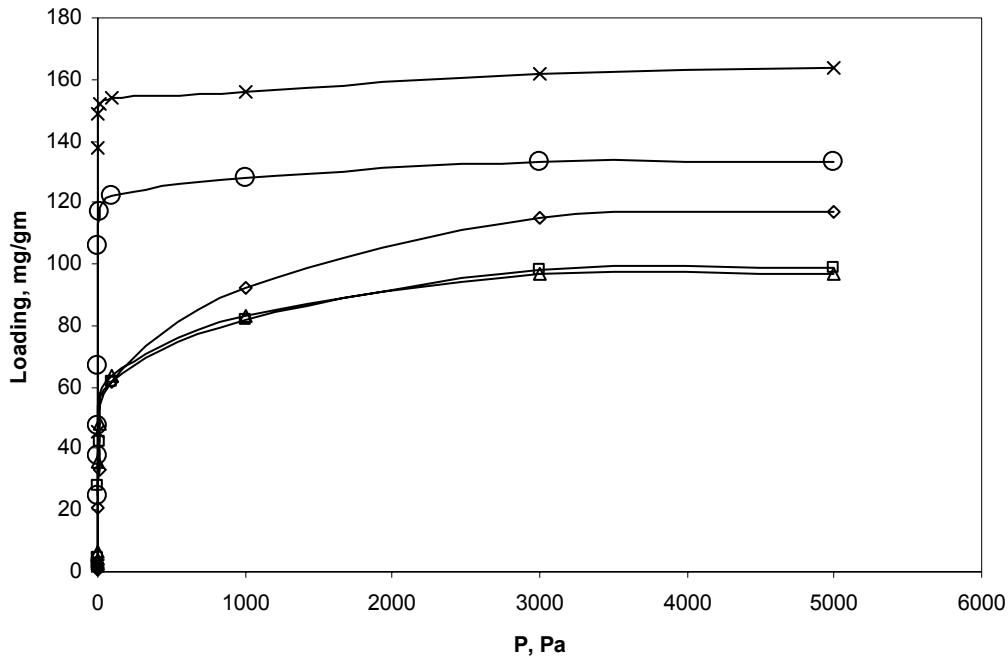
Fig. 8.4 Sorption of MEK in silicalite and mordenite with different Si/Al ratios: for silicalite, Si/Al = 47 (○), infinity (∗), and for mordenite, Si/Al = 197 (◊), 95 (□), 67 (Δ).
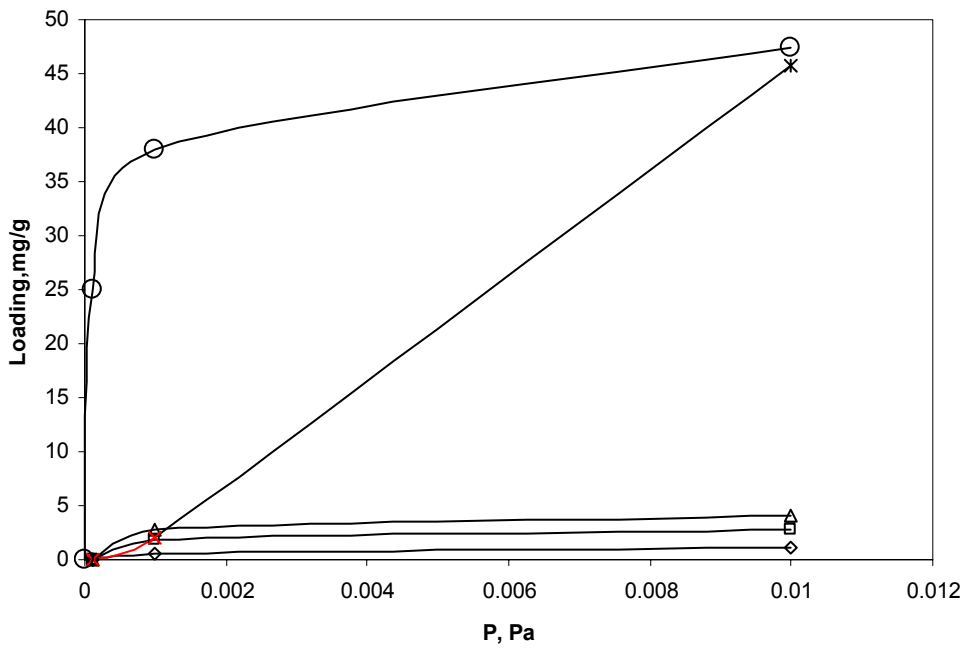
Fig. 8.5 Sorption of MEK in silicalite and mordenite with different Si/Al ratios at low pressures: for silicalite, Si/Al = 47 (○), infinity (∗), and for mordenite, Si/Al = 197 (◊), 95 (□), 67 (Δ).

153
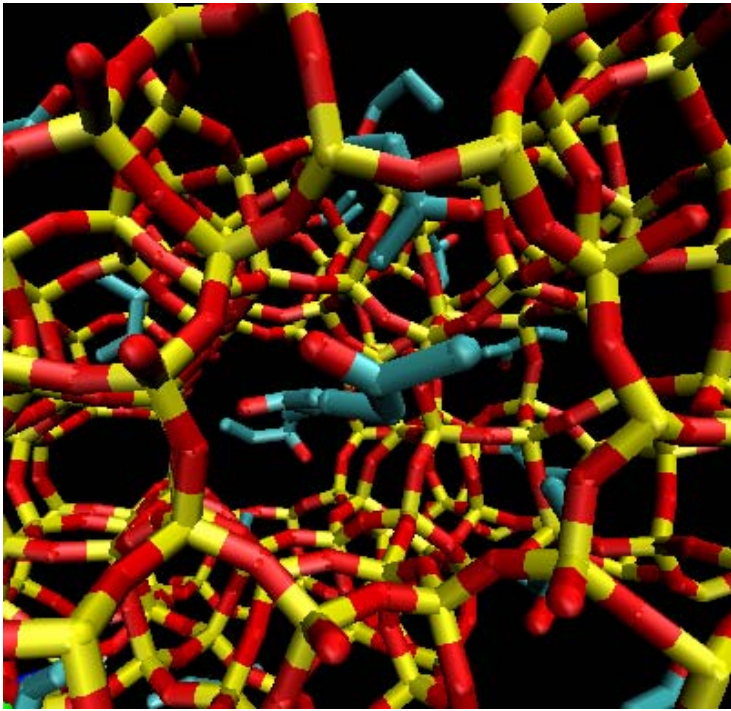
Fig. 8.6 MEK sorption in straight channels of silicalite with Si/Al = infinity. (Silicon – yellow, Oxygen - red, Carbon in methyl/ethyl groups – cyan).
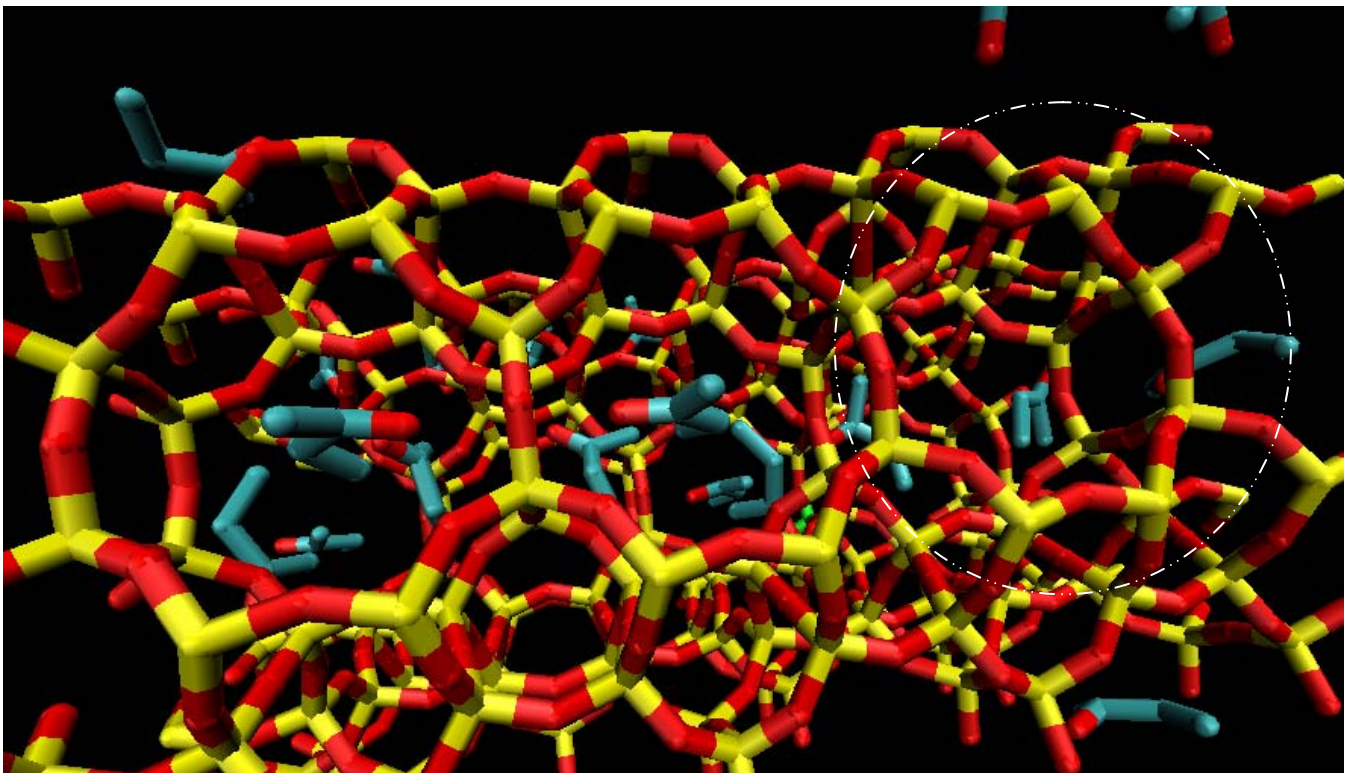
Fig. 8.7 MEK molecules in 8 membered ring channels of mordenite with Si/Al = 95. (Silicon – yellow, Oxygen – red, Carbon in methyl/ethyl groups – cyan)
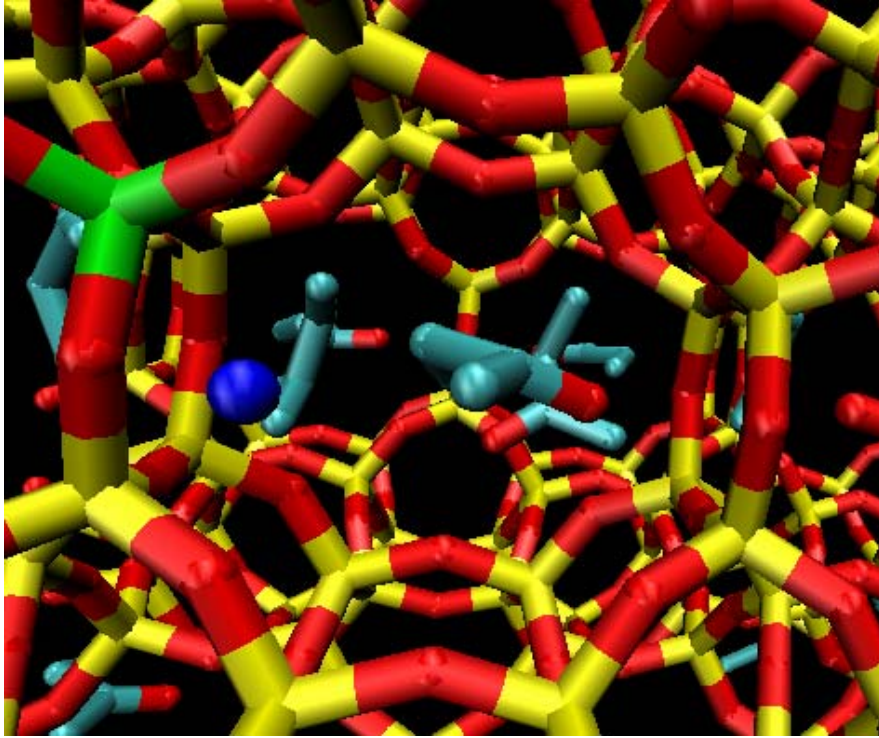
Fig. 8.8 MEK molecules in 8-membered ring channels of mordenite with Si/Al = 95. (Silicon – yellow, Oxygen in MEK carbonyl and silicalite – red, methyl/ethyl groups of MEK – cyan and, Sodium – blue, Aluminum - green).
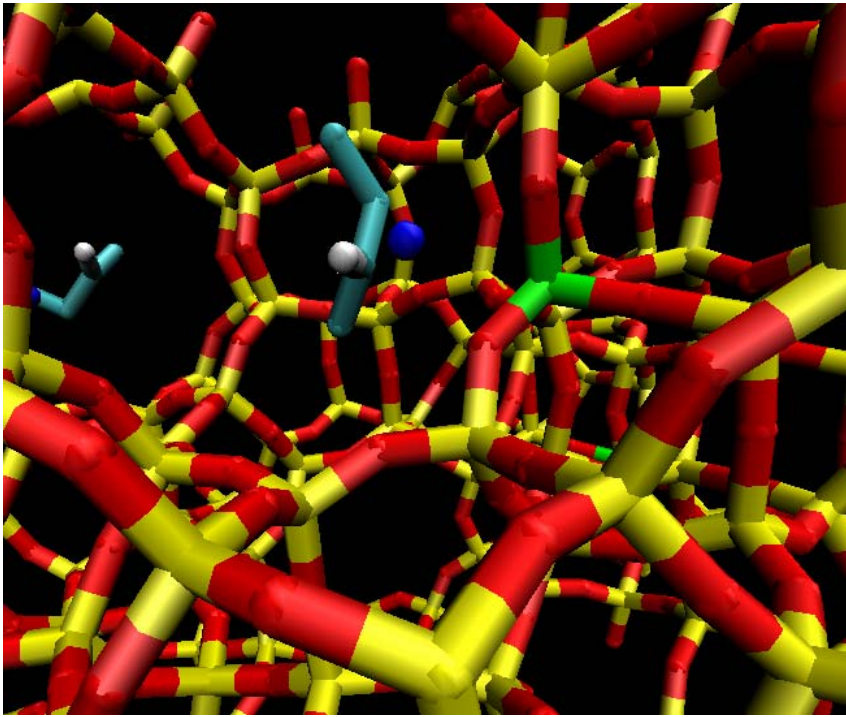
Fig. 8.9 A typical configuration of MEK molecules in silicalite with Si/Al = 47, (Sodium – blue, Silicone – yellow, 'O' of silicalite – red, methyl/ethyl groups of MEK – cyan, 'O' of carbonyl of MEK – white, Al – green).
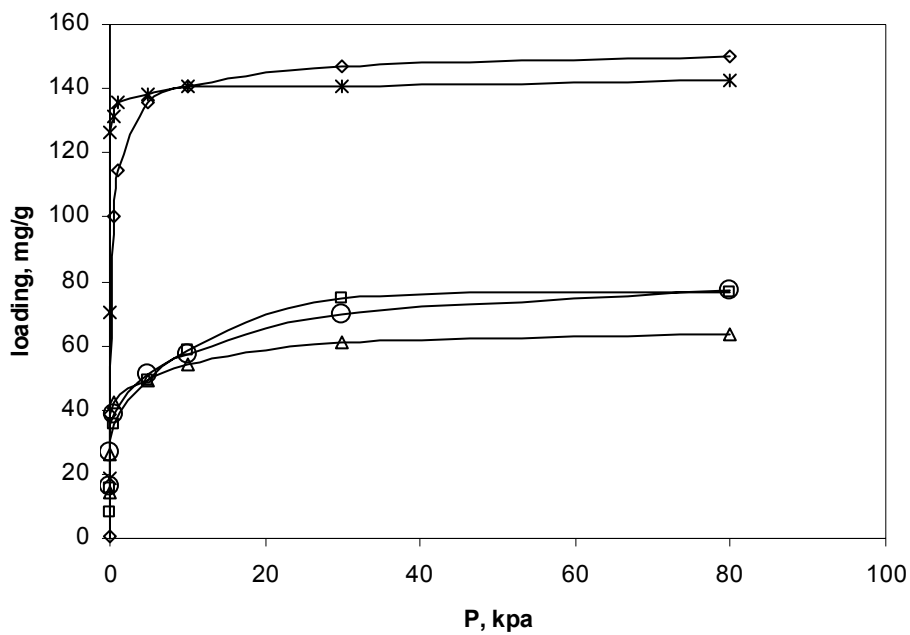
Fig. 8.10 Sorption of HCN in silicalite and mordenite with different Si/Al ratios: for silicalite, Si/Al = 47 (∗), infinity (◊), and for mordenite, Si/Al = 197 (□), 95 (Δ), 63 (○).
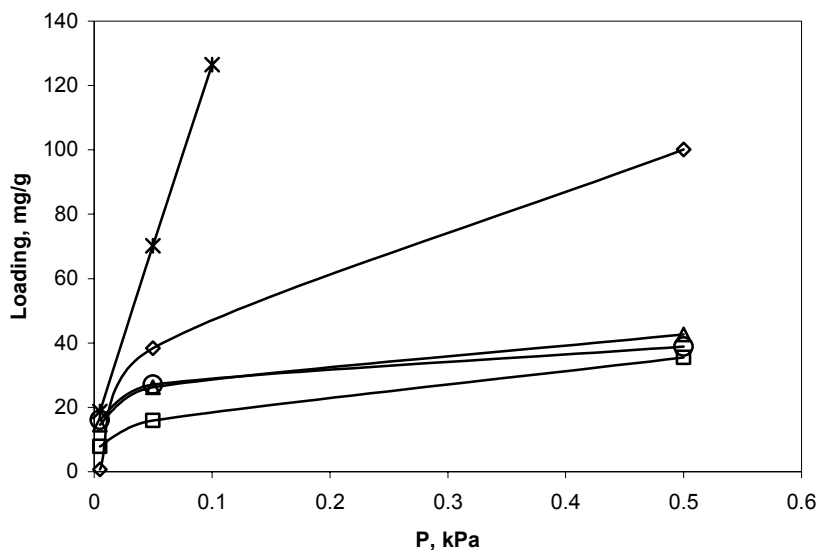
Fig. 8.11 Sorption of HCN in silicalite and mordenite with different Si/Al ratios at low pressures: for silicalite, Si/Al = 47 (∗), infinity (◊), and for mordenite, Si/Al = 197 (□), 95 (Δ), 63 (○).
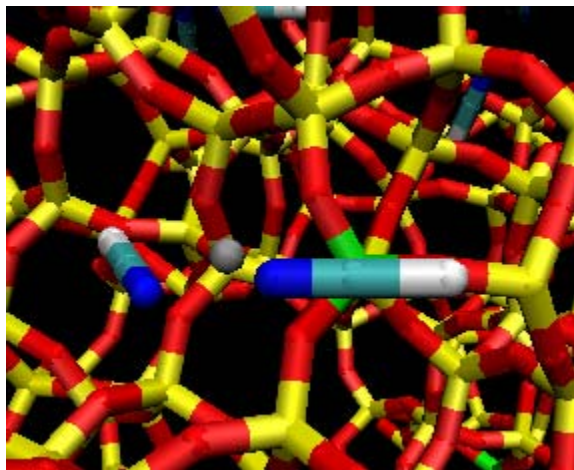
Fig. 8.12 HCN molecules in silicalite with Si/Al = 47, (Sodium – silver, 'N' – blue, Silicone – yellow, 'O' – red, 'C' – cyan, 'H' – white).
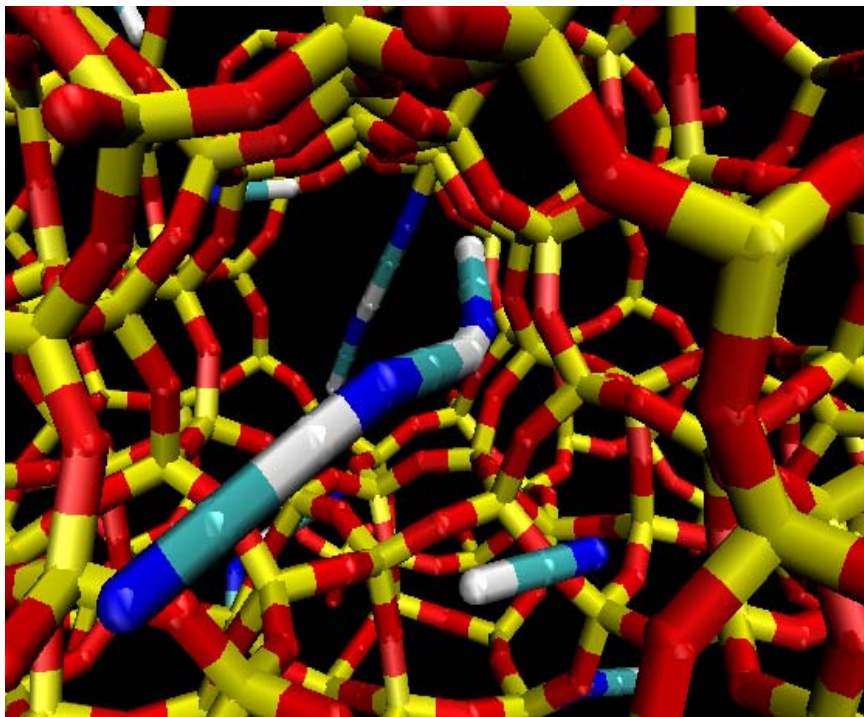
Fig. 8.13 A 'train' of HCN molecules through zig-zag channels of silicalite (N − blue, C − cyan, H– white).
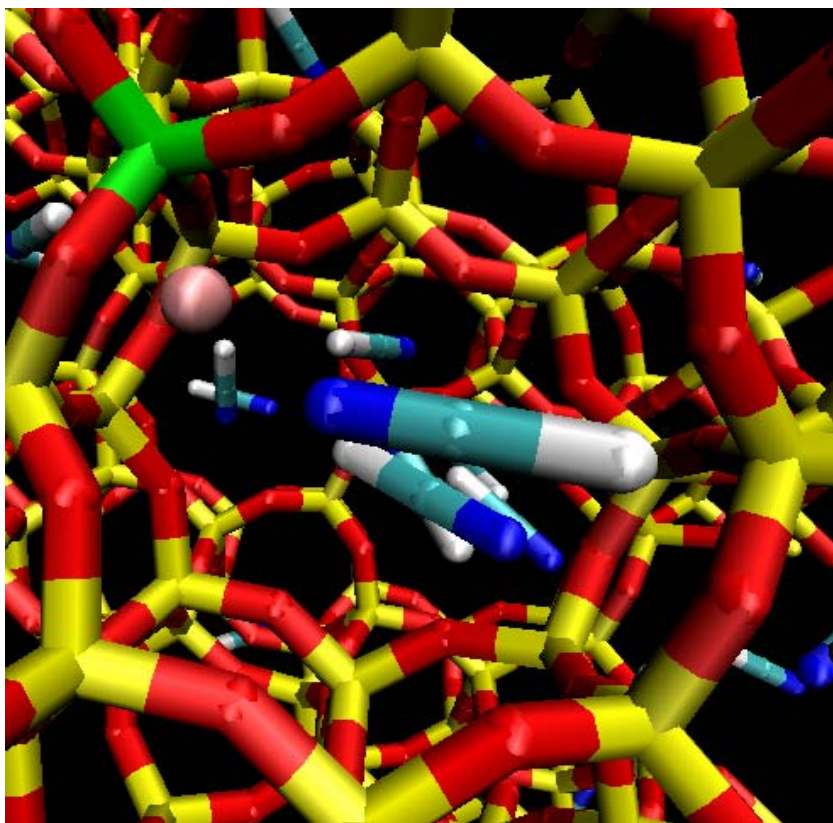
Fig. 8.14 HCN molecule in the 8-membered ring channel, 'N' of HCN is pointed towards the sodium cation (pink) which is near the Al atom (green).
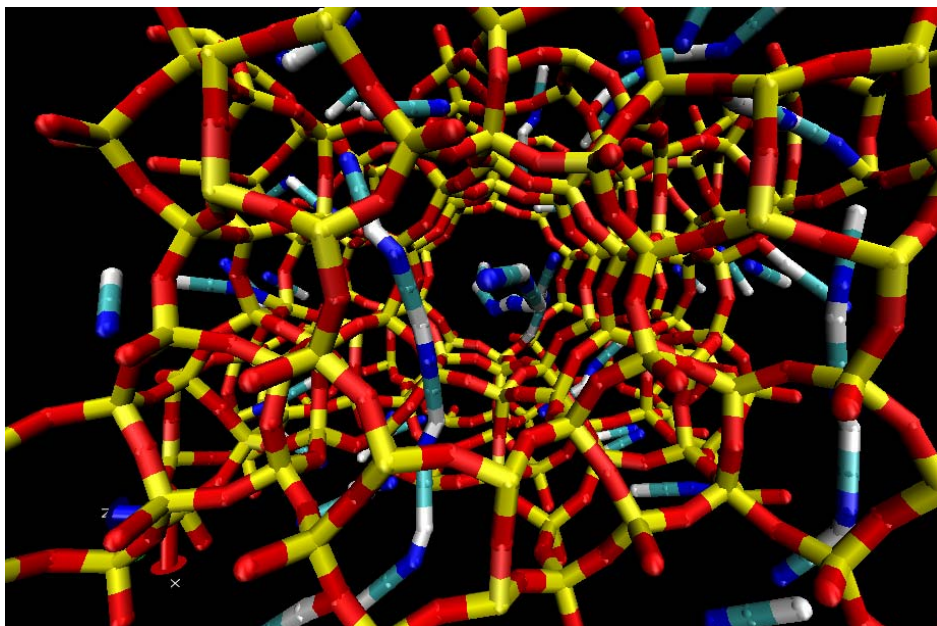
Fig. 8.15 Pore filling by clustering of HCN in 10-membered straight and zig-zag channels of silicalite due to hydrogen bonding. (Silicon – yellow, Oxygen – red, Hydrogen – white, Carbon – cyan, Nitrogen –blue, Sodium – green).
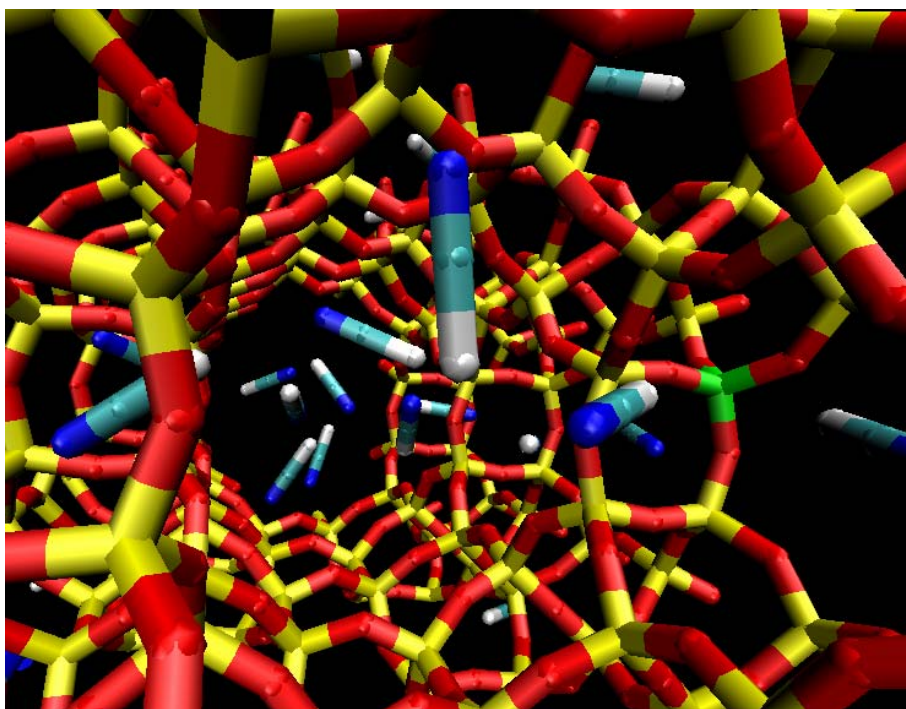
Fig. 8.16 HCN sorption in the mordenite with Si/Al = 197 (Silicon – yellow, Oxygen – red, Hydrogen – white, Carbon – cyan, Nitrogen – blue, Sodium – green)

Chapter 9

Concluding Remarks

1. Chapter 3 and 4 are focused on applying mean field perturbation theory for polar molecules and binary mixtures of polar molar molecules, especially the binary mixture which does not constitute Maximum and minimum boiling point mixture. The theory should be tested with binary polar mixtures like acetone-chloroform (maximum boiling point mixture) and carbon disulfide-acetone (minimum boiling point mixture) to test orientation averaged intermolecular potentials.

2. The simulated results in chapter 3 and 4 can not be compared directly with experimental results as no real adsorbents are available with silt shaped pore geometry with unimodal size distribution. However, results can be simulated for cylindrical pore which mimics carbon nano tubes and the simulated results can be compared with experimental sorption data available in the literature. Alternatively, orientation averaged intermolecular potentials should be tested for a variety of polar molecules by predicting vapor—liquid equilibrium properties.

3. In chapters 5 and 6 attempts have been made to mimic surfaces of real activated carbon by providing functional sites on the graphitic plates. However, carbons with other types of functional sites, especially lactone, lactols and carboxylic anhydride, should be simulated. It would be also interesting to characterize sorption in carbons with more than one type of functional sites and different combinations of them to decide the sorption capacity ranges of activated carbons.

4. In chapter 7, simulations in zeolites especially with silicalite, mordenite, and beta were obtained for very high Si/Al ratios (from 200 – 50). Sorption capacities at low Si/Al should be evaluated.

5. In chapters 5 and 7 all simulations on zeolites (Zeolite-X, silicalite, beta, and mordenite) were performed with sodium cations . However, it would be interesting to see how the affinity of mercury chloride, HCN, and MEK change with different size of mono-valent cations especially K^+, H^+, Ag^+, and Li^+ and divalent cations Ca, Mg, Ba, and Sr.

6. There is a need of experimental data available for HCN, MEK and $HgCl_2$ sorption on the adsorbents discussed in chapters 5 and 7 to compare simulated results in order to test zeolite models and force fields used to simulate sorption isotherms.

7. Based on the studies on mean field perturbation theory in chapters 4 and 5 and GCMC simulations in chapters 6-8, the following comparison can be made (Please see table 9.1). The computational time is the time to generate one data point in the adsorption isotherm. (Please notice that the basis for computational time is 3GH Intel processor with 512 MB RAM .)   The table 1 suggests that atomistic GCMC simulation technique can simulate sorption behaviors of large complex molecules (molecules with size greater than 6 Å) in the crystalline sorbents with complicated geometry(like zeolites) , however it requires sophisticated computational resources especially computers with 10-15 processors .This approach may require additional techniques of inserting large molecules in the sorbent's frame work. It can also be used for simulating small

molecule's sorption behaviors and can be considered as a widely used and useful technique.

Table 9.1 Comparison of different methodology for predicting sorption isotherms

	Analytical	Numerical (Monte-Carlo)	
	-Mean Field/DFTs	Molecular approach	Atom based simulation
Computational Time	Few secs.	Hours	1 day
Sorbent Geometry	Regular shape	Regular shape	All types
Sorbent Heterogeneity	Seldom	yes	yes
Rely on:	Molecular properties	Molecular properties	Atomic charge and atom size
Advantages	All thermodynamic functions	Accounts orientation dependency of electrostatic interactions	Account shape effects Suitable for large molecules
Limitations	Limited applicability	-Less suitable for molecules more than 6 Å -Doesn't account molecular shape effects	Heavy reliance on accurate atomic charge and their size values
Examples:	Sorption in graphitic carbon, dealuminated zeolite Y, silicalite-1	Sorption in activated carbon	Sorption in Zeolite-X, mordenites, zeolite beta

Appendix A

Characterization of the terms in Eqn. (5.15)

The pore density of component 2 is given by

$$\rho_{p2} = \frac{N_2}{As_z} \tag{A.1}$$

with:

$$a_{p2} = a_{b2}\left[1 - \left(\frac{3\sigma_{ff22}/\sigma_{fw2}}{4(\xi_2 - 2)}\right) + \left(\frac{\sigma^3_{ff22}/\sigma^3_{fw2}}{8(\xi_2 - 2)^3}\right)\right] \tag{A.2}$$

$$a_{b2} = \frac{8\pi\varepsilon_{ff22}\sigma^3_{ff22}}{3} \tag{A.3}$$

$$\xi_2 = s_z/\sigma_{fw2} \tag{A.4}$$

$$\sigma_{fw2} = \left(\sigma_{ff22}\sigma_w\right)^{1/2} \tag{A.5}$$

Characterization of the terms in Eqn. (5.16)

$$a_{p121} = a_{b121}\left[1 - \left(\frac{3\sigma_{ff12}/\sigma_{fw12}}{4(\xi_1 - 2)}\right) + \left(\frac{\sigma^3_{ff12}/\sigma^3_{fw12}}{8(\xi_1 - 2)^3}\right)\right] \tag{A.6}$$

$$a_{b121} = \frac{8\pi\varepsilon_{ff12}\sigma^3_{12}}{3} \tag{A.7}$$

$$\varepsilon_{ff12} = \left(\varepsilon_{ff1}\varepsilon_{ff2}\right)^{1/2} \tag{A.8}$$

$$\sigma_{fw12} = (1/3)(\sigma_{ff11} + \sigma_{ff22} + \sigma_w) \tag{A.9}$$

$$\sigma_{ff12} = (1/2)(\sigma_{ff11} + \sigma_{ff22}) \tag{A.10}$$

Characterization of the terms in Eqn. (5.24)

$$a_{p22} = \frac{4\pi a_{p2}}{3\sigma_{ff22}^3(s_z - 2\sigma_{fw2})}\left[-\frac{3}{2}\sigma_{ff22} + 2(s_z - 2\sigma_{fw2}) + \frac{\sigma_{ff22}^3}{4(s_z - 2\sigma_{fw2})^2}\right] \tag{A.11}$$

$$a_{p2} = \frac{1}{(4\pi\varepsilon_0)^2}\left[\left(\frac{2\mu_2^4}{3kT}\right) + 2\mu_2^2\alpha_2 + \left(\frac{3\alpha_2^2 I_2}{4}\right)\right] \tag{A.12}$$

Characterization of the terms in Eqn.(5.25)

$$a_{p121} = \frac{4\pi a_{p12}}{3\sigma_{ff12}^3(s_z - 2\sigma_{fw12})}\left[-\frac{3}{2}\sigma_{ff12} + 2(s_z - 2\sigma_{fw12}) + \frac{\sigma_{ff12}^3}{4(s_z - 2\sigma_{fw12})^2}\right] \tag{A.13}$$

where,

$$a_{p12} = \frac{1}{(4\pi\varepsilon_0)^2}\left[\left(\frac{3\alpha_1\alpha_2 (I_1 + I_2)}{I_1 I_2 4}\right)\right] + \frac{1}{(4\pi\varepsilon_0)^2}\left[\frac{\mu_1^2\mu_2^2}{3kT} + \mu_1^2\alpha_2 + \mu_2^2\alpha_1\right] \tag{A.14}$$

The chemical potentials for components 1 and 2 can be calculated as follows:

$$\left(\frac{\partial F_P}{\partial N_1}\right)_{N_2,T,V} = \mu_{P1} \tag{A.15}$$

$$\left(\frac{\partial F_P}{\partial N_2}\right)_{N_1,T,V} = \mu_{P2} \tag{A.16}$$

$$\left(\frac{\partial F_b}{\partial N_1}\right)_{N_2,T,V} = \mu_{b1} \tag{A.17}$$

163

$$\left(\frac{\partial F_b}{\partial N_2} \right)_{N_1,T,V} = \mu_{b2} \tag{A.18}$$

The chemical potentials of components 1 and 2 in the pore phase can be calculated as follows:

$$\mu_{P1} = \beta^{-1} \left[\frac{b_{p1}(\rho_{p1} + \rho_{p2})}{(1 - \rho_{p1}b_{p1} - \rho_{p2}b_{p2})} + \ln(1 - \rho_{p1}b_{p1} - \rho_{p2}b_{p2}) - \ln(\rho_{p1}\lambda_1^3) \right] + \psi_1$$
$$- 2a_{p1}\rho_{p1} - 2a_{p12}\rho_{p1} \tag{A.19}$$

$$\mu_{P2} = \beta^{-1} \left[\frac{b_{p2}(\rho_{p1} + \rho_{p2})}{(1 - \rho_{p1}b_{p1} - \rho_{p2}b_{p2})} + \ln(1 - \rho_{p1}b_{p1} - \rho_{p2}b_{p2}) - \ln(\rho_{p2}\lambda_2^3) \right]$$
$$+ \psi_2 - 2a_{p2}\rho_{p2} \tag{A.20}$$

The chemical potentials of components 1 and 2 in the bulk phase can be calculated as follows:

For $\rho_{b1} < \rho_{b2}$,

$$\mu_{b1} = \beta^{-1} \left[\frac{b_{b1}(\rho_{b1} + \rho_{b2})}{(1 - \rho_{b1}b_{b1} - \rho_{b2}b_{b2})} + \ln(1 - \rho_{b1}b_{b1} - \rho_{b2}b_{b2}) - \ln(\rho_{b1}\lambda_1^3) \right]$$
$$- 2a_{b1}\rho_{b1} - 2a_{b12}\rho_{b1} \tag{A.21}$$

$$\mu_{b2} = \beta^{-1} \left[\frac{b_{b2}(\rho_{b1} + \rho_{b2})}{(1 - \rho_{b1}b_{b2} - \rho_{b2}b_{b2})} + \ln(1 - \rho_{b1}b_{b1} - \rho_{b2}b_{b2}) - \ln(\rho_{b2}\lambda_2^3) \right]$$
$$- 2a_{b2}\rho_{b2} \tag{A.22}$$

While for, $\rho_{b2} < \rho_{b1}$

$$\mu_{b1} = \beta^{-1} \left[\frac{b_{b1}(\rho_{b1} + \rho_{b2})}{(1 - \rho_{b1}b_{b1} - \rho_{b2}b_{b2})} + \ln(1 - \rho_{b1}b_{b1} - \rho_{b2}b_{b2}) - \ln(\rho_{b1}\lambda_1^3) \right] - 2a_{b1}\rho_{b1} \tag{A.23}$$

$$\mu_{b2} = \beta^{-1}\left[\frac{b_{b2}(\rho_{b1} + \rho_{b2})}{(1 - \rho_{b1}b_{b2} - \rho_{b2}b_{b2})} + \ln(1 - \rho_{b1}b_{b1} - \rho_{b2}b_{b2}) - \ln(\rho_{b2}\lambda_2^3)\right] - 2a_{b2}\rho_{b2}$$

$$- 2a_{b12}\rho_{b2}$$

(A.24)